Low-energy electron interactions with two organometallic precursors for focused electron beam induced deposition: (η^3-C_3H_5)$Ru(CO)_3Br$ and (η^5-Cp)$Fe(CO)_2Mn(CO)_5$

Rachel M. Thorman

Faculty of Physical Sciences
University of Iceland
2017

Low-energy electron interactions with two organometallic precursors for focused electron beam induced deposition: (η^3-C_3H_5)$Ru(CO)_3Br$ and (η^5-Cp)$Fe(CO)_2Mn(CO)_5$

Rachel M. Thorman

Dissertation submitted in partial fulfillment of a
Philosophiae Doctor degree in Chemistry

Advisor
Oddur Ingólfsson

PhD Committee
Prof. D. Howard Fairbrother
Dr. Ivo Utke

Opponents
Prof. Dr. Petra Swiderek
University of Bremen, Germany
Prof. Dr. Hubertus Marbach
University of Erlangen-Nuremberg, Germany

Faculty of Physical Sciences
School of Engineering and Natural Sciences
University of Iceland
Reykjavik, October 2017

Low-energy electron interactions with two organometallic precursors for focused electron beam induced deposition: (η^3-C_3H_5)$Ru(CO)_3Br$ and (η^5-Cp)$Fe(CO)_2Mn(CO)_5$

Dissertation submitted in partial fulfillment of a *Philosophiae Doctor* degree in Chemistry

Faculty of Physical Sciences
School of Engineering and Natural Sciences
University of Iceland
Hjarðarhagi 2-6
107 Reykjavík, Reykjavik
Iceland

Telephone: 525-4000

Bibliographic information:
Rachel M. Thorman, 2017, *Low-energy electron interactions with two organometallic precursors for focused electron beam induced deposition: (η^3-C_3H_5)$Ru(CO)_3Br$ and (η^5-Cp)$Fe(CO)_2Mn(CO)_5$*, PhD dissertation, Faculty of Physical Sciences, University of Iceland, 130 pp.

ISBN XXISBN

Printing: XXPrinter
Reykjavik, Iceland, October 2017

Abstract

Focused electron beam induced deposition (FEBID) is a nanofabrication technique wherein electron-induced reactions are used to deposit pure metals from organometallic precursors under the area of a primary electron beam. It can be used to directly write three-dimensional nanostructures onto surfaces with uneven topographies, making it a distinctly versatile technique in the field of nanofabrication. However, FEBID currently faces two major limitations: deposit purity is limited by incomplete precursor decomposition and resolution is limited by deposition outside the area of the primary electron beam. Low-energy secondary electrons, which comprise a large proportion of the secondary electron spectrum of a surface impacted by a high-energy electron beam, have been shown to initiate deposition of FEBID precursors. Additionally, they are emitted from substrates in radii several orders of magnitude larger than the primary electron beam and to initiate reactions that produce incomplete ligand dissociation in organometallic molecules. Since the effect of low-energy secondary electrons cannot be directly examined *in situ* in FEBID, their role must be studied in other ways.

Gas phase experiments using crossed molecular/electron beam instruments can elucidate the fundamental low-energy electron-induced reactions that may initiate deposition in FEBID. Such experiments are performed under single-collision conditions, wherein an isolated molecule may interact with a single electron of well-defined energy, and ion production as a function of incident electron energy may be measured. At the lowest incident electron energies, an electron may be captured by a molecule, producing a transient negative ion (TNI). Transient negative ion formation can be seen as a vertical transition from the ground state of the neutral parent into a vibrationally and/or electronically excited state of the anion, which may then relax by re-emission of the electron (in electron scattering) or by dissociation. Dissociation of TNIs, called dissociative electron attachment (DEA), produces an anionic fragment and one or more neutral fragments, all of which may be produced in vibrationally and/or electronically excited states. Although single bond rupture generally has the highest cross-section for DEA to a given molecule, DEA can also produce complex molecular rearrangements and even bond formation. At higher energies, incident electrons may ionize a molecule, which may then dissociate in a process called dissociative ionization (DI). Dissociative ionization is generally associated with multiple bond ruptures. These are two low-energy electron-initiated processes relevant in FEBID.

The aim of this PhD project has been to study the effects of low-energy electron impact on organometallic FEBID precursors in the gas phase, with emphasis on DEA and DI, and to use insights gleaned from gas phase experiments to predict the viability

of these precursors for use in FEBID. Additionally, quantum chemical calculations are used to better understand the dynamics of dissociation of these precursors via DEA and DI. Two precursors were selected for study. First, $(\eta^3\text{-}C_3H_5)Ru(CO)_3Br$ was studied to compare the relative lability of π-facial ligands, carbonyls, and halides upon electron impact, in order to determine their utility in FEBID precursors. Further, $(\eta^5\text{-}Cp)Fe(CO)_2Mn(CO)_5$ was studied in order to explore the electronic structure of heteronuclear organometallic precursors and to predict its efficacy in the deposition of alloyed nanostructures. The gas phase results for each of these molecules were compared to surface studies performed by our collaborators in the Fairbrother group at Johns Hopkins University, and $(\eta^3\text{-}C_3H_5)Ru(CO)_3Br$ was additionally deposited under *in situ* FEBID conditions at EMPA in Thun, Switzerland. It is hoped that these contributions may expand knowledge in the field of electron-initiated reactions of organometallic FEBID precursors, particularly in the area of precursor design.

Útdráttur

Örprentun með skörpum rafeindageisla (e. Focused Electron Beam Induced Deposition, FEBID) er aðferð þar sem rafeindahvötuð efnahvörf eru notuð til að fella út hreina málma úr málm-lífrænum sameindum, svokölluðum forverasameindum. Með þessari tækni má með beinum hætti mynda þrívíða strúktúra á nanóskala á ójöfn yfirborð, sem býður upp á gríðarmikla möguleika. FEBID er þó enn sem komið er haldið töluverðum annmörkum: hreinleikinn er takmarkaður vegna ófullkomins niðurbrots forverasameindanna og upplausnin er takmörkuð vegna útfellinga utan rafeindageislans. Fjöldi lágorkurafeinda losna fyrir hverja rafeind úr rafeindageislanum sem rekst á yfirborðið og sýnt hefur verið fram á að slíkar lágorkurafeindir valda niðrubroti á forverasameindum í FEBID. Þessar lágorkurafeindir hafa áhrif langt utan rafeindageislans og hvata efnahvörf sem leiða af sér ófullkomið niðurbrot málm-lífrænu forverasameindanna. Þar sem ekki er hægt að rannsaka áhrif lágorkurafeinda í FEBID með beinum hætti, *in situ*, verður að gera það á annan veg.

Þvergeislatilraunir, þar sem sameinda- og rafeindageislar mætast undir réttu horni, geta sýnt fram á hvaða lágorku-rafeindadrifin efnahvörf skipta máli í FEBID. Slíkar tilraunir eru framkvæmdar við lágan þrýsting þar sem stakar sameindir hvarfast við stakar rafeindir með þekkta hreyfiroku. Með því móti má mæla magn jóna sem myndast sem fall af hreyfiorku rafeinda. Við árekstur lágorkurafeindar við sameind getur myndast svokölluð tímabundin neikvæð jón (e. Transient Negative Ion, TNI). Slíka jónir myndast yfirleitt í örvuðu titrings- og eða rafeindaástandi og verða því að leita leiða tli slökunar. Slík slökun getur átt sér stað með útkasti rafeindarinnar eða með rofi efnatengja. Síðarnefnda ferlið kallast rjúfandi rafeindarálagning (e. Dissociative Electron Attachment, DEA). Í DEA myndast ein neikvætt hlaðin jón og eitt eða fleiri óhlaðið niðurbrot sem öll geta verið í örvuðu ástandi. Þó rof á einu efnatengi sé líklegast í DEA geta einnig átt sér stað flókin umröðum og jafnvel tengjamyndun í ferlinu. Við hærri hreyfiorku rafeinda geta sameindir jónast og svo brotnað niður í ferli sem kallast rjúfandi jónun (e. Dissociative Ionization, DI). Í DI rofna vanalega fleiri en eitt efnatengi. Þessi tvö ferli, DEA og DI, eru tvö af nokkrum lágorkuferlum sem hafa líklega mest áhrif á FEBID.

Í þessu doktorsverkefni voru árekstrar lágorkurafeinda við málm-lífrænar FEBID forverasameindir rannsakaðar m.t.t. bæði DEA og DI. Þessar mælingar voru notar til að meta líkurnar á að þessar sameindir séu hentugar sem forverar í FEBID. Auk þess, var skammtafræðilegum útreikningum beitt til að fá betri innsýn í hvarfganga niðurbrotanna. Tvær sameindir voru skoðaðar, þ.e. $(\eta^3\text{-}C_3H_5)Ru(CO)_3Br$ og $(\eta^5\text{-}Cp)Fe(CO)_2Mn(CO)_5$. Sú fyrrnefnda var valin því hún inniheldur þrjár tengundir

tengla, þ.e. π-tengda, carbonyl hópa og halíð hóp. Niðurbrot þessara tengla voru metin innbyrgðis og því var hægt að áætla hvernig hver og einn hentar í FEBID. Síðari sameindin var valin til að rannsaka útfellingu á málmblendi á yfirborð. Mælingar á þessum sameindum í gasfasa voru bornar saman við mælingar á yfirborðum en einnig var $(\eta^3\text{-}C_3H_5)Ru(CO)_3Br$ skoðuð sérstaklega í FEBID. Þessar rannsóknir hjálpa til við skilning á því hver hlutverk lágorkurafeinda er í FEBID og einnig við að hanna forverasameindir sem hentugar eru í ferlið.

Dedication

To my parents, who have always told me I could do this.

Table of Contents

List of Figures

List of Tables

List of Original Papers

I: **The role of low-energy electrons in focused electron beam induced deposition: four case studies of representative precursors**
Rachel M. Thorman, Ragesh Kumar T. P., D. Howard Fairbrother and Oddur Ingólfsson
Beilstein J. Nanotechnol., 2015, 6, 1904–1926.

II: **Computational study of dissociative electron attachment to π-allyl ruthenium (II) tricarbonyl bromide**
Rachel M. Thorman, Ragnar Bjornsson, and Oddur Ingólfsson
Eur. Phys. J. D, 2016, 70, 164

III: **Low energy electron-induced decomposition of (η^3-C_3H_5)$Ru(CO)_3Br$, a potential focused electron beam induced deposition precursor with a heteroleptic ligand set**
Rachel M. Thorman, Joseph A. Brannaka, Lisa McElwee-White and Oddur Ingólfsson
Phys.Chem.Chem.Phys., 2017, 19, 13264

IV: **Low energy electron-induced decomposition of (η^5-Cp)$Fe(CO)_2Mn(CO)_5$, a potential bimetallic precursor for focused electron beam induced deposition of alloy structures**
Rachel M. Thorman, Ilyas Unlu, Kelsea Johnson, Ragnar Bjornsson, Lisa McElwee- White, Howard Fairbrother and Oddur Ingólfsson
submitted

Abbreviations

AD	Autodetachment
AE	Appearance energy
AES	Auger electron spectroscopy
AFM	Atomic force microscopy
BDE	Bond dissociation energy
BSE	Backscattered electron
CVD	Chemical vapor deposition
DD	Dipolar dissociation
DEA	Dissociative electron attachment
DFT	Density functional theory
DI	Dissociative ionization
DLPNO	Domain-based local pair natural orbital
EA	Electron affinity
EC	Electron capture
ECP	Effective core potential
EDX	Energy dispersive X-ray spectroscopy
EELS	Electron energy loss spectroscopy
FCF	Franck-Condon Factor
FEBID	Focused electron beam induced deposition
FWHM	Full-width-at-half-maximum
GGA	Generalized gradient approximation
GIS	Gas inlet system
HOMO	Highest-occupied molecular orbital
IVR	Intramolecular vibrational energy redistribution
LEE	Low-energy electron
LPNO	Local pair natural orbital
LUMO	Lowest-occupied molecular orbital
MS	Mass spectroscopy
ND	Neutral dissociation
SE	Secondary electron
SEM	Secondary electron microscope
SIGMA	SImply a Gas-phase MAchine
SOMO	Singly-occupied molecular orbital
TEM	Trochoidal electron monochromator
TNI	Transient negative ion
UHV	Ultra high vacuum
XPS	X-ray photoelectron spectroscopy
ZPE	Zero point energy

Acknowledgments

I would like to first and foremost thank the Icelandic Center for Research (RANNÍS) for my stipend and the University of Iceland Research fund for project related funding. I would additionally like to thank COST Action CM1301 (CELINA) for funding a short-term scientific mission to EMPA in Thun, Switzerland, as well as for providing a forum for scientific collaboration and inspiration.

I would additionally like to thank my advisor at the University of Iceland, Prof. Oddur Ingólfsson, for his effortless conviviality and for giving me the opportunity to work on this project, as well as for his feedback and editing on all my writing. I would also like to thank the past and present members of my research group, especially Mr. Ragesh Kumar T P, Dr. Benedikt Ómarsson, and Dr. Frímann Ómarsson, for teaching me how to use all of this instrumentation and giving support and feedback on my results. I would especially like to thank Dr. Frímann Ómarsson for translating my abstract into Icelandic. Additional thanks go to Dr. Ragnar Björnsson for teaching me everything I know about computational chemistry.

I would also like to thank Prof. Howard Fairbrother for starting me on this project and sending me to Iceland, as well as for being on my PhD committee. Additionally, I would like to thank Dr. Ivo Utke for being on my PhD committee and his colleagues at EMPA for their tutelage in FEBID. I would also like to thank Prof. Petra Swiderek and Prof. Hubertus Marbach for taking the role of opponents to my doctoral defense.

Finally, I would like to thank my friends and family for their love and support. Thank you to my Raunó friends, for welcoming me and making me feel at home in a country where I had no built-in safety net. Thank you to my parents: Dr. Raymond Thorman, Patricia Thorman, and Dr. John Hallowell, for your constant encouragement and support. I couldn't have made this work for the past four years without you. Last, but not least, I'd like to thank my boyfriend, Þórarinn Jónmundsson, for his love, support, patience, and a large quantity of Twix bars - we make a really good team.

1 Introduction

The interactions of electrons with molecules is of fundamental importance in chemistry. Electron density between atoms is the essential nature of covalent bonding; electron interaction with molecules can form and break bonds, excite molecules to increase reactivity, and even rearrange the structure of molecules. The product of electron-molecule interactions depends primarily on the energy of the impinging electron. High energy electrons (typically greater than 0.5 keV) are used in electron microscopy, wherein a surface is irradiated with a high energy, tightly focused electron beam. Mapping of nanoscale surface topography and composition at high-resolution can be performed using secondary electron microscopy (SEM) by detecting secondary electrons (SEs) and backscattered electrons (BSEs) emitted from the surface,[1] or using tunneling electron microscopy by detecting electrons that have been transmitted through 100 nm thin samples.[2] High energy electron beams can also be used to detect surface composition through Auger electron spectroscopy (AES), wherein high energy electrons stimulate the emission of Auger electrons from the first 2 nm of a surface, or energy-dispersive X-ray spectroscopy (EDS), wherein high energy electrons stimulate emission of characteristic X-rays from 1-2 μm into a surface.[3]

Low energy electrons (LEEs) produce significantly different interactions with molecules and surfaces. At low energies (generally < 20 eV), electrons can attach to molecules, producing unstable and reactive temporary negative ions (TNIs) which may then dissociate into neutral radical(s) and anionic fragments via dissociative electron attachment (DEA). Attachment is most efficient close to 0 eV, and high cross-sections are thus seen for these reactions at energies close to 0 eV.[4] These fragments, which may also be produced in excited states, can precipitate a chain of further reactions.[5] For example, DEA was found to produce F^- from surface NF_3 clusters mixed with CH_3Cl; the fluoride anions went on to initiate an S_N2 reaction with the CH_3Cl, yielding CH_3F.[6,7] DEA-initiated reactions have also been found to produce hydrogen peroxide in water ice,[8] as well as ozone in condensed diatomic oxygen films.[9] DEA has also been found to produce significant molecular rearrangement in some molecules;[5] see, e.g., DEA studies to tetrafluoro-*para*-benzoquinone,[10] several fluorinated benzene derivatives,[11] and formamide.[12] At energies at or above the ionization threshold of molecules, electron impact can produce positively charged species that may also dissociate into positive ions and neutral species. This process, called dissociative ionization (DI), can also produce excited radical and ionic species that can precipitate further reactions.[5,13,14] Electron-induced excitation of molecules can also produce neutral radical fragments via neutral dissociation (ND) or positive and negative ions via dipolar dissociation (DD), both of which may produce reactive, excited-state fragments. In each of these reaction

mechanisms, we can see that a single, low energy electron can interact with a molecule in order to yield considerable complex reactivity.

The reactivity of LEEs with molecules is thus relevant to multiple fields. LEEs produced by the interaction of high energy radiation (e.g. cosmic rays) with matter in space are known to induce reactions in interstellar ices and dust.[8,15] Additionally, free electrons within plasmas are known to have significant effect on plasma discharge processes.[16] Low energy electrons are also known to induce degradation of DNA.[17,18] In electron microscopy and spectroscopy, high energy electron beams impinging upon surfaces produce a broad spectrum of secondary electrons (SEs), the majority of which are produced at low energy.[19–21] The SEs produced in SEMs and transmission electron microscopes are thus generally well within the energy range of the reactions described above. Indeed, the first description of electron beam-induced deposition was from background gases in a secondary electron microscope in 1934![20,22] While this was initially considered a negative side effect of electron irradiation that should be avoided, it was later put to use depositing films.[20,23,24] Electron beams have more recently been used to purposefully deposit nanostructures on surfaces via focused electron beam induced deposition (FEBID).[5,19,20,25,26]

In FEBID, a tightly focused, high-energy electron beam in a high vacuum chamber is used to directly deposit nanostructures onto surfaces.[5,19,20,26] Precursor gases, which are generally organometallic molecules, are adsorbed onto a substrate and exposed to the electron beam. Ideally, the organometallic precursor molecules will fully dissociate under the area of the primary electron beam via electron-induced reactions, the metal centers will be deposited onto the surface and the volatile organic ligands will be pumped away. The electron beam can then be rastered around the surface to directly write a two dimensional design. The third dimension can be controlled via the dwell time, and FEBID can be used thus to deposit three dimensional nanostructures of nearly any design onto surfaces with any topographical features. FEBID can theoretically deposit nanostructures with a significantly higher spatial resolution[27] than conventional photolithography techniques, due to the tighter focus attainable for electron beams when compared to photon beams.[2] However, there are presently two major problems facing the use of FEBID for nanofabrication: (a) ligand contamination of FEBID deposits and (b) deposition outside the area of the primary electron beam. LEEs have been found to play a significant role in deposition of FEBID precursor molecules,[5,28] and contribute to both problems facing FEBID. It is thus important to understand the chemistry and physics of LEE interactions with organometallic FEBID precursors in order to optimize the use of FEBID as a nanofabrication tool.

Optimization of nanostructure fabrication using FEBID is a problem that can be attacked from multiple angles. During deposition, substrate heating has led to higher deposit metal purity for many studied compounds, likely due to less ligand codeposition.[20,29–31] Post-deposition processing is another popular method for purification of FEBID structures. Annealing deposited FEBID structures has been found to sometimes improve conductivity and purity. For example, *in vacuo* annealing of amorphous iron and carbon deposited from $Fe(CO)_5$ produced a crystalline mixture of carbides and α-iron.[32–34] Annealing can also be combined with use of reactive gases - see, e.g. the

annealing of deposits from WF_6 under an atmosphere of H_2.[35] Electron beam irradiation after deposition has been found to improve the conductivity of FEBID-deposited structures; this is potentially due to further decomposition of incompletely-dissociated organometallic precursors, removing co-deposited ligands.[36–39] Both methods can also change the nanostructure morphology, which may have a positive effect on FEBID-deposited nanostructures; however, they may also produce structural deformation.

Another avenue towards improving the quality of FEBID-grown nanostructures is via precursor design. Precursors used in FEBID have historically been used in chemical vapor deposition (CVD), a nanofabrication technique in which thin films of physisorbed organometallic precursors are heated in order to deposit a thin film of pure metal on a surface under high vacuum conditions.[19] Because of this, many precursors currently used for FEBID are optimized toward thermally-induced decomposition, and may not be ideal for decomposition using electron-initiated reactions. In order to optimize organometallic precursors for FEBID, then, it is important (i) to understand the LEE-induced reactions that induce deposition in FEBID and (ii) to compare various ligands used in precursor design for their suitability to FEBID. Additionally, as previously described, LEE-induced reactions can yield complex reactivity profiles, including producing reactive cation, anion, and radical species as well as extensive intramolecular rearrangement. It is possible, then, for FEBID researchers to design such complex reactivity into precursors. For example, one might imagine designing a precursor that takes advantage of the high electron affinity of a halide group to induce more complete dissociation via electron attachment. Another route might be to benefit from energy gained via bond formation, as seen in the formation of a CN triple bond and recombination of neutral fragments to H_2O in DEA to formamide,[5,12] or in the HF bond formation and rearrangement seen in electron attachment to several fluorinated benzene derivatives.[11]

Motivated by the potential importance of ligand architecture to deposition of FEBID precursors, we studied electron-induced dissociation of the potential FEBID precursor η^3-allyl ruthenium tricarbonyl bromide ((η^3-C_3H_5)$Ru(CO)_3Br$) in the gas phase and under deposition conditions.[40] We performed quantum chemical calculations of the energetic thresholds for DEA-induced dissociation pathways observed experimentally and compared several different levels of quantum chemical theory for their ability to accurately predict these thresholds in organometallic molecules.[41] We were also able to compare our gas phase data with surface science research performed by Spencer et al.[38] on this same molecule. Finally, we were able to deposit this precursor under FEBID conditions and compare it to a similar deposition of $Ru_3(CO)_{12}$, a precursor previously synthesized for use in CVD. The ruthenium-centered organometallic precursor (η^3-C_3H_5)$Ru(CO)_3Br$ was chosen specifically for its ligand architecture. It contains three ligands commonly found in FEBID precursors: a polyhapto π-facial ligand (the η^3-allyl), three carbonyl ligands, and a halide. By combining these three ligands in one organometallic precursor molecule, we were able to compare the varying types of ligands for their utility in FEBID. Further, by comparing our gas phase data with *in-situ* deposition data, we were able to shed some light on the value of using such gas phase data to predict FEBID deposit quality.

Deposition of alloyed nanostructures using FEBID has produced its own array of challenges. Alloy deposition has not as of yet been as extensively studied as elemental metal deposition; however, two main strategies toward alloy deposition have been employed: use of mixed precursor gases and use of multiple gas injection systems. These approaches have some potential advantages − use of multiple precursor gases can theoretically improve the flexibility of FEBID by producing nanostructures of tunable metal ratios. This has been found practicable in the deposition of CoSi nanostructures from $Co_2(CO)_8$ and Si_5H_{12}[42] and in the deposition of AuFe nanostructures from $Me_2AuC_5H_6F_3O_2$ and $Fe(CO)_5$.[43] However, some challenges also face these deposition strategies. The AuFe nanostructures previously mentioned had over 60 at.% carbon and oxygen contamination, and indeed ligand codeposition can be an even greater issue with the use of multiple precursors than with the use of a single precursor, as the number of ligands to dissociate from the metal centers increases. Another issue is inhomogeneity of the deposited nanostructures. An endeavor to deposit alloyed CoSi nanopillars from $Co_2(CO)_8$ and $Si(OC_2H_5)_4$ produced Co growth on the outside of the pillar, with silicon oxide growth inside the pillar.[44] Reproducibility of deposit metal ratios may also be a concern.

A recent study has aimed to combat some of these issues by using a single bimetallic precursor to directly grow an alloy. Poratti et al. used $HFeCo_3(CO)_{12}$ to grow a FeCo alloy at 80 at.% metal content with roughly 3:1 Co to Fe ratio (i.e. stoichiometric).[45] This precursor was further studied in the gas phase and in surface studies in order to determine the source of its exceptional FEBID behavior.[46–48] It was ultimately found to have interesting properties in DEA − it was found to be susceptible to DEA at up to 20 eV incident electron energy, which is higher than previously-reported DEA ion yields, with quasi-continuous electron attachment from approximately 1 eV up to 20 eV.[46,47] This unusual behavior was attributed to high density of metal-based highest occupied molecular orbitals (HOMOs) and low-energy CO π^* lowest unoccupied molecular orbitals (LUMOs); however, it seems that this unusual DEA behavior and molecular orbital structure is possibly not to thank for its high-quality FEBID deposits. Instead, it is possible that the high-purity FEBID deposits are achieved by thermal dissociation of CO ligands during deposition.[48,49]

Motivated by the prior success and intriguing behavior of $HFeCo_3(CO)_{12}$ both in the gas phase and under FEBID conditions, we have performed a gas phase study on DEA and DI to a smaller bimetallic iron-manganese precursor: cyclopentadienyl iron dicarbonyl manganese pentacarbonyl ($(\eta^5\text{-Cp})Fe(CO)_2Mn(CO)_5$).[50] We also performed quantum chemical calculations on the thresholds and reaction dynamics of the most important channels for DEA and DI-induced dissociation in order to aid our interpretation of the gas phase data. Additionally, we compared our gas phase observations to surface studies performed on the same precursor by collaborators in the Fairbrother lab at Johns Hopkins University. Ultimately, we aim to predict the viability of depositing an FeMn alloy in FEBID using this precursor by understanding the mechanisms of metal deposition for the molecule, as well as to suggests improvements to the design of future precursor molecules for deposition of alloyed nanostructures.

In chapter 2, I describe in detail the fundamental physical chemistry behind low-

energy gas phase electron-molecule interactions relevant to FEBID. In particular, I focus on the formation and decay of negative ions via electron capture as well as the formation and decay of positive ions via electron impact. Finally, I give an overview of fundamental electron interactions found in FEBID experiments. In chapter 3, I describe the experimental setup of the instrumentation used for both DEA and DI, the instrumentation used for FEBID experiments, and the relevant computational methods used for the quantum chemical calculations performed on both (η^3-C_3H_5)$Ru(CO)_3Br$ and (η^5-Cp)$Fe(CO)_2Mn(CO)_5$. In chapter 4, I give an overview of experimental results obtained in each of the previously described studies on (η^3-C_3H_5)$Ru(CO)_3Br$ and (η^5-Cp)$Fe(CO)_2Mn(CO)_5$. In chapter 4.1, I discuss the gas phase electron-induced dissociation of (η^3-C_3H_5)$Ru(CO)_3Br$ via DEA and via DI, and compare this to ultra-high vacuum (UHV) surface science studies of the precursor. I also discuss several quantum chemical computational methods used to calculate the DEA thresholds for observed fragments, and compare them to find the best method to use for calculations on DEA to organometallic FEBID precursors. Finally, I discuss the deposition of (η^3-C_3H_5)$Ru(CO)_3Br$ under FEBID conditions and compare it to the deposition of $Ru_3(CO)_{12}$. In chapter 4.2, I discuss the gas phase DEA- and DI-induced fragmentation of (η^5-Cp)$Fe(CO)_2Mn(CO)_5$, as well as quantum chemical calculations performed in order to aid interpretation of the gas phase behavior. I also compare this gas phase data to UHV surface science studies. Based on the results presented in chapter 4, I give a more generalized summary and outlook in chapter 5. Each study is described in more detail in the respective papers submitted as a part of this thesis.

2 Theoretical Overview

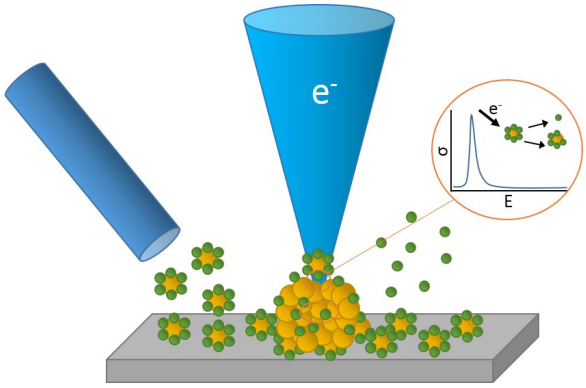

Figure 2.1. Schematic of the FEBID process. An organometallic precursor gas is introduced to a substrate under high vacuum via a gas inlet system (left). A high-energy, tightly-focused electron beam impacts the surface; electron-initiated reactions cause the metal center of the precursor to deposit under the area of the electron beam, while volatile ligands dissociate and are pumped away. We are interested in the underlying electron-initiated reactions that initiate the deposition process in FEBID.

The fundamental concept of focused electron beam induced deposition (FEBID) is relatively simple. A substrate is placed in a high vacuum chamber equipped with a high-energy electron beam, much like those found in a secondary electron microscope (SEM). Electron beams used in FEBID commonly range from 1-50 keV.[19,20,26] A precursor gas, frequently an organometallic molecule, is introduced into the chamber via a gas injection system (GIS) and is allowed to physisorb onto the substrate. Ideally, electron-driven reactions cause the desired metal to deposit under the area of the primary electron beam, while undesired organic ligands dissociate and are pumped away from the surface by the vacuum pumps. This is, of course, not necessarily what happens in a FEBID experiment and the understanding of fundamental electron-molecule interactions occurring in FEBID is paramount to the optimization of the FEBID process.[5,19,20,28]

Of initial importance in understanding these fundamental electron-molecule interactions is knowledge of the electrons available to initiate deposition at the precursor molecule/surface interface in FEBID experiments. Electron impact at a surface will

produce both elastically and inelastically scattered electrons, which will generate an energy profile of electrons from 0 eV up to the energy of the primary electron beam (see section 2.4).[19,20,51–54] Electrons at a surface may also be produced via other excitation processes, such as Auger electrons. Electrons may be scattered both inside and outside the area of the primary electron beam,[19–21,55] and the majority of these scattered electrons are produced at low energy, peaking well below 10 eV.[19,20,51–54] These low energy electrons (LEEs) are known to initiate deposition reactions in several studied precursors.[28,56–63] Understanding the reactions initiated by LEEs is therefore of central importance in FEBID. The fragmentation of molecules at low incident electron energies proceeds through four distinct processes: dissociative electron attachment (DEA), dissociative ionization (DI), neutral dissociation (ND), and dipolar dissociation (DD). These processes are depicted in equations 2.1 - 2.4, respectively.

$$AB + e^- \rightarrow [AB]^{(\ddagger)-} \rightarrow A^{(\ddagger)} + B^{(\ddagger)-} \tag{2.1}$$

$$AB + e^- \rightarrow [AB]^{(\ddagger)+} + 2e^- \rightarrow A^{(\ddagger)+} + B^{(\ddagger)} + 2e^- \tag{2.2}$$

$$AB + e^-(\varepsilon_1) \rightarrow [AB]^* + e^-(\varepsilon_2 < \varepsilon_1) \rightarrow A^{(\ddagger)} + B^{(\ddagger)} + + e^-(\varepsilon_2 < \varepsilon_1) \tag{2.3}$$

$$AB + e^-(\varepsilon_1) \rightarrow [AB]^* + e^-(\varepsilon_2 < \varepsilon_1) \rightarrow A^{(\ddagger)+} + B^{(\ddagger)-} + + e^-(\varepsilon_2 < \varepsilon_1) \tag{2.4}$$

In the above reactions, the ‡ symbol signifies that the parent ion or fragment(s) may be in vibrationally and/or electronically excited states, while the * symbol represents an electronically excited intermediate parent molecule leading to ND and DD. The ε_1 and ε_2 symbols denote the energy of the incident electron before and after the inelastic scattering event producing this excited intermediate. A brief description of ND and DD (equations 2.3 and 2.4, respectively) will be given here, while a more fundamental overview of DEA and DI will be given in sections 2.2.2 and 2.3, respectively, due to their overarching importance to this thesis.

Neutral dissociation is a non-resonant process wherein electron impact excites a molecule via an inelastic electron scattering event; the molecule then dissociates into two or more neutral fragments. As seen in eq. 2.3, the fragments may be produced at vibrationally or electronically excited states. The energetic threshold for ND is given purely by the bond dissociation energies (BDE) of the bonds broken during the process; this is commonly in the energy range of the lowest electronic transitions in the molecule.[64] Due to the lack of ionic products, ND has proven difficult to measure and has thus been a relatively neglected area of research. Recently, however, promising strides have been made by combining experimental studies of electronic excitation by electron impact and quantum chemical calculations of the excited state potential energy surfaces of $Pt(PF_3)_4$ in order to predict the relative importance of the ND channel for this molecule.[65]

Dipolar dissociation is a non-resonant process similar to ND; however, instead of dissociating into neutral fragments, the electronically excited parent molecule dissociates into an anion and a cation. The product anionic fragments may again be produced in vibrationally or electronically excited states, as seen in eq. 2.4. The energetic threshold for DD is given by the BDEs of bonds broken during the process and the ionization

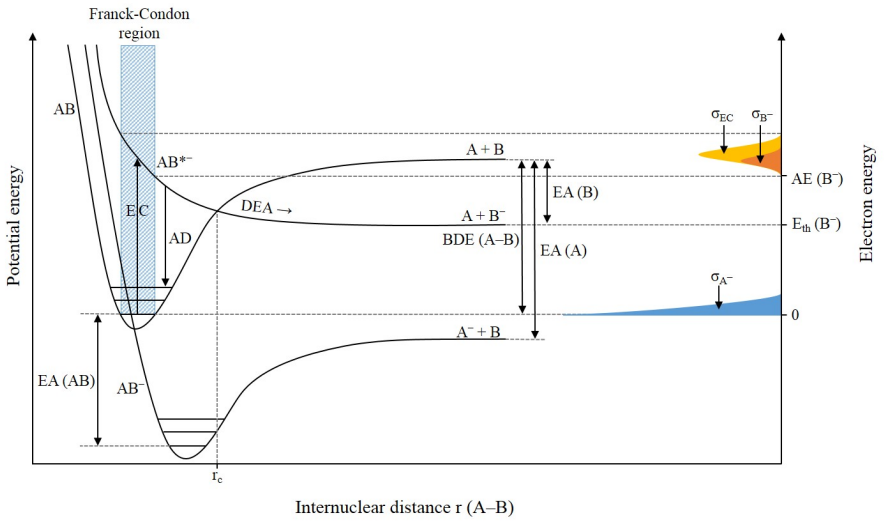

Figure 2.2. A depiction of electron attachment to a diatomic molecule AB. Electron attachment (also called electron capture, EC) from AB to AB$^{*}-$ *occurs within the Franck-Condon region, after which the molecule may relax by autodetachment (AD) or by dissociation (DEA). The bond dissociation energy (BDE) of A−B is also depicted, as are the electron affinities (EA) of AB, A, and B. Finally, the threshold energies and appearance energies of* A^- *and* B^- *are shown.*

energy of the cationic fragment minus the electron affinity of the anionic fragment. This process is likely less efficient than ND, however, as additional energy is required to overcome the coulombic attraction between the anionic and cationic fragments.

2.1 Transient negative ion formation

At the lowest incident electron energies, electron-molecule interactions are primarily governed by the formation of transient negative ions (TNIs, $AB^{(\ddagger)-}$ in eq. 2.1). Transient negative ions, also called resonances, are formed when a LEE attaches to a molecule. The electron affinity (EA) of a molecule is defined as the difference in energy between the ground state of the neutral molecule (E_n) and the ground state of the anion (E_a):

$$EA = -(E_a - E_n) \tag{2.5}$$

The EA of a molecule or fragment must therefore be positive in order to make a thermodynamically stable anion that may be measured via mass spectrometry.

According to the Franck-Condon principle, electronic transitions are swift compared

to nuclear motion, and so the point on the potential energy surface post-transition must lie directly above the point on the initial potential energy surface.[66] The electron capture process can thus be visualized as a vertical transition from the ground state of the parent molecule to accessible ground or excited states of the parent anion within the Franck-Condon region of overlap (see fig. 2.2). The probability of transition between the ground vibrational state of the neutral parent molecule to any vibrational state of the anion is therefore proportional to the square of the overlap integral of the vibrational wavefunction of the neutral ground state (Ψ_n) and that of the respective anionic state (Ψ_a), which may be vibrationally or electronically excited. This is known as the Franck-Condon factor (FCF, eq. 2.6):

$$FCF \propto |\langle \Psi_n | \Psi_a \rangle|^2 \tag{2.6}$$

If the ground state of the neutral molecule and that of the anion have the same geometries, a transition from the ground state of the molecule to the ground state of the anion will have the highest FCF and therefore the highest transition probability. However, as seen in fig. 2.2, the ground state geometry of the anion is generally quite different than that of the neutral molecule. Because of this, TNIs are formed via a vertical, rather than adiabatic, transition and generally in vibrationally or electronically excited anionic states, which must then redistribute excess energy via relaxation. The various ways in which TNIs may relax are shown visually in fig. 2.2 and discussed in section 2.2. The energy dependence of the cross section for electron capture (σ_{EC}) is approximated graphically in fig. 2.2 using the reflection principle. In this manner, the wavefunction of the initial state ($\langle \Psi_n |$, or a wavefunction on the potential energy curve AB in fig. 2.2) is reflected into the wavefunction of the final state ($|\Psi_a\rangle$, or a wavefunction on the potential energy curve AB^{*-} in fig. 2.2). The resulting cross-section is labeled σ_{EC} in fig. 2.2.

There are two main types of resonances formed when an electron is captured by a molecule: shape resonances and Feshbach resonances. These resonances are summarized in fig. 2.3. Generally, the difference between the two is that shape resonances are necessarily above the energy of the parent state, while Feshbach resonances are necessarily below. Each of these types of resonances may be core-excited, meaning that electronic excitation of a valent electron occurs concurrently with electron capture, or doubly core excited, etc.[67] Each of these types of resonances will be discussed in more detail in the following sections.

2.1.1 Single particle resonances

At electron energies below the lowest electronic excitation energies of the neutral molecule, electron capture proceeds via single particle shape resonances,[64] which are energetically slightly above the ground state of the neutral parent molecule, and via vibrational Feshbach resonances,[68] which are energetically below it. In-depth discussions of both shape and Feshbach resonances have been published previously,[64,67,69–72] and an overview of each will be given here. Generally speaking, shape resonances

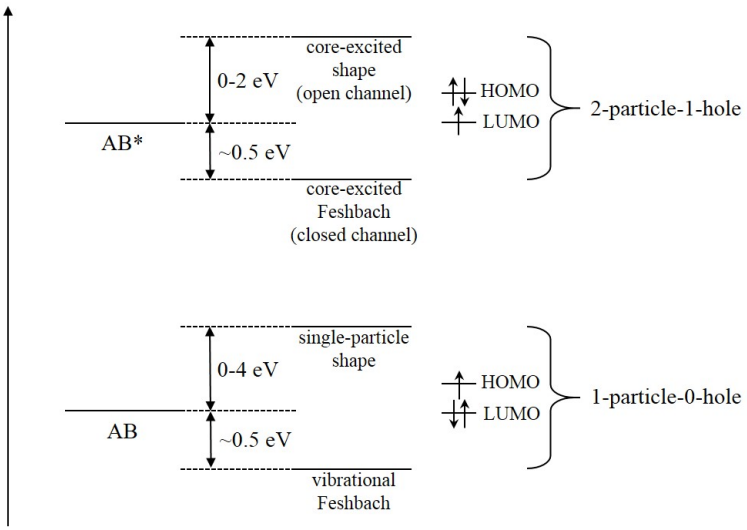

Figure 2.3. A schematic of the four main types of resonances. The two types of resonances that proceed from a neutral parent state (here, AB and AB) are Feschbach resonances and shape resonances. Feschbach resonances are necessarily below the energy of the parent state, while shape resonances are above. Resonances proceeding from the neutral ground state (here, AB) are single particle resonances. If electronic excitation occurs concurrently with electron capture (here, excitation to AB*), the resonances proceeding from the neutral excited state are core-excited. Approximate energy ranges are adapted from Christophorou et al.*[67]

are characterized by a loosely-bound electron capture state and are shorter-lived than Feshbach resonances, which are characterized by a bound negative ion state. Shape resonances are consequently much energetically broader than Feshbach resonances.

In order to understand shape resonances, it is first important to understand the nature of electrons. As electrons have wave-particle duality, one electron can be seen as a wave-packet consisting of contributions from various partial waves with angular momentum l, dependent on their energy. Close to 0 eV, $l = 0$ and s-wave attachment is thus dominant. At higher incident electron energies, however, higher angular momenta are observed. Selection rules require that the electron wave packet must have the same symmetry as the empty molecular orbital to which it attaches in order for electron capture to be possible.[64,71,72]

As a slow electron approaches a polarizable molecule, it induces a temporary dipole, which is felt by the electron as an attractive potential. This potential $V_\alpha(r)$, for a molecule with polarizability α, is described as follows:

$$V_\alpha(r) = -\frac{\alpha}{2r^4} \tag{2.7}$$

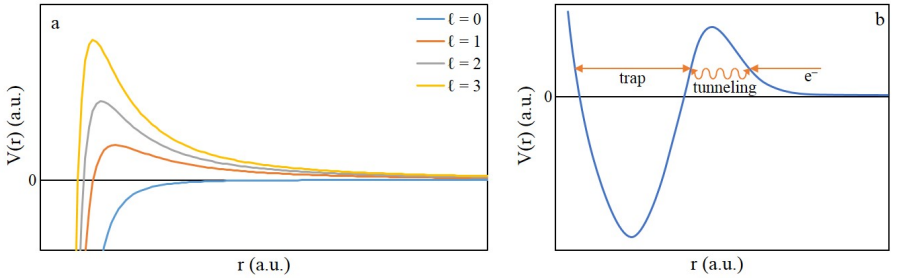

Figure 2.4. (a) These curves represent the effective potential felt by an electron of l = 0, 1, 2, and 3. An electron of l = 0 will feel no potential barrier; however, an electron of $l \neq 0$ will be repulsed from the molecule by the potential barrier. (b) Here, we see the total effective potential for a hypothetical electron of $l \neq 0$. The electron tunnels through its respective potential barrier, whereupon it encounters a potential well formed by the centrifugal barrier and a strong repulsive potential as it gets close to the valence electrons within the molecule, explained by the Pauli exclusion principle. The electron is trapped in the potential well by the repulsive centrifugal barrier until it can tunnel out again. This is a shape resonance.

At longer distances, however, a repulsive centrifugal potential is felt by the electron, produced by its angular momentum. This potential $V_l(r)$ is described as follows:

$$V_l(r) = \frac{l(l+1)}{2r^2} \tag{2.8}$$

The effective potential $V_{\alpha,l}(r)$ felt by an electron as it approaches a polarizable molecule is therefore:

$$V_{\alpha,l}(r) = V_\alpha(r) + V_l(r) = \frac{l(l+1)}{2r^2} - \frac{\alpha}{2r^4} \tag{2.9}$$

This effective potential is plotted in figure 2.4 for $l = 0$ - 3. As can be seen in this figure, for $l = 0$ (i.e. s-wave attachment), no potential barrier is formed, and thus electron capture at this energy is not expected via shape resonances. Conversely for $l \neq 0$, this potential produces a barrier that can "trap" an electron. The total effective potential for a hypothetical electron of $l \neq 0$ is shown generally in fig. 2.4b. As the electron gets even closer to the valence electrons within the molecule, past the centrifugal barrier, it feels a strong repulsive potential explained by the Pauli exclusion principle. This forms a potential well. As can be seen in this figure, the majority of electrons of $l \neq 0$ approaching the molecule will feel a strong repulsive force due to their angular momenta and will thus be repulsed from the molecule. However, there exists a probability that the electron will tunnel through this barrier into the potential well. While in the potential well, the electron gets trapped by the "shape" of the potential barrier (hence the name "shape resonance"), and will remain there until it can tunnel back out.

As shape resonances are formed by electron trapping within a potential barrier rather than by forming a bound state, they are considered open channel resonances. This is because the TNI can decay via autodetachment (AD, discussed in further detail) in order to form the original molecule and free electron. The lifetime of shape resonances is thus determined by the AD lifetime (τ_{AD}, see eq. 2.11), which can be on the order of 10^{-15} to 10^{-10} seconds.[64,72,73] Due to these relatively short lifetimes, shape resonances are generally broad (see eq. 2.11).

Vibrational Feshbach resonances are seen with molecules that are highly polarizable or have a permanent dipole moment. They are formed by a coupling of an incoming electron with the vibrations of the parent molecule. This is generally associated with the attachment of s-wave electrons, and are thus observed at very low incident electron energies. The probability of attachment at such low energies is proportional to $E^{-1/2}$,[74,75] and so vibrational Feshbach resonances can have very high cross-sections. Additionally, as the resonant state can lie slightly below the vibrationally excited states or even below the ground state of the neutral parent molecule (see, e.g. the intersection of the potential energy curves for AB and AB^- in fig. 2.2), the electron captured is in a bound state, leading to very long lifetimes and producing a very narrow resonance (see eq. 2.11). Finally, since the bound TNI state is formed below the energy of the neutral parent state, this type of resonance is considered closed channel, as the anion would have to absorb more energy in order to detach the bound electron.

2.1.2 Core-excited resonances

As an incoming electron is captured by a molecule at higher energies, it can cause electronic excitation concurrent with electron capture. This sort of resonance is also called a "2-particle-1-hole" resonance,[64] as the captured electron and excited electron reside in the higher energy molecular orbital, while a hole remains in the lower energy molecular orbital. These resonances can take two forms: one where the negative ion state is above the neutral excited state, called a "core-excited shape resonance", and one where the negative ion state is below the neutral excited state, called a "core-excited Feshbach resonance". The core-excited shape resonance is similar to the single particle shape resonance described previously; it is formed by a centrifugal trapping of the captured electron and is considered an open channel resonance as the AD channel is again open for this type of resonance. They are similarly short-lived, with consequent broadness. Core-excited Feshbach resonances, conversely, lie below the neutral excited state, and are consequently considered "closed channel" as the AD is closed. It thereby forms a bound ion state, producing long lifetimes. These long resonance lifetimes are accordingly quite narrow.

2.2 Transient negative ion decay

As TNIs are commonly formed in vibrationally and/or electronically excited states, several channels may proceed after negative ion formation. Some of the major channels are summarized in fig. 2.2. The main relaxation routes are autodetachment (AD) and dissociation (DEA), with competition from stabilization through intramolecular vibrational energy redistribution (IVR):

$$AB + e^-(\varepsilon_0) \rightarrow [AB]^{(\ddagger)-} \xrightarrow{AD} [AB]^{(\ddagger)} + e^-(\varepsilon_1 \leq \varepsilon_0) \tag{2.10a}$$

$$\xrightarrow{DEA} [A]^{(\ddagger)-} + B^{(\ddagger)} \tag{2.10b}$$

$$\xrightarrow{IVR} [AB]^{(\ddagger)-} \tag{2.10c}$$

2.2.1 Autodetachment

Autodetachment, shown in reaction scheme 2.10a, is the most prevalent relaxation channel. In AD, an electron is re-emitted from the TNI, producing the neutral molecule and a free electron. The free electron may have an energy less than or equal to the initial captured electron. If the energy of the electron after AD is equal to the energy before AD, it has been elastically scattered; otherwise, has been inelastically scattered. The neutral molecule after an inelastic scattering event may therefore be in an electronically and/or vibrationally excited state, as the impacting electron has transferred some of its kinetic energy to the neutral molecule. Inelastically scattered electrons may be measured by electron energy loss spectroscopy (EELS), which measures the energy difference between scattered electrons and their initial kinetic energy. This energy difference corresponds to the quanta of energy left within the molecule, which can provide information about its vibrational modes and electronic states. The angular distribution of scattered electrons can also be measured, providing information about the symmetry of the orbital wherein the electron was attached (i.e. the resonance), and thus also about the electronic configuration of the anion.

A diagram of AD can also be seen in fig. 2.2. The molecule attaches an electron via electron capture (EC) to an antibonding excited state of AB^- within the Franck-Condon region of overlap between it and the neutral parent AB. As the internuclear distance between A and B increases (essentially relaxing via transferring electronic energy to kinetic energy of the nuclei of A and B), the electron may detach until the two potential energy surfaces cross at the critical internuclear distance (marked r_c in fig. 2.2). Autodetachment can also produce the neutral parent molecule in a vibrationally and/or electronically excited state, as previously discussed and as can be seen in this figure. The width of this negative ion resonance (Γ) is thus finite, and the lifetime with respect to AD (τ_{AD}) can be given by Heisenberg's uncertainty principle, where $\hbar$ is the reduced Planck constant:

$$\tau_{AD} \sim \frac{\hbar}{\Gamma} \tag{2.11}$$

Based on eq. 2.11, we can see that if τ_{AD} is large, then Γ must be small (and vice versa); i.e. long-lived resonances (e.g. Feshbach resonances) will be appear in very narrow energy ranges in negative ion spectra, while short-lived resonances (e.g. shape resonances) will appear in very broad energy ranges.

2.2.2 Dissociation

Another potential method of TNI relaxation is via dissociation − this process is commonly called dissociative electron attachment (DEA). Electrons commonly attach into excited anionic states that overlap with the ground state of the neutral molecule within the Franck-Condon region, as seen in fig. 2.2. Excited states are commonly antibonding along at least one bond within the anion, so as the TNI relaxes, the bonds will begin to stretch. If we take fig. 2.2 as our example, our TNI was formed when an incident electron attaches to molecule AB into the antibonding orbital AB^{*-}. As the TNI relaxes, the excess electronic energy is converted into kinetic energy of the A and B nuclei as r(A−B) lengthens. AB^- can relax by emitting an electron in AD, discussed in the previous section, until the point where r(A−B) passes the point of overlap between the two energy surfaces AB and AB^{*-}, marked r_c in the figure. Past r_c, the TNI may only relax via dissociation. The cross-section for DEA is therefore defined by the cross-section for electron capture multiplied by the probability of TNI survival past this crossing point, which is given by the autodetachment lifetime described previously and the time (t) required for the internuclear separation to pass r_c:

$$\sigma_{DEA} \sim \sigma_{EC} \times e^{-\left(\frac{t}{\tau_{AD}}\right)} \tag{2.12}$$

Turning back to fig. 2.2, we can see σ_{DEA} for the formation of B^- from AB (σ_{B-}) graphically approximated as a proportion of σ_{EC}. With increased energy, σ_{DEA} drops off more quickly than σ_{EC}; this is because the probability of autodetachment is higher at higher energies. We can also find the energetic threshold for anionic fragment formation via DEA; for the reaction described in equation 2.1 and shown in fig. 2.2 producing B^-, this is defined by the bond dissociation energy of A−B, less the electron affinity of B:

$$E_{th}(B^-) = BDE(A-B) - EA(B) \tag{2.13}$$

As we can see in this figure, however, the appearance energy of anionic fragments is commonly higher than this threshold energy. This is because resonances may be observed above their respective energetic threshold, and excess energy (E^*) may manifest as electronic or vibrational excitation or as kinetic energy. The appearance energy is thus defined as follows:

$$AE(B^-) = E_{th} + E^* = BDE(A-B) - EA(B) + E^* \tag{2.14}$$

The above equations, of course, refer only to the thermodynamics of DEA wherein only a single bond is ruptured; however, DEA reactions are commonly known to produce multiple bond ruptures, generally via core-excited resonances, and can also produce complex reactivity with bond formation and molecular rearrangement.[10,11] It is thus useful for polyatomic molecules to view more generalized forms of the energetic threshold and appearance energy equations, where we consider the energetic threshold as given by the bond dissociation energies of the bonds broken less the bond dissociation energies of the bonds formed and the electron affinity of the anionic fragment:

$$E_{th}(B^-) = \sum_i^n BDE(parent) - (\sum_i^n BDE(product) + EA(B)) \tag{2.15}$$

The appearance energy, again, will be equivalent to the threshold energy plus some quantity of excess energy. It should also be noted that, under experimental conditions, the parent molecule will have some quantity of thermal energy and thermodynamic thresholds must therefore be calculated to reflect the experimental temperature in order to be compared with the experimentally determined appearance energies.

2.2.3 Stabilization

Another relaxation pathway for TNIs is stabilization via intramolecular energy redistribution (IVR). The lifetime of TNIs with respect to autodetachment can be very short or very long - from the femtosecond timescale for small molecules[73] to the microsecond or even millisecond timescale for large molecules.[68,76–78] As the window for detection of an ion via mass spectrometry can be on the microsecond timescale, these metastable anions may be detected by a mass spectrometer. One example of such a long-lived TNI is $[SF_6]^-$,[68] which is commonly used to calibrate the electron energy scale of electron monochromators close to 0 eV (see section 3). Close to 0 eV, molecules with positive electron affinities may attach an electron, but have no thermodynamically available dissociation mechanisms. Such TNIs may then emit the captured electron via autodetachment; however, a suitable TNI may have adequate vibrational degrees of freedom to redistribute the excess energy into different vibrational states of the anion, thus increasing the lifetime of the resonance. While these metastable TNIs are commonly found close to 0 eV, others are fond at higher energies, with $[C_{60}]^-$ observed up to 13 eV.[77,78]

2.3 Positive ion formation and decay

At higher incident electron energies, at or above the ionization energy of the parent molecule, electron impact can positively ionize the target molecule. The threshold energy (E_{th}) for production of the parent cation is given simply by the ionization energy (IE) of the parent molecule:

$$E_{th}([AB]^+) = IE(AB) \tag{2.16}$$

The electron-induced ejection of an electron, producing a cation, can be seen as a vertical transition from the ground state of the neutral parent molecule to either the ground state or an excited state of the cation within the Franck-Condon region of overlap with the probability of transition proportional to the FCF, similarly to negative ion formation. However, at such higher energies than those of negative ion formation, there exists a continuum of vibrationally and electronically excited states in which the cation may be formed. Further, no reattachment process exists to shorten the lifetime of the cation by returning it to a neutral molecule. Because of this, positive ion formation is a non-resonant process, exhibiting instead threshold behavior. The cross-section for positive ion formation, as well as those for dissociation via positive ion formation, increases from the energetic threshold, peaking between 50 and 100 eV, and then decreases as the cross-section for electron scattering decreases and the interaction time between incident electrons and the target molecule shortens.

Cations formed by electron impact are commonly formed in vibrationally and/or electronically excited states, as shown in eq. 2.2, and will then shed excess energy. Metastable parent cationic states may have adequately long lifetimes to be detected by mass spectrometry, especially at low incident electron energies close to the ionization energy of the neutral molecule. A parent cation may also decay into a fragment cation and one or more neutral fragments. This process is commonly called dissociative ionization. The energetic threshold for the formation of a fragment cation is given as the sum of the bond dissociation energies of bonds broken and the ionization energy of the ionized fragment, less the sum of the bond dissociation energies of any bonds formed (eq. 2.17).

$$E_{th}(A^+) = \sum_i^n BDE(parent) + IE(A^+) - \sum_i^n BDE(product) \tag{2.17}$$

Dissociative ionization processes are commonly significantly higher in energy than dissociative electron attachment processes − the former are active over a broad energy range above the ionization energy of the parent molecule (generally above 10 eV), while the latter are confined to a narrow energy range (generally below 10 eV). Additionally, as the incident electron energy increases, dissociative ionization will produce increasingly extensive fragmentation. As such, dissociative ionization to a molecule commonly produces far more fragmentation than dissociative electron attachment.

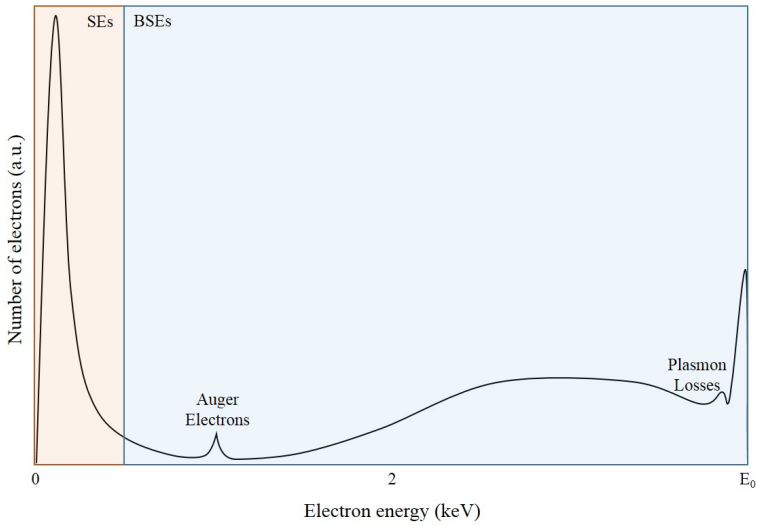

Figure 2.5. This is a schematic of the hypothetical electron energy distribution of a surface impacted by a high-energy electron beam of energy E_0. For convenience, in this thesis we will consider electrons below 50eV to be secondary electrons (SEs), while electrons above 50 eV will be considered backscattered electrons (BSEs). There are often several peaks due to Auger electrons, which are characteristic of the substrate composition, and plasmon losses, which are common in metals.

2.4 Relevant electron interactions in FEBID

2.4.1 Electron interactions with surfaces

As previously stated, in FEBID, a high-energy electron beam impinging on a surface is used to deposit metals from a layer of adsorbed precursor molecules. Electron impact at a surface will produce scattered electrons with an electron energy profile close to the surface. Electrons may be produced via elastic and inelastic collisions, as well as via other excitation processes. A schematic of a typical energy spectrum of electrons emitted from a substrate irradiated with a primary electron beam of energy E_0 is shown in fig. 2.5. As can be seen here, the majority of electrons emitted from the surface are secondary electrons (SEs), which are defined here as scattered electrons below 50 eV in energy. The energy distribution of electrons at a surface impacted by a high-energy primary electron beam commonly peaks far below 10 eV.[19,20,51–54] Backscattered electrons (BSEs), which are defined here for convenience as scattered electrons above 50 eV in energy, constitute the majority of the remaining electrons emitted by an electron beam-impacted surface. Some electrons are emitted via excitation processes; i.e. Auger electrons. These are electrons emitted when a core electron is ejected from an atom, and a photon is released when an outer electron drops down

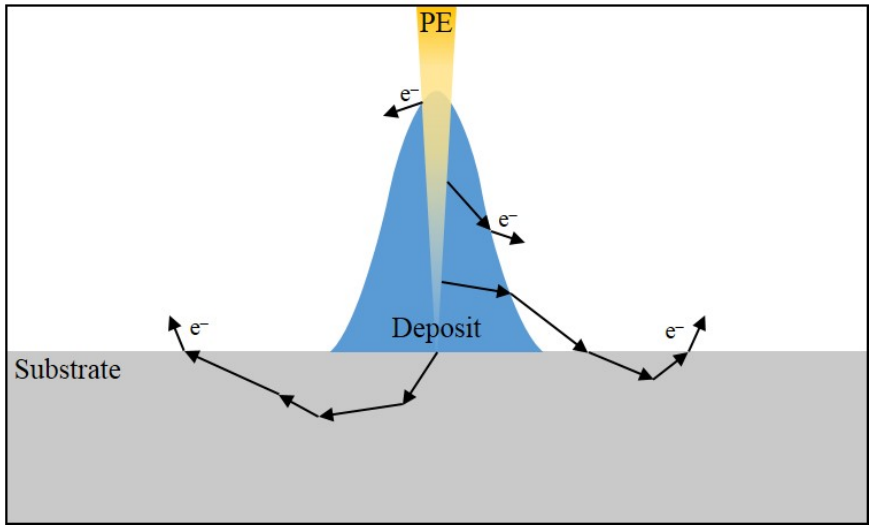

Figure 2.6. A high-energy primary electron beam (PE) impacts a substrate and growing deposit and is partly scattered through several processes. Electrons can be directly scattered off the deposit or off the substrate. Additionally, electrons can be scattered within the deposit or substrate, losing energy with each collision until they are emitted. Finally, such emitted electrons can then scatter back into the deposit or substrate, again scattering further before re-emission.

to replace it. This photon can then excite other electrons within the atom, potentially causing them to also be emitted with an energy characteristic of the Auger transition; this is why Auger electrons have well-defined peaks as seen in fig. 2.5. At energies close to the energy of the primary electron beam, we see additional peaks due to surface plasmon losses, which are common for metals,[79] as well as an elastically-scattered electron peak at the energy of the primary electron beam. As can be seen by this image, the bulk of electrons produced by electron beam impingement upon a surface lie well within the energy range of low-energy electron-induced dissociation mechanisms discussed previously in this chapter.

Additionally, it is important to note that electron scattering does not merely take place within the area of the primary electron beam. Indeed, electrons may be scattered in a radius several times that of the primary electron beam. Lower energy secondary electrons have a radial density one to two orders of magnitude larger than that of higher energy backscattered electrons.[19–21,55] The pattern of electron scattering in FEBID will depend on the topography and composition of the surface, as well as the primary electron beam energy. In order to model this, Monte Carlo simulations have been developed.[21,53] This topography and composition will, of course, change as the substrate changes via deposition. Electrons may also be scattered by the growing deposit. Heating is additionally known to be produced by energy transfer between the high-energy primary

electrons and the substrate.[20] A schematic of potential electron scattering behavior upon primary electron beam impact during FEBID is shown in fig. 2.6.

2.4.2 Electron interactions with precursor molecules

Both scattered electrons and primary electrons may interact with adsorbed precursor molecules to produce deposits; this is the mechanism underlying FEBID. As previously shown, the bulk of electrons produced upon primary electron beam impact with a surface are well within the energy range of low-energy electron-induced reactions like DEA and DI. Additionally, the only electrons available outside of the primary electron beam to induce deposition are low-energy electrons, with secondary electrons under 50 eV having the broadest radial density by one to two orders of magnitude. Thus, fundamental gas phase reactions such as those discussed in sections 2.2 and 2.3 may give some insight into mechanisms for deposition in FEBID from precursor molecules. Both DEA and DI have been shown to be important initial steps in the deposition of several FEBID precursors.[28] For example, the deposition of $Pt(PF_3)_4$ and $MeCpPtMe_3$ has been shown to begin with a single ligand loss through DEA.[56–59,80] In $(\eta^5\text{-Cp})Fe(CO)_2Mn(CO)_5$, it appears that DI is important in the initial deposition step.[50] In other molecules, such as $Co(CO)_3NO$,[60,61] $W(CO)_6$,[62,63] and $(\eta^3\text{-}C_3H_5)Ru(CO)_3Br$,[38,40] both low-energy processes play important roles. It must be noted that the environment may have an important influence on deposition - e.g. the geometry in which the precursor molecule has adsorbed, the effect of surface adsorption on unoccupied molecular orbitals, surface heating via electron impact, etc. Additionally, as FEBID proceeds, the environment of the precursor molecules changes; this will have varying effects on electron-precursor interactions. Despite these mitigating circumstances, fundamental gas phase electron-induced reactions can aid in the elucidation of surface deposition mechanisms of organometallic precursors in FEBID.

3 Methods

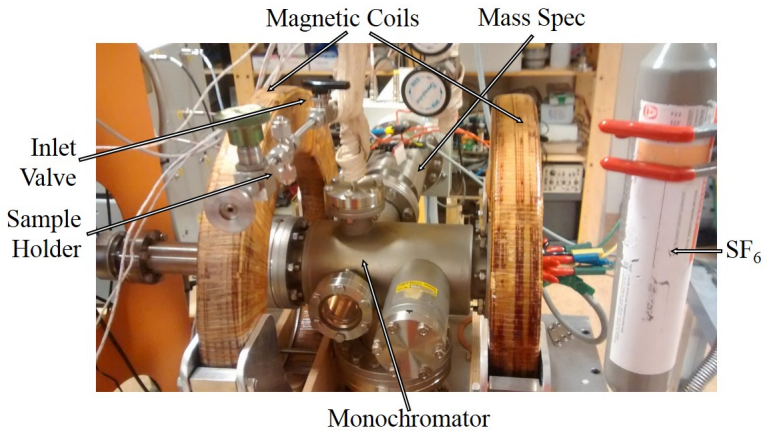

Figure 3.1. Image of SIGMA, a crossed molecular/electron beam instrument used for gas phase DEA and DI experiments at the University of Iceland. SIGMA was constructed by Elías Bjarnason. The setup pictured here was used for measurement of $(\eta^3\text{-}C_3H_5)Ru(CO)_3Br$, with the sample separated from the chamber merely by a quarter turn plug valve. For $(\eta^5\text{-}Cp)Fe(CO)_2Mn(CO)_5$, the same gas inlet manifold was used; however, the sample was separated from the chamber by a leak valve.

3.1 Experimental methods

Two different types of measurements are reported in this thesis - mass spectrometry measurements from a gas phase crossed-beam instrument and energy-dispersive X-ray spectrometry measurements from a secondary electron microscope. Gas phase experiments, which comprise the bulk of this thesis, were performed on a crossed effusive molecular-beam/electron-beam instrument at the University of Iceland. A general description of this instrument is given here, as well as a description of energy calibration for this instrument and determination of the appearance energies reported in this thesis. A more in-depth discussion of the operating principles of this instrument, which was

constructed by Elías Bjarnason as a part of his PhD research, is given in Bjarnason et al.[81] The *in situ* FEBID experiments, which were performed in collaboration with Dr. Ivo Utke at EMPA in Thun, Switzerland, were performed on two secondary electron microscopes - one of which was used for deposition and the other of which was used for EDX measurements. A general overview of the experimental setup for the FEBID studies reported in this thesis is also given here.

3.1.1 Gas phase experiments

SIGMA

Figure 3.1 shows SIGMA, or "SImply a Gas phase MAchine", which is the instrument used for gas phase experiments at the University of Iceland. SIGMA is a high vacuum, crossed effusive molecular beam/electron beam instrument equipped with a HIDEN Epic 1000 quadrupole mass spectrometer. The base pressure of the instrument is approximately 1×10^{-8} mbar, and typical pressures in the conducted experiments were on the order of 5 - 9 $\times$ 10^{-7} mbar. The effusive molecular beam is generated by subliming the respective target molecule in a stainless steel gas inlet system attached to the high-vacuum collision chamber. The inlet system in these experiments was constructed of a 9 mm, capped Swagelok T-fitting separated from the chamber by either a quarter turn plug valve (for (η^3-C_3H_5)Ru$(CO)_3$Br) or by a leak valve (for (η^5-Cp)Fe$(CO)_2$Mn$(CO)_5$). The electron beam was generated by a tungsten filament and energy-selected by a trochoidal electron monochromator (TEM), which will be described in the next section. The magnetic field used in the TEM is generated by two Helmholtz magnetic coils mounted outside the vacuum system, and measures approximately 40 Gauss. The TEM is heated to 120 °C by fluorescent bulbs in order to minimize deposition onto the lenses; however, despite this heating ruthenium deposition onto the lenses during measurements performed on (η^3-C_3H_5)Ru$(CO)_3$Br) resulted in degradation of the electron energy resolution during these experiments. Electrons produced by the TEM interact with the effusive molecular beam in the collision region, and ions produced by these interactions are extracted and focused into the mass spectrometer, which is equipped with a radio frequency generator operating within a 2-1000 *m/z* range. The mass spectrometer is also equipped with a second RF generator capable of operating within a lower mass range, but this was not used in the experiments reported in this thesis.

Trochoidal electron monochromator

Dissociative electron attachment and dissociative ionization experiments are performed over a very broad range of energies - from close to 0 eV in DEA experiments to over 100 eV in DI experiments. As the studies performed in this thesis include the measurement of appearance energies, it is important to use an electron beam with a narrow energy distribution. The trochoidal electron monochromator, first described by Stamatovic and Schulz,[82,83] is used to produce an electron beam with well-defined energy resolution that works within a broad energy range and can produce electrons at high intensity

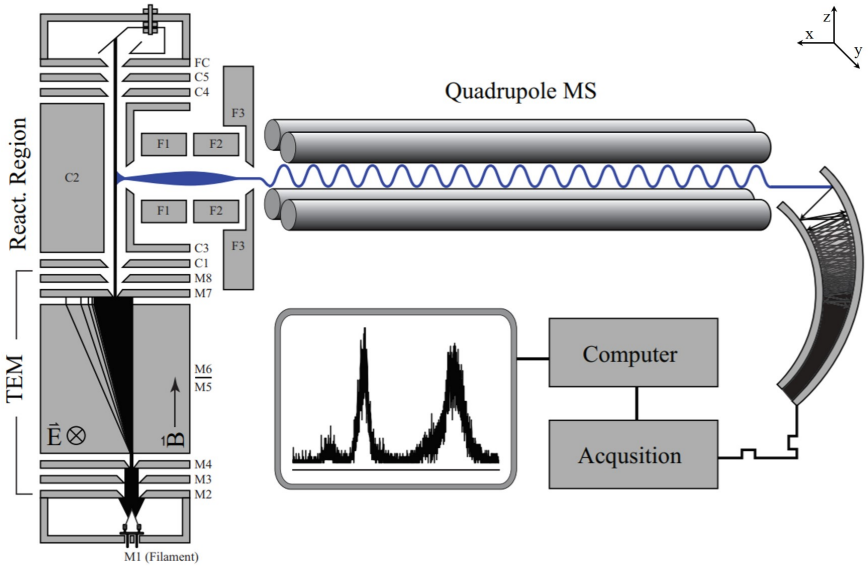

Figure 3.2. A schematic of SIGMA and the TEM used in these experiments. Electrons are generated by a tungsten filament and energy-selected by the TEM. Electrons interact with the effusive molecular beam in the collision region, here labeled "React. Region", and ions are extracted through the quadrupole mass spectrometer to an electron multiplier, which provides the analyzed signal. Reprinted from Ómarsson.[84] Copyright © 2013 Benedikt Ómarsson.

at very low energies. In a TEM, electrons are generated by a filament (in this case, a hairpin tungsten filament) in a broad energy range and are energy-selected, collimated, and focused by a series of electrostatic lenses crossed with a magnetic field. The lens plates are made of non-magnetic metal (in this case, molybdenum) and are electrically insulated from one another by ruby balls.

Figure 3.2 shows the TEM used in this instrument. Electrons generated by the tungsten filament, labeled here as M1, are channeled through lens elements M2 to M4. The aperture on the lens plates narrows from M2 to M4, so some collimating occurs here. Passing through M4, electrons enter the deflection region, which is between M5 and M6. Looking at fig. 3.2, we can see that thus far, the electrons have traveled in the z-direction. The electrons enter the electric field $\vec{E}$ between M5 and M6, which accelerates the electrons in the y-direction. The magnetic field $\vec{B}$ generated by the Helmholtz coils is orthogonal to the electric field, in the z-direction. These crossed fields cause the electrons entering through M4 to drift in a trochoidal (or, cycloidal) trajectory, displaced with a constant velocity ($\vec{v_x}$):

$$\vec{v_x} = \frac{\vec{E} \times \vec{B}}{|\vec{B}|^2} \tag{3.1}$$

As $\vec{E}$ and $\vec{B}$ are perpendicular, this equation simplifies to:

$$\vec{v}_x = \frac{E}{B} \tag{3.2}$$

Electrons will thus be displaced by a certain Δx dependent on the amount of time they spend in the deflection region. Faster electrons (with a higher $|\vec{v}_z|$) moving through the deflection region will be displaced less by the crossed fields, while slower electrons will be displaced more. The exit slit, M7, is offset by a specific Δx from entrance slit M4, and therefore only electrons of a narrow velocity range in the z-direction will be transmitted through the deflection region. This is the region wherein the electron energy selection in a TEM takes place.

After the deflection region, electrons travel through M7 - M9. These lenses refocus and collimate the electron beam into the collision region, where they will interact with the effusive molecular beam. They are also used to accelerate or decelerate the electrons to the target interaction energy. Upon entering the collision region through C1, electrons are allowed to interact with the target molecules, producing ions as described in sections 2.1-2.3. The ions are then extracted by a weak electric field (less than 1 V/cm) by C2 and C3, and focused into the quadrupole mass spectrometer by F1-F3. Beyond the collision region, C4 and C5 are used to divert excess electrons away from the collision region into the Faraday Cup (FC) in order to avoid multiple electron-molecule collisions. This also gives an estimate of the electron current running through the monochromator.

Energy calibration

Calibration of the electron energy scale and resolution in DEA experiments uses the well-studied ion yield of $[SF_6]^-$ from SF_6, which proceeds through a resonance with maximum ion yield close to 0 eV.[68,85] The maximum ion yield of $[SF_6]^-$ from SF_6 is thus used for these experiments in order to set the electron energy scale. The full-width-at-half-maximum (FWHM) of this resonance has been shown to be less than 1 meV wide,[85] while even an extremely well-resolved trochoidal electron monochromator generally has a FWHM greater than 30 meV.[86] The FWHM of the $[SF_6]^-$ ion yield can thus be considered wholly determined by the resolution of the electron beam. In these experiments, a typical FWHM of the incident beam was 120-140 meV; however, in the gas phase experiments using (η^3-C_3H_5)$Ru(CO)_3Br$, ruthenium deposition on the molybdenum lens elements degraded the electron beam resolution to 160-180 meV.

Determination of appearance energies

Determination of the appearance energies for ion yields produced by DEA to a molecule is executed here by straight-line fitting. Two methods have been previously used to determine appearance energies for negative ion yields: straight-line fitting and Wannier-type fitting. The Wannier-type function was derived as a threshold law for atomic ionization processes, and has since been used successfully to derive appearance energies

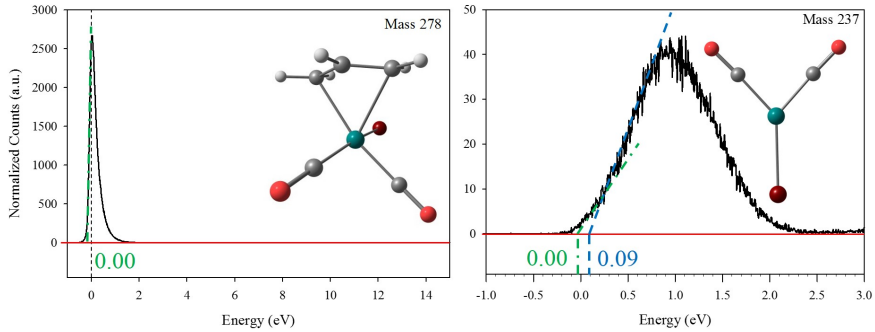

Figure 3.3. Left: Illustration of the fitting process for determination of DEA appearance energies at 0 eV. Appearance energies below 0 eV are indicative of the energy resolution of the instrument, rather than that of the ion yield. The ion yield thus has an AE of 0 eV, as is seen here for $[(\eta^3\text{-}C_3H_5)Ru(CO)_2Br]^-$. Right: Above 0 eV, a selected section of the rising edge of the data is fitted with a linear regression. An upper boundary line (blue) and a lower boundary line (green) for the appearance energy are visually fitted to the onset region and their intercepts with the base line (red) are determined. This determines the accuracy of the regression-calculated appearance energy. The ion yield for $[Ru(CO)_2Br]^-$ thus has an AE of 0.07 eV, with an upper boundary of 0.09 eV and a lower boundary of 0.00 eV. We estimate an overall accuracy for all appearance energies to be ±0.2 eV. The ion yields shown here to illustrate the fitting process are from DEA to $(\eta^3\text{-}C_3H_5)Ru(CO)_3Br$, shown with the calculated ground state anionic geometries of the respective fragment observed in each ion yield.

for polyatomic ionization processes and dissociative ionization processes.[87] This has been found empirically to reproduce thresholds for dissociative ionization processes very well. It has also been empirically found to reproduce thresholds for dissociative electron attachment processes. However, despite their success in describing experimental results, Wannier-type fits are not based on a physical derivation of DEA processes from first principles. Straight-line fitting was thus chosen as a good descriptor of the data presented in this thesis. This process is illustrated in fig. 3.3, which shows two fits performed on ion yields produced by DEA to $(\eta^3\text{-}C_3H_5)Ru(CO)_3Br$. As can be seen in the left fit, performed on the ion yield of $[(\eta^3\text{-}C_3H_5)Ru(CO)_2Br]^-$, the onset of ion yields below 0 eV reflects the electron energy resolution of the instrument. These yields are therefore taken to have an appearance energy at 0 eV. For ion yields with an onset above 0 eV, as seen on the right, we fitted a section of the rising edge of the ion yield data with a linear regression. This regression was compared with visually fitted upper and lower boundaries in order to estimate the accuracy of our appearance energy determination. As can be seen in fig. 3.3, a lower boundary of 0.00 eV was found in the appearance energy fitting of $[Ru(CO)_2Br]^-$, shown as a green dashed line. The upper boundary of 0.09 eV is represented by a blue dashed line. The appearance energy of this anion was calculated by the linear regression to be 0.07. In the studies reported in this thesis, an overall accuracy of ±0.2 eV has been estimated for all fragments.

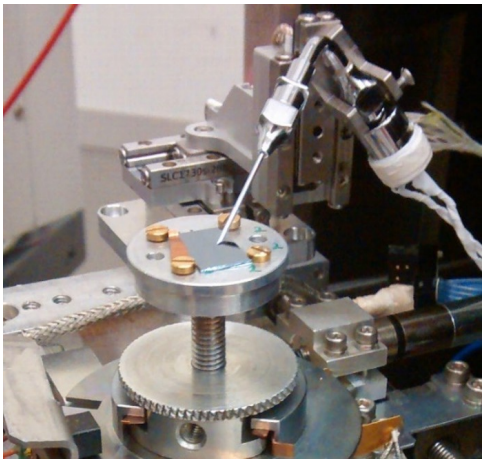

Figure 3.4. The gas inlet system used in deposition experiments. The GIS consists of a resistively-heated sample holder (right), an elbow, and a beveled-tip needle with a 0.9 mm diameter. The needle is held approximately 0.5 - 1 mm from the silicon substrate surface, at an angle of about 30 °. The entire setup is place inside a Hitachi S-3600 SEM for deposition.

3.1.2 FEBID experiments

The study on the deposition of $(\eta^3\text{-}C_3H_5)Ru(CO)_3Br$ and $Ru_3(CO)_{12}$ under *in situ* FEBID conditions has not been published prior to this thesis, and so experimental details will be given here. Deposition was performed at EMPA in Thun, Switzerland, in a Hitachi S-3600 SEM with a base pressure of approximately 10^{-5} mbar and a base temperature of approximately 26 °C. The gas inlet system is shown in fig. 3.4. Solid precursors were placed in a simplified stainless steel gas inlet system consisting of a sample holder, an elbow, and a 0.9 mm diameter beveled-tip needle. The needle was held approximately 0.5 - 1 mm from the substrate surface, with an angle of about 30 ° from the substrate. Precursors were sublimed using a Teflon-coated resistive heater with a CuNi heating coil. A 3 kV primary electron beam was used for deposition, with an emission current of 83 μA and a working distance of 15.8 mm. Analysis of the deposits via energy dispersive X-ray spectroscopy (EDX) and secondary electron microscopy (SEM) was performed on a second instrument: a Hitachi S-4800 SEM with a cold field emission electron source and an EDAX Genesis 4000 EDAX detector. A 5 kV primary electron beam was used for EDX and SEM imaging.

3.2 Computational methods

In this thesis, quantum chemical calculations were performed on (η^3-C_3H_5)$Ru(CO)_3Br$ and (η^5-Cp)$Fe(CO)_2Mn(CO)_5$ in order to aid in the interpretation of their dissociation channels in both DEA and DI studies. Molecules and ions were geometrically optimized using a density functional theory (DFT) method, BP86, and single point energy (SPE) calculations were performed on these optimized species using several methods, including the DFT method BP86, the hybrid method PBE0, and two coupled cluster methods: LPNO-pCCSD/2a and DLPNO-CCSD(T). Several basis sets were also used in these calculations. Computational methods for calculating the ground and excited state energies of atoms and molecules have been thoroughly described elsewhere;[88–93] a brief overview of the principles behind the calculation methods and basis sets used in this thesis is described here, as well as the methods of calculating the reaction thresholds reported.

3.2.1 Density functional theory and wavefunction-based theories

The time-independent Schrödinger equation (eq. 3.3) can, in principle, be solved to yield the time-independent ground and excited state wavefunctions for any atom or molecule.

$$\hat{H}\Psi = E\Psi \tag{3.3}$$

Here, $\hat{H}$ is the Hamiltonian operator, Ψ is the wavefunction, and E is the energy. As a quantum system becomes more complex, however, the Schrödinger equation becomes more complex. The Hamiltonian operator is dependent on the kinetic energy of the electrons and nuclei and the Coulombic potential energy of electron-nuclei interactions, electron-electron interactions, and nuclei-nuclei interactions. Of course, electronic and nuclear motion in atoms and molecules are interdependent. The Schrödinger equation therefore becomes analytically insolvable. Computational methods use several approximations in order to make a solvable equation to find the ground state and excited states of many-particle systems, i.e. atoms and molecules.

The first major simplification that can be made to these equations is the Born-Oppenheimer approximation. The Born-Oppenheimer approximation separates electronic and nuclear motion, allowing the Schrödinger equation to be broken into electronic and nuclear components. The electronic and nuclear motion may be separated because electrons and nuclei, having significantly different masses, move on significantly different timescales. Essentially, the nuclei may be held at a fixed point while the electronic component of the Schrödinger equation is solved. The nuclear component may then be solved using the approximated electronic potential in order to determine the zero-point energy and temperature-dependent vibrational motion of the system. This may be iterated over multiple nuclear coordinates in order to produce the Born-Oppenheimer potential energy surface for a molecule. The Born-Oppenheimer

approximation greatly simplifies several parts of the Schrödinger equation: particularly, the electron-nuclei and nuclei-nuclei interaction contributions. The kinetic energies of the electrons and nuclei have also been rendered solvable by using this method. However, electron-electron interactions must still be dealt with.

Interdependency of electrons and nuclei rendered the time-dependent Schrödinger equation analytically insolvable due to the number of interacting bodies, necessitating separation of electronic and nuclear motion in the Born-Oppenheimer approximation. The electron-electron interaction term is thus also rendered analytically insolvable due to the same many-body problem, as each electron is dependent on all other electrons in the system. We must therefore introduce another method to deal with this many electron problem: the variational method. The variational method introduces a trial wavefunction for the system of interest to calculate the energy of that system with that wavefunction. This energy will necessarily be greater than or equal to the actual ground state energy of the system. By systematically varying the trial wavefunction until the energy of the system cannot get any lower, we can approximate the ground state energy of the system. This is essentially what the Hartree-Fock method does: take a good initial guess at a ground state many-electron wavefunction, calculate the energy of the system, and then iteratively vary the wavefunction to minimize the energy until the energy of the system reaches a global minimum. This method is known as the wavefunction-based approach. Another approach, where electron density is varied instead of the wavefunction in order to derive the ground state energy, is called density functional theory (DFT). Despite this difference, the DFT approach uses the same basic concept as the wavefunction-based approach: functionals describing the electron density of a system are varied iteratively to minimize the energy of the system until it reaches a global minimum.

In the Hartree-Fock method, the energy difference between the Hartree-Fock energy calculated by varying the wavefunction and the exact solution of the time-independent Schrödinger equation using the Born-Oppenheimer approximation is defined as the electron correlation energy. Electron correlation comprises the interaction between electrons, and some electron correlation is accounted for by Hartree-Fock. This is the exchange energy, which accounts for electron behavior described by the Pauli Exclusion Principle, that no electrons with parallel spin may be found in the same quantum state simultaneously. Here, we consider the electron correlation term that is missing from Hartree-Fock to be describing the instantaneous Coulombic repulsion between electrons. Wavefunction-based methods, such as coupled cluster theory, have been developed that uses allowed electronic excitations to calculate wavefunctions that account for this electron correlation term. The coupled cluster method CCSD(T) (coupled cluster singles doubles perturbative triples) is considered exceedingly accurate and reliable; however, it is also quite computationally expensive.

Density functional theory methods, being based on electron density rather than on solving the many-electron wavefunction, are much cheaper computationally. This is because they reduce the number of variables from calculating N electrons with 3N coordinates in wavefunction-based theories to calculating the electron density function, which has only 3 coordinates. Density functional theory methods are solved similarly to Hartree-Fock methods; however, they include an exchange-correlation term instead

of the exchange term. This is the term that is iteratively optimized by DFT. Some methods, like the local density approximation, assume that the electron density is homogeneous; to account for the inhomogeneity of the electron cloud, generalized gradient approximations (GGAs) have been developed.

Due to their low computational cost and high level of accuracy in molecular geometric optimization, a DFT method was used to optimize the molecules and ions reported in this thesis. Density functional theory methods, however, are not always accurate when describing certain systems. Transition metals, which have significant electron correlation, can be especially difficult for DFT methods.[94–98] Hybrid-GGA functionals, which use a linear combination of the DFT exchange-correlation term and the exact exchange from Hartree-Fock theory, can increase the accuracy of the exchange-correlation functional used to calculate these systems.[95,99,100] Coupled cluster methods are excellent at calculating dynamic electron correlation; however, they are often computationally expensive.[101–107] Improvements in computational speeds and local correlation methods for use in coupled cluster calculations have made coupled cluster methods computationally “cheap” enough that they are now attainable for metal-centered molecules such as the ones presented in this thesis.

3.2.2 Basis sets

Both density functional theory and wavefunction theory methods construct their electron density functional or wavefunction from a linear combination of many functions. The set of functions used to compose this functional is called a basis set. There are many types of basis sets - in this thesis, we have used def2-TZVP,[108–110] ma-ZORA-def2-TZVPP and -QZVPP,[108,111–113] and aug-cc-pVTZ and -pVQZ.[114–117] There are several variables to note in each of these basis sets. One is the number of basis functions that correspond to each atomic orbital or electron. In these basis sets, "TZ" and "QZ" stand for triple-zeta and quadruple-zeta and therefore use 3 and 4 basis functions, respectively, for each atomic orbital or electron. Another issue is polarization, which can be added in by p-functions (or d-functions). Additionally, diffuse functions may be added, this is signified in two basis sets here by the keyword "aug". Finally, effective core potentials (ECPs, also called pseudopotentials) are used to approximate core electrons with a core potential function, rather than taking the more computationally expensive route of calculating these atomic orbitals or electrons directly. The ma-ZORA-def2-TZVPP and ma-ZORA-def2-QZVPP basis sets do not use ECPs.

All molecules and ions studied in this thesis were geometrically optimized using the BP86 method,[118,119] which is a DFT method that utilizes the generalized gradient approximation (GGA).[120] This method was also used to calculate the zero point vibrational energy (ZPE) and the thermal corrections. A hybrid-GGA functional, PBE0,[99] was tested for use in calculating energetic thresholds for DEA to (η^3-C_3H_5)$Ru(CO)_3Br$, as was the coupled cluster method LPNO-pCCSD/2a[101–103] (the wavefunction-based method pCCSD/2a in conjunction with the local pair natural orbital (LPNO) methodology for scaling). Quantum chemical calculations of (η^3-C_3H_5)$Ru(CO)_3Br$ were performed using Orca 3;[121] however, the recent implementation of Orca 4[122] was

used in calculations of (η^5-Cp)Fe(CO)$_2$Mn(CO)$_5$. This allowed us to use the coupled cluster method DLPNO-CCSD(T)[104–107] for single point energy calculations, which pairs the domain-based local pair natural orbital methodology for scaling with the wavefunction-based method CCSD(T) - the gold standard of quantum chemistry.

3.2.3 Threshold calculations

The energetic threshold of a reaction may be given by the enthalpy of reaction at 0 K (ΔH_{rxn}). The reaction enthalpy is defined by the sum of the total energy of all products formed in the reaction less the energy of the reactants. Here, this is merely the parent molecule.

$$\Delta H_{rxn} = \sum H(products) - H(parent) \tag{3.4}$$

The enthalpy of any fragment or of the parent consists of two terms: the zero-point vibrational energy (ZPE) and the single point energy(SPE). Additionally, thermal corrections were added to the parent molecule. This is because DEA experiments were carried out at various energies dependent on the sublimation temperature of the molecule, and excess thermal energy might then lower the energetic threshold at which the observed fragments might appear. The thermochemical threshold given in eq. 3.4 can then be rewritten:

$$\Delta H_{rxn} = \sum_{i=1}^{N} (E_i^{ZPE} + E_i^{SPE}) - (E_{parent}^{ZPE} + E_{parent}^{SPE} + E_{parent}^{thermal}) \tag{3.5}$$

Where N is the number of fragments produced by a given DEA process, energies E_i refer to the energies of individual fragments formed by the DEA process, and energies E_{parent} refer to the energies of the parent molecule. In each of the calculations given in this paper, the ZPE and thermal energies (shown in eq. 3.5 as E^{ZPE} and $E^{thermal}$) were calculated using the BP86 method with the def2-TZVP basis set. The SPE (shown in eq. 3.5 as E^{SPE}) was calculated by several methodologies, including BP86, PBE0, LPNO-pCCSD/2a, and DLPNO-CCSD(T). The method used for SPE calculation in each case is indicated in the text and figures/tables. Ultimately, the coupled cluster methods were found to be the most accurate predictors of the observed energetic thresholds.

4 Results

4.1 Low-energy electron interactions with (η^3-C_3H_5)$Ru(CO)_3Br$

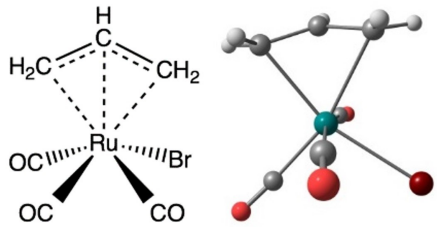

Figure 4.1. Chemical structure diagram (left) and calculated ground state geometry (right) of η^3-allyl ruthenium tricarbonyl bromide. The ground state geometry was calculated at the BP86 level of theory with the def2-TZVP basis set.

4.1.1 Introduction and Motivation

Elucidation of the fundamental electron-induced reactions relevant in focused electron beam induced deposition (FEBID) of organometallic precursor molecules is a challenge that must be approached from several different angles. Gas phase crossed-electron/molecular beam experiments are used to observe electron-initiated reactions at varying incident electron energy under single collision conditions. From these, we can identify the branching ratios of dissociative electron attachment (DEA), dissociative ionization (DI), and dipolar dissociation (DD) reactions by measuring the relative abundance of positive and/or negative ions as a function of incident electron energy.[28,40,50,56,58,60,62] Ideally, knowledge of the relative or absolute cross-sections for dissociation products of these fundamental gas phase electron-induced reactions can provide a basis to predict the potential behavior of these molecules in FEBID.[5,28] A second step in this process is the use of ultra-high vacuum (UHV) surface science studies. In UHV studies, thin films of organometallic precursors adsorbed on cooled surfaces are exposed to incremental doses of higher energy primary electrons (in the referenced study, a 500 eV flood gun is used), while gas phase products are monitored by mass spectrometry (MS) and the surface composition is monitored by X-ray photoelectron

spectroscopy (XPS).[38,39,57,59,61,63] This allows the study of purely electron-initiated deposition processes on the surface, free of thermal effects, so that potential initial steps similar to dissociation processes observed in the gas phase might be revealed. These UHV studies are an additional tool to aid in predicting the behavior of the precursor molecule in FEBID. Finally, *in situ* FEBID studies are performed, where deposit size can be measured using secondary electron microscopy (SEM) or atomic force microscopy (AFM) and deposit composition can be measured using energy dispersive X-ray spectroscopy (EDS).[5,19,20,25,26] Many parameters can be varied during *in situ* FEBID studies, including precursor sublimation temperature and deposition time, as well as substrate temperature, precursor flux, primary electron beam energy, etc.

These *in situ* FEBID studies are ultimately used to determine the desirability of specific precursors for FEBID; however, they cannot provide insight into the fundamental reaction processes that ultimately determine the deposit composition. Motivated by this, we undertook an effort to study the electron-induced deposition of a potential FEBID precursor - π-allyl ruthenium tricarbonyl bromide ((η^3-C_3H_5)$Ru(CO)_3Br$) - in the gas phase and under FEBID conditions in order to see how well our gas phase observations could predict the performance of this precursor in FEBID. Additionally, we compared our gas phase studies of this precursor to UHV surface science studies performed by Spencer et al.[38] in an effort to elucidate the initial decomposition step leading to the electron-induced deposition of (η^3-C_3H_5)$Ru(CO)_3Br$. We thus endeavored to determine which LEE-induced processes might be most important in determining the ultimate composition of FEBID deposits using this precursor molecule. Finally, we modeled experimentally observed fragments produced by DEA to (η^3-C_3H_5)$Ru(CO)_3Br$ using quantum chemical calculations using DFT, hybrid, and coupled cluster methods in order to determine which level of theory is required to accurately describe DEA of organometallic molecules. Modeling these experimentally determined results can provide more information on why the observed dissociation products are produced upon electron capture, and as models grow more accurate, these calculations may be able to predict the results of electron-induced dissociation at various incident electron energies.

This specific precursor was chosen for this study largely for its interesting ligand architecture. The allyl ligand is a multicoordinate π-facial ligand, similar to the methylcyclopentadienyl ligand that has been used in the well-studied FEBID precursor $MeCpPtMe_3$.[57–59,123,124] Such ligands are desirable for adding stability to FEBID precursors; long shelf life is a desirable quality for commercially successful precursors. However, cyclopentadienyl ligands and their derivatives have been found to be poor dissociators upon electron impact and capture[50,57,58] – ideally, use of a ligand with lower hapticity might provide stability for the precursor while simultaneously decreasing the carbon content of FEBID deposits. The bromide ligand, as a halide, is generally considered a good potential leaving group in DEA. Additionally, it has been shown in recent studies that it may be removed via post-deposition irradiation.[38,39] Finally, carbonyl ligands are known to be generally good leaving groups both via DEA and via DI in several organometallic FEBID precursors.[60,62,125] This provides a good standard to which we can compare the dissociation efficiency of the other ligands. Additionally, ruthenium is the least expensive platinum group metal and thus has several industrial applications,[126] as well as being in the same group as iron and therefore potentially

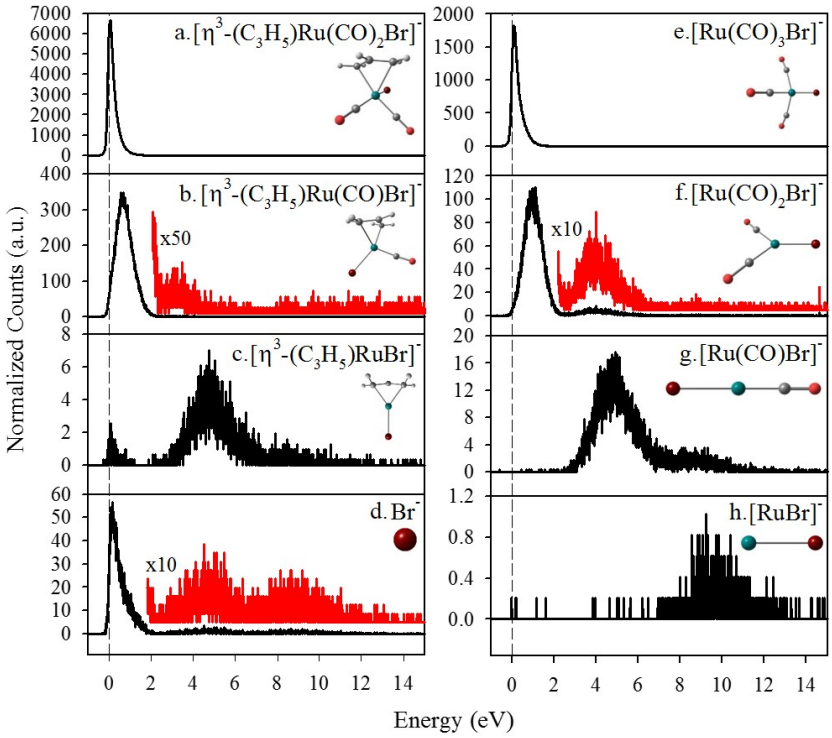

Figure 4.2. Normalized ionization curves of negative ionic fragments produced from DEA to (η^3-C_3H_5)Ru(CO)$_3$Br, shown with their respective chemical formulae and ground state anionic geometries calculated at the BP86 level of theory using the def2-TZVP basis set. Two major channels are observed: the $[M - nCO]^-$ channel, seen in yields a - c, and then $[M - nCO - allyl]^-$ channel, seen in yields e - h. Bromide is also observed, seen in yield d.

supporting similar ligand architectures. Ultimately, the experimental results of gas phase, surface, and FEBID studies on the electron-induced dissociation and deposition of (η^3-C_3H_5)Ru(CO)$_3$Br may allow the optimization of future FEBID precursor design.

4.1.2 Results and Discussion

Dissociative electron attachment and quantum chemical calculations

Figure 4.2 shows the negative ion spectra of the eight main fragments observed via DEA to (η^3-C_3H_5)Ru(CO)$_3$Br. Two major channels are observed: (i) sequential CO loss ($[M - nCO]^-$, n = 1 - 3), shown in fig. 4.2a - 4.2c, and (ii) allyl loss accompanied by sequential CO loss ($[M - nCO - allyl]^-$, n = 0 - 3), shown in fig. 4.2e - 4.2h.

Bromide loss is also observed, albeit with low intensity, in fig. 4.2d. It is important to note that each experimentally observed negative ion fragment contains bromide; in DEA to this molecule, the bromide-containing fragment always retains the negative charge. Each negative ion yield spectrum is pressure-normalized, and presented at a nominal target pressure of 5×10^{-7} mbar. The molecular structures of each of these fragments optimized at the BP86 level of theory using the def2-TZVP basis set are shown alongside their respective negative ion yields. All fragments were easily identifiable via their characteristic isotopic distributions.

The most dominant fragment observed in DEA to (η^3-C_3H_5)$Ru(CO)_3Br$ is single carbonyl loss ([(η^3-C_3H_5)$Ru(CO)_2Br]^-$, fig. 4.2a), closely followed by the allyl loss fragment ($[Ru(CO)_3Br]^-$, fig. 4.2e). Each of these fragments constitutes a single ligand loss and proceeds via a low-energy resonance with a maximum probability for anionic fragment formation centered close to 0 eV. Bromide, which is also produced via single bond cleavage, is also evident through this resonance (Br^-, fig 4.2d). The dominance of single bond breakage, as is evident in each of these fragments, is typical in DEA.[56,58] As previously discussed, the threshold for DEA to a molecule can be approximated by equation 2.15, restated here for ease of reading:

$$E_{th}([M-X]^-) \approx \sum_i^n BDE(parent) - (\sum_i^n BDE(product) + EA[M-X]) \qquad (4.1)$$

Essentially, the threshold for the reaction producing a given anion $[M - X]^-$ is approximately equal to the sum of the bond dissociation energies (BDEs) of the bonds broken in the parent molecule less the sum of the BDEs of the bonds formed in the product ion and neutral fragments and the electron affinity (EA) of the charge retaining fragment. Hence, with a threshold close to 0 eV and lack of significant bond formation, the energy provided to the system by the electron affinity of the charge-retaining fragment will generally be sufficient for only a single bond breakage.

It must be noted that each of these dissociation channels must be exothermic in order to be thermochemically accessible at these low energies. Each of the single ligand loss channels were found to be exothermic, with the thresholds for formation of $[M - 1CO]^-$, $[M - allyl]^-$, and Br^- calculated to be -1.36, -0.91, and -0.76 eV, respectively, at the LPNO-pCCSD/2a level of theory using the aug-cc-pVTZ basis set. We additionally note that the principal fragments $[M - 1CO]^-$ and $[M - allyl]^-$ being produced via a narrow resonance with maximum anionic fragment yield close to 0 eV is also typical in DEA. The cross section for electron attachment close to 0 eV is proportional to $E^{-1/2}$, making electron attachment most efficient as the incident electron energy approaches 0 eV.[4,75] Further, as discussed in chapter 2, electron attachment close to 0 eV is associated with relatively long-lived resonances, which produce narrow peaks in the ion yield as seen here. These narrow ion yields with maximum intensity close to 0 eV are commonly associated with vibrational Feshbach resonances, which may only be formed if the electron affinity of the parent molecule is positive. The adiabatic electron affinity of (η^3-C_3H_5)$Ru(CO)_3Br$ was calculated to be 1.27 eV; we therefore attribute these single ligand loss channels to a vibrational Feshbach resonance.

Double ligand loss, producing [(η^3-C_3H_5)Ru(CO)Br]$^-$ ([M − 2CO]$^-$, fig. 4.2b) and [$Ru(CO)_2Br$]$^-$ ([M − 1CO − allyl]$^-$, fig. 4.2e), similarly appears at energies close to 0 eV. The double carbonyl loss fragment was calculated to be endothermic by 0.07 eV, while the single carbonyl and allyl loss fragment was calculated to be endothermic by 0.16 eV. The low appearance energies of these two fragments suggest that they may proceed via the same resonance as that which produces the single ligand loss fragments; however, their increased energetic threshold due to the multiple bonds broken results in a drastically decreased DEA cross section for each of these fragments as compared to the principal fragments [M − 1CO]$^-$ and [M − allyl]$^-$.

Triple ligand loss, producing [(η^3-C_3H_5)RuBr]$^-$ ([M − 3CO]$^-$, fig. 4.2c) and [Ru(CO)Br]$^-$ ([M − 2CO − allyl]$^-$, fig. 4.2g), proceeds through a resonance with a maximum ion yield around 4-5 eV. Both double ligand loss fragments are also observed through this resonance, as is the bromide loss fragment. This is within the energy regime where we expect the lowest-energy core-excited resonances to exist; however, it is also within the higher part of the energy range of single-particle shape resonances.[67] In the current experiment, we cannot distinguish the resonance or resonances that may contribute to the observed negative ion yields. Finally, quadruple ligand loss, producing [RuBr]$^-$ ([M − 3CO − allyl]$^-$, fig. 4.2h), is observed through a broad contribution peaking around 9 eV. Both triple ligand loss fragments, as well as the bromide loss fragment, are also observed via this contribution. The resonance(s) associated with this contribution to the ion yield is within the energy range of core-excited resonances. As bromide is observed at 0 eV, it is likely that the bromide-producing channels via these higher-lying resonances are associated with further fragmentation of the neutral bromide loss fragment.

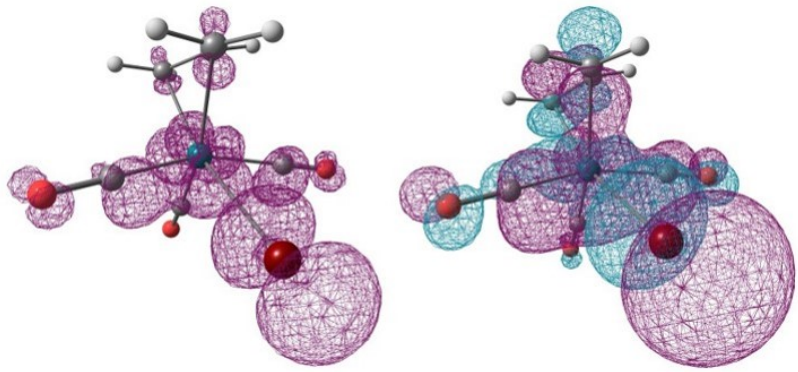

Figure 4.3. Spin density isosurface (left) and SOMO isosurface (right) of [(η^3-C_3H_5)$Ru(CO)_3Br$]$^-$ in its relaxed (ground state) geometry. These isosurfaces were calculated with a contour value of 0.0250000. As can be seen here, the electron attaches into an orbital with considerable ruthenium d-character. The SOMO is bonding along two Ru−C bonds, nonbonding along one Ru−C bond, and antibonding along the Ru−Br bond. This results in a significant lengthening of the Ru−Br bond from the neutral ground state to the anionic ground state.

Table 4.1. Calculated bond lengths of (η^3-C_3H_5)Ru(CO)$_3$Br in the neutral ground state and in the anionic ground state. These geometries were calculated at the BP86 level of theory using the def2-TZVP basis set. Significant lengthening of the Ru−Br bond is seen here, confirming electron attachment into an orbital with significant antibonding character along the Ru−Br coordinate. Compared to the Ru−Br bond, all other bonds remain essentially unchanged upon electron attachment.

Bond	Neutral bond length Å	Anionic bond length Å
Ru−Br	2.59	3.14
Ru−CO (1)	1.97	1.96
Ru−CO (2)	1.91	1.89
Ru−CO (3)	1.95	1.96
Ru−CH_2 (1)	2.27	2.34
Ru−CH_2 (2)	2.35	2.33
Ru−CH (1)	2.24	2.25

It is instructive to compare the low efficiency of Br^- with the comparatively higher efficiencies of both double ligand loss channels. Due to its high electron affinity, bromide was expected to be a good leaving group in this molecule. Additionally, as can be seen in fig. 4.3, analysis of the calculated spin density isosurface of the TNI [(η^3-C_3H_5)Ru(CO)$_3$Br]$^-$ (4.3a) as well as the singly occupied molecular orbital (SOMO) (fig. 4.3b) shows that the captured electron attaches to an orbital largely centered on the ruthenium atom with strong Ru *d*-orbital character and significant antibonding character along the Ru−Br bond. The SOMO is bonding along 2 Ru−CO bonds, and non-bonding along the third Ru−CO bond. The calculated bond lengths of the optimized molecular structures before and after electron capture are summarized in table 4.1. The bonding and non-bonding Ru−CO bonds cannot be differentiated by bond length before or after electron attachment; the Ru−CO bond lengths are essentially all the same length both before and after electron attachment. The bond lengths between the ruthenium and the allyl ligand are also unchanged with electron capture. The Ru−Br bond, however, significantly lengthens upon electron capture, confirming the capture of the electron into an orbital with significant antibonding character along this bond coordinate.

In order to better understand the low efficiency of the bromide formation channel, we can first turn to the calculated threshold energies of the observed channels for DEA to (η^3-C_3H_5)Ru(CO)$_3$Br, summarized schematically in Figure 4.4 and shown along with the optimized molecular structures of each observed fragment and the experimentally observed appearance energies for each fragment. The molecular structures were optimized using the DFT BP86 functional using the def2-ZVP basis set, and zero point energy contributions as well as thermal contributions in accordance with the current experimental temperature (298 K, 0.37 eV) were calculated at this level of theory. The energetic thresholds to produce the observed fragments via DEA to (η^3-C_3H_5)Ru(CO)$_3$Br were calculated at three levels of theory: BP86 (a DFT method based on the generalized gradiant approximation (GGA)), PBE0 (a hybrid-GGA functional),

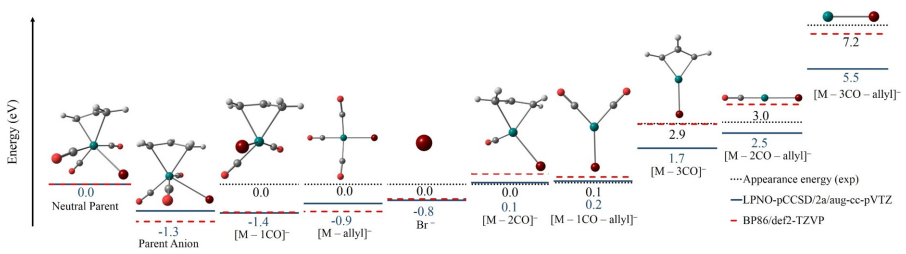

Figure 4.4. This is a schematic of the calculated energetic thresholds of experimentally observed fragments produced by DEA to (η^3-C_3H_5)$Ru(CO)_3Br$, calculated at the BP86/def2-TZVP and LPNO-pCCSD/2a/aug-cc-pVTZ levels of theory. The dotted black line indicates the experimentally observed appearance energy of each fragment, while the dashed red line indicates the calculated threshold at the BP86/def2-TZVP level of theory and the solid blue line indicates the calculated threshold at the LPNO-pCCSD/2a/aug-cc-pVTZ level of theory.

and LPNO-pCCSD/2a (a coupled cluster method consisting of the wavefunction-based method pCCSD/2a in conjunction with the local pair natural orbital (LPNO) methodology) (see section 3.2). As discussed in section 2, the appearance energy of a fragment must be above the thermally-corrected energetic threshold of its formation. In figure 4.4, we can see that this is not the case for the calculated energetic thresholds for the formation of three of the experimentally observed fragments using the BP86 method: $[M - 1CO - allyl]^-$, $[M - 2CO]^-$, and $[M - 2CO - allyl]^-$. This is, of course, not thermodynamically possible.

In order to more accurately predict the energetic thresholds for formation of these fragments via DEA to (η^3-C_3H_5)$Ru(CO)_3Br$, we compared the three aforementioned computational methods and several basis sets used to calculate these three fragments, as well as the fragment $[M - 3CO]^-$. These calculations are summarized in table 4.2. Four different basis sets are shown in this table: def2-TZVP (a balanced polarized triple-zeta basis set using effective core potentials (ECPS)), ma-ZORA-def2-TZVPP (a diffuse, polarized triple-zeta basis set using all-electron relativistic ZORA calculations), ma-ZORA-def2-QZVPP (a similar, quadruple-zeta basis set), and aug-cc-pVTZ (a diffuse, polarized triple-zeta basis set). Multiple basis sets were used with the GGA-DFT BP86 in order to determine whether the poor agreement with experimental values for these fragments were due to basis set incompleteness or the use of ECPs. Calculations with the hybrid-GGA functional PBE0 and the coupled cluster method LPNO-pCCSD/2a were used to determine if either of these methods would give a better description of the thermodynamics of these channels. As we can see in this table, none of the basis sets used with the BP86 method provided adequately accurate energetic thresholds for all four fragments, and PBE0 was also inadequate. In contrast, the coupled cluster method LPNO-pCCSD/2a gives energetic thresholds at or below the appearance energies of these fragments with an accuracy of 0.1 eV (the approximate width of the electron beam).

Table 4.2. Comparison of thermodynamic threshold energies for fragment formation at the experimental temperature calculated by three different computational methods and several basis sets with the respective experimentally determined appearance energies. The appearance energy of a fragment must be at or above the energetic threshold; any calculation that gives an energetic threshold for anionic fragment formation above the experimentally observed appearance energy therefore does not accurately describe the reaction. The coupled cluster method LPNO-pCCSD/2a shows the most promising results of the compared methods.

Fragment	Appearance Energy (eV)	BP86/ def2-TZVP	BP86/ma-ZORA-def2-TZVPP	BP86/ma-ZORA-def2-QZVPP
M − 2CO	0.00	0.51	0.68	0.67
M − 1CO − allyl	0.07	0.35	0.44	0.42
M − 3CO	2.91	2.88	3.23	3.15
M − 2CO − allyl	2.98	3.81	3.99	3.93
Fragment	Appearance Energy (eV)		PBE0/ma-ZORA-def2-TZVPP	LPNO-pCCSD/ 2a/aug-cc-pVTZ
M − 2CO	0.00		0.63	0.07
M − 1CO − allyl	0.07		0.53	0.16
M − 3CO	2.91		2.75	1.73
M − 2CO − allyl	2.98		4.80	2.45

Turning back to figure 4.4, we can see that the thermodynamic threshold for bromide loss is higher than those for carbonyl loss and for allyl loss, which would explain why these two channels are more efficient than the bromide loss channel. However, the threshold for allyl loss is only 0.15 eV more exothermic than that for bromide loss, so we would expect the branching ratio for bromide loss to be at a similar order of magnitude to allyl loss. Ultimately, it seems that the low efficiency of bromide loss at 0 eV cannot fully be explained by the thermodynamics of the respective channels operative at 0 eV, and instead dissociation dynamics are likely to be more significant than thermodynamics for these channels. It should be noted that each of the anionic fragments observed in DEA to (η^3-C_3H_5)$Ru(CO)_3Br$ contain a bromide ligand. It is likely that the bromide ligand contributes to the stability of the charge-retaining fragments, potentially by increasing the electron affinities of these fragments and making dissociation channels accessible.

Dissociative ionization

Figure 4.5 shows the dissociative ionization spectrum of (η^3-C_3H_5)$Ru(CO)_3Br$ taken at 75 eV between 90 and 320 amu. As previously discussed, DI is a non-resonant process exhibiting threshold behavior, where the cross-sections for channels producing each cationic fragment will rapidly increase with increasing incident electron energy from their respective thresholds to a maximum between 50 and 100 eV. After this peak, the cross-sections will slowly decrease. A spectrum recorded at 75 eV should

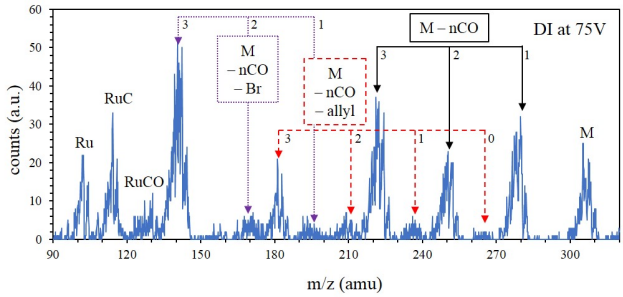

Figure 4.5. Spectrum of the dissociative ionization of (η^3-C_3H_5)$Ru(CO)_3Br$ recorded at 75 eV. Three major regressions are seen here - $[M - nCO]^+$, $[M - nCO - allyl]^+$, and $[M - nCO - Br]^+$. As can be seen here, significantly more fragmentation of the parent molecules is observed via DI than via DEA, and bromine in particular is appreciably more labile. The parent cation and bare ruthenium cation are also present, as is $[RuC]^+$.

be high enough in energy that the fragmentation processes have all passed their peak, and the relative cross-sections for each observed fragment should thus be directly comparable. Importantly, our experimental setup cannot differentiate isobaric fragments; as ruthenium and bromine both have significant isotope distributions, fragments with varying quantities of hydrogen cannot be discerned.

As seen in figure 4.5, DI of (η^3-C_3H_5)$Ru(CO)_3Br$ produces 3 main channels: sequential CO loss ($[M - nCO]^+$, n = 1 - 3), allyl loss accompanied by sequential CO loss ($[M - nCO - allyl]^+$, n = 0 - 3), and Br loss accompanied by sequential CO loss $[M - nCO - Br]^+$, n = 1 - 3). The parent cation and the bare ruthenium cation are also observed, as are ruthenium carbide ($[RuC]^+$), two of the ligands ($[CO]^+$ and $[C_3H_5]^+$), and fragmentation of the allyl ligand ($[C_3H_3]^+$). The bromine cation is not observed. The dominant channel is the sequential CO loss channel, and the dominant fragments are $[M - 3CO - Br]^+$ and $[M - 3CO]^+$. Although the isotope distribution of the loss of bromine ($[M - Br]^+$) overlaps with that of triple carbonyl loss ($[M - 3CO]^+$), comparison of the isotope distribution within this region with those of $[M - Br]^+$ and $[M - 3CO]^+$ determined that $[M - Br]^+$ does not significantly contribute in this region.

Table 4.3 shows the relative intensities of each fragment observed in DEA and DI of (η^3-C_3H_5)$Ru(CO)_3Br$, as well as the average number of each type of ligand lost per dissociation incident. Relative intensities for DEA were determined by integrating the pressure-normalized ion yield for each fragment recorded at the principal isotope *m/z* ratio and normalizing it to the single carbonyl loss peak (*m/z* = 278). For DI, relative intensities were determined by integrating over the isotope distribution for each fragment and again normalizing it to the single carbonyl loss isotope distribution. While the branching ratios for DEA and DI cannot be directly compared with each other via this method, they can be compared internally. The number of ligands of each type

Table 4.3. Comparison of the relative intensities of ions produced by electron-initiated dissociation of (η^3-C_3H_5)$Ru(CO)_3Br$ via DEA and via DI. The average number of each type of ligand (CO, allyl, and Br) lost per dissociation event by DEA and DI is also shown. Significantly more fragmentation is observed through DI-initiated decomposition than through DEA - an average of about 1 CO, 0.2 allyl, and no bromide ligands are lost per dissociation event via DEA, while an average of about 2 COs, 0.3 allyl, and 0.4 bromine ligands are lost per dissociation event via DI.

Fragment	*m/z*	DEA Rel. Intensity	DI Rel. Intensity
$[(\eta^3\text{-}C_3H_5)Ru(CO)_3Br]^{+/-}$	306		68.3
$[(\eta^3\text{-}C_3H_5)Ru(CO)_2Br]^{+/-}$	278	100.0	100.0
$[Ru(CO)_3Br]^{+/-}$	265	29.7	4.0
$[(\eta^3\text{-}C_3H_5)Ru(CO)Br]^{+/-}$	250	12.3	74.7
$[Ru(CO)_2Br]^{+/-}$	237	4.4	12.9
$[(\eta^3\text{-}C_3H_5)RuBr]^{+/-}$	222	0.4	119.7
$[Ru(CO)Br]^{+/-}$	209	1.2	14.2
$[(\eta^3\text{-}C_3H_5)Ru(CO)_2]^{+/-}$	199		12.5
$[RuBr]^{+/-}$	181	0.02	42.4
$[(\eta^3\text{-}C_3H_5)Ru(CO)]^{+/-}$	171		19.1
$[(\eta^3\text{-}C_3H_5)Ru]^{+/-}$	143		178.6
$[Ru(CO)]^{+/-}$	130		24.9
$[RuC]^{+/-}$	114		69.8
$Ru^{+/-}$	102		43.1
$Br^{+/-}$	79	1.6	
$[RuC]^{+/-}$	57		6.2
$[C_3H_5]^{+/-}$	41		31.8
$[C_3H_3]^{+/-}$	39		30.9
$[CO]^{+/-}/N_2^{+/-}$	28		43.9
Average CO loss		0.9	2.1
Average allyl loss		0.2	0.3
Average Br loss		0.0	0.4

lost per dissociation incident were calculated by taking the relative intensity of each ruthenium-centered fragment and multiplying it by the number of respective ligands lost, then dividing this number by the total intensity of all ruthenium-centered fragment. Using this, we can compare the extent of fragmentation via DEA and DI.

As seen in table 4.3, much more extensive fragmentation is observed via DI when compared to fragmentation via DEA. This is as expected − DI is a higher-energy process, providing more energy for bond dissociation. Additionally, DEA is most efficient close to 0 eV, where the least fragmentation is expected to occur. Bromine is significantly more labile via DI than via DEA, with 0.4 bromine ligands lost per dissociation incident compared to an average of 0 bromide ligands lost per incident via DEA. Additionally, DI produces more than twice the number of carbonyl ligands lost per dissociation incident

as compared to DEA. Allyl loss is similar via DEA and DI; however, when compared to carbonyl loss, allyl loss is much less significant via DI than via DEA. Generally, when using these results to predict the behavior of (η^3-C_3H_5)$Ru(CO)_3Br$ in FEBID, we can expect to see more carbonyl ligands and bromide ligands lost (albeit marginally) if DI is more important in the deposition of (η^3-C_3H_5)$Ru(CO)_3Br$. Conversely, if DEA is more important, we can expect to see more carbonaceous deposits and persistent bromine.

Comparison to surface data

An ultra-high vacuum (UHV) surface study was also performed on (η^3-C_3H_5)$Ru(CO)_3Br$ in a recent study by Spencer et al. at Johns Hopkins University.[38] In this study, (η^3-C_3H_5)$Ru(CO)_3Br$ was adsorbed in nanometer-thick films onto amorphous carbon and gold substrates cooled to approximately 100 K, and incrementally irradiated with electrons using a 500 eV flood gun. Changes in the elemental composition of the films were observed via X-ray photoelectron spectroscopy (XPS), while electron-induced desorption of gaseous molecules from the surface during irradiation was monitored by mass spectroscopy (MS). Each of these techniques reveal a swift initial loss of CO from the surface before leveling off at about 20% of the original quantity, measured by the O (1s) signal. Neither the allyl nor the bromine are found to desorb from the surface during the initial electron irradiation step; however, bromine loss is observed after prolonged electron irradiation.

The significant carbonyl loss and complete lack of allyl loss observed under the UHV surface studies of electron-irradiated (η^3-C_3H_5)$Ru(CO)_3Br$ films fits within the profile of DI-induced deposition; however, the persistence of the bromine ligand is more consistent with DEA as the initial deposition mechanism. It is thus difficult to determine from this data whether DEA or DI may be more important in deposit formation from (η^3-C_3H_5)$Ru(CO)_3Br$; it seems likely that a combination of the two processes contribute to deposition here. Additionally, the effects of the surface on DEA and DI channels and other potential contributing reactions, such as neutral dissociation, have not been considered in this study. However, the study can be used to examine the relative labilities of the ligands used and their consequent desirability in FEBID precursors. Carbonyl ligands are good leaving groups both via DEA and via DI, as has been found for other FEBID precursors.[58,62,127] Conversely, the η^3-allyl ligand and the bromide ligand are evidently both poor leaving groups. These are both consistent with studied precursors utilizing π-facial ligands[58,59] and halides.[39] However, halides have been found removable via extended electron irradiation.[38,39] Therefore, although π-facial ligands like η^3-allyl may not be desirable for use in FEBID, halides may be despite their persistence.

Deposition and comparison with $Ru_3(CO)_{12}$

In order to determine the potential performance of (η^3-C_3H_5)$Ru(CO)_3Br$ under actual FEBID conditions, FEBID experiments were performed wherein $1\mu m^2$ squares were

Table 4.4. Comparison of deposition of ruthenium from (η^3-C_3H_5)$Ru(CO)_3Br$ and $Ru_3(CO)_{12}$. The two precursors were sublimed at 69 - 74 °C, and deposited for 10 to 30 minutes. The thickness of deposits is estimated by the elemental percentage of silicon - the maximum escape depth of X-rays measured in EDX is 1 - 2 µm. Deposit purity is estimated by the ratio of carbon to ruthenium and bromine to ruthenium in the deposit. As can be seen here, (η^3-C_3H_5)$Ru(CO)_3Br$ produce significantly larger and purer ruthenium deposits than the CVD precursor $Ru_3(CO)_{12}$.

Precursor	Sublimation Temp (±1°C)	Deposition Time (min)	Si at.%	C:Ru Ratio	Br:Ru Ratio
(η^3-C_3H_5)$Ru(CO)_3Br$	73	10	28.9	1.8	0.73
(η^3-C_3H_5)$Ru(CO)_3Br$	74	20	1.7	1.2	0.85
(η^3-C_3H_5)$Ru(CO)_3Br$	74	30	1.5	1.2	0.83
$Ru_3(CO)_{12}$	69	10	76.1	2.1	–
$Ru_3(CO)_{12}$	72	20	56.9	2.1	–
$Ru_3(CO)_{12}$	70	30	59.3	2.3	–

deposited from (η^3-C_3H_5)$Ru(CO)_3Br$ onto clean silicon substrates, varying both sublimation temperature and deposition time in order to find optimal deposition conditions. Three different precursor sublimation temperatures were used – 38 °C, 74 °C, and 119 °C – and three different deposition times – 10, 20, and 30 minutes. Energy dispersive X-ray spectroscopy (EDX) was used to measure the C:Ru and Br:Ru ratios, as well as the approximate deposit thickness (evidenced by the disappearance of the Si EDX peak). Deposition at 38 °C showed a high atomic percentage of silicon (77.4 - 91.7 at.%), even after 30 minutes of deposition; this was determined to be too low a temperature to deposit ruthenium from (η^3-C_3H_5)$Ru(CO)_3Br$ under these experimental conditions. Deposition at 119 °C failed to deposit ruthenium entirely; we attribute this to decomposition of the compound in the sample holder and consequent failure to sublime.

Deposition of ruthenium from (η^3-C_3H_5)$Ru(CO)_3Br$ at 74 °C is summarized in table 4.4. While 10 minutes of deposition produces 28.9 at.% Si, 20 and 30 minutes of deposition produces 1.7 at.% and 1.5 at.%, indicating that the sample thickness is nearing the sampling depth of the characteristic X-rays measured in EDX (about 1-2 μm). The best C:Ru ratio is found for the 30 minute deposition time, and is 1:1. This is six times lower than the molecular formula of the precursor, which has a 6:1 carbon-to-ruthenium ratio. The Br:Ru ratio is 0.83:1, which is approximately the same as that of the precursor. This is similar to results found in the UHV surface study: bromine is persistent during deposition. However, as seen in the surface study, further electron irradiation in the absence of the gaseous precursor may produce bromine dissociation from the deposit.

As a comparison, $1\mu m^2$ squares were also deposited from $Ru_3(CO)_{12}$, a previously used chemical vapor deposition (CVD) precursor, using two sublimation temperatures and three deposition times. Deposits from $Ru_3(CO)_{12}$ at approximately 70 °C are also summarized in table 4.4; deposits at 119 °C failed to deposit ruthenium. The deposits

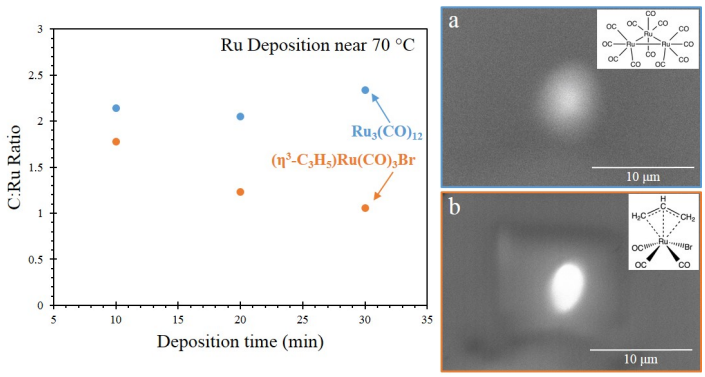

Figure 4.6. Left: a comparison of the elemental composition of deposits formed from $(\eta^3\text{-}C_3H_5)Ru(CO)_3Br$ and $Ru_3(CO)_{12}$ near 70 °C at deposition times of 10, 20, and 30 minutes. As can be seen here, deposits formed from $(\eta^3\text{-}C_3H_5)Ru(CO)_3Br$ had significantly less carbon contamination than those formed from the CVD precursor $Ru_3(CO)_{12}$. Right: SEM images of deposits formed from (a) $Ru_3(CO)_{12}$, and (b) $(\eta^3\text{-}C_3H_5)Ru(CO)_3Br$.

from $Ru_3(CO)_{12}$ are much thinner than those from $(\eta^3\text{-}C_3H_5)Ru(CO)_3Br$, as evidenced by the significant Si at.% even after 30 minutes of deposition. The average C:Ru ratio in the deposits is about 2:1, which is only half the ratio in the molecular formula of the precursor, which is 4:1. These deposits are therefore lower in quality than those for deposition from $(\eta^3\text{-}C_3H_5)Ru(CO)_3Br$. Results from both precursors are summarized in fig. 4.6 with SEM images of deposits from each precursor.

It is interesting to note that deposits produced from $(\eta^3\text{-}C_3H_5)Ru(CO)_3Br$ have a much higher purity than expected based on both the gas phase and surface studies discussed here. Gas phase electron-induced dissociation via DI produced an average dissociation of approximately two carbonyl ligands, 0.3 allyl ligands, and 0.4 Br ligands. Surface studies of electron-induced deposition of films from $(\eta^3\text{-}C_3H_5)Ru(CO)_3Br$ showed significant carbonyl loss during deposition, but no allyl or Br loss. Based on these results, we would expect a minimum carbon-to-ruthenium ratio of 3:1 in the deposits, assuming essentially no allyl loss. Under *in situ* FEBID experiments, we observe little Br loss, which is consistent with both gas phase experiments and surface studies. The remarkable carbon loss seen in FEBID, producing a 1:1 carbon-to-ruthenium ratio, is in conflict with the gas phase and surface studies. This must be a product of significant decomposition of the allyl ligand and either dissociation from the surface or diffusion away from the deposition area. This may be a result of thermal effects: UHV experiments are commonly performed on cooled (< 150 K) surfaces, while the *in situ* FEBID studies were performed on a surface at room temperature. Additional heating of the surface due to energy transfer from the primary electron beam is also possible.[20] Further studies are necessary to determine the source of this discrepancy.

4.2 Low-energy electron interactions with (η^5-Cp)Fe(CO)$_2$Mn(CO)$_5$

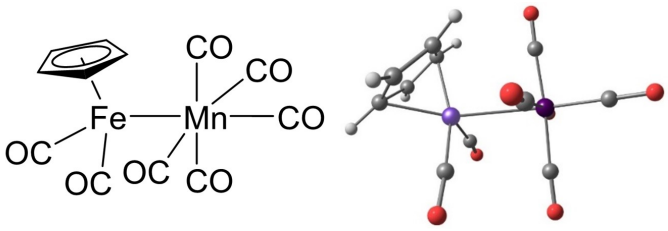

Figure 4.7. Chemical structure diagram (left) and calculated ground state geometry (right) of η^5-cyclopentadienyl iron dicarbonyl manganese pentacarbonyl. The ground state geometry was calculated at the BP86 level of theory with the def2-TZVP basis set.

4.2.1 Introduction and Motivation

Deposition of alloyed nanostructures presents a set of unique problems in FEBID. Unlike pure metal deposition, the deposition of alloyed nanostructures has historically involved use of multiple gas injection systems in order to mix precursor gases *in situ*. Several issues can manifest from this deposition strategy. First, the use of multiple precursors generally increases the total number of ligands that must be dissociated in order to deposit pure metal nanostructures; this naturally leads to an increased potential for ligand codeposition and contamination. Additionally, precursors may require very different deposition conditions in order to produce optimal deposits. Optimization of deposition conditions (e.g. precursor flux, electron flux, substrate temperature, etc) for a mix of precursor gases will thus necessitate sub-optimal deposition conditions for at least one of the precursors, producing inferior deposits. Indeed, ligand contamination has historically been an issue in alloyed nanostructure deposition.[25,43] Additionally, the difficulty of finely controlling several precursor inlet systems during deposition can lead to issues with reproducibility and homogeneity of the deposits.[25,42,44]

In order to combat these problems, recent FEBID studies have been performed using heteronuclear bimetallic precursors. Porrati et al. deposited an FeCo alloy from the precursor $HFeCo_3(CO)_{12}$, attaining greater than 80 at.% metal purity.[45] The deposit had a 3:1 Co:Fe ratio, as is the case in the precursor, making this a promising avenue toward depositing high-quality alloys of reproducible composition using FEBID. This precursor was further studied in a UHV surface study alongside a structurally similar precursor, $H_2Fe(Ru)_3(CO)_{13}$, in order to determine whether the architecture of this molecule was a major factor in the high quality of deposits produced from $HFeCo_3(CO)_{12}$.[48,49] It was determined via these surface studies that, although $HFeCo_3(CO)_{12}$ and $H_2Fe(Ru)_3(CO)_{13}$ undergo similar deposition profiles

when exposed to 500 eV electron irradiation on a cooled surface under UHV conditions, post-deposition heating showed very different thermally-induced behavior of the two deposits. This is potentially the source of the better performance of $HFeCo_3(CO)_{12}$ when compared to $H_2Fe(Ru)_3(CO)_{13}$ in electron-induced deposition: while deposits from $HFeCo_3(CO)_{12}$ achieved a high purity when deposited under UHV conditions and heated to room temperature, $H_2Fe(Ru)_3(CO)_{13}$ only produced deposits with approximately 20 at.% metal purity under these same conditions. To date, these are the only two heterometallic precursors that have been studied. A great deal of exploration in this area is clearly necessary in order to determine the quality and efficiency of alloy deposition from heterometallic precursors. This was our primary motivation in studying the low-energy electron-induced dissociation of (η^5-Cp)Fe(CO)$_2$Mn(CO)$_5$ in the gas phase: to expand our knowledge on electron-induced reactivity of heterometallic precursors for potential use in FEBID.

Such molecules that may be useful in FEBID are also interesting from a fundamental science perspective. The low-energy electron-induced dissociation of $HFeCo_3(CO)_{12}$ was also studied in the gas phase, where it was found to have remarkable behavior. The molecule exhibited quasicontinuous electron attachment from about 1 eV up to 20 eV, which is exceedingly high.[46,47] This was attributed to the high density of low-energy unoccupied π^* orbitals from the bridging and terminal carbonyl ligands and metal-based HOMOs, allowing for multiple-particle-multiple-hole excitations. In this way, the molecular orbital structure of $HFeCo_3(CO)_{12}$ begins to mimic the electronic band structure exhibited by bulk metals and semiconductors. This was another aim of studying gas phase electron interactions with (η^5-Cp)Fe(CO)$_2$Mn(CO)$_5$ - to determine if such interesting behavior might be exhibited by a smaller molecule with fewer metal-based HOMOs and fewer unoccupied ligand-based LUMOs.

4.2.2 Results and Discussion

Dissociative electron attachment and quantum chemical calculations

The negative ion yields produced by DEA to (η^5-Cp)Fe(CO)$_2$Mn(CO)$_5$ are shown in figures 4.8 and 4.9. Each negative ion yield has been pressure-normalized and is displayed here at a nominal target pressure of 5×10^{-7} mbar. There are two main dissociation channels shown in these figures: fig. 4.8 shows sequential CO loss ($[M - nCO]^-$, n = 1 - 5), while fig. 4.9 shows Fe-Mn bond dissociation accompanied by CO loss ($[Mn(CO)_{5-n}]^-$, n = 0, 1). Further CO loss in this channel is not observed. In these figures, fragments are labeled stoichiometrically, as it is not possible to differentiate isomeric fragments via this instrument - e.g. the ion yield shown in $[CpFeMn(CO)_6]^-$ consists of isomers $[(\eta^5\text{-Cp})Fe(CO)Mn(CO)_5]^-$ and $[((\eta^5\text{-Cp})Fe(CO)_2Mn(CO)_4]^-$. Because of this, quantum chemical calculations were used in order to determine the isomers present for several reaction channels.

The most dominant fragments seen in DEA to (η^5-Cp)Fe(CO)$_2$Mn(CO)$_5$ are $[CpFeMn(CO)_6]^-$ (*m/z* = 344) and $[Mn(CO)_5]^-$ (*m/z* = 195), shown in figures 4.8a and 4.9a, respectively. Both fragments may be produced via a single ligand dissociation

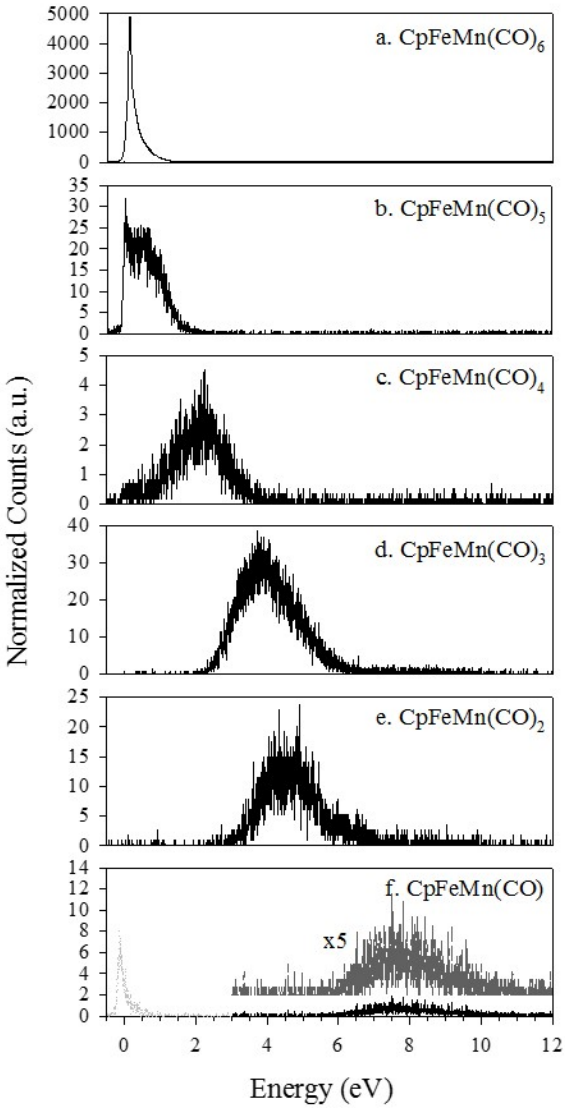

Figure 4.8. Normalized ionization curves of negative ionic fragments produced by DEA to (η^5-Cp)Fe(CO)$_2$Mn(CO)$_5$. The regression [CpFeMn(CO)$_{6-n}$]$^-$, n = 0 - 5, is depicted here. Three distinct channels are observed here: one (or several) low energy resonance(s) producing fragments with n = 0 - 2, one (or several) higher energy, core-excited resonance(s) producing fragments with n = 3, 4, and one (or several) high energy, core-excited resonance(s) producing the n = 5 fragment.

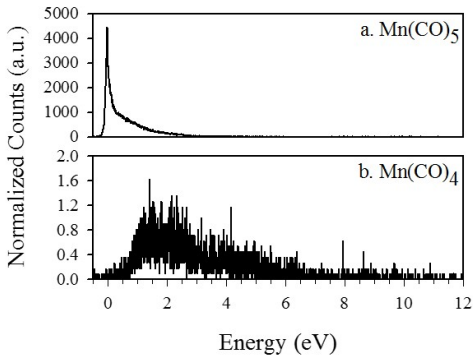

Figure 4.9. Normalized ionization curves of negative ionic fragments produced by DEA to (η^5-Cp)Fe(CO)$_2$Mn(CO)$_5$. The regression [Mn(CO)$_{5-n}$]$^-$, n = 0, 1, is depicted here. No further CO loss from the Mn-centered moiety is observed. The [Mn(CO)$_5$]$^-$ yield consists of a narrow peak close to 0 eV that broadens considerably above about 0.15 eV. This suggests that the channel for the formation of [Mn(CO)$_5$]$^-$ competes with the channel for [CpFeMn(CO)$_6$]$^-$ formation (see fig. 4.8), and calculations determine that [Mn(CO)$_5$]$^-$ may be formed by decomposition of [CpFe(CO)Mn(CO)$_5$]$^-$ at these higher energies.

and both are formed via a resonance producing an ion yield centered close to 0 eV. As previously discussed, these conditions are both consistent with typical fragmentation channels in DEA. Due to the narrow width of the peaks and the low appearance energy of these ion yields, we assign these channels to a vibrational Feshbach resonance at low energies. A close examination of the ion yields for these two fragments reveals that the [Mn(CO)$_5$]$^-$ yield peaks at approximately 0 eV, while the [CpFeMn(CO)$_6$]$^-$ yield peaks slightly higher, at approximately 0.15 eV. Turning our attention to the [Mn(CO)$_5$]$^-$ ion curve, we see a significant broadening of this peak at energies above about 0.15 eV. This suggests that more than one resonance may contribute to this ion yield. Taken together with the [CpFeMn(CO)$_6$]$^-$ yield, we see that these two ions bear some signs of being produced by competing channels.

When examining the negative ion yields for [Mn(CO)$_5$]$^-$ and [CpFeMn(CO)$_6$]$^-$, it is important to note that each of these anionic fragments can be made through multiple fragmentation channels. In the case of [Mn(CO)$_5$]$^-$, this fragment may be produced concurrently with the neutral fragment CpFe(CO)$_2$ via simple Fe−Mn bond rupture or it may be produced with concomitant loss of one or two carbonyl ligands from the iron-centered moiety. Additionally, [CpFeMn(CO)$_6$]$^-$ may be produced by losing a carbonyl ligand from either the iron center or from the manganese center, producing either [CpFe(CO)$_2$Mn(CO)$_4$]$^-$ or [CpFe(CO)Mn(CO)$_5$]$^-$. Thus, we can imagine a reaction pathway that might initially produce [CpFe(CO)Mn(CO)$_5$]$^-$, which may then decay to [Mn(CO)$_5$]$^-$ at adequately high energies:

Table 4.5. Selected calculated thresholds for several reaction pathways in DEA to (η^5-Cp)Fe(CO)$_2$Mn(CO)$_5$. The observed [Mn(CO)$_5$]$^-$ fragment can be produced with concurrent carbonyl loss from the iron-centered moiety. Based on the ion yields of the [Mn(CO)$_5$]$^-$ and [CpFeMn(CO)$_6$]$^-$ fragments and these calculations, we conclude that [CpFe(CO)Mn(CO)$_5$]$^-$ will fragment into [Mn(CO)$_5$]$^-$ and CpFe(CO) at higher incident electron energies. Thresholds were calculated at the DLPNO-CCSD(T) level of theory using the aug-cc-pVQZ basis set.

Anionic fragment		Neutral fragment A	Neutral fragment B	Threshold (eV)	Appearance energy (eV)
Mn(CO)$_5$	(1)	CpFe(CO)$_2$	–	-1.8	0.0
Mn(CO)$_5$	(2)	CpFe(CO)	CO	0.5	–
Mn(CO)$_5$	(3)	CpFe	2CO	2.5	–
CpFe(CO)$_2$Mn(CO)$_4$	(a)	CO	–	-1.3	0.0
CpFe(CO)Mn(CO)$_5$	(b)	CO	–	-1.5	–

$$\begin{aligned} [CpFe(CO)_2Mn(CO)_5]^{\ddagger -} &\rightarrow [CpFe(CO)Mn(CO)_5]^{\ddagger -} + CO \\ [CpFe(CO)Mn(CO)_5]^{\ddagger -} &\rightarrow [CpFe(CO)]^{\ddagger} + [Mn(CO)_5]^{\ddagger -} \end{aligned} \tag{4.2}$$

In order to determine the likelihood of such a reaction channel at the experimentally-observed energies, quantum chemical calculations were performed to find the energetic thresholds of reaction channels producing [Mn(CO)$_5$]$^-$ with accompanying carbonyl loss from the iron-centered neutral fragment (CpFe(CO)$_{2-n}$, n = 0 - 2). Additionally, the energetic thresholds of reaction channels producing the isomers [CpFe(CO)$_2$Mn(CO)$_4$]$^-$ and [CpFe(CO)Mn(CO)$_5$]$^-$ were also calculated. Molecular and anionic structures were geometrically optimized using the DFT GGA functional BP86, which was also used to find zero point energies and thermal contributions from the parent molecule to the energetic thresholds. Single point energy calculations were performed using the coupled cluster method DLPNO-CCSD(T) with the diffuse triple zeta and quadruple zeta basis sets aug-cc-pVTZ and aug-cc-pVQZ in order to control for basis set error. These thresholds are summarized in table 4.5, along with the respective experimentally-determined appearance energies.

The calculated thresholds show that the formation of [Mn(CO)$_5$]$^-$ via single bond rupture is exothermic by 1.8 eV, while the formation of [CpFe(CO)$_2$Mn(CO)$_4$]$^-$ and [CpFe(CO)Mn(CO)$_5$]$^-$ are exothermic by 1.3 and 1.5 eV, respectively. It is therefore thermochemically possible that both [CpFe(CO)$_2$Mn(CO)$_4$]$^-$ and [CpFe(CO)Mn(CO)$_5$]$^-$ are produced by electron attachment to (η^5-Cp)Fe(CO)$_2$Mn(CO)$_5$ close to 0 eV. Additionally, formation of [Mn(CO)$_5$]$^-$ with accompanying single CO loss from the iron-centered moiety is endothermic by merely 0.5 eV, putting it well within range of the broadened higher-energy tail of the ion yield seen in fig. 4.9a. The threshold for the formation of [Mn(CO)$_5$]$^-$ with double carbonyl loss from the iron-centered moiety, however, is endothermic by 2.5 eV. Thus, while it is within the higher-energy tail of the ion yield, it is unlikely that this channel contributes significantly to the [Mn(CO)$_5$]$^-$ ion

yield.

Turning back to fig. 4.9b, we can see that the ion yield for $[Mn(CO)_4]^-$ follows the high-energy tail of the $[Mn(CO)_5]^-$ ion yield curve. In order to determine the dominant $[CpFeMn(CO)_6]^-$ isomer produced via DEA to (η^5-Cp)Fe(CO)$_2$Mn(CO)$_5$, we may consider the branching ratios of the two potential routes toward formation of the $[Mn(CO)_4]^-$ fragment: decay of $[CpFe(CO)_2Mn(CO)_4]^-$ to $[Mn(CO)_4]^-$ at adequately high energies (eq. 4.3) or carbonyl ligand loss from $[Mn(CO)_5]^-$ (eq. 4.4).

$$\begin{aligned} [CpFe(CO)_2Mn(CO)_5]^{\ddagger -} &\rightarrow [CpFe(CO)_2Mn(CO)_4]^{\ddagger -} + CO \\ [CpFe(CO)_2Mn(CO)_4]^{\ddagger -} &\rightarrow [CpFe(CO)_2]^{\ddagger} + [Mn(CO)_4]^{\ddagger -} \end{aligned} \tag{4.3}$$

$$\begin{aligned} [CpFe(CO)_2Mn(CO)_5]^{\ddagger -} &\rightarrow [[CpFe(CO)_2]^{\ddagger} + Mn(CO)_5)]^{\ddagger -} \\ Mn(CO)_5)]^{\ddagger -} &\rightarrow [Mn(CO)4]^{\ddagger -} + CO \end{aligned} \tag{4.4}$$

The calculated threshold energy of $[Mn(CO)_4]^-$ is 0.5 eV, which agrees well with its appearance energy of 0.5 eV. This threshold is, of course, the same for either route of formation as it is a state function. The ion yield for $[Mn(CO)_4]^-$, however, gives us a clue. The intensity of $[Mn(CO)_4]^-$ at its peak, which is close to 1.5 eV, is extremely low – less than 0.5% of the $[Mn(CO)_5]^-$ intensity. At this energy, we expect significant $[Mn(CO)_5]^-$ formation via the reaction path described in eq. 4.2, which has the same energetic threshold as $[Mn(CO)_4]^-$ formation. This suggests that carbonyl loss from the manganese center of the initially formed resonance is insignificant, and that the $[Mn(CO)_4]^-$ fragment is formed by carbonyl loss from $[Mn(CO)_5]^-$ at higher energies. These reaction channels are illustrated schematically in fig. 4.10.

For the $[CpFeMn(CO)_{6-n}]^-$ series, as n increases we see a general increase in fragment appearance energy. This follows our previous discussion of the threshold energy for negative fragment formation via DEA: an increased number of bond dissociations will require increased reaction energy. For n = 1 and 2 ($[CpFeMn(CO)_5]^-$, *m/z* = 316 , and $[CpFeMn(CO)_4]^-$, *m/z* = 288, respectively), we can see that each of these fragments appears to be produced within the higher energy tail of the same resonance(s) producing $[Mn(CO)_5]^-$, $[CpFeMn(CO)_6]^-$, and $[Mn(CO)_4]^-$. In the ion yield spectrum of $[CpFeMn(CO)_5]^-$ (fig. 2b), we see a narrow, low-intensity peak close to 0 eV. We attribute this to hot band transitions from the higher energy tail of the Maxwell-Boltzmann internal energy distribution at the experimental temperature. The ion yields for the fragments corresponding to n = 3 and 4 ($[CpFeMn(CO)_3]^-$, *m/z* = 260, and $[CpFeMn(CO)_2]^-$, *m/z* = 232, respectively) show broad contributions peaking close to 3.8 and 4.3 eV, respectively. These contributions are attributed to one or more core-excited resonances corresponding to one of the first HOMO/LUMO transitions in the anion. The ion yield for $[CpFeMn(CO)_2]^-$ is shifted to a slightly higher energy than that of ($[CpFeMn(CO)_3]^-$; we attribute this to the increased energetic threshold for $[CpFeMn(CO)_2]^-$ formation and consequent increased efficiency at the higher energy side of the resonance. Finally, the fragment n = 5 ($[CpFeMn(CO)]^-$, *m/z* = 204)

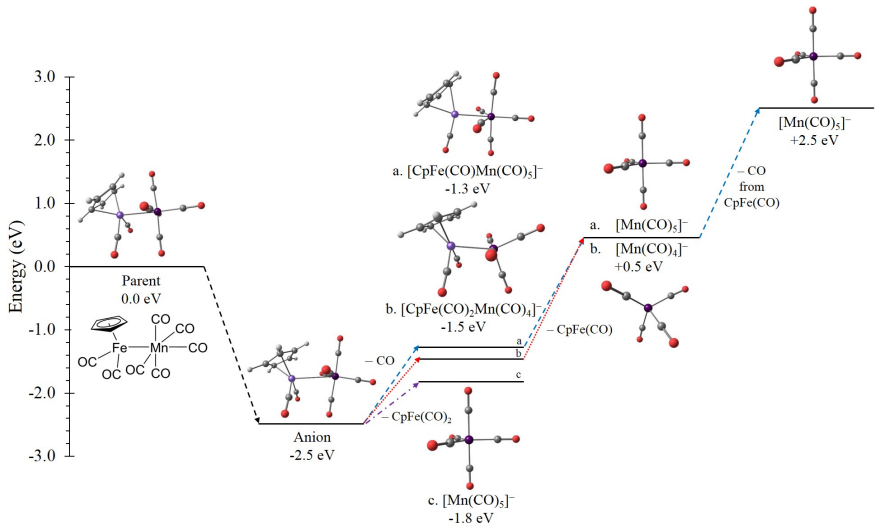

Figure 4.10. Schematic of selected calculated thresholds for DEA to (η^5-Cp)Fe(CO)$_2$Mn(CO)$_5$. The [Mn(CO)$_5$]$^-$ fragment may be produced at a threshold of -1.8 eV by direct dissociation of the Fe−Mn bond, as shown in path (c). Additionally, it may be produced by fragmentation of the [CpFe(CO)Mn(CO)$_5$]$^-$ fragment at a threshold of 0.5 eV, as shown in path (a). If the neutral CpFe(CO) fragment loses another CO ligand, this will produce [Mn(CO)$_5$]$^-$ at a threshold of 2.5 eV, also shown in path (a). Another isomer of [CpFeMn(CO)$_6$]$^-$, [CpFe(CO)$_2$Mn(CO)$_4$]$^-$, may dissociate to form [Mn(CO)$_4$]$^-$ at a threshold of 0.5 eV; this is shown in path (b).

appears as a broader, lower intensity contribution with a maximum at about 8 eV; this is attributed to a higher-lying core-excited resonance.

It is interesting to examine the dissociation dynamics of (η^5-Cp)Fe(CO)$_2$Mn(CO)$_5$ upon electron capture. One of the two major fragmentation products is [Mn(CO)$_5$]$^-$; the converse fragment, [CpFe(CO)$_2$]$^-$, is not observed. This fits with general chemical intuition regarding this molecule − the cyclopentadienyl ligand on the iron center is strongly electron-donating, while the carbonyl ligands (5 of which are on the manganese center) are π-acids. This produces an electron-rich iron moiety, which is unlikely to attach an electron, and an electron-poor manganese moiety, which appears to be the perfect target for a captured electron. However, quantum chemical calculations show that the electron affinity of CpFe(CO)$_2$ is 1.64 eV, and the threshold for formation of [CpFe(CO)$_2$]$^-$ under experimental conditions is exothermic by 0.42 eV. As this pathway is thermochemically accessible at low incident electron energies, we would expect to see some, albeit small, branching ratio for this reaction channel. The absence of this channel suggests that these reactions are governed largely by the dissociation dynamics during the separation of the metal-centered fragments.

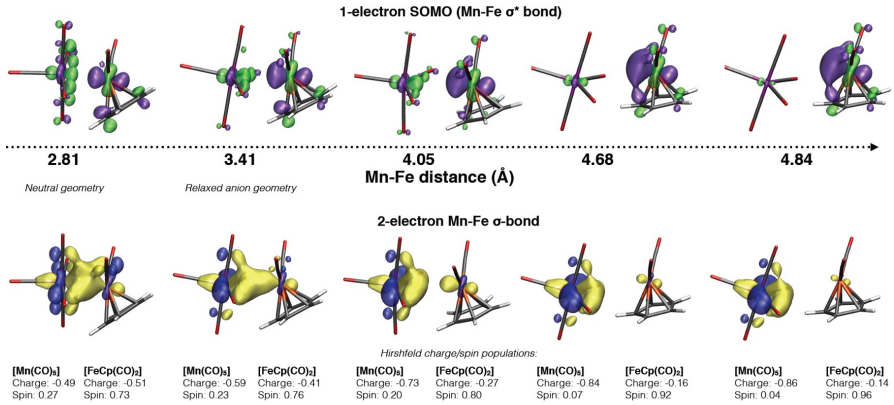

Figure 4.11. Orbital isosurface scan of the elongation of the Fe−Mn bond upon electron attachment. Top: changing geometry of the SOMO, which is a σ-antibonding orbital. The SOMO changes from an Fe-centered antibonding orbital to a localized Fe d-orbital. Bottom: changing geometry of the HOMO − 2, which is a 2-electron σ-bonding orbital. The HOMO − 2 changes from a slightly Mn-centered bonding orbital to a localized Mn d-orbital. An unpaired electron is retained by the Fe-centered moiety, giving it a neutral charge and +1 spin, while the 2-electron orbital is retained by the Mn-centered fragment, giving it a -1 charge and no excess spin, as seen in the evolution of the Hirshfeld population and spin analysis shown below the orbitals.*

In order to understand these dissociation dynamics, an orbital analysis of the dissociating molecular anion was performed, shown in fig. 4.11. A relaxed isosurface scan was performed on the anion, varying the Fe−Mn distance from 2.81 Å (the optimized bond length of the neutral molecule, representing a vertical transition from the ground state of the neutral molecule to the anionic state) to 4.84 Å (representing fully separated fragments) and geometrically optimizing the anion/fragments at several points along this coordinate. Of particular interest are the HOMO − 2, which is a *d*-based Fe-Mn σ-bonding orbital, and the SOMO, which is the singly-occupied Fe-Mn σ*-antibonding counterpart. This gives the Fe−Mn bond in the molecular anion a formal bond order of 0.5; quantum chemical calculations give a Mayer bond order of 0.4 between Fe and Mn (compared to 0.9 - 1.2 for the Mn−C bonds).

The elongation of the Fe−Mn bond during dissociation, as well as the evolution of the σ*-antibonding orbital (top) and the σ-bonding orbital (bottom), are shown in fig. 4.11. Additionally, the Hirshfeld charge and spin population analysis are shown for the two metal centers at each point along the scan coordinate. As can be seen in this figure, the antibonding SOMO changes from an Fe-centered antibonding orbital in the vertically attached parent anion to a localized Fe *d*-orbital in the neutral CpFe(CO)$_2$ fragment. The 2-electron bonding HOMO − 2, conversely, evolves from a slightly Mn-centered σ-bonding orbital to a localized Mn *d*-orbital in the [Mn(CO)$_5$]$^-$ fragment.

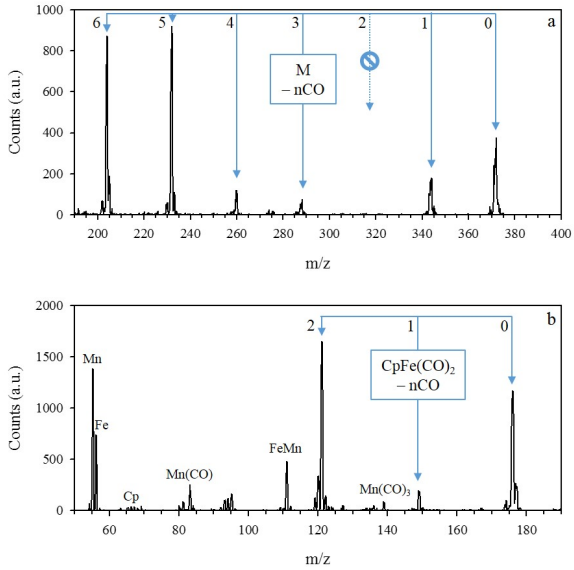

Figure 4.12. Spectra of dissociative ionization to (η^5-Cp)Fe(CO)$_2$Mn(CO)$_5$ recorded at 70 eV. (a) Spectrum from m/z = 190 - 400. This shows the regression $[M - nCO]^+$ where n = 0 - 6. Interestingly, the fragment corresponding to m = 2 is not observed, see text for more discussion. (b) Spectrum from m/z = 50 - 190. This shows the regression $[CpFe(CO)_{2-n}]^+$, where n = 0 - 2. The bare metal center and both metal cations are also observed.

The Hirshfeld population analysis confirms this picture: the charge is retained by the Mn-centered fragment, with Mn having a (-1) oxidation state due to its retention of the 2-electron bonding orbital, while the spin is retained by the Fe-centered fragment due to its retention of the singly-occupied antibonding orbital. This full picture of the dynamics of the Fe−Mn bond dissociation thus explains the retention of charge by the manganese-centered moiety, rather than by the iron.

Dissociative ionization

Figure 4.12 shows the dissociative ionization mass spectra of (η^5-Cp)Fe(CO)$_2$Mn(CO)$_5$ at 70 eV. As can be seen here, DI of (η^5-Cp)Fe(CO)$_2$Mn(CO)$_5$ produces two major regressions: sequential carbonyl loss ($[M - nCO]^+$, n = 0 - 6) and Fe-Mn bond rupture accompanied by sequential carbonyl loss ($[CpFe(CO)_{2-n}]^+$, n = 0 - 2). The bare metal center ($[FeMn]^+$) is also observed, as are the bare metal cations. The $[FeMn]^+$ isotope distribution overlaps with that of $[Mn(CO)_2]^+$; however, upon examination of the isotope distribution in this region we assign the peak as $[FeMn]^+$; $[Mn(CO)_2]^+$ does

not contribute signifcantly to this peak.

The sequential carbonyl loss regression is shown in fig. 4.12a, which comprises the DI mass spectrum in the *m/z* range from 190 to 400. The parent cation in observed, as is dissociation of up to six carbonyls. Unlike in the DEA spectra, DI favors more complete dissociation; the most abundant fragments in this regression are $[M - 5CO]^+$ and $[M - 6CO]^+$ ($[CpFeMn(CO)_2]^+$ and $[CpFeMn(CO)]^+$, respectively). This is generally as expected in DI; however, the regression does follow an interesting pattern: the parent cation and $[M - 1CO]^+$ ($[CpFeMn(CO)_7]^+$ and $[CpFeMn(CO)_6]^+$, respectively) are the next most abundant fragments in this regression. The triple and quadruple carbonyl loss fragments $[CpFeMn(CO)_4]^+$ and $[CpFeMn(CO)_3]^+$, respectively, are the least abundant of the observed carbonyl loss fragments in this regression, and the double carbonyl loss fragment ($[CpFeMn(CO)_5]^+$) is not observed. We consider this, again, to likely be associated with the kinetics of dissociative ionization of (η^5-Cp)Fe(CO)$_2$Mn(CO)$_5$. The detection window of the instrument used in this experiment is approximately 50 μs; the products of any reactions that take longer than this will not be observed. Long-lived metastable intermediates may thus be detected within this window, while short-lived intermediates will not.

Energetic thresholds for the formation of $[CpFeMn(CO)_7]^+$, $[CpFeMn(CO)_6]^+$, and $[CpFeMn(CO)_5]^+$ were calculated at the DLPNO-CCSD(T) level of theory using the aug-cc-pVTZ basis set and were found to be 6.4, 7.4, and 9.4 eV, respectively. This suggests that each of them should be observed in the 70 eV electron-impact spectrum. However, the ground state of $[CpFeMn(CO)_5]^+$ was found to have three bridging carbonyls, similarly to that of the neutral CpFeMn(CO)$_5$.[128] The ground state of $[CpFeMn(CO)_6]^+$ was calculated to only have a single bridging carbonyl. We thus expect that carbonyl loss is fast compared to rearrangement of the carbonyls into this triply-bridged state − i.e. carbonyl loss from the higher-energy intermediate $[CpFeMn(CO)_5]^+$ fragment to produce $[CpFeMn(CO)_4]^+$, etc, occurs much faster than rearrangement into the triply-bridged structure and consequent stabilization with respect to further carbonyl loss. This reduction in the lifetime of the higher-energy $[CpFeMn(CO)_5]^+$ intermediate thus renders it undetectable by our mass spectrometer. Conversely, $[CpFeMn(CO)_7]^+$ and $[CpFeMn(CO)_6]^+$ are metastable, longer-lived intermediates and are therefore detectable. The most intense fragments of this regression, $[CpFeMn(CO)_2]^+$ and $[CpFeMn(CO)]^+$, have likely expelled much of their initial internal energy by extensive carbonyl loss and have consequently long lifetimes. Similar behavior is observed in the other major regression, shown in fig. 4.12b. Significant intensities are observed for $[CpFe(CO)_2]^+$ and $[CpFe]^+$, while $[CpFe(CO)]^+$ is observed at low intensity. We attribute this to instability in the $[CpFe(CO)]^+$ intermediate, causing it to fragment too quickly to be observed with appreciable intensity.

Summary of gas phase dissociation and comparison with surface

The relative intensities of DEA fragments produced in the energy range of 0 - 12 eV and DI fragments produced at 70 eV are shown in table 4.6. The relative DEA intensities were calculated by integrating the pressure-normalized intensities of the

Table 4.6. Relative intensities of fragments produced by electron-induced dissociation of (η^5-Cp)Fe(CO)$_2$Mn(CO)$_5$ via DEA and DI, and the average carbonyl ligand loss per dissociation incident for DEA and DI. Molecular formulae are shown stoichiometrically. Calculations of the upper and lower boundaries of CO loss per dissociation incident are discussed in the text. As can be seen here, DI produces significantly more fragmentation than DEA. Each DI-induced dissociation incident at 70 eV dissociates between 3 and 6 CO ligands, while DEA-induced dissociation incidents dissociate between 0.6 and 2 CO ligands.

Mass	Fragment	DEA	DI
372	$[CpFeMn(CO)_7]^{+/-}$		190
344	$[CpFeMn(CO)_6]^{+/-}$	100	100
316	$[CpFeMn(CO)_5]^{+/-}$	2	
288	$[CpFeMn(CO)_4]^{+/-}$	0.4	31
260	$[CpFeMn(CO)_3]^{+/-}$	5	53
232	$[CpFeMn(CO)_2]^{+/-}$	2	387
204	$[CpFeMn(CO)]^{+/-}$	0.2	380
195	$[Mn(CO)_5]^{+/-}$	135	5
177	$[CpFe(CO)_2]^{+/-}$		458
167	$[Mn(CO)_4]^{+/-}$	0.2	7
149	$[CpFe(CO)]^{+/-}$		20
139	$[Mn(CO)_3]^{+/-}$		17
121	$[CpFe]^{+/-}$		491
111	$[FeMn]^{+/-}$		118
83	$[Mn(CO)]^{+/-}$		45
66	$Cp^{+/-}$		15
56	$Fe^{+/-}$		114
55	$Mn^{+/-}$		196
44	$[CO_2]^{+/-}$		14
28	$[CO]^{+/-}$		185
16	$O^{+/-}$		6
Avg.	CO loss (lower bound)	0.6	3
Avg.	CO loss (upper bound)	2	6

respective fragments over 0 - 12 eV and normalizing these to the single carbonyl loss fragment. For DI, relative intensities were calculated by integrating the isotope distribution for each fragment and again normalizing to the single carbonyl loss fragment. The average number of carbonyls lost per dissociation incident was calculated by multiplying the relative intensity of each fragment by the number of carbonyls lost in order to produce that fragment and then dividing this by the total intensity of all fragments. The lower limit of carbonyl loss was calculated by assuming no carbonyl loss from neutral counterparts, while the upper loss was calculated by assuming full dissociation of carbonyl ligands from neutral counterparts.

As can be seen in this table, fragmentation is much more extensive via DI than

via DEA. The two most intense fragments produced via DEA are $[Mn(CO)_5]^-$ and $[CpFeMn(CO)_6]^-$; together, these two fragments comprise 96% of the total anionic yield. Both of these fragments are largely produced by single bond rupture, especially at low energies. Based on previously discussed calculations, we therefore expect the number of carbonyl ligands lost per DEA-induced dissociation incident to be between 0.6 and 1. Conversely, in DI, much more extensive fragmentation is dominant, and we expect between 3 and 6 carbonyl ligands to dissociate with each DI-induced dissociation incident. If we assume the branching ratios for DEA and DI of surface-adsorbed (η^5-Cp)Fe(CO)$_2$Mn(CO)$_5$ are similar to those in the gas phase, we may then expect significantly less carbonaceous deposits from (η^5-Cp)Fe(CO)$_2$Mn(CO)$_5$ if deposition were to proceed via DI rather than via DEA.

As a part of an ongoing collaboration, colleagues in the Fairbrother group at Johns Hopkins University adsorbed (η^5-Cp)Fe(CO)$_2$Mn(CO)$_5$ in 0.5 - 3 nm-thick films onto a polycrystalline gold surface cooled to 105 K and irradiated these films with incremental doses of electrons from a 500 eV flood gun. X-ray photoelectron spectroscopy (XPS) was used to monitor the composition of the surface, while MS was used to monitor species desorbing from the surface. The data reported here is part of a larger study of the electron-induced deposition of (η^5-Cp)Fe(CO)$_2$Mn(CO)$_5$ that will be published separately. Figure 4.13 shows XPS spectra in the C (1s) and O (1s) regions before and after irradiation with 9.36×10^{15} e$^-$/cm^2. In the C (1s) region, we can see two peaks: a lower-energy peak at approximately 285.2 eV attributed to the five cyclopentadienyl carbon atoms, and a higher-energy peak at approximately 287.6 eV attributed to the seven carbonyl carbon atoms. An additional π to π^* shake-up peak at higher binding energy is also associated with the carbonyl carbon atoms; however, it cannot be differentiated from the background due to its low intensity. Electron irradiation produces little change in the cyclopentadienyl carbon peak; however, the carbonyl carbon peak decreases significantly. In the O (1s) region, we can also see two peaks: a lower-energy peak at approximately 534.5 eV attributed to the seven carbonyl oxygen atoms, and a higher-energy peak at approximately 541.2 eV attributed to the π to π^* shake-up peak also associated with the carbonyl oxygen atoms. Electron irradiation produces a significantly less intense and broader O (1s) peak that has shifted to a slightly lower binding energy, while the π to π^* shake-up peak disappears.

The changes in each of these regions are consistent with significant dissociation and desorption of carbonyl ligands, with no desorption of the cyclopentadienyl ligand. The total oxygen-to-carbon ratio in the deposit changes from 0.6:1 in the adsorbed molecule, which is slightly above the stoichiometry of the molecule (7:12), to approximately 0.3:1 (2:7) after electron irradiation. The O (1s) peak area decreases to about 30% of its initial value. These changes suggest that an average of about 5 carbonyl ligands per molecule desorb from the surface during electron irradiation. These results are within the range of that which is expected for DI-initiated deposition. However, it must be noted that the effective damage yield of a molecule on a surface exposed to a primary electron beam is a convolution of the cross-sections for the various electron-initiated processes with the secondary electron emission spectrum of the substrate. The potential effect of surface adsorption on the cross-sections of DEA and DI to this molecule, as well as the potential efficiency of ND to this molecule, cannot be commented on here but should nevertheless

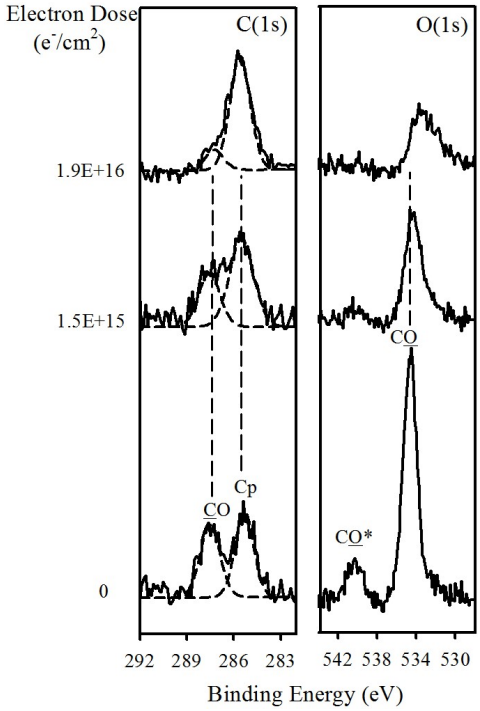

Figure 4.13. XPS analysis of the C(1s) and O(1s) regions for films of (η^5-Cp)Fe(CO)$_2$Mn(CO)$_5$ molecules on a polycrystalline gold surface before and after electron irradiation with a dose of 1.9 $\times$ 10^{16} e$^-$/cm^2. In the C(1s) region, the carbonyl carbon peak swiftly decreases in intensity, while the cyclopentadienyl carbon peak remains approximately the same. In the O(1s) region, the π to π shakeup peak disappears quickly, while the oxygen peak decreases in intensity, broadens, and shifts to lower binding energy.*

not be overlooked. Based on the evidence here, we conclude that DI plays an important role in the initial deposition step of an FeMn alloy from (η^5-Cp)Fe(CO)$_2$Mn(CO)$_5$. Additionally, as the cyclopentadienyl ligand and two carbonyl ligands remain on the surface after electron irradiation, post-deposition processing will be necessary in order to produce pure FeMn alloy deposits from this molecule.

5 Summary and Outlook

Low-energy electron interactions with organometallic molecules are important in focused electron beam induced deposition, and gas phase studies may be able to predict the viability of specific organometallic molecules for use in focused electron beam induced deposition. Two low-energy electron-induced dissociation channels relevant to FEBID - dissociative electron attachment and dissociative ionization - have been studied here. Dissociative electron attachment is largely associated with single bond ruptures close to 0 eV incident electron energy, while dissociative ionization generally produces multiple bond ruptures at higher energies. Each of these reaction pathways may produce reactive products that can initiate deposition in FEBID. Molecules with initial deposition steps governed by DEA may produce deposits with higher levels of ligand contamination due to the low number of bond ruptures associated with DEA. However, precursors may be designed to include intramolecular reactive pathways that increase molecular decomposition at low incident electron energies. Precursor optimization is an important area of continued study in the aim of improving FEBID as a nanofabrication technique.

In the area of precursor design, we have examined the viability of carbonyl ligands, halides, and polyhaptic ligands for FEBID precursors by studying two organometallic molecules: η^3-allyl ruthenium tricarbonyl bromide and η^5-cyclopentadienyl iron dicarbonyl manganese pentacarbonyl. Carbonyl ligands are very favorable dissociators in both DEA and DI of organometallic FEBID precursors when compared to these other two ligands, and should continue to be used in precursor design. Halides, despite their persistence in the gas phase and during surface deposition, may be beneficial for FEBID precursors. They may help stabilize anionic fragments produced by DEA to an organometallic molecule, or increase the electron affinity of anionic fragments such that specific dissociation channels are thermodynamically accessible. Previously, the energy produced by HF bond formation has been found to induce significant rearrangement in DEA to several fluorinated benzene analogues.[11] Similar reactions involving halides might be designed into organometallic FEBID precursors in order to increase the DEA-induced decomposition of organometallic molecules. Persistent halides may then be removed by post-deposition electron irradiation.[38,39]

Polyhaptic ligands, i.e. η^3-allyl and η^5-cyclopentadienyl, were found to be poor ligands for use in FEBID precursors, as they are persistent in the gas phase and on surfaces and are not removable by post-deposition electron irradiation. They may, however, be advantageous if other processing techniques prove capable of removing them from FEBID nanostructures. Preliminary studies on the deposition of η^3-allyl

ruthenium tricarbonyl bromide under *in situ* FEBID conditions produced a higher purity deposit than predicted by either gas phase studies or surface studies. The 1:1 carbon-to-ruthenium ratio achieved by 30 minutes of deposition at 74 °C necessitates some decomposition of the allyl ligand and either evaporation from the surface or diffusion outside the deposition area. It is possible that thermal effects account for this - surface studies are performed at very low temperatures in order to prevent desorption of target species, and the increased substrate temperature in addition to the energies transferred to the surface by both the deposition electron beam and the electron beam used in EDX may produce significant heating. Further studies on this compound may be able to better elucidate this discrepancy.

We have also shown that gas phase experiments can be used to predict behavior of adsorbed organometallic molecules upon electron beam impact. Although it is difficult to comment with certainty on the specific dissociation channels that lead to the deposition of either η^3-allyl ruthenium tricarbonyl bromide or η^5-cyclopentadienyl iron dicarbonyl manganese pentacarbonyl due to lack of data on the efficiency of the neutral dissociation channels or the effects of surface adsorption on the gas phase electron-induced dissociation channels, gas phase experiments can readily determine the utility of specific ligands, as described above. Gas phase experiments demonstrated the persistence of both the polyhaptic ligands and the bromide ligand upon electron-initiated decomposition, and surface studies performed on these molecules showed similar results. Additionally, relative and absolute cross sections for electron-induced processes determined by gas phase experiments may be used in future computational modeling of the FEBID process.

Quantum chemical computational techniques may also be used to better understand the dissociation channels observed in gas phase DEA and DI experiments on organometallic molecules. The energetic thresholds for these reaction pathways may be calculated by coupled cluster methods, and studies of molecular orbital isosurfaces may also give great insight into electron attachment and dissociation processes. Our current project uses experimental results to inform calculations of observed fragments; however, engines to predict DI spectra are already in use[129] and predictions of DEA-induced fragmentation may well be on their way. The use of computational chemistry to aid in interpretation of experimentally observed data has become increasingly useful as computational costs have decreased.

Ultimately, the two major organometallic precursors studied in this thesis - η^3-allyl ruthenium tricarbonyl bromide and η^5-cyclopentadienyl iron dicarbonyl manganese pentacarbonyl - were both determined to be poor precursors for deposition of either ruthenium or of an iron manganese alloy via the FEBID technique. This is largely due to the inclusion of polyhaptic ligands, which have been concluded to be poor dissociators upon electron impact, in both molecules. Despite this, we have demonstrated that the techniques used to study these two precursors may be used to predict the viability of more potential FEBID precursors, and that the studied ligands (with the exception of the polyhaptic ligands) are useful in future FEBID precursor design.

References

[1] Rudolf Reichelt. Scanning Electron Microscopy. In *Science of Microscopy*, pages 133–272. Springer New York, New York, NY, 2007.

[2] Angus I. Kirkland, Shery L. Y. Chang, and John L. Hutchison. Atomic Resolution Transmission Electron Microscopy. In *Science of Microscopy*, pages 3–64. Springer New York, New York, NY, 2007.

[3] Gianluigi Botton. Analytical Electron Microscopy. In *Science of Microscopy*, pages 273–405. Springer New York, New York, NY, 2007.

[4] D. Klar, M. W. Ruf, and H. Hotop. Dissociative electron attachment to CCl_4 molecules at low electron energies with meV resolution. *International Journal of Mass Spectrometry*, 205(1-3):93–110, 2001.

[5] Esther Böhler, Jonas Warneke, and Petra Swiderek. Control of chemical reactions and synthesis by low-energy electrons. *Chemical Society Reviews*, 42(24):9219, 2013.

[6] Richard Balog, Judith Langer, Sascha Gohlke, Michal Stano, Hassan Abdoul-Carime, and Eugen Illenberger. Low energy electron driven reactions in free and bound molecules: From unimolecular processes in the gas phase to complex reactions in a condensed environment, 2004.

[7] Lars Lehmann and Eugen Illenberger. Nucleophilic displacement (S_N2) reactions in binary van der waals clusters induced by resonant electron capture. *International Journal of Mass Spectrometry*, 185:463–475, 1999.

[8] Xiaoning Pan, Andrew D. Bass, Jean Paul Jay-Gerin, and Léon Sanche. A mechanism for the production of hydrogen peroxide and the hydroperoxyl radical on icy satellites by low-energy electrons. *Icarus*, 172(2):521–525, 2004.

[9] S. Lacombe, F. Cemic, K. Jacobi, M. Hedhili, Y. Le Coat, R. Azria, and M. Tronc. Electron-Induced Synthesis of Ozone in a Dioxygen Matrix. *Physical Review Letters*, 79(6):1146–1149, 1997.

[10] Benedikt Ómarsson and Oddur Ingólfsson. Stabilization, fragmentation and rearrangement reactions in low-energy electron interaction with tetrafluoro-para-benzoquinone: a combined theoretical and experimental study. *Physical Chemistry Chemical Physics*, 15(39):16758, 2013.

[11] Benedikt Ómarsson, Elías H. Bjarnason, Sean A. Haughey, Thomas A. Field, Alexander Abramov, Peter Klüpfel, Hannes Jónsson, and Oddur Ingólfsson. Molecular rearrangement reactions in the gas phase triggered by electron attachment. *Physical Chemistry Chemical Physics*, 15(13):4754, 2013.

[12] T. Hamann, A. Edtbauer, F. Ferreira da Silva, Stephan Denifl, Paul Scheier, and P. Swiderek. Dissociative electron attachment to gas-phase formamide. *Physical Chemistry Chemical Physics*, 13(26):12305, 2011.

[13] Thorben Hamann, Esther Böhler, and Petra Swiderek. Low-energy-electron-induced hydroamination of an alkene. *Angewandte Chemie - International Edition*, 48(25):4643–4645, 2009.

[14] C. Q. Jiao, C. A. DeJoseph, and A. Garscadden. Ion chemistries in hexamethyldisiloxane. *Journal of Vacuum Science & Technology A: Vacuum, Surfaces, and Films*, 23(5):1295–1304, 2005.

[15] Michael C. Boyer, Nathalie Rivas, Audrey A. Tran, Clarissa A. Verish, and Christopher R. Arumainayagam. The role of low-energy ($\leq$ 20 eV) electrons in astrochemistry. *Surface Science*, 652:26–32, 2016.

[16] Loucas G Christophorou and James K Olthoff. Electron interactions with plasma processing gases: Present status and future needs. In *Applied Surface Science*, volume 192, pages 309–326, 2002.

[17] I. Bald, E. Illenberger, and J. Kopyra. The Molecular Mechanisms of DNA Single-Strand Breaks Induced by Low-Energy Electrons (<3eV). In *Reference Module in Chemistry, Molecular Sciences and Chemical Engineering*, number December 2014, pages –. Elsevier, 2014.

[18] H. D. Flosadóttir, B. Ómarsson, I. Bald, and O. Ingólfsson. Metastable decay of DNA components and their compositions - A perspective on the role of reactive electron scattering in radiation damage. *Eur. Phys. J. D*, 66(13), 2012.

[19] Ivo Utke, Patrik Hoffmann, and John Melngailis. Gas-assisted focused electron beam and ion beam processing and fabrication. *Journal of Vacuum Science & Technology B: Microelectronics and Nanometer Structures*, 26(4):1197, 2008.

[20] W. F. Van Dorp and C. W. Hagen. A critical literature review of focused electron beam induced deposition. *Journal of Applied Physics*, 104(8):081301, 2008.

[21] N. Silvis-Cividjian, C.W. Hagen, L.H.A. Leunissen, and P. Kruit. The role of secondary electrons in electron-beam-induced-deposition spatial resolution. *Microelectronic Engineering*, 61-62:693–699, 2002.

[22] R. Lariviere Stewart. Insulating films formed under electron and ion bombardment. *Physical Review*, 45(7):488–490, 1934.

[23] Robert W. Christy. Formation of thin polymer films by electron bombardment. *Journal of Applied Physics*, 31(9):1680–1683, 1960.

[24] Allen G. Baker and William C. Morris. Deposition of Metallic Films by Electron Impact Decomposition of Organometallic Vapors. *Review of Scientific Instruments*, 32(4):458–458, 1961.

[25] J M De Teresa, A Fernández-Pacheco, R Córdoba, L Serrano-Ramón, S Sangiao, and M R Ibarra. Review of magnetic nanostructures grown by focused electron beam induced deposition (FEBID). *Journal of Physics D: Applied Physics*, 49(24):243003, 2016.

[26] S. J. Randolph, J. D. Fowlkes, and P. D. Rack. Focused, Nanoscale Electron-Beam-Induced Deposition and Etching. *Critical Reviews in Solid State and Materials Sciences*, 31(3):55–89, 2006.

[27] Willem F. Van Dorp, Bob Van Someren, Cornells W. Hagen, Pieter Kruit, and Peter A. Crozier. Approaching the resolution limit of nanometer-scale electron beam-induced deposition. *Nano Letters*, 5(7):1303–1307, 2005.

[28] Rachel M Thorman, T. P. Ragesh Kumar, D. Howard Fairbrother, and Oddur Ingólfsson. The role of low-energy electrons in focused electron beam induced deposition: Four case studies of representative precursors. *Beilstein Journal of Nanotechnology*, 6(1):1904–1926, 2015.

[29] Shinji Matsui and Katsumi Mori. New selective deposition technology by electron-beam induced surface reaction. *Journal of Vacuum Science & Technology B: Microelectronics and Nanometer Structures*, 4(1):299, 1986.

[30] H W P Koops, C Schossler, A. Kaya, and M. Weber. Conductive dots, wires, and supertips for field electron emitters produced by electron-beam induced deposition on samples having increased temperature. *Journal of Vacuum Science & Technology B*, 14(6):4105–4109, 1996.

[31] S. Wang, Y.-M. Sun, Q. Wang, and J. M. White. Electron-beam induced initial growth of platinum films using $Pt(PF_3)_4$. *Journal of Vacuum Science & Technology B: Microelectronics and Nanometer Structures*, 22(4):1803, 2004.

[32] Masaki Takeguchi, Masayuki Shimojo, and Kazuo Furuya. Fabrication of alpha-iron and iron carbide nanostructures by electron-beam induced chemical vapor deposition and postdeposition heat treatment. *Japanese Journal of Applied Physics, Part 1: Regular Papers and Short Notes and Review Papers*, 44(7 B):5631–5634, 2005.

[33] Masaki Takeguchi, Masayuki Shimojo, and Kazuo Furuya. Fabrication of magnetic nanostructures using electron beam induced chemical vapour deposition. *Nanotechnology*, 16(8):1321–1325, 2005.

[34] M. Shimojo, M. Takeguchi, M. Tanaka, K. Mitsuishi, and K. Furuya. Electron beam-induced deposition using iron carbonyl and the effects of heat treatment on nanostructure. *Applied Physics A: Materials Science and Processing*, 79(8):1869–1872, 2004.

[35] M Komuro, H Hiroshima, and A Takechi. Miniature tunnel junction by electron-beam-induced deposition. *Nanotechnology*, 9(2):104–107, 1998.

[36] M. A. Bruk, E. N. Zhikharev, E. I. Grigor'ev, A. V. Spirin, V. A. Kal'nov, and I. E. Kardash. Focused electron beam-induced deposition of iron- and carbon-containing nanostructures from triiron dodecacarbonyl vapor. *High Energy Chemistry*, 39(2):65–68, 2005.

[37] P. C. Hoyle. Electron beam induced deposition from $W(CO)_6$ at 2 to 20 keV and its applications. *Journal of Vacuum Science & Technology B: Microelectronics and Nanometer Structures*, 14(2):662, 1996.

[38] Julie A. Spencer, Joseph A. Brannaka, Michael Barclay, Lisa McElwee-White, and D. Howard Fairbrother. Electron-Induced Surface Reactions of

η^3-Allyl Ruthenium Tricarbonyl Bromide [(η^3-C_3H_5)$Ru(CO)_3Br$]: Contrasting the Behavior of Different Ligands. *The Journal of Physical Chemistry C*, 119(27):15349–15359, 2015.

[39] Julie A. Spencer, Yung Chien Wu, Lisa McElwee-White, and D. Howard Fairbrother. Electron Induced Surface Reactions of cis-$Pt(CO)_2Cl_2$: A Route to Focused Electron Beam Induced Deposition of Pure Pt Nanostructures. *Journal of the American Chemical Society*, 138(29):9172–9182, 2016.

[40] Rachel M. Thorman, Joseph A. Brannaka, Lisa McElwee-White, and Oddur Ingólfsson. Low energy electron-induced decomposition of (η^3-C_3H_5)$Ru(CO)_3Br$, a potential focused electron beam induced deposition precursor with a heteroleptic ligand set. *Phys. Chem. Chem. Phys.*, 19:13264–13271, 2017.

[41] Rachel M. Thorman, Ragnar Bjornsson, and Oddur Ingólfsson. Computational study of dissociative electron attachment to π-allyl ruthenium (II) tricarbonyl bromide. *The European Physical Journal D*, 70(8):164, 2016.

[42] F. Porrati, B. Kämpken, A. Terfort, and M. Huth. Fabrication and electrical transport properties of binary Co-Si nanostructures prepared by focused electron beam-induced deposition. *Journal of Applied Physics*, 113(5):053707, 2013.

[43] Mostafa Moonir Shawrav, Domagoj Belic, Marco Gavagnin, Stefan Wachter, Markus Schinnerl, Heinz D. Wanzenboeck, and Emmerich Bertagnolli. Electron beam-induced CVD of nanoalloys for nanoelectronics. *Chemical Vapor Deposition*, 20(7-9):251–257, 2014.

[44] M J Perez-Roldan, F Tatti, P Vavassori, A Berger, and A Chuvilin. Segregation of materials in double precursor electron-beam-induced-deposition: a route to functional magnetic nanostructures. *Nanotechnology*, 26(37):375302, 2015.

[45] F Porrati, M Pohlit, J Müller, S Barth, F Biegger, C Gspan, H Plank, and M Huth. Direct writing of CoFe alloy nanostructures by focused electron beam induced deposition from a heteronuclear precursor. *Nanotechnology*, 26(47):475701, 2015.

[46] R. K. T P, Sven Barth, Ragnar Bjornsson, and Oddur Ingólfsson. Structure and energetics in dissociative electron attachment to $HFeCo_3(CO)_{12}$. *European Physical Journal D*, 70(8):163, 2016.

[47] Ragesh Kumar T P, Ragnar Bjornsson, Sven Barth, and Oddur Ingólfsson. Formation and decay of negative ion states up to 11 eV above the ionization energy of the nanofabrication precursor $HFeCo_3(CO)_{12}$. *Chem. Sci.*, 8(9):5949–5952, 2017.

[48] Ragesh Kumar T P, Ilyas Unlu, Sven Barth, Oddur Ingólfsson, and D. Howard Fairbrother. Electron Induced Surface Reactions of $HFeCo_3(CO)_{12}$, a Bimetallic Precursor for Focused Electron Beam Induced Deposition (FEBID). *Submitted*, 2017.

[49] Ragesh Kumar T P, Paul Weirich, Lukas Hrachowina, Marc Hanefeld, Ragnar Bjornsson, Helgi Rafn Hrodmarsson, Sven Barth, D. Howard Fairbrother, Michael Huth, and Oddur Ingólfsson. Electron Interactions with the heteronuclear carbonyl precursor ($H_2FeRu_3(CO)_{13}$): from fundamental gas phase and

surface science studies to focused electron beam induced deposition. *submitted*, 2017.

[50] Rachel M. Thorman, Ilyas Unlu, Kelsea Johnson, Ragnar Bjornsson, Lisa McElwee-White, Howard Fairbrother, and Oddur Ingólfsson. Low energy electron-induced decomposition of (η^5-Cp)Fe(CO)$_2$Mn(CO)$_5$, a potential bimetallic precursor for focused electron beam induced deposition of alloy structures. *submitted*, 2017.

[51] J. Schaefer and J. Hoelzl. A contribution to the dependence of secondary electron emission from the work function and fermi energy. *Thin Solid Films*, 13(1):81–86, 1972.

[52] Jørgen Schou. Secondary-Electron Emission from Solids by Electron and Proton-Bombardment - DTU. *Scanning Microscopy*, page 1988, 1988.

[53] Kaoru Ohya, Akio Harada, Jun Kawata, and Kenji Nishimura. Monte Carlo simulation of yield and energy distribution of secondary electrons emitted from metal surfaces. *Japanese Journal of Applied Physics, Part 1: Regular Papers and Short Notes and Review Papers*, 35(12 A):6226–6232, 1996.

[54] A.P. Knights and P.G. Coleman. Secondary electron emission from Ag(100) stimulated by positron and electron impact. *Applied Surface Science*, 85(C):43–48, 1995.

[55] Roland Schmied, Jason D Fowlkes, Robert Winkler, Phillip D Rack, and Harald Plank. Fundamental edge broadening effects during focused electron beam induced nanosynthesis. *Beilstein Journal of Nanotechnology*, 6(1):462–471, 2015.

[56] Olivier May, Dušan Kubala, and Michael Allan. Dissociative electron attachment to Pt(PF$_3$)$_4$ - a precursor for focused electron beam induced processing (FEBIP). *Physical chemistry chemical physics : PCCP*, 14(9):2979–82, 2012.

[57] W. F. van Dorp, J. D. Wnuk, J. M. Gorham, D. H. Fairbrother, T. E. Madey, and C. W. Hagen. Electron induced dissociation of trimethyl (methylcyclopentadienyl) platinum (IV): Total cross section as a function of incident electron energy. *Journal of Applied Physics*, 106(7):074903, 2009.

[58] Sarah Engmann, Michal Stano, Stefan Matejčík, and Oddur Ingólfsson. Gas phase low energy electron induced decomposition of the focused electron beam induced deposition (FEBID) precursor trimethyl (methylcyclopentadienyl) platinum(IV) (MeCpPtMe$_3$). *Physical chemistry chemical physics : PCCP*, 14(42):14611–8, 2012.

[59] Joshua D. Wnuk, Justin M. Gorham, Samantha G. Rosenberg, Willem F. van Dorp, Theodore E. Madey, Cornelis W. Hagen, and D. Howard Fairbrother. Electron Induced Surface Reactions of the Organometallic Precursor Trimethyl(methylcyclopentadienyl)platinum(IV). *The Journal of Physical Chemistry C*, 113(6):2487–2496, 2009.

[60] Sarah Engmann, Michal Stano, Peter Papp, Michael J. Brunger, Štefan Matejčík, and Oddur Ingólfsson. Absolute cross sections for dissociative electron attach-

ment and dissociative ionization of cobalt tricarbonyl nitrosyl in the energy range from 0 eV to 140 eV. *Journal of Chemical Physics*, 138(4):044305, 2013.

[61] Samantha G. Rosenberg, Michael Barclay, and D. Howard Fairbrother. Electron Beam Induced Reactions of Adsorbed Cobalt Tricarbonyl Nitrosyl ($Co(CO)_3NO$) Molecules. *The Journal of Physical Chemistry C*, 117(31):16053–16064, 2013.

[62] K. Wnorowski, M. Stano, C. Matias, S. Denifl, W. Barszczewska, and Š. Matejčík. Low-energy electron interactions with tungsten hexacarbonyl - $W(CO)_6$. *Rapid Communications in Mass Spectrometry*, 26(17):2093–2098, 2012.

[63] Samantha G Rosenberg, Michael Barclay, and D Howard Fairbrother. Electron induced reactions of surface adsorbed tungsten hexacarbonyl ($W(CO)_6$). *Phys. Chem. Chem. Phys. Phys. Chem. Chem. Phys*, 15(15):4002–4015, 2013.

[64] L. G. Christophorou. *Electron-molecule interactions and their applications*. Academic Press, 1984.

[65] Matija Zlatar, Michael Allan, and Juraj Fedor. Excited States of $Pt(PF_3)_4$ and Their Role in Focused Electron Beam Nanofabrication. *The Journal of Physical Chemistry C*, 120(19):10667–10674, 2016.

[66] Edward U. Condon. Nuclear motions associated with electron transitions in diatomic molecules. *Physical Review*, 32(6):858–872, 1928.

[67] L G Christophorou. Negative ions of polyatomic molecules. *Environmental Health Perspectives*, 36:3–32, 1980.

[68] P. W. Harland and J. C. J. Thynne. Autodetachment lifetimes, attachment cross sections, and negative ions formed by sulfur hexafluoride and sulfur tetrafluoride. *The Journal of Physical Chemistry*, 75(23):3517–3523, 1971.

[69] Howard S. Taylor. Models, Interpretations, and Calculations Concerning Resonant Electron Scattering Processes in Atoms and Molecules. *Advances in Chemical Physics*, 18:91–147, 1970.

[70] Ilya I. Fabrikant, Samuel Eden, Nigel J. Mason, and Juraj Fedor. Recent Progress in Dissociative Electron Attachment. In *Advances In Atomic, Molecular, and Optical Physics*, volume 66, pages 545–657. 2017.

[71] George J. Schulz. Resonances in Electron Impact on Atoms. *Reviews of Modern Physics*, 45(3):378–422, 1973.

[72] George J. Schulz. Resonances in Electron Impact on Diatomic Molecules. *Reviews of Modern Physics*, 45(3):423–486, 1973.

[73] D T Birtwistle and A Herzenberg. Vibrational excitation of N2 by resonance scattering of electrons. *Journal of Physics B: Atomic and Molecular Physics*, 4(1):53–70, 1971.

[74] H. Hotop, M.-W. Ruf, M. Allan, and I.I. Fabrikant. Resonance and Threshold Phenomena in Low-Energy Electron Collisions with Molecules and Clusters. In *Physica Scripta*, volume 2004, pages 85–216. 2003.

[75] Erich Vogt and Gregory H. Wannier. Scattering of Ions by Polarization Forces. *Physical Review*, 95(5):1190–1198, 1954.

[76] R. L. Hettich, R. N. Compton, and R. H. Ritchie. Doubly charged negative ions of carbon-60. *Physical Review Letters*, 67(10):1242–1245, 1991.

[77] M. Lezius, P. Scheier, and T.D. Märk. Free electron attachment to C60 and C70. *Chemical Physics Letters*, 203(2-3):232–236, 1993.

[78] Sylwia Ptasińska, Olof Echt, Stephan Denifl, Michal Stano, Philipp Sulzer, Fabio Zappa, Aleksandar Stamatovic, Paul Scheier, and Tilmann D Märk. Electron attachment to higher fullerenes and to Sc3N@C80. *The journal of physical chemistry. A*, 110(27):8451–6, 2006.

[79] J M Pitarke, V M Silkin, E V Chulkov, and P M Echenique. Theory of surface plasmons and surface-plasmon polaritons. *Reports on Progress in Physics*, 70(1):1–87, 2007.

[80] Kees Landheer, Samantha G. Rosenberg, Laurent Bernau, Petra Swiderek, Ivo Utke, Cornelis W. Hagen, and D. Howard Fairbrother. Low-Energy Electron-Induced Decomposition and Reactions of Adsorbed Tetrakis(trifluorophosphine)platinum [$Pt(PF_3)_4$]. *The Journal of Physical Chemistry C*, 115(35):17452–17463, 2011.

[81] Elías H. Bjarnason, Benedikt Ómarsson, Sarah Engmann, Frímann H. Ómarsson, and Oddur Ingólfsson. Dissociative electron attachment to titatinum tetrachloride and titanium tetraisopropoxide. *The European Physical Journal D*, 68(5):121, 2014.

[82] A. Stamatovic and G. J. Schulz. Trochoidal Electron Monochromator. *Review of Scientific Instruments*, 39(11):1752–1753, 1968.

[83] A Stamatovic and G J Schulz. Characteristics of the Trochoidal Electron Monochromator. *Review of Scientific Instruments*, 41(3):423–427, 1970.

[84] Benedikt Ómarsson. *Promoting reaction channels in dissociative electron attachment through bond formation and rearrangement*. 2014.

[85] D. Klar, M. W. Ruf, and H. Hotop. Attachment of electrons to molecules at submillielectronvolt resolution. *Chemical Physics Letters*, 189(4-5):448–454, 1992.

[86] M. Braun, M. W. Ruf, H. Hotop, P. Cicman, P. Scheier, T. D. Märk, E. Illenberger, R. P. Tuckett, and C. A. Mayhew. High resolution studies of low-energy electron attachment to SF5Cl: Product anions and absolute cross sections. *International Journal of Mass Spectrometry*, 252(3):234–241, 2006.

[87] S. Matt, O. Echt, R. Wörgötter, V. Grill, Paul Scheier, C. Lifshitz, and A. Muñoz. Appearance and ionization energies of multiply-charged C70 parent ions produced by electron impact ionization. *Chemical Physics Letters*, 264(1-2):149–156, 1997.

[88] Peter M.W. Gill. Density Functional Theory (DFT), Hartree-Fock (HF), and the Self-consistent Field, 1994.

[89] Kieron Burke and Lucas O. Wagner. DFT in a nutshell. *International Journal of Quantum Chemistry*, 113(2):96–101, 2013.

[90] Viktor N Staroverov. Density-functional approximations for exchange and correlation The challenge of density-functional theory. pages 125–156, 2013.

[91] John P. Perdew, Adrienn Ruzsinszky, Lucian A. Constantin, Jianwei Sun, and Gábor I. Csonka. Some Fundamental Issues in Ground-State Density Functional Theory: A Guide for the Perplexed. *Journal of Chemical Theory and Computation*, 5(4):902–908, 2009.

[92] Axel D. Becke. Perspective: Fifty years of density-functional theory in chemical physics. *The Journal of Chemical Physics*, 140(18):18A301, 2014.

[93] Rodney J. Bartlett and Monika Musiał. Coupled-cluster theory in quantum chemistry. *Rev. Mod. Phys.*, 79:291–352, 2007.

[94] Miriam M Quintal, Amir Karton, Mark A Iron, A Daniel Boese, and Jan M L Martin. Benchmark study of DFT functionals for late-transition-metal reactions. *The journal of physical chemistry. A*, 110(2):709–16, 2006.

[95] Thomas Weymuth, Erik P A Couzijn, Peter Chen, and Markus Reiher. New Benchmark Set of Transition-Metal Coordination Reactions for the Assessment of Density Functionals. *Journal of chemical theory and computation*, 10(8):3092–103, 2014.

[96] Mark P Waller, Heiko Braun, Nils Hojdis, and Michael Bühl. Geometries of Second-Row Transition-Metal Complexes from Density-Functional Theory. *Journal of chemical theory and computation*, 3(6):2234–42, 2007.

[97] Michael Bühl and Hendrik Kabrede. Geometries of Transition-Metal Complexes from Density-Functional Theory. *Journal of Chemical Theory and Computation*, 2(5):1282–1290, 2006.

[98] Michael Bühl, Christoph Reimann, Dimitrios A Pantazis, Thomas Bredow, and Frank Neese. Geometries of Third-Row Transition-Metal Complexes from Density-Functional Theory. *Journal of Chemical Theory and Computation*, 4(9):1449–1459, 2008.

[99] Carlo Adamo and Vincenzo Barone. Toward reliable density functional methods without adjustable parameters: The PBE0 model. *The Journal of Chemical Physics*, 110(13):6158–6170, 1999.

[100] Carlos A. Jiménez-Hoyos, Benjamin G Janesko, and Gustavo E Scuseria. Evaluation of Range-Separated Hybrid and Other Density Functional Approaches on Test Sets Relevant for Transition Metal-Based Homogeneous Catalysts †. *The Journal of Physical Chemistry A*, 113(43):11742–11749, 2009.

[101] Lee M J Huntington, Andreas Hansen, Frank Neese, and Marcel Nooijen. Accurate thermochemistry from a parameterized coupled-cluster singles and doubles model and a local pair natural orbital based implementation for applications to larger systems. *The Journal of Chemical Physics*, 136(6):064101, 2012.

[102] Lee M J Huntington and Marcel Nooijen. pCCSD: Parameterized coupled-cluster theory with single and double excitations. *The Journal of Chemical Physics*, 133(18):184109, 2010.

[103] Frank Neese, Andreas Hansen, and Dimitrios G Liakos. Efficient and accurate approximations to the local coupled cluster singles doubles method using a truncated pair natural orbital basis. *The Journal of Chemical Physics*, 131(6):064103, 2009.

[104] Christoph Riplinger and Frank Neese. An efficient and near linear scaling pair natural orbital based local coupled cluster method. *The Journal of Chemical Physics*, 138(3):034106, 2013.

[105] Christoph Riplinger, Barbara Sandhoefer, Andreas Hansen, and Frank Neese. Natural triple excitations in local coupled cluster calculations with pair natural orbitals. *The Journal of Chemical Physics*, 139(13):134101, 2013.

[106] Christoph Riplinger, Peter Pinski, Ute Becker, Edward F Valeev, and Frank Neese. Sparse maps-A systematic infrastructure for reduced-scaling electronic structure methods. II. Linear scaling domain based pair natural orbital coupled cluster theory. *The Journal of Chemical Physics*, 144(2):024109, 2016.

[107] Masaaki Saitow, Ute Becker, Christoph Riplinger, Edward F. Valeev, and Frank Neese. A new near-linear scaling, efficient and accurate, open-shell domain-based local pair natural orbital coupled cluster singles and doubles theory. *The Journal of Chemical Physics*, 146(16):164105, 2017.

[108] Florian Weigend, Reinhart Ahlrichs, K. A. Peterson, T. H. Dunning, R. M. Pitzer, and A. Bergner. Balanced basis sets of split valence, triple zeta valence and quadruple zeta valence quality for H to Rn: Design and assessment of accuracy. *Physical Chemistry Chemical Physics*, 7(18):3297, 2005.

[109] Stefan Grimme, Jens Antony, Stephan Ehrlich, and Helge Krieg. A consistent and accurate *ab initio* parametrization of density functional dispersion correction (DFT-D) for the 94 elements H-Pu. *The Journal of Chemical Physics*, 132(15):154104, 2010.

[110] Stefan Grimme, Stephan Ehrlich, and Lars Goerigk. Effect of the damping function in dispersion corrected density functional theory. *Journal of Computational Chemistry*, 32(7):1456–1465, 2011.

[111] E van Lenthe, E J Baerends, and J G Snijders. Relativistic regular two-component Hamiltonians. *The Journal of Chemical Physics*, 99(6):4597, 1993.

[112] Christoph van Wüllen. Molecular density functional calculations in the regular relativistic approximation: Method, application to coinage metal diatomics, hydrides, fluorides and chlorides, and comparison with first-order relativistic calculations. *The Journal of Chemical Physics*, 109(2):392, 1998.

[113] Dimitrios A Pantazis, Xian-Yang Chen, Clark R Landis, and Frank Neese. All-Electron Scalar Relativistic Basis Sets for Third-Row Transition Metal Atoms. *Journal of chemical theory and computation*, 4(6):908–19, 2008.

[114] Thom H. Dunning. Gaussian basis sets for use in correlated molecular calculations. I. The atoms boron through neon and hydrogen. *The Journal of Chemical Physics*, 90(2):1007, 1989.

[115] Kirk A. Peterson, Detlev Figgen, Erich Goll, Hermann Stoll, and Michael Dolg. Systematically convergent basis sets with relativistic pseudopotentials. II. Small-core pseudopotentials and correlation consistent basis sets for the post-d group 16–18 elements. *The Journal of Chemical Physics*, 119(21):11113, 2003.

[116] Kirk A Peterson, Detlev Figgen, Michael Dolg, and Hermann Stoll. Energy-consistent relativistic pseudopotentials and correlation consistent basis sets for the 4d elements Y-Pd. *The Journal of Chemical Physics*, 126(12):124101, 2007.

[117] Nikolai B. Balabanov and Kirk A. Peterson. Systematically convergent basis sets for transition metals. I. All-electron correlation consistent basis sets for the 3d elements Sc–Zn. *The Journal of Chemical Physics*, 123(6):064107, 2005.

[118] A. D. Becke. Density-functional exchange-energy approximation with correct asymptotic behavior. *Physical Review A*, 38(6):3098–3100, 1988.

[119] John P. Perdew. Density-functional approximation for the correlation energy of the inhomogeneous electron gas. *Physical Review B*, 33(12):8822–8824, 1986.

[120] John P. Perdew, Kieron Burke, and Matthias Ernzerhof. Generalized Gradient Approximation Made Simple. *Physical Review Letters*, 77(18):3865–3868, 1996.

[121] Frank Neese. The ORCA program system - WIREs Computational Molecular Science. *WIREs Comput Mol Sci*, 2(1):73–78, 2012.

[122] Frank Neese. Software update: the ORCA program system, version 4.0. *Wiley Interdisciplinary Reviews: Computational Molecular Science*, page e1327, 2017.

[123] M. N. Hedhili, J. H. Bredehöft, and P. Swiderek. Electron-Induced Reactions of $MeCpPtMe_3$ Investigated by HREELS. *The Journal of Physical Chemistry C*, 113(30):13282–13286, 2009.

[124] Samantha G. Rosenberg, Kees Landheer, Cornelis W. Hagen, and D. Howard Fairbrother. Substrate temperature and electron fluence effects on metallic films created by electron beam induced deposition. *Journal of Vacuum Science & Technology B: Microelectronics and Nanometer Structures*, 30(5):051805, 2012.

[125] Patricia M. George and J. L. Beauchamp. Dissociative electron attachment reactions of transition metal carbonyls and their apparent influence on the thermalization of electrons by CO_2. *J. Chem. Phys.*, 76(1982):2959–2964, 1982.

[126] Chepuri R.K. Rao and D. C. Trivedi. Chemical and electrochemical depositions of platinum group metals and their applications, 2005.

[127] Michal Lacko, Peter Papp, Karol Wnorowski, and Štefan Matejčík. Electron-induced ionization and dissociative ionization of iron pentacarbonyl molecules. *The European Physical Journal D*, 69(3):84, 2015.

[128] Xiuli Feng, Nan Li, Liqiang Lv, R. Bruce King, J. P. Piquemal, D. N. Beratan, W. Yang, N. S. Dalal, N. Kaur, and D. Zipse. Unsaturation in binuclear heterometallic carbonyls: the cyclopentadienyliron manganese carbonyl $CpFeMn(CO)_n$ system as a hybrid of the $Cp_2Fe_2(CO)_n$ and $Mn_2(CO)_n$ systems. *New J. Chem.*, 40(9):7482–7492, 2016.

[129] Vilhjálmur Ásgeirsson, Christoph A. Bauer, and Stefan Grimme. Quantum chemical calculation of electron ionization mass spectra for general organic and inorganic molecules. *Chem. Sci.*, 8(7):4879–4895, 2017.

Article I

The role of low-energy electrons in focused electron beam induced deposition: four case studies of representative precursors

Rachel M. Thorman, Ragesh Kumar T. P., D. Howard Fairbrother and Oddur Ingólfsson

Beilstein J. Nanotechnol. 2015, 6, 1904–1926.

Rachel Thorman wrote and edited the bulk of the text in this review manuscript, under the joint expertise of Prof. Howard Fairbrother and Prof. Oddur Ingólfsson. Extensive assistance was provided by Ragesh Kumar T.P. in creation and adaptation of figures and formatting of the manuscript.

BEILSTEIN JOURNAL OF NANOTECHNOLOGY

The role of low-energy electrons in focused electron beam induced deposition: four case studies of representative precursors

Rachel M. Thorman[1,2], Ragesh Kumar T. P.[1], D. Howard Fairbrother[2] and Oddur Ingólfsson[*1]

Review

Open Access

Address:
[1]Science Institute and Department of Chemistry, University of Iceland, Reykjavík, Iceland and [2]Department of Chemistry, Johns Hopkins University, Baltimore, Maryland, USA

Email:
Oddur Ingólfsson* - odduring@hi.is

* Corresponding author

Keywords:
dipolar dissociation; dissociative electron attachment; dissociative ionization; focused electron beam induced deposition (FEBID); low-energy electron-induced fragmentation; neutral dissociation

Beilstein J. Nanotechnol. **2015,** *6,* 1904–1926.
doi:10.3762/bjnano.6.194

Received: 20 May 2015
Accepted: 12 August 2015
Published: 16 September 2015

This article is part of the Thematic Series "Focused particle beam-induced processing".

Guest Editor: M. Huth

Abstract

Focused electron beam induced deposition (FEBID) is a single-step, direct-write nanofabrication technique capable of writing three-dimensional metal-containing nanoscale structures on surfaces using electron-induced reactions of organometallic precursors. Currently FEBID is, however, limited in resolution due to deposition outside the area of the primary electron beam and in metal purity due to incomplete precursor decomposition. Both limitations are likely in part caused by reactions of precursor molecules with low-energy (<100 eV) secondary electrons generated by interactions of the primary beam with the substrate. These low-energy electrons are abundant both inside and outside the area of the primary electron beam and are associated with reactions causing incomplete ligand dissociation from FEBID precursors. As it is not possible to directly study the effects of secondary electrons in situ in FEBID, other means must be used to elucidate their role. In this context, gas phase studies can obtain well-resolved information on low-energy electron-induced reactions with FEBID precursors by studying isolated molecules interacting with single electrons of well-defined energy. In contrast, ultra-high vacuum surface studies on adsorbed precursor molecules can provide information on surface speciation and identify species desorbing from a substrate during electron irradiation under conditions more representative of FEBID. Comparing gas phase and surface science studies allows for insight into the primary deposition mechanisms for individual precursors; ideally, this information can be used to design future FEBID precursors and optimize deposition conditions. In this review, we give a summary of different low-energy electron-induced fragmentation processes that can be initiated by the secondary electrons generated in FEBID, specifically, dissociative electron attachment, dissociative ionization, neutral dissociation, and dipolar dissociation, emphasizing the different nature and energy dependence of each process. We then explore the value of studying these processes through comparative gas phase and surface studies for four commonly-used FEBID precursors:

Beilstein J. Nanotechnol. **2015,** *6,* 1904–1926.

$MeCpPtMe_3$, $Pt(PF_3)_4$, $Co(CO)_3NO$, and $W(CO)_6$. Through these case studies, it is evident that this combination of studies can provide valuable insight into potential mechanisms governing deposit formation in FEBID. Although further experiments and new approaches are needed, these studies are an important stepping-stone toward better understanding the fundamental physics behind the deposition process and establishing design criteria for optimized FEBID precursors.

Review

1 Introduction

Focused electron beam induced deposition (FEBID) [1-3] is a direct-write method capable of creating nanostructures with potential scientific and industrial applications. The advantages of FEBID stem from its ability to write 3D nanostructures of close to any geometry and to write on uneven surfaces. In FEBID (Figure 1), a focused high-energy electron beam impinges on a surface of a substrate that is continuously exposed to a gas stream of precursor molecules as a material source for the intended deposit. The precursor molecules are physisorbed on the surface in dynamic equilibrium with the gas feed, and ideally decompose under the electron beam to leave a well-defined deposit on the surface. The lateral dimensions of deposited structures are controlled by moving the electron beam and the vertical dimensions are controlled through variation of the dwell time.

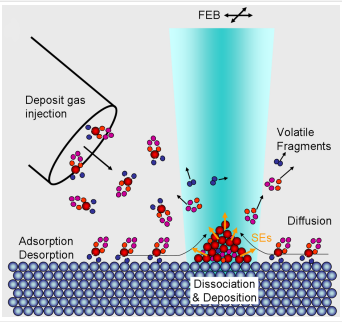

Figure 1: Schematic representation of the FEBID process (reproduced with permission from [2], Copyright (2008) American Vacuum Society): Precursor molecules are supplied through a gas injection system, shown on the left side, and are physisorbed on the surface in dynamic equilibrium with the gas feed. Ideally, the precursor molecules decompose under the electron beam (shown with turquoise shading) to leave a well-defined deposit on the surface, while volatile fragments are pumped away. Diffusion of the physisorbed molecules and the generation of secondary electrons (SEs) are also indicated with black and orange arrows, respectively.

Precursor molecules used for depositing metal-containing nanostructures are typically organometallic compounds with a central metal atom and ligand architectures that lend the compounds the following attributes: i) sufficient vapor pressure to facilitate their introduction into a vacuum chamber, ii) chemical stability under ambient conditions and iii) non-toxicity and easy handling. These criteria are the same as those that define suitable precursors for chemical vapor deposition (CVD) [4,5]. Because of this, as well as their widespread commercial availability, FEBID has to-date mainly relied on existing CVD precursors. There is, however, a fundamental difference between the physics and chemistry behind precursor decomposition and deposit formation in CVD and in FEBID. While CVD is primarily thermally driven, FEBID is initiated by electron/molecule interactions. Although thermal effects and surface-induced reactions may also play a significant role in FEBID, the initial electron-driven step will play an important role in defining the final composition of the deposits.

Because the physics and chemistry determining the spatial resolution, aspect ratio, and composition of FEBID deposits is complex, FEBID is unlikely to reach its full capacity through empirical process parameter optimization with currently available CVD precursors. Rather, a sound understanding of the chemistry and physics governing the deposit formation and the translation of such understanding to design parameters for precursor molecules tailored for FEBID is necessary.

In terms of the electron-induced processes in FEBID, it is clear that the confinement of electron/molecule interactions to the focal width of the incident high-energy electron beam is compromised by elastic and inelastic scattering processes. A portion of the high-energy electrons impinging on the surface and penetrating into the substrate will be backscattered and will exit the surface within an area defined by the scattering angle and the electron energy, rather than by the focal width of the incident beam. Unlike the primary electrons (PEs), which are confined to the focal width of the PE beam, these lower energy scattered electrons will be able to initiate electron-driven reactions outside the area of the PE beam. Moreover, the PEs lose energy as a result of inelastic, ionizing processes which, in turn, give rise to a large amount of secondary electrons (SEs) produced within the substrate. More importantly, these SEs are also produced at or close to the surface of the substrate where they may induce fragmentation of the adsorbed precursor mole-

cules (Figure 2). The reactivity of the SEs with precursor molecules is thus critical in determining the spatial resolution of the deposit. This is even more important with regard to achievable aspect ratios of vertical structures as both backward and forward scattered primary electrons (PEs) and SEs will reach the surface of their sides (Figure 2b).

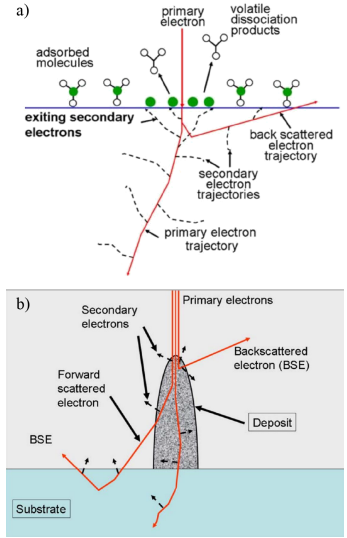

Figure 2: Schematic representation of elastic and inelastic scattering of high-energy primary electrons impinging on a solid substrate and of the generation of SEs through inelastic ionization processes (reproduced with permission from [2], Copyright (2008) American Vacuum Society). (a) Primary electrons impinging on the surface and penetrating the substrate will in part be backscattered and will exit the surface within an area defined by the scattering angle and the electron energy. These electrons lose energy as a result of inelastic, ionizing processes, which in turn, give rise to a large amount of secondary electrons (SEs) produced within the substrate, and more importantly, these SEs are also produced at or close to the surface of the substrate. (b) The same process depicted for a three-dimensional structure growing under the exposure of precursor molecules to the high-energy PE beam. In this case, forward scattered electrons can also reach the surface and produce SEs at the sides of the structure. This may lead to stronger restrictions on the achievable aspect ratios than apply for the achievable resolution of thin layer deposition.

In general, the SE energy distribution extends with appreciable intensities down to 0 eV, peaks well below 10 eV, and has a higher-energy tail stretching well above 50 eV. The actual form (peak position and width) of the SE *energy distribution* depends largely on the nature of the substrate (work function, Fermi energy, and *Z*-value (atomic number)), and to a lesser extent on the PE energy (as long as it is above about 100 eV) [6-8]. Conversely, the SE *yield* depends significantly on both the nature of the substrate and the PE energy. Note that the former represents the distributions of SE energies while the latter means the total SE yield as function of PE energy. The principal variable determining the influence of the PE energy on the SE yield at the surface is their penetration depth. This, in turn, depends mainly on the *Z*-value of the substrate. In general, the SE yield reaches a distinct maximum well below 1 keV PE energy, before decreasing rapidly again, as is discussed in more detail in context to the commonly used FEBID precursor $MeCpPtMe_3$ in section 4.1.

Figure 3 shows the experimentally determined SE energy distribution for 400 eV PEs impinging on a Ni(111) surface [6] and for 1 keV electrons impinging on a Ag(100) surface [9], along with the approximate electron energy ranges in which the principal electron induced processes are operative, i.e., dissociative electron attachment (DEA), neutral dissociation (ND), and dissociative ionization (DI). While the secondary electron inten-

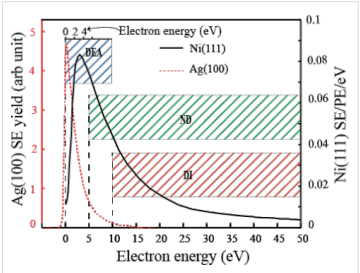

Figure 3: Experimentally measured SE spectra from Ni(111) [6] irradiated by PEs with 400 eV impact energy (black solid line) and from Ag(100) [9] subjected to PEs with 1 keV impact energy (red dotted line). The left-hand *y*-axis shows the relative SE intensity from Ag(100), while the right-hand *y*-axis shows the absolute SE intensity from Ni(111) in SEs per PE per eV (SE/PE/eV). The vertical bars show the approximate electron energy ranges in which the principal electron induced processes are operative, i.e., dissociative electron attachment (DEA), neutral dissociation (ND), and dissociative ionization (DI). The relative extent of these different electron-induced fragmentation processes will depend not only on their relative cross sections, but also on the actual SE energy distribution. From the data shown here, for example, high cross section DEA processes at low energies would likely be dominating for Ag(100) while the integral efficiency of DI and ND processes at higher energies would be more important for Ni(111) (see also [10]).

sity from Ni(111) peaks at about 4 eV with a value close to 0.1 SEs/PE/eV (100 SEs per 1 keV electron) and is still approximately 0.02 SEs/PE/eV at 15 eV [6], the SE intensity from Ag(100) peaks below 1 eV and is already down to 1/10 of the peak intensity at 5 eV [9]. Hence, it is clear that deposit formation in FEBID will be governed by a convolution of the efficiencies of the relevant electron-stimulated processes occurring at the surface and the SE energy distribution at the surface of the substrate. In the case of three-dimensional structures this would be the surface of the growing deposit. Thus, to describe the physics and chemistry of the deposition process in FEBID, the effect of these SEs must be well understood.

This notion that the low energy SEs produced in FEBID may play a significant and even a determining role in the deposit formation has been verified both by simulations [11] and by experiments [12]. In recent years, it has motivated a number of gas phase studies focusing on the energy dependence of the branching ratios and cross sections for various low energy (0–100 eV) electron-induced reactions with organometallic precursors such as $Pt(PF_3)_4$ [13,14], $MeCpPtMe_3$ [15], $W(CO)_6$ [16,17], $Cu(hfac)_2$ and $Pd(hfac)_2$ [18], $Co(CO)_3NO$ [10] and $Fe(CO)_5$ [19]. These processes, which are comprised of DEA, DI, ND, and dipolar dissociation (DD), cannot be distinguished in FEBID or surface experiments with high-energy PE beams, where the precursor molecules are simultaneously exposed to a distribution of low energy SEs in addition to the PEs. However, in gas phase experiments, where these precursor molecules interact with well-defined low energy electron beams, the energy dependence and extent of individual fragmentation processes may be unambiguously determined. Such data, in conjunction with surface experiments with high-energy PE beams, may in turn help to understand the mechanism and extent of action of the low energy SEs in the actual FEBID of the same precursor molecules.

In this contribution, we first give a short summary of the different low energy electron-induced fragmentation processes that can occur (DEA, DI, ND, and DD) with emphasis on the different nature and different energy dependence of these processes. We then explore the value of studying these processes through comparative gas phase and surface studies with reference to previously performed gas phase and surface studies of four organometallic FEBID precursors: trimethyl(methylcyclopentadienyl)platinum(IV) ($MeCpPtMe_3$) [15,20,21], tetrakis(trifluorophosphine)-platinum(0) ($Pt(PF_3)_4$) [13,14,22,23], cobalt tricarbonyl nitrosyl ($Co(CO)_3NO$) [10,24,25] and tungsten hexacarbonyl ($W(CO)_6$) [16,17,26]. We also discuss these results in the general context of the use of these precursors in FEBID and as part of the ongoing effort to understand the fragmentation mechanisms behind deposit formation. Finally, future perspectives and the relevance of these studies to establishing design criteria for precursor molecules specifically tailored for FEBID will be discussed.

2 Low energy electron-induced fragmentation

In the secondary electron energy range relevant for FEBID (<100 eV), there are four distinct mechanisms by which low energy electrons may cause molecular fragmentation, and thus initiate deposition of typical organometallic precursors. These mechanisms are: dissociative electron attachment (DEA), dissociative ionization (DI), neutral dissociation (ND) and dipolar dissociation (DD) [27-32] as depicted in Equations 1–4.

$$AB + e^- \rightarrow AB^{(\ddagger)-} \rightarrow A^{(\ddagger)-} + B^{(\ddagger)} \quad (1)$$

$$AB + e^- \rightarrow AB^{(\ddagger)+} + 2e^- \rightarrow A^{(\ddagger)+} + B^{(\ddagger)} + 2e^- \quad (2)$$

$$AB + e^-(\varepsilon_1) \rightarrow [AB]^* + e^-(\varepsilon_2 < \varepsilon_1) \rightarrow A^{(\ddagger)} + B^{(\ddagger)} \quad (3)$$

$$AB + e^-(\varepsilon_1) \rightarrow [AB]^* + e^-(\varepsilon_2 < \varepsilon_1) \rightarrow A^{(\ddagger)+} + B^{(\ddagger)-} \quad (4)$$

Here; "$(\ddagger)$" denotes that the fragment(s) may be in a vibrationally and/or electronically excited state, "*" denotes the electronic excitation of the intermediate leading to ND and DD, and ε_1 and ε_2 denote the incident energy of the electron and its remaining energy after the inelastic scattering process, respectively.

Dissociative electron attachment (Equation 1) is a resonant process in which an electron is initially captured by the molecule to form a transient negative ion (TNI). This can be understood as a vertical transition from the ground state of the neutral molecule to the ground (or any accessible excited state) of the anion, as is shown in Figure 4. Consequently, the TNI formed is generally in a vibrationally and/or electronically excited state. Under collision-free conditions, it relaxes rapidly either through re-emission of the electron (autodetachment; AD) or through dissociation (DEA). Dissociative electron attachment is active below the ionization threshold of the molecule and generally most efficient at very low incidents energies. The cross section for a given DEA process is defined by the initial attachment cross section multiplied by the probability that the TNI survives nuclear relaxation beyond the crossing point of the respective potential energy curves (r_c in Figure 4). Thus, DEA is confined to narrow energy ranges defined by the Franck–Condon overlap of the wave function of neutral ground state and the respective

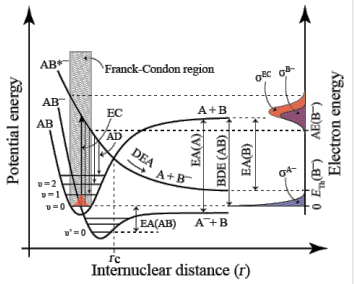

Figure 4: Simplified two-dimensional potential energy diagram for quasi-diatomic dissociation through electron attachment (DEA). The neutral ground state (AB) is depicted along with the anionic ground state (AB^-) and an electronically excited anionic state (AB^{*-}). Electron capture (EC) proceeds through a vertical transition (thick vertical arrow) within the Franck–Condon region (shaded area) and leads to the formation of a transient negative ion (TNI; AB^- or AB^{*-} in this case). The TNI formed can then relax through reemission of the electron (autodetachment; AD) which is depicted with thin vertical arrows from AB^{*-} to the neutral electronic ground state. In the case where this reemission process results in a transition to the ground vibrational state, the scattering process is elastic while the other arrows depict vibrationally inelastic processes. The TNI may also relax through nuclear relaxation along the respective anionic potential energy surfaces (DEA). The dissociative asymptotes are here shown to lead to A^-/B and B^-/A for AB^- and AB^{*-} respectively. For AB^- the potential energy curve is shown crossing the vibrational ground state of the neutral; the AB^- dissociative asymptote lies below this energy. Hence, the electron affinity of A (EA(A)) is larger than the bond dissociation energy of AB (BDE(AB)). Attachment of a 0 eV electron may thus lead directly to the formation of A^-. For AB^{*-} a nuclear relaxation beyond the crossing point with the neutral ground state (r_c) must lead to dissociation, as AD is not possible for nuclear separation beyond this point. The thermochemical threshold for this process ($E_{th}(B^-)$) is given by the difference between the electron affinity of B and the BDE(AB) as depicted on the right-hand *y*-axis. The appearance energy (AE) for the fragment B^-, conversely, is defined by the Franck–Condon overlap and is, in this case, substantially higher than $E_{th}(B^-)$. This is depicted on the right-hand *y*-axis, in terms of the *reflection principle*, which shows the energy dependence of the electron capture cross section (σ^{EC}) as a reflection of the Franck–Condon overlap. The DEA cross section (σ^{B^-}), which is the product of the attachment cross section and the survival probability of the TNI, i.e., the likelihood that the nuclear relaxation exceeds r_c before autodetachment is also shown.

negative ion states, and by the survival probability of the TNI with regard to AD. At very low electron energies where s-wave attachment dominates, the cross section is proportional to $E^{-1/2}$ [33] (see also [34]) and the cross section is thus highest at threshold (i.e., close to 0 eV). The survival probability is also high close to the threshold as the distance to the crossing point of the anionic ground state is short (as is depicted in Figure 4). Such a threshold process is depicted for the lower anionic potential curve in Figure 4, which is shown crossing the ground vibrational state of the neutral molecule, favoring transitions at or close to 0 eV incident electron energy (see also the caption to Figure 4).

For FEBID, the consequence of DEA being most efficient close to 0 eV incident electron energy is that this process is only likely to contribute significantly to precursor decomposition at very low incident electron energies. Moreover, as dissociation will generally proceed along the initial anionic potential energy surface, selective single bond ruptures dominate in DEA. For such a process to be thermochemically accessible at 0 eV, the electron affinity of the neutral corresponding to the anionic fragment formed (A in Equation 1) must exceed the bond dissociation energy (BDE) of the bond being broken (A–B in Equation 1).

It should, however, be noted that the treatment here is simplified to a quasi-diatomic model and molecular rearrangement and formation of new bonds upon electron capture can in some cases lead to considerably more fragmentation with fairly high cross sections at low incident energies. Good examples of such reactions are the extensive fragmentation of tetrafluorophenol and tetrafluoroaniline [35] as well as that of the commonly used FEBID precursor ligands tri- and hexafluoroacetylacetone [36]. In each of these cases, low energy electron attachment leads to the formation of neutral HF, which in turn releases the 5.9 eV HF BDE [37] and promotes further fragmentation of the parent molecule. This is also observed for other molecules such as the amino acids glycine [38] and valine [39], and hexafluoroacetone azine [40], wherein the formation of molecular hydrogen and ethane enables the otherwise thermochemically inhibited formation of CN^- at low incident electron energies. With a suitable choice of ligands, such intramolecular reactions may thus also provide a new means to enhance fragmentation of potential FEBID precursors through DEA.

Perhaps more important in FEBID is the fact that interaction of precursor molecules with the surface of the substrate may alter the DEA cross sections substantially. This may be simply due to the enabled energy transfer offering a new relaxation path that competes with DEA (and AD). Conversely, in other instances polarization interactions may stabilize the TNI with respect to autodetachment and facilitate DEA [41,42].

Dissociative ionization (Equation 2) is fundamentally different from DEA. Here, energy transfer from the incident electron leads to removal of a bound electron from the target molecule and the formation of a parent cation. Similarly to DEA, this can be depicted as a vertical transition of an initially bound electron to the ionization continuum of the molecule as shown in Figure 5. However, if the incident energy in the electron/molecule collision exceeds the ionization energy of the respective

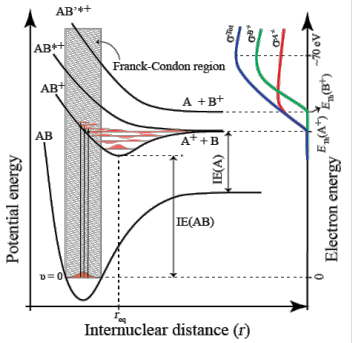

Figure 5: Simplified two-dimensional potential energy diagram for a quasi-diatomic dissociation through electron impact ionization (DI). The ionization process is depicted as a vertical transition from the neutral ground state to the cationic ground state and higher lying cationic states within the Franck–Condon region (shaded area). In this representation the cationic ground state has a considerably larger equilibrium bond length (r_{eq}) compared to the neutral, leading to a significant transition probability to vibrational states that are energetically above the dissociation limit. For simplification, the excited cationic states (AB^{+*} and AB^{+**}) are shown to be purely repulsive. In this representation the parent cation is formed as long as the electron incident energy is above the ionization energy of AB (IE(AB)) but below the dissociation threshold leading to the formation of A^+ ($E_{Th}(A^+)$). The higher-lying excited cationic state (AB^{+**}) is shown to lead to the formation of B^+. The threshold for this channel is given by the sum of the ionization energy of B (IE(B)) and the bond dissociation energy of AB (BDE(AB)). On the right-hand *y*-axis, the energy dependence of the relative cross section for the formation of A^+ and B^+ (σ^{A+} and σ^{B+}) are shown as red and green lines and the total DI cross section (σ^{Tot}) is shown with a solid line as the sum of the two partial cross sections. The threshold energy (E_{Th}) for the formation of the fragments A^+ and B^+ are indicated on the right-hand *y*-axis and the maximum total DI cross section is shown to be at 70 eV. In the case of a polyatomic molecule, the situation is considerably more complex and intramolecular energy re-distribution, multiple fragmentations and rearrangement reactions may dominate the ion formation at higher energies.

molecule, part of the "excess" energy can be transferred to the molecule. This will leave the parent cation in a vibrationally and/or electronically excited state, which often leads to fragmentation. In this case, the extent of the fragmentation and the branching ratios between different fragmentation channels depends on the internal energy of the ion and the thermochemical threshold (or activation energies) for the respective processes. The onset for DI in terms of electron energy is therefore generally slightly above the ionization energy of the molecule and is initially defined by a single bond rupture. With increasing incident electron energy, however, the branching ratios shift more and more to favor multiple bond ruptures, while the total cross section approaches a maximum (typically at around 50–70 eV) before decreasing slowly again. At higher incident electron energies, the interaction time is shorter and the scattering cross section (and thus the DI cross section) decreases again (see pages 23–25 in [43]).

The consequence for FEBID is that DI is likely to contribute to more extensive fragmentation of the precursor molecules when compared to DEA, and moreover that DI will typically only contribute through precursor interaction with the high-energy tail of the SE energy distribution (above about 10 eV). Since DI is a non-resonant process, the total cross section remains fairly constant over a large energy range above the respective thresholds. This will often result in a substantial integral overlap with the SE energy distribution. Hence, while DEA can only proceed through resonances confined to narrow energy ranges below about 10 eV, DI is active from slightly above the molecule's ionization energy to well above 100 eV.

Neutral dissociation through electronic excitation (Equation 3) has characteristics of both DEA and DI. As depicted in Figure 6, it shows a threshold behavior similar to DI, as the initial electronic excitation energy defines the threshold for the process (if it is higher than the respective BDEs). The cross section for individual processes then gradually increases as the electron energy increases and more higher-lying excitation channels open up, also contributing to the total cross section. Unlike DI, the energy transfer is largely confined to the electronic excitation energy, though the resulting electronic states may generally be expected to be vibrationally excited. The available energy is thus limited by the energy characterizing the respective electronic transition in the molecule and the excess vibrational energy associated with the transition. Neutral dissociation is therefore not expected to lead to as extensive fragmentation as DI. However, as the first excited states in organometallic compounds may be as low as 3–4 eV and the ligand BDE is usually low compared to covalent bonds, ND may be active at much lower energies than DI. Similar to DI, ND may still maintain fairly high cross sections for incident electron energies, even in excess of 100 eV (depending on the energy transfer efficiency). Furthermore, electronic excitation from bonding orbitals to strongly anti-bonding orbitals can result in direct dissociation along the respective repulsive potential energy surface, similarly to DEA. In fact, recent quantum mechanical calculations on the potential energy surfaces of selected electronically excited states of $Pt(PF_3)_4$ show the repulsive nature of these states along the metal–ligand bond [44]. However, although these calculations are a considerable achievement, they do not predict whether the remaining internal energy leads to further fragmentation or is channeled into kinetic energy of the departing fragments. Also, in a recent dissociative excitation study on $Fe(CO)_5$ [19], measurements on

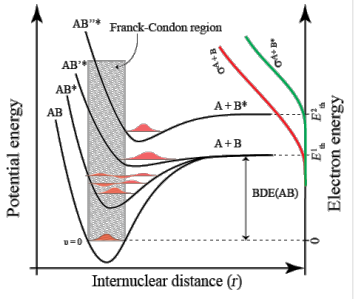

Figure 6: Simplified two-dimensional potential energy diagram for a quasi-diatomic dissociation through electronic excitation, i.e., neutral dissociation (ND). The excitation process is depicted as a vertical transition from the neutral ground state to electronically excited states accessible within the Franck–Condon region (shaded area). Here, the two lower-lying excited states AB^{*} and $AB^{*\prime}$ are shown as bound states and dissociation can only proceed through transitions to vibrationally excited states that are energetically above the respective dissociation limit. In this representation, both AB^{*} and $AB^{*\prime}$ dissociate to form A and B in their respective ground states. The highest-lying excited state (AB^{**}), on the other hand, is shown to be purely repulsive and to dissociate directly to form A and B^{*}. On the right-hand *y*-axis, the energy dependence of the relative cross section for the formation of A and B and A and B^{*} (σ^{A+B} and $\sigma^{A+B^{*}}$) are shown as red and green lines and the total cross section for ND (σ^{Tot}) is shown with a solid line as the sum of the two partial cross sections. The threshold energy (E_{Th}) for the respective processes is indicated on the right-hand *y*-axis. Similarly to DI and DEA, the situation in ND is more complex in the case of a polyatomic molecule, and intramolecular energy redistribution, multiple fragmentations, and rearrangement reactions may play an important role.

the incident electron energy dependence of the induced fluorescence of the fragments formed were attributed to ND processes leading to partial and even complete CO loss up on electron impact. However, as is the case for the studies on $Pt(PF_3)_4$ these studies do not give measures of the efficiency of these processes.

Dipolar dissociation (Equation 4) proceeds similarly to ND, but the Coulomb interaction between the negatively and positively charged fragments must be overcome. The thermochemical threshold for this process is given by the sum of the respective BDEs and the ionization energy of the precursor of the positive ion formed less the electron affinity of the precursor of the negative ion formed. The threshold is thus generally higher than that for DEA and ND but lower than that for DI. To our knowledge there are no current gas phase studies on DD of relevant FEBID precursors and generally DD is not a very efficient process (see T. D. Märk and references therein on pages 276–277 in [27]) It is, however, worth mentioning that a recent study on electron-stimulated negative ion desorption from $Fe(CO)_5$ films shows a significant contribution to the desorption yield from dipolar dissociation [45].

In addition to the different energy dependence of these electron-stimulated processes and the different extent of fragmentation, it should be emphasized that the fragmentation paths will also be distinctly different. While DEA predominantly leads to the formation of a closed shell anion and a neutral, radical counterpart, DI will predominantly result in a closed shell cation and neutral radical counterparts and ND in neutral radical fragments. Thus, one would expect that that the relative importance of these processes in FEBIP will not only define the initial step in the deposition process, but may also strongly influence further surface, thermal, or electron-induced chemical transformation of the deposit.

3 Gas phase vs surface studies

To study low energy electron-induced processes in the gas phase, a low energy electron beam with a resolution of about 100 meV is crossed with an effusive beam of FEBID precursor molecules and the electron energy dependence for the formation of charged fragments is monitored by mass spectrometry (MS) with sufficient resolution and dynamic range to unambiguously detect all fragments formed. For experimental detail relevant to the DEA and DI data discussed here, see [46-48]. Using this methodology, an accurate assessment of the branching ratios for individual DEA and DI fragmentation channels may be achieved and, with careful calibration, absolute cross sections may be determined. Such instruments may also be used to determine the extent of DD, but the extent of ND must currently be estimated from scattering experiments measuring the cross sections for the underlying electronic excitations. For experimental detail on the determination of the scattering cross sections discussed here, see [49]. Regardless of the experimental apparatus or the electron-stimulated processes being investigated, all of these gas phase experiments study single electron/molecule collision events for isolated species and thus do not necessarily reflect the low energy electron-induced decomposition pathways of the same molecules when adsorbed onto a substrate. This may be addressed with well-controlled UHV surface experiments where the precursors are adsorbed onto a substrate and exposed to electrons with relatively high energy (400–500 eV). In such surface experiments, the desorbing fragments are analyzed with MS and the composition of the remaining deposit can be analyzed with techniques such as X-ray photoelectron spectroscopy (XPS), reflection-absorption IR spectroscopy (RAIRS), and/or high-resolution electron energy loss spectroscopy (HREELS). For experimental details on the UHV surface experiments discussed here, see [25,50]. The shortcoming of these surface experiments is,

however, that the precursor molecules are subjected to interactions with SEs with an energy distribution (similar to that in FEBID), in contrast to the well-defined incident energies that characterize the gas phase studies. The energy dependence of the observed processes is therefore not known directly. Consequently, a comparison of the products formed in gas phase and surface science studies combined with the energy dependence of the branching ratios (i.e., the products) obtained in gas phase experiments is needed to identify the dominant processes (e.g., DEA vs DI) occurring in the surface reactions. Such comparison provides valuable insight into the dominant low energy electron-induced processes occurring with FEBID precursors adsorbed on surfaces and may eventually aid the formulation of distinct criteria defining suitable ligand structure and composition for future FEBID precursors.

4 Case studies

4.1 Trimethyl(methylcyclopentadienyl)platinum(IV); $MeCpPtMe_3$

The organometallic compound trimethyl(methylcyclopentadienyl)platinum(IV) ($MeCpPtMe_3$) was first tested as a CVD precursor by Xue et al. [51] in 1989 and was found to create high-purity platinum films, with purities greater than 99 atom % platinum when examined by XPS. Despite its high deposit purity using thermal deposition techniques, $MeCpPtMe_3$ has not been found to produce high-purity deposits in direct FEBID and such deposits do not exceed about 20 atom % Pt [52-54]. In this context, Botman et al. [54] examined FEBID-constructed platinum structures deposited at various surface power densities, calculated from the deposition beam voltage and current and the SE escape area of the substrate. The platinum purity of the unprocessed deposit was optimized to a maximum of approximately 16 atom % at power densities at and above 10 $\mu W/\mu m^2$, but substantially reduced platinum purities were observed at lower power densities (as low as 5.5 atom %). With thermal and electron beam-assisted in situ and post-deposition treatment with processing gases, however, considerably higher Pt content has been achieved [55,56], and resistivity only about six times that of bulk Pt may be attained [57,58]. Such approaches include exposure to atomic hydrogen [54], water [59,60] and oxygen [57,58,61,62], but also the combination of FEBID with atomic layer deposition [63] and with laser exposure [64] have proven advantageous. Despite the poor purity of Pt deposits created from $MeCpPtMe_3$ in the absence of any purification strategies, $MeCpPtMe_3$ has continued to be used as a FEBID precursor due to its stability, good vapor pressure under FEBID conditions, and commercial availability.

A 2012 study by S. Engmann et al. [15] deals with the gas phase dissociation of $MeCpPtMe_3$ upon exposure to low-energy electrons. Gas phase experiments were performed using a crossed electron beam/effusive molecular beam apparatus and product ions were measured using mass spectrometry; the apparatus and methods have each been described in detail [46]. As previously described, electrons with incident energies below the ionization threshold of the parent molecule (7.7 eV for $MeCpPtMe_3$ [15]) can only produce ionic fragments via DEA (DD usually sets in at higher energies). Hence, negative ions collected from electron/molecule interactions at such low incident electron energies are DEA products.

Figure 7 shows the negative ion yields from DEA to $MeCpPtMe_3$ in the incident electron energy range of 0–14 eV. The highest intensity DEA fragment is at m/z 304 and results from a single methyl loss (CH_3), yielding the $[MeCpPtMe_2]^-$ ion. This fragment is almost exclusively produced through a low energy resonance, which the authors assigned to a single electron occupation of the LUMO of $MeCpPtMe_3$. This is anticipated to be predominantly antibonding along the Pt–CH_3 coordinate [65,66]. The onset of the $[MeCpPtMe_2]^-$ formation in the DEA ion yield curves is close to 0 eV, and the peak intensity of this fragment is close to 0.5 eV. Multiple ligand loss through DEA, on the other hand, proceeds predominantly through a higher energy resonance, which the authors assigned as a core-excited resonance (two-particle-one-hole resonance) associated with a HOMO–LUMO transition. The fragment formation through this resonance peaks close to 4.5 eV. From thermochemical considerations it is clear that multiple ligand loss through DEA is in all cases accompanied by significant

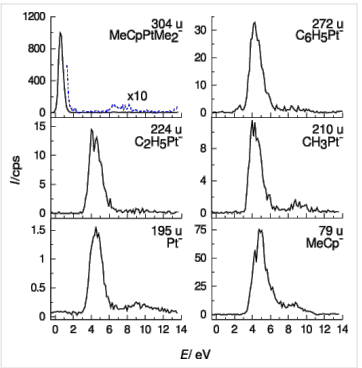

Figure 7: Energy-dependent relative cross sections (ion yields) of negative ion fragments produced by DEA to $MeCpPtMe_3$. Reproduced with permission from [15], Copyright (2012) Royal Society of Chemistry.

rearrangement and new bond formation. This can be seen particularly well in the case of the $[C_7H_{11}Pt]^-$ fragment (*m*/*z* 290), which is the only multiple ligand loss fragment formed through the low energy resonance close to 0 eV (though with very low intensity). For the formation of this fragment, the authors proposed a reaction pathway involving the elimination of an ethyl radical via the intramolecular attack of a leaving methyl radical on another methyl ligand and a H-shift from one of the methyl ligands to the central Pt, thereby reducing the central Pt(IV) to Pt(II) [15]. Such extensive rearrangement reactions have, to our knowledge, not been observed for DEA to other organometallic compounds, but have been observed for a number of covalently bonded compounds as discussed in the previous section. In addition to the resonances discussed above, all fragments observed also appear at higher energies through broad low intensity contributions.

Finally, $[C_7H_9Pt]^-$ (*m*/*z* 288) is observed through a fairly narrow contribution peaking at 2.3 eV [15] (not shown here). This fragment may be attributed to a loss of an ethyl radical and H_2 or, alternately, to the loss of an ethane molecule and a hydrogen radical, and is assigned as a single particle shape resonance. The ratio of the highest-intensity DEA fragment, $[MeCpPtMe_2]^-$ to the next highest fragment, $[MeCp]^-$ (*m*/*z* 79) (leaving a neutral fragment with a maximum C/Pt ratio of 3:1), is approximately 13:1, and all other fragments resulting from multiple ligand loss appear with even lower intensity. Hence, single methyl loss dominates in DEA of $MeCpPtMe_3$.

Figure 8 shows the positive ion mass spectrum of $MeCpPtMe_3$ recorded at 100 eV incident electron energy, where DI dominates [15]. The principal DI channels are the loss of two or three methyl ligands and the loss of two or three methyl ligands along with one or more hydrogen. The loss of one methyl group (and one methyl group and one or more hydrogen) is about an order of magnitude less efficient, and all other fragmentation channels are even less efficient. The DI fragmentation patterns are complicated by the presence of isobaric fragments generated through hydrogen loss – specifically, through the overlap of fragments with different platinum isotopes and those with differing extent of hydrogen loss. Thus, a determination of the threshold energy for individual fragments was not possible, but it is safe to assume that the relative ratios observed at 100 eV impact energy represent fairly well the ratios over the bulk of the relevant SE energy distribution in FEBID.

From this comparison of gas phase DEA and DI data on $MeCpPtMe_3$, it is evident that the most efficient DEA channel is the loss of one methyl ligand. In contrast, the highest intensity DI channel is the loss of two methyl groups, along with the loss of two methyl groups and one or more hydrogen atoms. The second most efficient DI channel is half as intense and

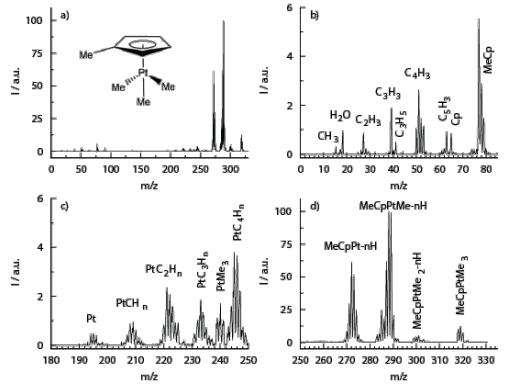

Figure 8: Positive ion mass spectrum of $MeCpPtMe_3$ recorded with electron energy of 100 eV (reproduced with permission from [15], Copyright (2012) Royal Society of Chemistry); (a) overview of the full mass range (*m*/*z* 0–330), (b), (c) and (d); expanded portion of the spectrum for *m*/*z* 0–85, *m*/*z* 180–250 and *m*/*z* 250–330, respectively.

corresponds to the loss of three methyl ligands along with the loss of three methyl ligands and one or more hydrogen.

Assuming that $MeCpPtMe_3$ adsorbed on a surface will react similarly to the gas phase, DEA to $MeCpPtMe_3$ adsorbed on a surface should lead to a reduction of the C/Pt ratio from the initial 9:1 in the intact molecule to close to 8:1, while DI of $MeCpPtMe_3$ adsorbed on a surface should lead to a deposition with C/Pt ratio between 7:1 and 6:1.

A 2009 paper by J. D. Wnuk et al. [21] describes such surface experiments performed using $MeCpPtMe_3$. These experiments were performed using UHV chambers equipped with XPS and MS, and with RAIRS, respectively, as well as commercial flood guns for use as electron sources. The $MeCpPtMe_3$ precursor was physisorbed onto gold substrates at about 180 K and irradiated with electrons with 500 eV impact energy. During electron irradiation, a MS with a 70 eV electron impact ionization source was used to monitor desorption of volatile decomposition products from the surface, while XPS and RAIRS were used to monitor the evolution of the composition of the forming deposit. Figure 9 shows the mass spectrum of species desorbing from the surface before and during electron irradiation.

The only visible species during electron irradiation are at *m*/*z* 15, 16, and 2. These are assigned to CH_3^+, CH_4^+, and H_2^+, with the former two appearing at the ratio observed in electron impact ionization of gas phase methane (CH_4). The initial loss of a methyl radical is likely to result from a Pt–CH_3 bond rupture rather than by dissociation of the methyl group from the MeCp ligand, as the BDE for the latter is expected to be more than 2 eV higher than for the former [15]. This was confirmed by Wnuk et al. [21] through a supplementary study of the analogue cyclopentadienyltrimethylplatinum(IV) ($CpPtMe_3$), which produced a similar mass spectrum during electron irradiation, despite the lack of the methyl group on the Cp ring. The conversion of the dissociated methyl radicals to the methane observed in the mass spectra is less clear as it could arise either from intra- or intermolecular reactions at the surface or from reactions of desorbed methyl radicals at the walls of the UHV chamber. While $MeCpPtMe_3$ was found to desorb from the surface when it was heated to room temperature prior to electron irradiation, no compounds were found to desorb from the surface after electron irradiation. Hence, through electron irradiation, a chemical change clearly converted the physisorbed $MeCpPtMe_3$ to a chemically bound deposit containing platinum and carbon.

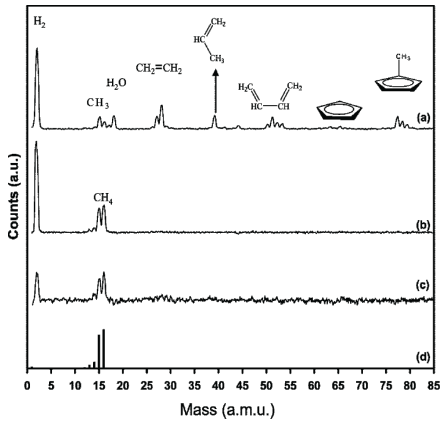

Figure 9: Positive ion mass spectra of $MeCpPtMe_3$ in the *m*/*z* range of 0–85 (reproduced with permission from Wnuk et al. [21], Copyright (2009) American Chemical Society): (a) gas phase spectrum recorded at 70 eV impact energy; (b) positive ion mass spectrum of volatile species desorbing from a $MeCpPtMe_3$ film, adsorbed onto a gold substrate at 180 K, under irradiation with 500 eV electrons; (c) positive ion mass spectrum of volatile species desorbing from a $CpPtMe_3$ film, adsorbed onto a gold substrate at 180 K, under irradiation with 500 eV electrons; (d) reference mass spectra of gas phase CH_4 (adapted from NIST [67]).

In addition to the mass spectra recorded to monitor desorbing fragments, the evolution of the surface composition with increasing electron dose was monitored by XPS and RAIRS. The XPS spectra showed that the fractional Pt coverage stayed constant, but a partial reduction of Pt(IV) to a lower oxidation state took place. The C/Pt ratio decreased from the initial 9:1 of the precursor molecule to about 8:1 upon electron irradiation, as is shown in Figure 10. This ratio was found to remain the same for initial film thicknesses of 1–3 nm and for incident electron irradiation with 500 and 200 eV electron energy. Furthermore, the RAIRS data showed a systematic loss of absorbance in the ν(C–H) stretching region with increasing electron dose. The authors interpreted their findings as due to an initial electron-induced Pt–CH_3 bond rupture caused by DEA, which was initiated by low energy secondary electrons.

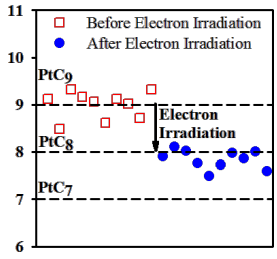

Figure 10: Changes in the C/Pt ratio of a 3.16 nm thick film of $MeCpPtMe_3$ adsorbed on a gold surface at 180 K (reproduced with permission from Wnuk et al. [21], Copyright (2009) American Chemical Society). The open squares show the C/Pt ratio before electron irradiation and filled circles show the C/Pt ratio after irradiation with 500 eV electrons. The dashed horizontal lines indicate the expected C/Pt ratio for films with stoichiometry of PtC_9, PtC_8 and PtC_7.

This is consistent with the expected single ligand loss through DEA, as observed in the gas phase experiments. Moreover, considering the currently available gas phase data, this implies that electron-induced decomposition of surface-adsorbed $MeCpPtMe_3$ is predominantly caused by secondary electrons with incident energy below 1 eV.

Interestingly, the cross section for methane desorption from adsorbed $MeCpPtMe_3$ exhibits a qualitatively similar PE energy dependence as that expected for the SE yield. This is also true for the $MeCpPtMe_3$ deposition yield as function of incident electron energy, and may be taken as further support for the notation that the low energy SEs are driving the deposition. To demonstrate this, Figure 11a compares a best fit to the cross section for methane desorption from $MeCpPtMe_3$ physisorbed on a gold surface (Z = 79) and the calculated PE energy dependence of the SE yield from tungsten (Z =74). The comparison with tungsten is chosen as its atomic number, which strongly influences the PE energy dependence of the SE yield, is close to that of gold. Further, Figure 11b compares the PE energy dependence of the $MeCpPtMe_3$ deposition yield on a silicon surface (Z = 14) and the calculated PE energy dependence of

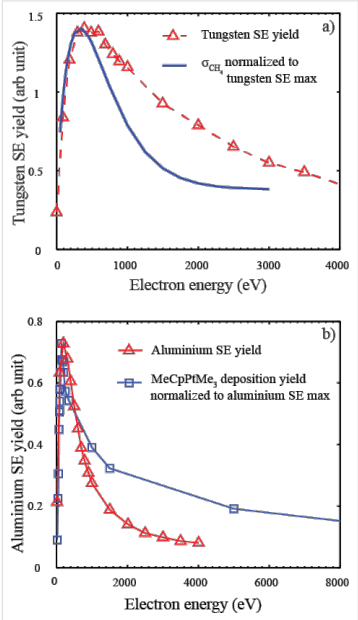

Figure 11: a) A line of best fit to the cross section for methane desorption from $MeCpPtMe_3$ adsorbed on a gold surface (Z = 97) and exposed to electron irradiation in the energy range from 0 to about 3000 eV (solid blue line), compared to energy dependence of the SE yield of tungsten (Z = 94) as a function of primary electron energy (red triangles). b) The deposition yield of $MeCpPtMe_3$ on a silicon surface (Z = 14) as a function of the PE beam energy in the range from about 0–5000 eV (blue squares) compared to the energy dependence of the SE yield from aluminum (Z = 13) as a function of primary electron energy (red triangles). The methane desorption cross sections (a) are adapted from Wnuk et al. [68] and the deposition yield (b) is adapted from Botman et al. [12]. The calculated SE yields are adapted from Ohya et al. [8] (using the partial wave expansion for the cross-section). Lines connecting the symbols are only meant to guide the eye.

the SE yield from aluminum (Z = 13). Here, one has to keep in mind the influence of the growing deposit on the effective Z-number in the measurements of the deposition yield, as this may be closer to that of carbon. In both cases (Figure 11a and Figure 11b) the calculated energy dependence is adapted from Ohya et al. [8]. The scatter in the cross section data for the methane desorption is considerable and the same is true for the errors in the deposition cross section. Furthermore, the exact peak position and the general form of the energy dependence of the calculated SE yield depend strongly on the model used and the Z-number of the respective substrate material, with the work function and Fermi level of the substrate also playing a role. Nevertheless, the qualitative similarities between the energy dependence of the measured cross sections and that of the calculated SE yields is evident and clearly supports the notation that the role of the SEs is dominating in the deposit formation.

4.2 Tetrakis(trifluorophosphine)platinum(0) $Pt(PF_3)_4$

Tetrakis (trifluorophosphine) platinum (0) ($Pt(PF_3)_4$), is a Pt-containing FEBID precursor that does no contain carbon; this has the potential advantage that unlike $MeCpPtMe_3$, it cannot create carbon-contaminated deposits. It is liquid at ambient temperatures, has a vapor pressure of 65 Torr, and is fairly stable at room temperature when stored under a PF_3 atmosphere [69,70]. It has been shown to produce pure Pt deposits using CVD [70]. In FEBID, deposits with a Pt content as high as 81 atom % have been achieved [71]. This is a considerably higher Pt content than achieved by FEBID of $MeCpPtMe_3$, where deposits typically contain less than 20% Pt [52-54]. Post-deposition procedures have also been studied and found to further improve the percent platinum content and conductivity. In this context, a platinum content of about 94 atom % has been attained through annealing in the presence of H_2O [72] and a resistance of 0.24×10^{-3} Ω·cm (only an order of magnitude higher than the bulk value for Pt) has been reached through annealing under nitrogen and a mixture of nitrogen with 5% hydrogen [73]. Tetrakis(trifluorophosphine)platinum is also one of the best-studied FEBID precursor with regards to the molecular mechanisms behind its deposition. These studies include absolute cross section measurements for DEA of $Pt(PF_3)_4$ [14] and a determination of the thermal electron attachment rate constant and the associated activation energy using a flowing-afterglow Langmuir probe [74] as well as absolute cross section measurements for elastic, vibrational, and electronic scattering [13]. Collectively, these studies provide insight into electron energy loss processes that occur through interaction with the precursor and internal excitation of the precursor, and the potential role of ND in the deposit formation. All of these gas phase studies can be compared with a UHV surface study by Landheer et al. [23], where mass spectrometry was used to monitor desorption of volatile decomposition products and XPS and HREELS were used to monitor the evolution of the deposit during irradiation.

Figure 12 shows the energy dependence of the DEA cross sections for $Pt(PF_3)_4$ in the energy range from 0–12 eV and Figure 13 shows a positive ion FT-ICR mass spectrum of $Pt(PF_3)_4$ ionized with an axial beam of 20 eV electrons. The DEA spectra are dominated by single ligand (PF_3) loss peaking at about 0.5 eV with the very high cross section of 2×10^{-16} cm^2. This value is only about an order of magnitude lower than the maximum theoretical cross section for s-wave attachment at this energy [27]. All other channels are about two orders of magnitude less efficient; from these, the loss of two PF_3 ligands also proceeds through the resonance appearing close to 0.5 eV in the DEA spectra. Further fragmentation leading to the formation of $[Pt(PF_3)]^-$ and $[Pt(PF_3)F]^-$ proceeds predominantly through a higher lying resonance appearing close to 6 eV in the DEA ion yield, and F^- appears through a broad contribution close to 12 eV.

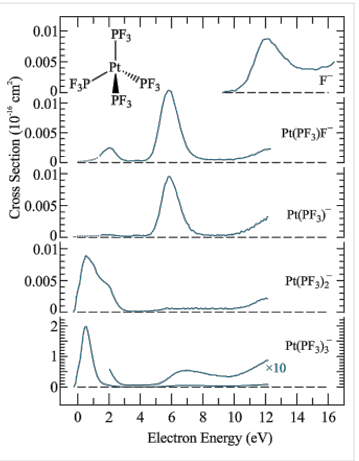

Figure 12: Energy-dependent absolute cross sections for negative ion fragments produced by DEA to $Pt(PF_3)_4$ (reproduced with permission from May et al. [14], Copyright (2012) Royal Society of Chemistry).

Unfortunately no quantitative data on the energy dependence of DI is available for $Pt(PF_3)_4$, but the FT-ICR spectrum [22] allows for qualitative comparison (see Figure 13).

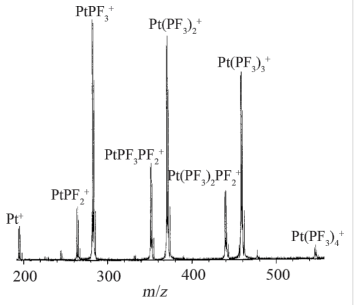

Figure 13: Electron ionization FT-ICR mass spectrum of $Pt(PF_3)_4$ recorded at 20 eV incident electron energy (reproduced with permission from [22], Copyright (1997) American Chemical Society).

It is clear from this spectrum that even at 20 eV electron impact energy, DI leads to considerably more extensive fragmentation than DEA. While single ligand loss is dominant in DEA, the relative cross sections for the loss of one, two, and three ligands in DI at 20 eV are all comparable. Additionally, both the loss of one fluorine atom in addition to the respective ligands (e.g., $Pt(PF_3)_2PF_2$), and the formation of the bare platinum cation contribute appreciably to the total DI yield. For higher electron impact energies, it is safe to assume that the DI branching ratios will shift further to favor more extensive fragmentation. This is a general behavior, an example of which can be seen clearly for the energy dependence of DI of $W(CO)_6$ [17] and $Co(CO)_3NO$ [10], which are discussed hereafter. Thus, DEA to $Pt(PF_3)_4$ leads predominantly to single ligand loss while DI integrated over the energy range of the SEs generated in FEBID will predominantly lead to more extensive fragmentation.

In addition to the absolute DEA cross sections shown in Figure 12, Allan [13] has determined absolute cross sections for the angular dependence and energy dependence of elastic, vibrational, and electronic scattering of electrons from $Pt(PF_3)_4$ (mainly focused on the region below 20 eV incident electron energy). While elastic scattering will influence the spatial distribution of the secondary electrons and vibrational scattering will contribute to heating of the precursor molecules and substrate, electronic excitations may lead to direct ND, and therefore potentially play a significant role in the initial step in the FEBID process. Figure 14a,b compares the electron energy loss spectra for $Pt(PF_3)_4$ for different residual electron energies (Figure 14a) and the incident electron energy dependence of the absolute cross sections for electronic excitation (Figure 14b)

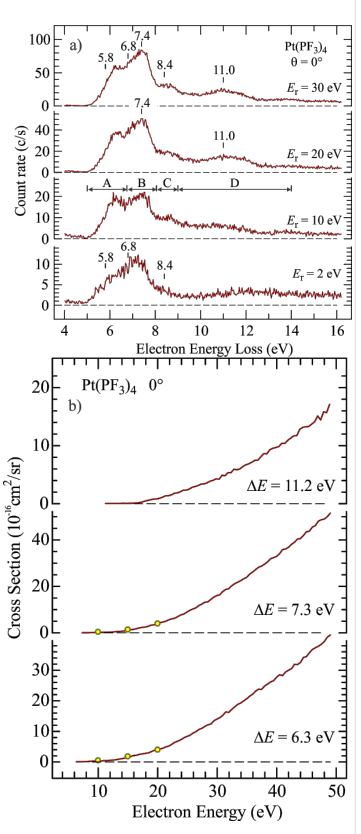

Figure 14: (a) Electron energy loss spectra of $Pt(PF_3)_4$ recorded at 0° angle with varying residual energies. The sections marked A–D in the third panel represent the energy ranges in which integration is performed to obtain absolute values. (b) Absolute electron excitation cross sections as a function of electron energy integrated over the energy loss ranges signified as A, B and D in Figure 14a. These cross sections are recorded at 0° angle and electron energy losses of 6.3 eV, 7.3 eV and 11.2 eV. Both figures (a) and (b) are reproduced with permission from [13], Copyright (2011) American Institute of Physics.

integrated over the energy ranges signified as A, B, and D in the third panel of Figure 14a. The data is recorded at 0° scattering angle. It is clear that the electronic excitations in $Pt(PF_3)_4$ have cross sections comparable to those measured for DEA. Unfortunately, no conclusive data exists on the extent and nature of the dissociation processes resulting from these electronic excitations. From the mass spectra reported by Hammill et al. [22] one can, however, speculate on the energetics involved and, therefore, on the possible extent of neutral fragmentation from the individual electronic excitations. It can be seen from Figure 12 that the bare Pt cation is produced from $Pt(PF_3)_4$ at 20 eV electron impact energy. Since the ionization energy of Pt is 9 eV [75], the 11 eV of residual energy must be sufficient to effect the loss of all four PF_3 ligands, indicating that the average $Pt–PF_3$ ligand bond dissociation energy is less than 2.75 eV. Thus the loss of two ligands may already be energetically accessible through the bulk of the excitation region marked A in Figure 14a, and three or even all four ligands may be lost through ND via the higher lying electronic excitations.

Recent quantum mechanical calculations on these states show that the potential surfaces of the four lowest electronically excited states are dissociative with respect to a single ligand loss, similarly to the DEA process [44]. However, as is apparent from the calculations above, the remaining internal energy may lead to further dissociation.

Under UHV conditions, Landheer et al. [23] have studied the decomposition of $Pt(PF_3)_4$ molecules, adsorbed at low temperatures (<170 K), upon irradiation with 500 eV electrons. In these experiments, neutral fragments desorbing from the substrate during electron irradiation were monitored by mass spectrometry, and while the chemical composition of the remaining film was probed by XPS, HREELS was used to study the change in vibrational modes of the adsorbed molecules. Figure 15 shows a time-resolved mass spectrum monitoring the PF_3 desorption during electron exposure after an initial electron dose of 0, 1.5×10^{14}, 2.5×10^{15}, and 4.2×10^{14} e^-/cm^2.

Figure 16 shows the electron dose dependence of the fractional platinum, phosphorous, and fluorine coverage determined by XPS [23]. The mass spectrum clearly shows an electron-initiated PF_3 desorption, and that this desorption comes to a halt at an electron dose slightly above 10^{15} e^-/cm^2. The loss of phosphorous and fluorine in the same electron dose range is also apparent from the XPS data, which shows that both the fractional phosphorous and fluorine contents decrease rapidly, and at the same rate as one another, to 75% of their initial 1:4 ratio. Electron exposures above 3×10^{15} e^-/cm^2 resulted in additional fluorine loss and oxygen deposition, while the fractional phosphorous content remained stable at 75% of its initial value

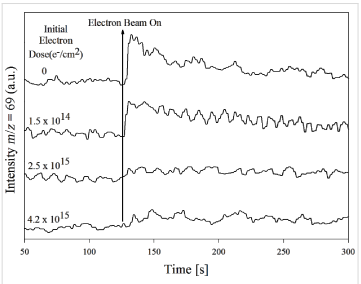

Figure 15: Time-resolved mass spectra of gas phase PF_3 (positive $[PF_2]^+$ ions produced by 70 eV electron impact are recorded) desorbing from films of $Pt(PF_3)_4$ adsorbed on an Au surface at 180 K when these are irradiated with 500 eV electrons. The time at which the electron beam is turned on is represented with a vertical line. Reproduced with permission from [23], Copyright (2011) American Chemical Society.

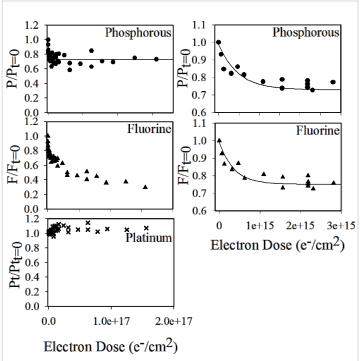

Figure 16: Electron dose dependence of the fractional coverage of Phosphorous ($P/P_{D=0}$), Fluorine ($F/F_{D=0}$) and Platinum ($Pt/Pt_{D=0}$). The left-hand side plots show the changes in fractional coverage for the full range of electron doses up to 2×10^{17} e^-/cm^2. The right-hand side plots show the phosphorous and fluorine fractional coverage for the initial period of electron exposure up to 2×10^{15} e^-/cm^2. Solid lines in the plot show a fit to experimental values based on the first order loss process. Reproduced with permission from [23], Copyright (2011) American Chemical Society.

[23]. The authors interpreted these observations as a two-step process. In the first step, electron interaction with $Pt(PF_3)_4$ leads to a single $Pt–PF_3$ bond rupture and transformation of the

adsorbed $Pt(PF_3)_4$ to $Pt(PF_3)_3$. This explains why the phosphorous and fluorine signals decrease at the same rate to 75% of their initial values while the P/F ratio remains constant. In the second step, further electron exposure nearly exclusively leads to P–F bond rupture and the coordinately unsaturated phosphorous reacts with residual water to form phosphorous oxides.

If we compare the evidence of single PF_3 ligand loss as the initial step in the deposit formation (as shown by the XPS data) with the existing experimental gas phase data, the observed single ligand loss points strongly towards DEA, rather than DI, as the initiator of deposition. This is not conclusive, however, as the role of ND is not certain without further information on the relaxation of the respective electronically excited states. Interestingly, if DEA is in fact the dominating process, the electron-induced deposition of $Pt(PF_3)_4$ is initiated by SEs with an incident electron energy of less than 1 eV, and the rest of the SE energy distribution as well as the primary electrons play an insignificant part in this primary step. Conversely, if ND in fact plays an important role in the initial single ligand loss, then energies above about 10 eV will also be important as is apparent in Figure 14. This notion, however, presumes that the processes observed in the gas phase remain similar with regards to the fragmentation, when $Pt(PF_3)_4$ molecules are adsorbed on surfaces.

4.3 Cobalt tricarbonyl nitrosyl; $[Co(CO)_3NO]$ and tungsten hexacarbonyl $[W(CO)_6]$

Cobalt tricarbonyl nitrosyl $[Co(CO)_3NO]$ was initially introduced in CVD as a liquid, easy-to-handle Co source. [76-78]. In CVD, Crawford et al. [78] reported an average composition of $CoN_{0.5}O_{0.9}$ with only traces of carbon when using Ar or N_2 as carrier a gas at deposition temperatures below 380 °C. Above 400 °C, the authors found the deposits to consist of a mixture of CoO and Co metal. Deposition under hydrogen atmosphere, on the other hand, was found to result in pure cobalt deposits already at 350 °C [76,77]. Cobalt tricarbonyl nitrosyl has a normal boiling point of 78.6 °C, a vapor pressure of 91 Torr at 20 °C [79], and a thermal decomposition temperature of about 130–140 °C measured on SiO_2 [80]. It is also commercially available and relatively nontoxic. Furthermore, the commonly used Co precursor $Co_2(CO)_8$ is unstable under vacuum and tends to polymerize, releasing CO. This, in turn, may lead to pressure buildup in precursor reservoirs, complicating the protocol for its use [81]. Consequently, a number of FEBID studies and an electron beam-induced surface activation (EBISA) study have been conducted on $Co(CO)_3NO$ [80-83]. In these studies, at room temperature, the Co content of the deposits was found to be about 40–50 atom %, independent of beam energy and current. The Co/N and Co/C ratios are similar in these deposits (about 3.5:1), while the initial ratios in the precursor molecule are 1:1 and 1:3, respectively. Hence, carbon loss is clearly much more pronounced than nitrogen loss. Furthermore, EDX and TEM studies along with resistivity measurements indicate that the deposit consists of Co nanograins embedded in an insulating CoO matrix [82]. The chemical speciation of the nitrogen and carbon in the deposits remains an open question in these studies. However, as the bulk of the oxygen is bound as CoO, the nitrogen is likely bound as the respective cobalt nitride.

Focused electron beam induced deposition of $Co(CO)_3NO$ at elevated substrate temperatures [80] leads to a substantial decrease in the carbon content (by about a factor of three). At 50 °C, the oxygen content decreases fairly abruptly to about 50% of its initial value (from 15 to about 7.5 atom %); at 100 °C, the nitrogen content increases by approximately the same atomic percentage. The cobalt content, gradually increases from about 40 atom % at room temperature to about 50 atom % at 200 °C. This results in a composition of approximately $CoC_{0.15}O_{0.45}N_{0.45}$. We are not aware of studies on post-deposition or in situ purification of the deposits formed with $Co(CO)_3NO$, but in a recent study, the combination of annealing, H_2 exposure, and electron irradiation of deposits formed with $Co_2(CO)_8$ was found to result in compact, carbon and oxygen free Co layers [84].

In a 2011 gas phase study, Engmann et al. [24] published absolute cross section values for DEA to $Co(CO)_3NO$. These were the first absolute cross section values published for DEA to any potential FEBID precursor. The energy dependence of these cross sections is shown in Figure 17.

Similar to $MeCpPtMe_3$ and $Pt(PF_3)_4$, the most efficient channel in DEA to $Co(CO)_3NO$ is a single ligand loss close to 0 eV. Moreover, the absolute cross section for single ligand loss through DEA is very high. For $Co(CO)_3NO$, the loss of one CO ligand was assigned to the formation of a single particle resonance resulting in a maximum $[Co(CO)_2NO]^-$ yield close to 1 eV incident energy, while hot band transitions associated with the same resonance result in another maximum close to 0 eV. The maximum cross section for $[Co(CO)_2NO]^-$ formation was found to be about 4×10^{-16} cm^2 and, although the uncertainty associated with these measurements is considerably larger than these associated with the measurements by May et al. for $Pt(PF_3)_4$ [14], these cross sections are clearly very high. The loss of the NO ligand is also observed but is confined to the energy range from about 1–3 eV with a peak intensity close to 2 eV and a maximum cross-section that is an order of magnitude lower than that for the single CO loss. This NO loss channel was assigned as a low-lying two-particle-one-hole resonance associated with a HOMO–LUMO transition. The loss of

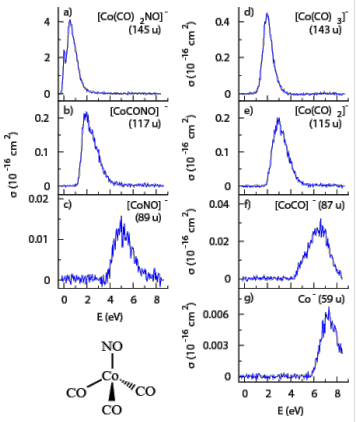

Figure 17: Energy-dependent absolute DEA cross sections for $Co(CO)_3NO$ (reproduced with permission from [10], Copyright (2013) American Institute of Physics).

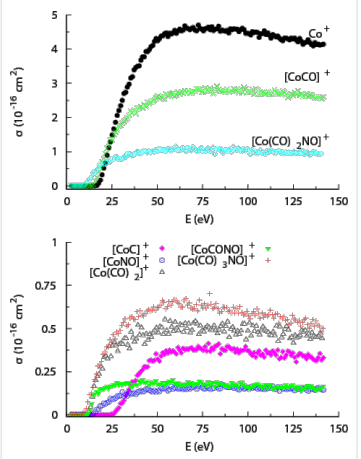

Figure 18: Energy dependence of the partial cross sections for positive ion fragments formed from $Co(CO)_3NO$ (reproduced with permission from [10], Copyright (2013) American Institute of Physics).

two or more ligands, i.e., the formation of $[Co(CO)NO]^-$, $[Co(CO)_2]^-$, $[CoNO]^-$, and $[CoCO]^-$, is observed in the range from about 2 eV to about 6 eV and is attributed to further decomposition of $[Co(CO)_2NO]^-$ and $[Co(CO)_3]^-$ at the high energy tail of the respective resonances, where there is sufficient energy to induce further fragmentation. However, the maximum cross section for the formation of these fragments in this energy range is only about 5% of the cross section for single CO loss for $[Co(CO)NO]^-$ and $[Co(CO)_2]^-$, and about 0.5% for $[CoNO]^-$ and $[CoCO]^-$. $[Co(CO)]^-$ is also formed through a higher-lying core-excited resonance but with a maximum cross section close to 0.5% of that for single CO loss, while the bare Co^- ion is also formed through the same resonance with a cross section that is close to 0.2% of that for single CO loss.

Figure 18 shows the absolute cross sections for the various fragments produced through DI of $Co(CO)_3NO$ as a function of the incident electron energy. At the maximum of the total cross section, around 50 eV, the most intense DI fragment is the bare cobalt cation (Co^+) with a maximum absolute cross section of about 4.6×10^{-16} cm^2, i.e., similar to that for a single CO loss through DEA. The second most efficient channel at this energy is the formation of $[CoCO]^+$, with an absolute cross section of about 2.8×10^{-16} cm^2. Hence, DI of $Co(CO)_3NO$, unlike DEA, results largely in complete or almost complete dissociation of the precursor molecule. The relative cross sections for the loss of a single CO ligand or the NO group are nonetheless still appreciable, and at about 50 eV they amount to about 25% and 12.5% of that for the Co^+ formation, respectively. Interestingly, the formation of $[CoC]^+$ is also observed with a fairly high cross section above its formation threshold – about 3×10^{-16} cm^2. All cross sections mentioned here are for incident energies of about 50 eV, where all channels have reached their maximum cross sections (Figure 18). At higher energies the cross-sections remain fairly constant. Conversely, the threshold for the individual channels is very different; for example, while the appearance energy for single CO loss is at about 8.47 ± 0.15 eV, that for Co^+ formation is about 14.90 ± 0.15 eV [85]. The energy-dependent cross sections for these processes cross at about 25 eV and the single CO loss is thus the more efficient channel in the energy range from 8.47 ± 0.15 eV to about 25 eV (Figure 18).

As discussed previously, to properly evaluate the efficiency of individual DEA and DI channels determined in gas phase studies in the context of FEBID, it is important to consider not only the energy-dependent reaction cross sections (as shown in

Figure 17 and Figure 18), but also the energy distribution of the secondary electrons produced from the substrate and their overlap with the respective cross sections for each dissociation channel. This is a reflection of the fact that the overall efficiency of a given reaction pathway mediated by DEA, DI, or ND will be a convolution of the energy-dependent reaction cross section and the secondary electron yield at each energy. To demonstrate this, Figure 19 shows the partial cross section for single CO loss from $Co(CO)_3NO$ through both DEA and DI along with the cross section for the formation of Co^+ through DI. On the same plot the measured SE distributions from Ni(111) and Ag(100) are also shown.

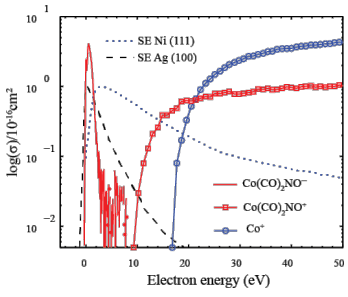

Figure 19: The partial cross sections for single CO loss through DEA (red solid line), for single CO loss through DI (red open squares), and for Co^+ formation through DI (blue open circles), all adapted from Engmann et al. [10]. Also shown are the measured SE distributions from Ni(111) adapted from Schaefer et al. [6] (blue dotted line) and the measured SE distributions from Ag(100) adapted from Knights et al. [9] (black dashed line).

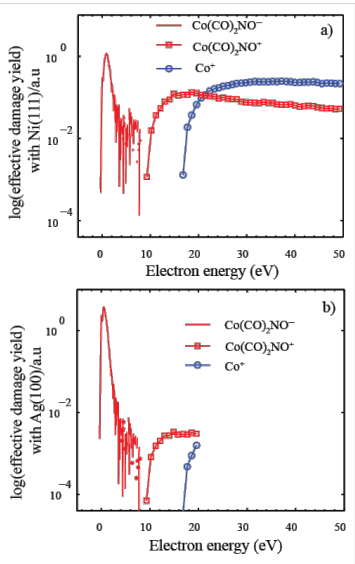

Figure 20: Predicted relative effective damage yield for single CO loss through DEA (red solid line), for single CO loss through DI (red open squares) and for the formation of Co^+ through DI (blue open circles). Damage yields are derived from the product of the respective partial cross sections and the normalized measured SE yields for (a) Ni(111) and (b) Ag(100). The cross sections are adapted from [10] and the SE yields for Ni(111) and Ag(100) from [6] and [9], respectively.

Using the information contained in Figure 19, Figure 20a and Figure 20b show the predicted relative effective damage yield for each channel, derived from the product of the respective ion yields and the normalized measured SE yields for Ni(111) and Ag(100), respectively. It is clear from this comparison that the SE energy distribution will influence not only the relative importance of DEA compared to ND and DI, but may also cause the relative efficiency of individual DI channels to differ significantly from their relative cross sections in the gas phase. We recognize that the energy distribution of the SEs from the single crystal Ni(111) and Ag(100) surfaces is not likely to accurately reflect the SE energy distribution in a FEBID experiment where the substrate is polycrystalline or, as deposition proceeds, the deposit surface itself. The physisorbed precursor molecule and the background gas also play a role. Nevertheless, it is obvious from Figure 20b that a SE energy distribution similar to that for Ag(100) would strongly favor DEA over DI, and from the observed DI channels those with the lowest threshold energies would dominate, yielding a single CO loss rather than leading to Co^+ formation. For the SE energy distribution measured for Ni(111) (Figure 20a), on the other hand, the integral damage yields through DEA and DI are comparable with Co^+ formation being favored over single CO loss in DI.

Judging from the gas phase data alone, one would expect that if the decomposition of adsorbed $Co(CO)_3NO$ molecules is driven solely by DEA, it would mainly occur through CO desorption (see Figure 17) and would lead to a reduction of the relative Co/C/O ratio from 1:3:4 to about 1:2:3. The loss of nitrogen should be insignificant. In contrast, for a DI-driven decomposition process, NO desorption would be significant based on the integral cross sections (Figure 18) and the expected Co/N ratio

remaining on the surface should be reduced from the initial 1:1 to about 1:0.25.

This can be compared with a UHV surface study of adsorbed $Co(CO)_3NO$ by Rosenberg et al. [25]. In this study the authors used XPS, MS, and RAIRS to examine metal–ligand bond dissociation caused by irradiation of the adsorbed precursor molecules with 500 eV primary electrons. Figure 21 shows mass spectra of (a) gas phase $Co(CO)_3NO$ and (b) the fragments desorbing during the electron irradiation of approximately 8–10 monolayers of $Co(CO)_3NO$ adsorbed on a polycrystalline Au surface. In the gas phase mass spectrum, the ratio of CO (*m*/*z* 28) to NO (*m*/*z* 30) is close to the stoichiometric composition of $Co(CO)_3NO$. Conversely, the mass spectrum recorded during electron exposure of adsorbed $Co(CO)_3NO$ shows dominating CO desorption while the NO contribution is insignificant. This is observed for electron doses up to about 5×10^{16} e^-/cm^2, above which the CO desorption comes to a halt.

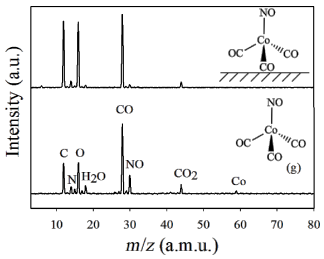

Figure 21: Positive ion (DI) mass spectra of (a) gas phase $Co(CO)_3NO$, (b) volatile species desorbing from a 2.5 nm thick $Co(CO)_3NO$ film, adsorbed onto a gold substrate at 105 K, during irradiation with an electron dose of 5×10^{16} e^-/cm^2 at an electron energy of 500 eV (reproduced with permission from [25], Copyright (2013) American Chemical Society).

The dominance of CO desorption from adsorbed $Co(CO)_3NO$ molecules exposed to electron irradiation is also reflected in the composition of the remaining deposit as measured with XPS [25]. Figure 22 shows the evolution of the fractional carbon, nitrogen, and oxygen content on the surface, referenced to the composition of the precursor prior to electron irradiation. While the fractional nitrogen content stays constant during the whole exposure time, the fractional oxygen and carbon contents fall to about 50% of their initial value by an electron dose of 5×10^{16} e^-/cm^2. Above 5×10^{16} e^-/cm^2, however, the fractional oxygen and carbon contents stay constant up to electron doses as high as 10^{18} e^-/cm^2. Although the fractional nitrogen content stays constant throughout the electron doses studied, it is reduced from the initial nitrosyl to a nitride species [25]. Reduction of the carbonyl carbon to graphitic carbon and concurrent conversion of the carbonyl and nitrosyl oxygen to an oxide species is also observed. While the nitride speciation change occurs at electron doses below 5×10^{16} e^-/cm^2 and is coincident with CO ejection, the carbon and oxygen changes primarily take place at higher electron doses. Furthermore, as a result of electron irradiation, changes in the cobalt region suggest the formation of a cobalt oxide and/or cobalt nitride.

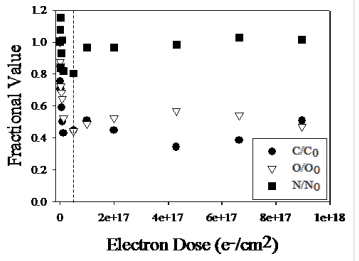

Figure 22: Electron dose dependence of the fractional coverage of carbon, oxygen and nitrogen from $Co(CO)_3NO$ adsorbed onto a gold substrate at 105 K and exposed to 500 eV electrons. The vertical dotted line represents an electron dose of 5×10^{16} e^-/cm^2 (reproduced with permission from [25], Copyright (2013) American Chemical Society).

The authors interpreted their data as a two-step process governing the electron-induced deposition of adsorbed $Co(CO)_3NO$. The first (deposition) step occurs at low electron dose. In this step, one or more (an average of 1.5) CO ligands dissociate from the parent molecule and the NO ligand decomposes, producing a nitride species. The lack of NO desorption is also evident in the MS, which shows significant CO desorption from the surface. During this period, the cobalt is slightly oxidized and shows a peak broadening to a higher binding energy, likely resultant from oxide and/or nitride formation. This step is complete at an electron dose of about 5×10^{16} e^-/cm^2.

After this point, the second (decomposition) step can be observed. The partially decarbonylated species remaining; $[(CO)_xOCoN]$, undergoes an electron-stimulated decomposition of the remaining CO ligand(s) and adsorbed carbon is

formed. More cobalt oxide is formed; likely due to reactions between reactive oxygen species released from the decomposition of the remaining CO ligands and Co atoms. The chemical composition of the final product formed due to electron irradiation of the physisorbed $Co(CO)_3NO$ film is a mixture of metallic cobalt, cobalt oxide and nitride, and adsorbed carbon. A similar evolution was observed when adsorbed $Co(CO)_3NO$ was exposed to X-ray radiation, indicating that the bulk of the decomposition is induced by SEs, rather than the 500 eV PEs [25].

Returning to the gas phase measurements of $Co(CO)_3NO$, a decomposition process dominated by DEA would be expected to proceed through loss of a single CO ligand while DI would occur via a much more complete fragmentation. For an electron energy of 50 eV where the DI cross-sections reach their maximum values, a weighted average loss of slightly above 2 CO ligands is predicted for a DI process. The weighted average is estimated as the sum of the partial cross sections for the individual dissociation channels at 50 eV, multiplied by the number of CO ligands lost in each channel and divided by the total DI cross section at 50 eV. The average CO loss of about 1.5 observed in the surface experiments is therefore intermediate to what would be expected from a DEA- and DI-driven decomposition when considering the existing gas phase data alone. Cleavage of the N=O bond is neither observed in gas phase DEA, nor in DI. This is not surprising, as the BDE of nitric oxide is about 6.5 eV [37] and the activation barrier for the electron-induced formation of a nitride species from gaseous $Co(CO)_3NO$ is likely to be considerable. From comparison of surface and gas phase data it is thus likely that the decomposition observed at surfaces is initiated by a CO loss as proposed by Rosenberg et al. [25], though the gas phase experiments do not allow any clear conjecture on the underlying process (i.e., if the initial CO loss is through DEA or DI). The surface science studies, however, indicate that the decomposition of the unstable intermediate left after the initial CO loss proceeds through a surface-catalyzed conversion of the nitrogen from the nitrosyl group to the nitride species observed, which is consistent with CVD and FEBID from $Co(CO)_3NO$ showing the persistence of nitrogen in the deposits.

In summary for $Co(CO)_3NO$, comparisons of currently available gas phase and surface science studies do not provide a definitive clear-cut answer as to the initial dissociation mechanism, although a combination from both DEA and DI channels seems most likely. However, even this assertion is speculative in the absence of any information on potential ND channels and a detailed analysis of the overlap between the individual DI and DEA channels and the actual SE energy distribution from the surface (which is currently not available).

Finally, it is worthwhile to take a brief look at gas phase and surface studies on the metal carbonyl compound $W(CO)_6$. A recent DEA study of this compound by Wnorowski et al. [16] shows that, again, single CO loss is the most efficient channel and is confined to a fairly narrow energy region below 1 eV incident electron energy. Both the loss of two and three CO units, however, are fairly efficient through DEA and the integral ion yields for these channels are about 50% and 25% of that for a single CO loss, respectively. The loss of four CO units is also observed in DEA, but at higher energies (7–12 eV) and with low intensities (about 2.5% of that for single CO loss). No further fragmentation is observed in DEA to $W(CO)_6$. Dissociative ionization of $W(CO)_6$ is considerably more complex [17]. The loss of one CO (formation of $[W(CO)_5]^+$) has an appearance energy of about 10 eV and the appearance energy for the formation of W^+ (loss of all ligands) is at about 20 eV. The intermediate fragments, $[W(CO)_n]^+$ (n = 1–4), appear at energies between these two fragments. Above 20 eV, the relative cross section for the formation of these cations stays fairly constant, with the formation of W^+ (n = 0) as the most efficient channel and the relative cross section for the loss of one CO at about 50% of that for the W^+ formation. The relative cross sections for the formation of other $[W(CO)_n]^+$ (n = 1–4) are, again, intermediate to these two. Above 20 eV, however, the formation of $[(CO)_nWC]^+$ (n = 0–3) appears, and at about 40 eV the efficiency of these channels is on the same order of magnitude as the respective $[W(CO)_n]^+$ channels. Further, both the doubly charged $[W(CO)_n]^{2+}$ and $[(CO)_nWC]^{2+}$ are also formed above 40 eV, though with efficiencies about an order of magnitude less than for their respective singly-charged species.

Despite the complexity of the DI fragmentation, a rough estimate of the DI average weighted CO loss of approximately 4 can be deduced from these ion yield curves at about 40 eV, where all single ionization channels are close to their maximum. This can be compared to an estimated DEA weighted average CO loss of 2. Thus, for a direct translation of the gas phase data to the surface experiments, considerably less CO loss would be expected for DEA-initiated deposition than for DI-initiated deposition; one would also expect considerable carbide formation via DI.

Similar surface experiments to those described in previous sections (500 eV PEs and Au surface at 160 K) have been conducted by Rosenberg et al. for $W(CO)_6$ [26]. As expected, the mass spectrum of desorbed species upon electron irradiation shows CO as the dominating species. Further, the CO desorption decreases rapidly with increasing electron dose and above a dose of about 1×10^{17} e^-/cm^2 the CO desorption becomes insignificant. Consistent with these findings, XPS data reveals an average loss of 2 CO units for an electron dose of

about 7×10^{16} e^-/cm^2. Above about 7×10^{16} e^-/cm^2, the dominant pathway becomes CO ligand decomposition rather than desorption, and the remaining $W(CO)_n$ is converted to graphitic carbon and a W(VI) oxide. The final deposits were found to consist of tungsten oxides encrusted in a carbonaceous matrix and no signs of carbide formation were observed.

In summary, the surface study revealed a deposition process for $W(CO)_6$ that is similar to the other compounds examined here: a two-step process wherein the first is an electron-induced ligand loss and the second is characterized by decomposition of the remaining ligands. The number of ligands lost in the initial step is close to that observed in DEA rather than in DI and the absence of any carbide formation also favors DEA over DI. However, we stress again that ND is not included in these considerations, and the actual energy distribution of the secondary electrons is not taken into account when comparing the weighted average CO loss in the gas phase experiments.

Conclusion

Here we have compared gas phase and surface data on low energy electron interaction with the common FEBID precursors $MeCpPtMe_3$, $Pt(PF_3)_4$, $Co(CO)_3NO$, and $W(CO)_6$. For $Pt(PF_3)_4$ and $MeCpPtMe_3$, single ligand loss dominates the initial step in their electron-induced decomposition at surfaces. This is also the most efficient DEA fragmentation channel in the gas phase, while DI predominantly leads to more complete fragmentation. Furthermore, in both cases single ligand loss through DEA in the gas phase is essentially exclusively confined to the electron energy range below 1 eV. Hence, an uncritical comparison between the current gas phase and surface data, as discussed here, indicates that the initial electron-induced fragmentation of these precursors is principally through DEA, and is primarily effected through secondary electrons with incident energies below 1 eV.

For the carbonylated precursors $Co(CO)_3NO$ and $W(CO)_6$, deposition is somewhat different. For $Co(CO)_3NO$, the surface studies show an initial average CO loss of about 1.5 ligands upon electron irradiation and essentially no NO loss. In gas phase DEA, the main channel is a single CO loss and the second most efficient channel is the loss of NO, with an absolute cross section that is about 10% of that for the single CO loss. The DEA-induced loss of two CO ligands has an absolute cross section that is about 5% of that for single CO loss. In gas phase DI above 50 eV, the loss of all ligands (formation of Co^+) dominates and the weighted average CO loss above 50 eV is about 2. The weighted average NO loss in gas phase DI is about 0.7. It is therefore clear that, for $Co(CO)_3NO$, neither the gas phase DEA nor the DI results correlate directly with the observed surface results. This is especially true in terms of accounting for the lack of nitrogen loss and the chemical transformation of the nitrogen species in the surface experiments. Indeed, the results obtained for $Co(CO)_3NO$ highlight the potentially important role that the surface can play in modifying the nature of the electron stimulated decomposition step.

For $W(CO)_6$, the surface experiments show an initial CO ligand loss corresponding to an average of about 2. In gas phase DEA, single CO loss dominates below 1 eV, but the integral ion yield for the loss of two CO ligands is significant in the range of 2.5–4.5 eV and the loss of three CO ligands is also appreciable in the energy range of 3–6 eV. The weighted average CO loss through DEA in the gas phase estimated from the ion yield curves is about 2. Similarly to the other compounds, gas phase DI leads to much more extended fragmentation and an estimated average CO loss above about 40 eV is close to 4. Here, we find that the CO loss in the initial deposition step for $W(CO)_6$ suggests DEA as the likely candidate; however, this is not conclusive. It is possible that for $Co(CO)_3NO$ and $W(CO)_6$, deposition is a reflection of both DEA and DI processes.

It is unsurprising that low energy electron-induced decomposition of these organometallic compounds manifests differently when isolated in the gas phase and adsorbed on a surface. As previously mentioned, different relaxation processes are available at the surface and the lifetime of DEA resonances can be affected by polarization interactions with the surface. Furthermore, orientation effects may play a large role when molecules are adsorbed on surfaces – an effect that might explain the lack of NO desorption from $Co(CO)_3NO$ in the surface experiments. Additionally, the electron-induced loss of a single ligand from a precursor molecule may promote further ligand loss through surface interactions and/or chemical conversion of ligands (e.g., NO ligand in $Co(CO)_3NO$), as is evident for all compounds compared here. This may be true even if such destabilization is not observed in the gas phase.

Furthermore, the current comparison is solely based on DEA and DI data from gas phase experiments and no systematic studies on ND cross sections and branching ratios exist. As has been demonstrated for $Pt(PF_3)_4$, the electronically inelastic cross sections can be very high and, in the gas phase, these are likely to relax predominantly through dissociation. Considerable progress is currently being made through quantum mechanical calculations on $Pt(PF_3)_4$, describing the potential energy surfaces for such electronically excited states [44]. These confirm the repulsive nature of the calculated states along a $Pt–PF_3$ bond, indicating at least an initial single ligand loss. The resulting $Pt(PF_3)_3$ fragment may nevertheless contain enough internal energy for more extensive fragmentation, and thus,

without further information on the branching ratios and cross sections for ND, a comparison between gas phase and surface data at this time remains incomplete.

Another major issue is that in the current surface experiments the adsorbed precursor molecules are exposed to electrons with fairly high energy, around 500 eV. The precursor molecules are thereby subjected to interaction with secondary electrons with a broad energy distribution and the energy dependence of individual processes are not manifested on the surface. Rather, these experiments reflect the cross sections for all processes (at the surface) convoluted with the SE energy distribution. This significantly complicates the direct comparison between gas phase and surface science studies.

To address these points, new experimental approaches are needed, most noticeably: a) ones that allow for the exploration of branching ratios and absolute cross sections for ND channels, which are perhaps achievable through a combination of the current crossed electron/molecule beam experiment with post-ionization sources; b) more detailed information on the secondary electron yield from surfaces exposed to electrons, including the surfaces that form as FEBID structures begin to grow; and c) experiments that allow electron energy-dependent studies on deposit formation and ligand desorption from adsorbed precursor molecules at lower energies, that includes the regime from about 0–15 eV (there are already a few laboratories with such setups, but to date their focus has been on other research topics). Moreover, the energy resolution of these electron sources must be sufficient to allow individual DEA resonances to be resolved, while the energy range must also be sufficient to scan through the onset region of DI and ND up to the maximum efficiency of these processes (typically in the regime between 50–70 eV). Our current inability to predict which precursors will react through which dissociation channels also highlights the need for a better theoretical understanding of electron/molecule interactions.

Despite the uncertainties associated with the current comparison, the comparison of gas phase and surface experiments on potential FEBID precursors is clearly an important step on the way to better understanding their initial decomposition mechanisms, illuminating the first step in the deposit formation in FEBID. For example, comparison between gas phase and surface studies has clearly implicated DEA rather than DI as the mechanism responsible for the initial decomposition of two of the precursors studied ($MeCpPtMe_3$and $Pt(PF_3)_4$). This is the kind of information which in turn may aid the targeted design of precursors, whose initial decomposition step promotes further decomposition, and the control of which may thus be essential to optimize their performance.

Acknowledgements

This work was supported by the Icelandic Center of Research (RANNIS) and the University of Iceland Research Fund, and was conducted within the framework of the COST Action CM1301;Chemistry for Electron-Induced Nanofabrication (CELINA). RKTP acknowledges a doctoral grant from the University of Iceland Research Fund and RMT acknowledges a doctoral grant from RANNIS. RKTP and RMT acknowledge financial support from the COST Action CM1301; CELINA, for short term scientific missions (STSMs). DHF thanks the donors of the American Chemical Society Petroleum Research Fund for support of this work (PRF Grant # 54519-ND5).

References

1. Chattopadhyay, S.; Chen, L.-C.; Chen, K.-H. *Crit. Rev. Solid State Mater. Sci.* **2006,** *31,* 15–53. doi:10.1080/10408430600689299
2. Utke, I.; Hoffmann, P.; Melngailis, J. *J. Vac. Sci. Technol., B* **2008,** *26,* 1197. doi:10.1116/1.2955728
3. van Dorp, W. F.; Hagen, C. W. *J. Appl. Phys.* **2008,** *104,* 081301. doi:10.1063/1.2977587
4. Jasinski, J. M.; Meyerson, B. S.; Scott, B. A. *Annu. Rev. Phys. Chem.* **1987,** *38,* 109–140. doi:10.1146/annurev.pc.38.100187.000545
5. Choy, K. L. *Prog. Mater. Sci.* **2003,** *48,* 57–170. doi:10.1016/S0079-6425(01)00009-3
6. Schaefer, J.; Hoelzl, J. *Thin Solid Films* **1972,** *13,* 81–86. doi:10.1016/0040-6090(72)90158-7
7. Schou, J. *Scanning Microsc.* **1988,** *2,* 607.
8. Ohya, K.; Harada, A.; Kawata, J.; Nishimura, K. *Jpn. J. Appl. Phys.* **1996,** *35,* 6226–6232. doi:10.1143/JJAP.35.6226
9. Knights, A. P.; Coleman, P. G. *Appl. Surf. Sci.* **1995,** *85,* 43–48. doi:10.1016/0169-4332(94)00306-8
10. Engmann, S.; Stano, M.; Papp, P.; Brunger, M. J.; Matejčík, Š.; Ingólfsson, O. *J. Chem. Phys.* **2013,** *138,* 044305. doi:10.1063/1.4776756
11. Silvis-Cividjian, N.; Hagen, C. W.; Leunissen, L. H. A.; Kruit, P. *Microelectron. Eng.* **2002,** *61–62,* 693–699. doi:10.1016/S0167-9317(02)00515-4
12. Botman, A.; de Winter, D. A. M.; Mulders, J. J. L. *J. Vac. Sci. Technol., B* **2008,** *26,* 2460–2463. doi:10.1116/1.2976576
13. Allan, M. *J. Chem. Phys.* **2011,** *134,* 204309. doi:10.1063/1.3594206
14. May, O.; Kubala, D.; Allan, M. *Phys. Chem. Chem. Phys.* **2012,** *14,* 2979–2982. doi:10.1039/C2CP23268E
15. Engmann, S.; Stano, M.; Matejčík, Š.; Ingólfsson, O. *Phys. Chem. Chem. Phys.* **2012,** *14,* 14611–14618. doi:10.1039/c2cp42637d
16. Wnorowski, K.; Stano, M.; Matias, C.; Denifl, S.; Barszczewska, W.; Matejčíka, Š. *Rapid Commun. Mass Spectrom.* **2012,** *26,* 2093–2098. doi:10.1002/rcm.6324
17. Wnorowski, K.; Stano, M.; Barszczewska, W.; Jówko, A.; Matejčík, Š. *Int. J. Mass Spectrom.* **2012,** *314,* 42–48. doi:10.1016/j.ijms.2012.02.002
18. Engmann, S.; Ómarsson, B.; Lacko, M.; Stano, M.; Matejčík, Š.; Ingólfsson, O. *J. Chem. Phys.* **2013,** *138,* 234309. doi:10.1063/1.4810877
19. Lacko, M.; Papp, P.; Wnorowski, K.; Matejčík, Š. *Eur. Phys. J. D* **2015,** *69,* 1–9. doi:10.1140/epjd/e2015-50721-8

20. van Dorp, W. F.; Wnuk, J. D.; Gorham, J. M.; Fairbrother, D. H.; Madey, T. E.; Hagen, C. W. *J. Appl. Phys.* **2009,** *106,* 074903. doi:10.1063/1.3225091
21. Wnuk, J. D.; Gorham, J. M.; Rosenberg, S. G.; van Dorp, W. F.; Madey, T. E.; Hagen, C. W.; Fairbrother, D. H. *J. Phys. Chem. C* **2009,** *113,* 2487–2496. doi:10.1021/jp807824c
22. Hammill, C. L.; Clark, R. J.; Ross, C. W.; Marshall, A. G., III; Schmutz, J. *Inorg. Chem.* **1997,** *36,* 5973–5977. doi:10.1021/ic970590a
23. Landheer, K.; Rosenberg, S. G.; Bernau, L.; Swiderek, P.; Utke, I.; Hagen, C. W.; Fairbrother, D. H. *J. Phys. Chem. C* **2011,** *115,* 17452–17463. doi:10.1021/jp204189k
24. Engmann, S.; Stano, M.; Matejčík, Š.; Ingólfsson, O. *Angew. Chem., Int. Ed.* **2011,** *50,* 9475–9477. doi:10.1002/anie.201103234
25. Rosenberg, S. G.; Barclay, M.; Fairbrother, D. H. *J. Phys. Chem. C* **2013,** *117,* 16053–16064. doi:10.1021/jp404905t
26. Rosenberg, S. G.; Barclay, M.; Fairbrother, D. H. *Phys. Chem. Chem. Phys.* **2013,** *15,* 4002–4015. doi:10.1039/c3cp43902j
27. Christophoru, L. G. *Electron-Molecule Interactions and their Applications;* Academic Press: Orlando, FL. U.S.A., 1984; Vol. 1.
28. McConkey, J. W.; Malone, C.; Johnson, P.; Winstead, C.; McKoy, V.; Kanik, I. *Phys. Rep.* **2008,** *466,* 1–103. doi:10.1016/j.physrep.2008.05.001
29. Hotop, H.; Ruf, M.-W.; Allan, M.; Fabrikant, I. I. *Adv. At., Mol., Opt. Phys.* **2003,** *49,* 85–216. doi:10.1016/S1049-250X(03)80004-6
30. Bald, I.; Langer, J.; Tegeder, P.; Ingólfsson, O. *Int. J. Mass Spectrom.* **2008,** *277,* 4–25. doi:10.1016/j.ijms.2008.06.013
31. Arumainayagam, C. R.; Lee, H.-L.; Nelson, R. B.; Haines, D. R.; Gunawardane, R. P. *Surf. Sci. Rep.* **2010,** *65,* 1–44. doi:10.1016/j.surfrep.2009.09.001
32. Böhler, E.; Warneke, J.; Swiderek, P. *Chem. Soc. Rev.* **2013,** *42,* 9219–9231. doi:10.1039/c3cs60180c
33. Wigner, E. P. *Phys. Rev.* **1948,** *73,* 1002. doi:10.1103/PhysRev.73.1002
34. Schramm, A.; Weber, J. M.; Kreil, J.; Klar, D.; Ruf, M.-W.; Hotop, H. *Phys. Rev. Lett.* **1998,** *81,* 778. doi:10.1103/PhysRevLett.81.778
35. Ómarsson, B.; Bjarnason, E. H.; Ingólfsson, O.; Haughey, S.; Field, T. A. *Chem. Phys. Lett.* **2012,** *539–540,* 7–10. doi:10.1016/j.cplett.2012.04.059
36. Ómarsson, B.; Engmann, S.; Ingólfsson, O. *RSC Adv.* **2014,** *4,* 33222. doi:10.1039/C4RA04451G
37. Luo, Y.-R. *Comprehensive handbook of chemical bond energies;* CRC Press: Boca Raton, FL, U.S.A., 2007. doi:10.1201/9781420007282
38. Mauracher, A.; Denifl, S.; Aleem, A.; Wendt, N.; Zappa, F.; Cicman, P.; Probst, M.; Märk, T.; Scheier, P.; Flosadóttir, H.; Ingólfsson, O.; Illenberger, E. *Phys. Chem. Chem. Phys.* **2007,** *9,* 5680–5685. doi:10.1039/b709140k
39. Papp, P.; Urban, J.; Matejčík, Š.; Stano, M.; Ingolfsson, O. *J. Chem. Phys.* **2006,** *125,* 204301. doi:10.1063/1.2400236
40. Bald, I.; Dabkowska, I.; Illenberger, E.; Ingólfsson, O. *Phys. Chem. Chem. Phys.* **2007,** *9,* 2983–2990. doi:10.1039/b702482g
41. Ingólfsson, O.; Weik, F.; Illenberger, E. *Int. Rev. Phys. Chem.* **1996,** *15,* 133–151. doi:10.1080/01442359609353178
42. Tegeder, P.; Lehmann, L.; Ingólfsson, O.; Illenberger, E. *Z. Phys. Chem.* **1996,** *195,* 217–236. doi:10.1524/zpch.1996.195.Part_1_2.217
43. Franz, G. *Low pressure plasmas and microstructuring technology;* Springer: Berlin, Germany, 2009. doi:10.1007/978-3-540-85849-2
44. Zlatar, M. *JAMA, J. Am. Med. Assoc.* **2015,** in press.
45. Massey, S.; Bass, A. D.; Sanche, L. *J. Phys. Chem. C* **2015,** *119,* 12708–12719. doi:10.1021/acs.jpcc.5b02684
46. Matejčik, Š.; Foltin, V.; Stano, M.; Skalný, J. D. *Int. J. Mass Spectrom.* **2003,** *223–224,* 9–19. doi:10.1016/S1387-3806(02)00776-5
47. Dressler, R.; Allan, M. *Chem. Phys.* **1985,** *92,* 449–455. doi:10.1016/0301-0104(85)85038-2
48. Bjarnason, E. H.; Ómarsson, B.; Engmann, S.; Ómarsson, F. H.; Ingólfsson, O. *Eur. Phys. J. D* **2014,** *68,* 1–8. doi:10.1140/epjd/e2014-50091-9
49. Allan, M. *J. Phys. B: At., Mol. Opt. Phys.* **1992,** *25,* 1559. doi:10.1088/0953-4075/25/7/025
50. Ipolyi, I.; Michaelis, W.; Swiderek, P. *Phys. Chem. Chem. Phys.* **2007,** *9,* 180–191. doi:10.1039/B612261B
51. Xue, Z.; Strouse, M. J.; Shuh, D. K.; Knobler, C. B.; Kaesz, H. D.; Hicks, R. F.; Williams, R. S. *J. Am. Chem. Soc.* **1989,** *111,* 8779–8784. doi:10.1021/ja00206a002
52. Yavas, O.; Ochiai, C.; Takai, M.; Hosono, A.; Okuda, S. *Appl. Phys. Lett.* **2000,** *76,* 3319–3321. doi:10.1063/1.126638
53. Yavas, O.; Ochiai, C.; Takai, M.; Park, Y. K.; Lehrer, C.; Lipp, S.; Frey, L.; Ryssel, H.; Hosono, A.; Okuda, S. *J. Vac. Sci. Technol., B* **2000,** *18,* 976–979. doi:10.1116/1.591310
54. Botman, A.; Hesselberth, M.; Mulders, J. J. L. *Microelectron. Eng.* **2008,** *85,* 1139–1142. doi:10.1016/j.mee.2007.12.036
55. Botman, A. P. J. M. Towards high purity nanostructures from electron beam induced deposition of platinum. Ph.D. Thesis, Delft University of Technology, Delft, Netherlands, 2009.
56. Botman, A.; Mulders, J. J. L.; Hagen, C. W. *Nanotechnology* **2009,** *20,* 372001. doi:10.1088/0957-4484/20/37/372001
57. Mehendale, S.; Mulders, J. J. L.; Trompenaars, P. H. F. *Nanotechnology* **2013,** *24,* 145303. doi:10.1088/0957-4484/24/14/145303
58. Villamor, E.; Casanova, F.; Trompenaars, P. H. F.; Mulders, J. J. L. *Nanotechnology* **2015,** *26,* 095303. doi:10.1088/0957-4484/26/9/095303
59. Langford, R. M.; Ozkaya, D.; Sheridan, J.; Chater, R. *Microsc. Microanal.* **2004,** *10,* 1122–1123. doi:10.1017/S1431927604883417
60. Geier, B.; Gspan, C.; Winkler, R.; Schmied, R.; Fowlkes, J. D.; Fitzek, H.; Rauch, S.; Rattenberger, J.; Rack, P. D.; Plank, H. *J. Phys. Chem. C* **2014,** *118,* 14009–14016. doi:10.1021/jp503442b
61. Plank, H.; Noh, J. H.; Fowlkes, J. D.; Lester, K.; Lewis, B. B.; Rack, P. D. *ACS Appl. Mater. Interfaces* **2014,** *6,* 1018–1024. doi:10.1021/am4045458
62. Botman, A.; Mulders, J. J. L.; Weemaes, R.; Mentink, S. *Nanotechnology* **2006,** *17,* 3779. doi:10.1088/0957-4484/17/15/028
63. Mackus, A. J. M.; Mulders, J. J. L.; van de Sanden, M. C. M.; Kessels, W. M. M. *J. Appl. Phys.* **2010,** *107,* 116102. doi:10.1063/1.3431351
64. Stanford, M. G.; Lewis, B. B.; Noh, J. H.; Fowlkes, J. D.; Roberts, N. A.; Plank, H.; Rack, P. D. *ACS Appl. Mater. Interfaces* **2014,** *6,* 21256–21263. doi:10.1021/am506246z
65. Yang, D. S.; Bancroft, G. M.; Puddephatt, R. J.; Tan, K. H.; Cutler, J. N.; Bozek, J. D. *Inorg. Chem.* **1990,** *29,* 4956–4960. doi:10.1021/ic00349a025
66. Shen, J.; Muthukumar, K.; Jeschke, H. O.; Valentí, R. *New J. Phys.* **2012,** *14,* 073040. doi:10.1088/1367-2630/14/7/073040

67. Stein, S. E. Mass Spectra. In *NIST Chemistry WebBook, NIST Standard Reference Database Number 69*; Linstrom, P. J.; Mallard, W. G., Eds.; National Institute of Standards and Technology: Gaithersburg, MD, U.S.A.. http://webbook.nist.gov (accessed on May 18, 2015).
68. Wnuk, J. D.; Rosenberg, S. G.; Gorham, J. M.; van Dorp, W. F.; Hagen, C. W.; Fairbrother, D. H. *Surf. Sci.* **2011,** *605,* 257–266. doi:10.1016/j.susc.2010.10.035
69. Kruck, T.; Baur, K. *Angew. Chem., Int. Ed. Engl.* **1965,** *4,* 521. doi:10.1002/anie.196505211
70. Rand, M. J. *J. Electrochem. Soc.* **1973,** *120,* 686–693. doi:10.1149/1.2403534
71. Barry, J. D.; Ervin, M.; Molstad, J.; Wickenden, A.; Brintlinger, T.; Hoffman, P.; Meingailis, J. *J. Vac. Sci. Technol., B* **2006,** *24,* 3165–3168. doi:10.1116/1.2395962
72. Elbadawi, C.; Toth, M.; Lobo, C. J. *ACS Appl. Mater. Interfaces* **2013,** *5,* 9372–9376. doi:10.1021/am403167d
73. O'Regan, C.; Lee, A.; Holmes, J. D.; Petkov, N.; Trompenaars, P.; Mulders, H. *J. Vac. Sci. Technol., B* **2013,** *31,* 021807. doi:10.1116/1.4794343
74. Friedman, J. F.; Miller, T. M.; Friedman-Schaffer, J. K.; Viggiano, A. A.; Rekha, G. K.; Stevens, A. E. *J. Chem. Phys.* **2008,** *128,* 104303. doi:10.1063/1.2831391
75. Lias, S. G.; Liebman, J. F. Ion Energetics Data. In *NIST Chemistry WebBook, NIST Standard Reference Database Number 69*; Lindstrom, P. J.; Mallard, W. G., Eds.; National Institute of Standards and Technology: Gaithersburg, MD, U.S.A.. http://webbook.nist.gov (accessed on May 19, 2015).
76. Ivanova, A. R.; Nuesca, G.; Chen, X.; Goldberg, C.; Kaloyeros, A. E.; Arkles, B.; Sullivan, J. J. *J. Electrochem. Soc.* **1999,** *146,* 2139–2145. doi:10.1149/1.1391904
77. Lane, P. A.; Oliver, P. E.; Wright, P. J.; Reeves, C. L.; Pitt, A. D.; Cockayne, B. *Chem. Vap. Deposition* **1998,** *4,* 183–186. doi:10.1002/(SICI)1521-3862(199810)04:05<183::AID-CVDE183>3.0.CO;2-M
78. Crawford, N. R. M.; Knutsen, J. S.; Yang, K.-A.; Haugstad, G.; McKernan, S.; McCormick, F. B.; Gladfelter, W. L. *Chem. Vap. Deposition* **1998,** *4,* 181–183. doi:10.1002/(SICI)1521-3862(199810)04:05<181::AID-CVDE181>3.0.CO;2-U
79. Gilmont, P.; Blanchard, A. A.; Mason, C. M.; Barnard, R. L. Dicobalt Octacarbonyl, Cobalt Nitrosyl Tricarbonyl, and Cobalt Tetracarbomyl Hydride. In *Inorganic Syntheses;* Fernelius, W. C., Ed.; John Wiley & Sons: Hoboken, NJ, U.S.A., 1946; Vol. 2, pp 240 ff. doi:10.1002/9780470132333.ch76
80. Mulders, J. J. L.; Belova, L. M.; Riazanova, A. *Nanotechnology* **2011,** *22,* 055302. doi:10.1088/0957-4484/22/5/055302
81. Gazzadi, G. C.; Mulders, J. J. L.; Trompenaars, P.; Ghirri, A.; Rota, A.; Affronte, M.; Frabboni, S. *Microelectron. Eng.* **2011,** *88,* 1955–1958. doi:10.1016/j.mee.2010.12.031
82. Gazzadi, G. C.; Mulders, H.; Trompenaars, P.; Ghirri, A.; Affronte, M.; Grillo, V.; Frabboni, S. *J. Phys. Chem. C* **2011,** *115,* 19606–19611. doi:10.1021/jp206562h
83. Vollnhals, F.; Drost, M.; Tu, F.; Carrasco, E.; Späth, A.; Fink, R. H.; Steinrück, H.-P.; Marbach, H. *Beilstein J. Nanotechnol.* **2014,** *5,* 1175–1185. doi:10.3762/bjnano.5.129
84. Begun, E.; Dobrovolskiy, O. V.; Kompaniiets, M.; Sachser, R.; Gspan, C.; Plank, H.; Huth, M. *Nanotechnology* **2015,** *26,* 075301. doi:10.1088/0957-4484/26/7/075301
85. Papp, P.; Engmann, S.; Kučera, M.; Stano, M.; Matejčík, Š.; Ingólfsson, O. *Int. J. Mass Spectrom.* **2013,** *356,* 24–32. doi:10.1016/j.ijms.2013.09.011

License and Terms

Article II

Computational study of dissociative electron attachment to π-allyl ruthenium (II) tricarbonyl bromide

Rachel M. Thorman, Ragnar Bjornsson, and Oddur Ingólfsson

Eur. Phys. J. D (2016) 70: 164

Rachel Thorman performed all computational work and analysis, under the expertise of Dr. Ragnar Björnsson. She wrote the first draft of the manuscript and contributed to editing. She also performed all experimental work and analysis to which the computational work is compared, under the expertise of Prof. Oddur Ingólfsson.

Eur. Phys. J. D (2016) 70: 164
DOI: 10.1140/epjd/e2016-70166-9

THE EUROPEAN PHYSICAL JOURNAL D

Regular Article

Computational study of dissociative electron attachment to π-allyl ruthenium (II) tricarbonyl bromide*

Rachel M. Thorman, Ragnar Bjornsson[a], and Oddur Ingólfsson[b]

Science Institute and Department of Chemistry, University of Iceland, Dunhagi 3, 107 Reykjavík, Iceland

Received 4 March 2016 / Received in final form 7 June 2016
Published online 30 August 2016 –

Abstract. Motivated by the current interest in low energy electron induced fragmentation of organometallic complexes in focused electron beam induced deposition (FEBID) we have evaluated different theoretical protocols for the calculation of thermochemical threshold energies for DEA to the organometallic complex π-allyl ruthenium (II) tricarbonyl bromide. Several different computational methods including density functional theory (DFT), hybrid-DFT and coupled cluster were evaluated for their ability to predict these threshold energies and compared with the respective experimental values. Density functional theory and hybrid DFT methods were surprisingly found to have poor reliability in the modelling of several DEA reactions; however, the coupled cluster method LPNO-pCCSD/2a was found to produce much more accurate results. Using the local correlation pair natural orbital (LPNO) methodology, high level coupled cluster calculations for open-shell systems of this size are now affordable, paving the way for reliable theoretical DEA predictions of such compounds.

1 Introduction

Focused electron beam induced deposition (FEBID) is a nanofabrication technique used to directly write three-dimensional nanostructures of nearly any geometry on three-dimensional surfaces [1,2]. In FEBID, a focused high-energy electron beam impinges upon a target surface within a high vacuum chamber with a partial pressure of a precursor gas. Ideally, electron-driven reactions with these precursor molecules, which are commonly organometallics, result in controlled deposition of, e.g., the target metal under the area of the primary electron beam while undesirable ligands are pumped off [1,2].

The interaction of a primary electron beam with a surface, however, produces backscattered and secondary electrons of a wide range of energies, with a substantial number of the secondary electrons having energies close to 0 eV [3,4]. These low-energy secondary electrons may be significantly more plentiful at the interaction surface than primary electrons [1,5]. Further, scattering of the primary electrons leads to production of secondary electrons both within and outside the area of the primary electron beam, potentially leading to poor resolution for FEBID structures [1]. Low-energy secondary electrons are also known to be the primary drivers of deposition for several FEBID precursors [5–7]. Thus, to produce high purity, high resolution nanostructures using FEBID, the interaction of low-energy electrons with FEBID precursors must be well understood. Motivated by this notion the first gas phase studies specifically aimed at characterizing the interaction of low energy electrons with FEBID precursor molecules were conducted in 2011 and 2012 [8–12].

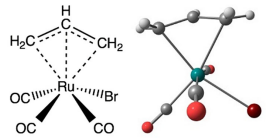

Fig. 1. π-allyl ruthenium (II) tricarbonyl bromide.

In this contribution we compare different theoretical approaches to the calculation of thermochemical threshold energies for DEA to the organometallic precursor π-allyl ruthenium (II) tricarbonyl bromide (π-$(C_3H_5)Ru(CO)_3Br$, see Fig. 1) with the aim of establishing a theoretical protocol for reliable theoretical DEA predictions for such compounds. In DEA, which is a resonant process, a low-energy electron (generally below 10 eV) attaches to a molecule, producing a transient negative ion (TNI) (see e.g. Ref. [13]). Relaxation of this TNI can result in dissociation, producing one negative

* Contribution to the Topical Issue "Advances in Positron and Electron Scattering", edited by Paulo Limao-Vieira, Gustavo Garcia, E. Krishnakumar, James Sullivan, Hajime Tanuma and Zoran Petrovic.

[a] e-mail: ragnarbj@hi.is
[b] e-mail: oddur@hi.is

ion fragment detectable via mass spectrometry and one or more neutral fragments, as shown in reaction (1):

$$AB + e^- \rightarrow AB^{(\ddagger)-} \rightarrow A^{(\ddagger)-} + B^{(\ddagger)}. \quad (1)$$

In this context, ‡ indicates that both the TNI and fragments produced may be in an electronically and/or vibrationally excited state. For a single bond rupture, the threshold energy ($E_{\rm th}$) of DEA reactions can be expressed as the bond dissociation energy (BDE) of the relevant bond (A-B in reaction (1)) less the electron affinity (EA) of the charge-retaining fragment:

$$E_{\rm th} = BDE\,(\text{A-B}) - EA\,(\text{A})\,. \quad (2)$$

However DEA reaction channels producing negative ion fragments are commonly seen well above their threshold energy. This is due to the resonant nature of the DEA process – TNIs must be formed in the region of Franck-Condon overlap between the potential energy surfaces of the parent molecule and the respective TNI (see e.g. Ref. [13]). Consequently negative ion fragments produced in DEA often appear at energies higher than the thermochemical threshold for the respective reaction. The appearance energy (AE) of DEA fragments is thus always at or above the calculated threshold energy ($E_{\rm th}$) of the reaction.

$$AE = E_{\rm th} + E^*. \quad (3)$$

For cases where the AE is higher than $E_{\rm th}$ the excess energy (E^*) will appear as electronic vibrational, rotational or translational energy of the fragments formed.

Dissociative electron attachment to π-allyl ruthenium tricarbonyl bromide is characterized by two main channels: the loss of 1–3 CO and the loss of the allyl group accompanied by the loss of 0–3 CO. In addition, the formation of Br^- is observed but with low intensity [14]. In the current contribution, several different computational methods are used to predict threshold energies for these processes and these are compared with the experimental appearance energies. Here we have used BP86 [15,16] (a DFT method based on the generalized gradient approximation (GGA) and PBE0 (a hybrid-GGA functional) [17,18] as well as the wave function-based method pCCSD/2a [19,20] in conjunction with the local pair natural orbital (LPNO) methodology [21].

2 Methods

2.1 Quantum chemical calculations

All calculations were performed using ORCA [22]. All structures were optimized at the BP86/def2-TZVP level of theory (using the def2 effective core potential [23] for bromine and ruthenium core electrons), including the D3(BJ) dispersion correction by Grimme et al. [24,25]. Harmonic vibrational frequencies were also calculated at this level that were used to derive zero point vibrational energy and thermal energy corrections. Single-point energy calculations were then performed on the BP86 optimized geometries with other methods. Cartesian coordinates of molecule and fragments are given as supplementary information. The single-point energy calculations using GGA and hybrid-GGA functionals were performed as all-electron calculations (no ECP) using the scalar relativistic approximation ZORA [26,27] and relativistically recontracted versions of def2-TZVPP and def2-QZVPP [23,28]. Coupled cluster calculations were performed at the LPNO-pCCSD/2a level of theory, using the correlation-consistent basis sets and accompanying ECPs (for Ru and Br) [29–32]: aug-cc-pVTZ(-PP). Quasi-restricted orbitals [33] were used as a reference in the coupled cluster calculations, which reduces spin contamination from the UHF step.

2.2 Experimental

Dissociative electron attachment experiments were performed on a crossed electron/molecule beam setup under single collision conditions, as detailed in reference [34]. A brief description is given here. A trochoidal electron monochromator is used to generate an electron beam with an energy resolution in the range of 110–140 meV (due to deposition of the compound on the monochromator lenses, the resolution degrades during extended experiments). The electron beam is crossed with an effusive beam of the target gas. The target gas is generated by sublimation of the solid π-$(C_3H_5)Ru(CO)_3Br$ sample into the reaction chamber through a capillary tube. The sample is sublimated at room temperature (approximately 298 K) in order to maintain a working pressure of $4–6 \times 10^{-7}$ mbar. To prevent adhesion of the compound to the monochromator and extraction lenses, the chamber temperature is held at about 393 K. A weak electric field is used to extract negative ions formed in the collision region of the reaction chamber, which are then analysed by quadrupole mass spectrometry. The well-studied SF_6^-/SF_6 ion yield at 0 eV was used to calibrate the electron beam energy and determine its energy resolution (the FWHM of the SF_6^- yield). Appearance energies for each measured ion were determined by a simple linear extrapolation from the rising side of the ion yield to the base line. This approach does not, however, represent a physically meaningful interpretation of the onset region of the negative ion formation in DEA and should not be taken as such. Based on both visual inspection and variation between similar data sets, these values are estimated to be accurate within ±0.2 eV.

3 Results and discussion

3.1 DEA threshold energies

DEA to π-allyl ruthenium tricarbonyl bromide produces eight ionic fragments detectable by mass spectrometry at m/Z = 278, 265, 250, 237, 79, 222, 209, and 181. These masses were assigned to the negative ions $[\pi\text{-}(C_3H_5)Ru(CO)_2Br]^-$, $[Ru(CO)_3Br]^-$, $[\pi\text{-}(C_3H_5)Ru(CO)Br]^-$, $[Ru(CO)_2Br]^-$, Br^-, $[\pi\text{-}(C_3H_5)RuBr]^-$, $[Ru(CO)Br]^-$,

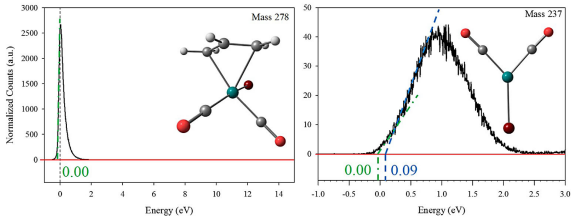

Fig. 2. Ionic yields of $m/Z = 278$ (M-1CO) and 237 (M-1CO-allyl), with calculated structures shown for each. Green lines on the graphs show the lower bound of the appearance energy, while blue lines on the graphs show the upper bound. These upper and lower boundaries were determined by visually fitting a line to the onset region and determining its intercept with the base line (red). Appearance energies were determined by fitting a selected section of the rising edge of the data with a linear regression, noted with a black arrow on Mass 237; when compared to these upper and lower boundaries, we estimate these to be accurate within ±0.2 eV. The onset of ion yields below 0 eV (e.g. Mass 278) reflects the instrumental electron energy resolution, placing the AEs for the respective processes at 0 eV.

Table 1. BP86/def2-TZVP and LPNO-pCCSD/2a/aug-cc-pVTZ calculated threshold energies (eV) compared with experimental appearance energies of eight ionic fragments.

Fragment	Appearance energy (eV)	BP86/def2-TZVP	LPNO-pCCSD/ 2a/aug-cc-pVTZ
M-1CO	0.00	−1.34	−1.36
M-1CO-allyl	0.07	0.35	0.16
M-2CO	0.00	0.51	0.07
M-2CO-allyl	2.98	3.82	2.45
M-3CO	2.91	2.88	1.73
M-3CO-allyl	7.61	7.19	5.51
M-allyl	0.00	−1.30	−0.91
M-Br	0.00	−0.71	−0.76

and $[RuBr]^-$, respectively. This represents a sequential CO loss $[M - nCO]^-$ with $n = 1$–3, the loss of the allyl group also accompanied by a sequential CO loss $[M - allyl - mCO]^-$ with $m = 0$–3 and the loss of the bromide ion [M – Br]. Single CO loss is the dominant channel, and the allyl loss is about 1/4 of this signal. Both channels appear at about 0 eV, while the additional loss of one CO from these channels is about 20 times less intense than the respective single CO and allyl loss. Bromine formation (Br^-) is also observed close to 0 eV, but the intensity of this signal is two orders of magnitude less than that for single CO loss. Further CO loss is observed with low intensity, but the bare ruthenium anion is not detected. A detailed discussion of these channels in context to previous surface science studies [35] and the potential influence of the ligand structure on precursor performance in FEBID will be offered separately [14].

Experimental appearance energies were determined by fitting a selected section of the rising edge of the data with a linear regression. These were compared with upper and lower boundaries which were determined by visually fitting a line to the onset region and determining its intercept with the base line, examples of which can be seen in Figure 2; from visual judgment and the variation between calculated appearance energies and the upper and lower boundaries as noted by the green and blue dashed lines shown in Figure 2, we estimate these to be accurate within ±0.2 eV. The onset of ion yields below 0 eV reflects the instrumental electron energy resolution, placing the AEs for the respective processes at 0 eV.

All calculated threshold values include a zero point energy contribution calculated from BP86/def2-TZVP harmonic vibrational frequencies and a thermal energy contribution of 0.37 eV. The latter was calculated using the estimated thermal energy of the neutral molecule (from harmonic vibrational, rotational and translational contributions) at room temperature (298 K).

Table 1 compares the experimentally determined AEs with the thermally and zero point energy corrected threshold energies calculated using the BP86 DFT functional and the def2-TZVP basis set. BP86 is a GGA functional commonly used in the organometallic and inorganic chemistry community, and both BP86 and the hybrid-GGA PBE0 functional have been found to give very reliable structures of transition metal complexes [36–38]. Furthermore, in thermochemical benchmarking studies on

Table 2. Comparison of computational methods and basis sets with experimentally determined appearance energies.

Fragment	Appearance Energy (eV)	BP86/ def2-TZVP	BP86/ma-ZORA-def2-TZVPP	BP86/ma-ZORA-def2-QZVPP	PBE0/ma-ZORA-def2-TZVPP	LPNO-pCCSD/ 2a/aug-cc-pVTZ
M-2CO	0.00	0.51	0.68	0.67	0.63	0.07
M-1CO-allyl	0.07	0.35	0.44	0.42	0.53	0.16
M-3CO	2.91	2.88	3.23	3.15	2.75	1.73
M-2CO-allyl	2.98	3.82	3.99	3.93	4.80	2.45

transition metal compounds, PBE0 is often among the best performers [39–41]. As each of these fragments anions has been experimentally observed, they can necessarily be assumed to have positive electron affinities and this was confirmed by calculations. All fragments geometrically optimized via the BP86 functional were confirmed to have positive vibrational frequencies. Further, potential alternate isomers and spin states were investigated in order to ensure that the lowest energy state was indeed determined for each fragment. Interestingly, the triplet states of the metal-containing fragments $[M - 2CO - allyl]^-$ and $[M - 3CO - allyl]^-$ were found to be lower in energy than their respective singlet states. For the loss of one CO and subsequent formation of $[M - 1CO]^-$, the threshold value predicted by BP86/def2-TZVP is below the experimental appearance energy, as it must be; this is also the case for $[M - allyl]^-$, $[M - 3CO]^-$, $[M - 3CO - allyl]^-$ and $[M - Br]^-$. However, the BP86 threshold energies for the formation of $[M - 1CO - allyl]^-$, $[M - 2CO]^-$, and $[M - 2CO - allyl]^-$ are all computed to be considerably higher in energy than the experimental appearance energies, a clear inconsistency between theory and experiment.

A comparison of different quantum chemical methods was therefore undertaken using these fragments and $[M - 3CO]^-$ to see whether the inconsistent results were due to basis set incompleteness, error due to the use of effective core potentials (ECPs), whether a hybrid-GGA functional (PBE0) would perform better or whether a coupled cluster method would give a better description of the thermochemistry. This comparison is shown in Table 2. When switching from using ECPs (BP86/def2-TZVP level of theory) to all-electron relativistic ZORA calculations (BP86/ma-ZORA-def2-TZVPP) and with even larger basis sets (BP86/ma-ZORA-def2-QZVPP), we see that the BP86 results do not improve. On the contrary, the inconsistency between the BP86 computed thresholds and the experimental AEs becomes even more severe. This is the case for all these fragments, with the BP86/ma-ZORA-def2-QZVPP computed threshold of the $[M - 2CO - allyl]^-$ fragment being a whole 1 eV higher than the experimental AE.

When switching to a hybrid-GGA functional (PBE0; also performed with the all-electron relativistic ZORA method and the ma-ZORA-def2-TZVPP basis set) the disagreement with the experimental AEs is generally larger than at the BP86/def2-TZVP level of theory. Most extreme is the formation of $[M - 2CO - allyl]^-$ fragment, which computed threshold value, increases from 3.82 eV with BP86/def2-TZVP to 4.80 eV with PBE0, hence 1.82 eV higher than the experimental AE. An exception from this trend is the PBE0 threshold for the formation of $[M - 3CO]^-$ which is below the experimental AE and even slightly lower than the BP86/def2-TZVP value. Clearly the thermochemistry of the DEA processes involving this compound present considerable challenges to density functional theory approximations.

Finally, the coupled cluster method LPNO-pCCSD/2a was used to calculate these energy thresholds using the aug-cc-pVTZ basis set. The pCCSD/2a method is a parameterized coupled cluster method at the singles doubles level that was found in extensive thermochemical benchmarking to give results very close to CCSD(T), the gold standard of quantum chemistry [20]. For completeness, the threshold values for all 8 fragments were computed at the LPNO-pCCSD/2a level of theory and are listed in Table 1 along with the experimental AEs and the BP86/def2-TZVP values. For comparison with the different BP86 approaches and with PBE0, the relevant LPNO-pCCSD/2a values are also listed in Table 2. While the GGA-DFT and hybrid-DFT approaches were all found to overestimate the threshold energies to a similar extent, LPNO-pCCSD/2a was found to give results in good agreement with the experimental AEs, i.e., being either lower than the AEs or at most 0.1 eV higher.

Figure 3 shows a schematic energy diagram of the calculated energies of all fragments at the LPNO-pCCSD/2a/aug-cc-pVTZ level of theory along with the structure of the respective fragments optimized at the BP86 level of theory. Experimental AEs and calculated energy thresholds at the BP86/def2-TZVP level of theory are also shown for comparison. Consistent with our experimental observations, there is an increased thermodynamic threshold for multiple ligand loss via DEA and these thresholds are well reproduced, only at the LPNO-pCCSD/2a/aug-cc-pVTZ level of theory.

3.2 Geometric analysis, spin densities and molecular orbitals

The dominant pathway in DEA to π-allyl ruthenium tricarbonyl bromide is single carbonyl loss followed by allyl loss. Experimentally determined DEA relative ion yields are summarized in Table 3. Bromide loss was not a significant reaction pathway, which is interesting given the comparatively high electron affinity of bromine (3.36 eV) [42]. Analysis of the spin density and the singly occupied molecular orbital (SOMO) was thus undertaken in an attempt

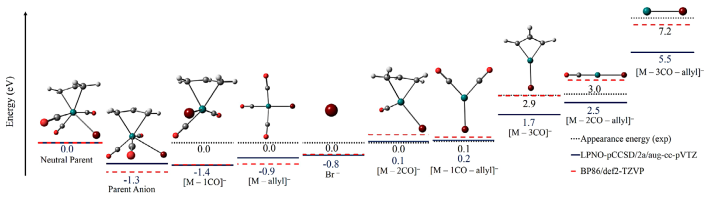

Fig. 3. Schematic of calculated DEA energies of experimentally observed fragments, calculated at the LPNO-pCCSD/2a/aug-cc-pVTZ and BP86/def2-TZVP levels of theory. The black dotted line indicates the appearance energy, while the blue solid line indicates the calculated threshold at the LPNO-pCCSD/2a/aug-cc-pVTZ level of theory and the red dashed line indicates the calculated threshold at the BP86/def2-TZVP level of theory.

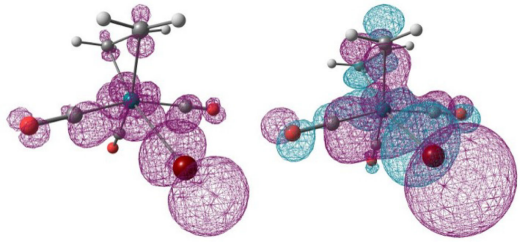

Fig. 4. Spin density isosurface (left) and SOMO isosurface (right) of π-allyl ruthenium tricarbonyl bromide anion, calculated with a contour value of 0.025000.

Table 3. Summary of DEA relative ion yield intensities.

Fragment	m/z	DEA rel. intensity
$[\pi\text{-}C_3H_5Ru(CO)_2Br]^-$	278	100.0
$[Ru(CO)_3Br]^-$	265	27.4
$[\pi\text{-}C_3H_5Ru(CO)Br]^-$	250	5.2
$[Ru(CO)_2Br]^-$	237	1.7
$[\pi\text{-}C_3H_5RuBr]^-$	222	0.1
$[Ru(CO)Br]^-$	209	0.3
$[RuBr]^-$	181	0.03
Br^-	79	0.9

Table 4. Summary of bond lengths of π-allyl ruthenium (II) tricarbonyl bromide before and after electron attachment.

Bond	Neutral molecule bond length (Å)	Anion bond length (Å)
Ru-Br	2.59	3.14
Ru-CO (1)	1.97	1.96
Ru-CO (2)	1.91	1.89
Ru-CO (3)	1.95	1.96
Ru-CH_2 (1)	2.27	2.34
Ru-CH_2 (2)	2.35	2.33
Ru-CH	2.24	2.25

to deduce information on the primary location of the electron in the relaxed structure of the parent anion, and to infer some information on the role of various ligands in the DEA process. Electron attachment to π-allyl ruthenium tricarbonyl bromide results in a lengthening of the Ru-Br bond (bond lengths for the relaxed anionic and neutral ground state structures are summarized in Tab. 4), but all other ligand bond lengths are practically the same in the neutral and anionic structure. Based on analysis of the spin density and the SOMO (Fig. 4), the excess electron appears to reside in an orbital centred largely on the central ruthenium atom, with a strong ruthenium d-orbital character. The SOMO appears to be bonding in nature along two Ru-CO bonds (denoted as Ru-CO (1) and Ru-CO (3) in Tab. 4), non-bonding along the third Ru-CO bond (Ru-CO (2)), and antibonding along the Ru-Br bond. This results in a relatively unchanged Ru-CO bond length, while the Ru-Br bond is significantly lengthened. The electron density of the added electron in this anion is mainly on the central ruthenium atom, resulting in the experimentally observed anionic fragments

tending to also be ruthenium-centred fragments. Due to the antibonding nature of the Ru-Br bond in the anion, and the aforementioned electron affinity of Br, we would have expected to see Br^- as a more prominent channel in our experiments; however, as seen in Figure 3, the calculated thresholds for the two most abundant fragments ($[M - 1CO]^-$ and $[M - allyl]^-$) are lower in energy than those of Br^-. This suggests that significant stability is afforded by the presence of Br in the ruthenium-centred fragment anions, which is supported by the electron spin density retained by Br both in the molecular anion and in the Br-containing fragment anions. This is not necessarily the case for all other fragments; where these are higher in intensity than the Br^- formation, kinetic considerations are likely to be more significant than thermodynamics.

4 Conclusions

Quantum chemical calculations were performed for DEA reactions to π-allyl ruthenium (II) tricarbonyl bromide, an organometallic molecule under consideration for use in FEBID. The calculated threshold values are compared to experimentally determined appearance energies, and of the different methods used to perform these calculations – which included GGA and hybrid-GGA DFT functionals, and coupled cluster methods – only the LPNO-pCCSD/2a method gave results in accordance with the measured appearance energies for all fragments. Recent developments in local correlation coupled cluster methods are thus allowing modelling of DEA reactions to go beyond the limited accuracy of DFT methods. CCSD-based methods formally scale as N^6 (or N^7 as in CCSD(T), the gold standard of quantum chemistry) and are thus often too expensive to be used in general computational chemistry research. Use of local pair natural orbital (LPNO) methodology reduces the scaling of the method allowing such calculations to be carried out with dramatically reduced computational cost. Recent DLPNO methodology approaches linear scaling of such calculations [43] but is not yet available for open-shell compounds.

This bodes well for future calculations of reaction energies in DEA to small, metal-centred molecules. Examination of the molecular anion's spin density, as well as its SOMO, sheds some light on the electron-induced dissociation of π-allyl ruthenium tricarbonyl bromide; however, this information does not offer a complete picture of the dissociation dynamics observed in our experiments. The spin densities and SOMOs of molecular anions must be examined in conjunction with calculated DEA thresholds of fragment anions in order to gain a better understanding of a molecule's potential performance in FEBID.

It is a pleasure to contribute to this special issue in honour of Michael Allan and Steve Buckman. Michael Allan has contributed significantly to our understanding of fundamental processes in low energy electron-molecule interaction and Steve Buckman has likewise contributed significantly to our understanding of analogous positron interactions. Michael Allan's and Steve Buckman's impact on the electron and positron community is also substantial and has taught us that science can be simultaneously intellectually stimulating and socially rewarding. OI extends his thanks to both Michael Allan and Steve Buckman for their hospitality during his visits at their research groups. This work was supported by the Icelandic Center of Research (RANNIS), Grant No. 13049305(1-3), and the University of Iceland Research Fund, and was conducted within the framework of the COST Action CM1301; Chemistry for ELectron-Induced Nanofabrication (CELINA). RMT acknowledges financial support from the COST Action CM1301; CELINA for short term scientific mission (STSM). RB acknowledges support from the Icelandic Research Fund, Grant No. 141218051.

References

1. I. Utke, P. Hoffmann, J. Melngailis, J. Vaccum Sci. Technol. B **26**, 1197 (2008)
2. W.F. van Dorp, C.W. Hagen, J. Appl. Phys. **104**, 081301 (2008)
3. J. Schaefer, J. Hoelzl, Thin Solid Films **13**, 81 (1972)
4. A.P. Knights, P.G. Coleman, Appl. Surf. Sci. **85**, 43 (1995)
5. N. Silvis-Cividjian, C.W. Hagen, L.H.A. Leunissen, P. Kruit, Microelectron. Eng. **61-62**, 693–699 (2002)
6. A. Botman, D.A.M. de Winter, J.J.L. Mulders, J. Vaccum Sci. Technol. B **26**, 2460 (2008)
7. R.M. Thorman, T.P. Kumar, R., D.H. Fairbrother, O. Ingólfsson, Beilstein J. Nanotechnol. **6**, 1904 (2015)
8. O. May, D. Kubala, M. Allan, Phys. Chem. Chem. Phys. **14**, 2979 (2012)
9. M. Allan, J. Chem. Phys. **134**, 204309 (2011)
10. S. Engmann, M. Stano, Š. Matejčík, O. Ingólfsson, Phys. Chem. Chem. Phys. **14**, 14611 (2012)
11. S. Engmann, M. Stano, Š. Matejčík, O. Ingólfsson, Angew. Chem. Int. Ed. Engl. **50**, 9475 (2011)
12. S. Engmann, M. Stano, P. Papp, M.J. Brunger, Š. Matejčík, O. Ingólfsson, J. Chem. Phys. **138**, 044305 (2013)
13. I. Bald, J. Langer, P. Tegeder, O. Ingólfsson, Int. J. Mass Spectrom. **277**, 4 (2008)
14. R.M. Thorman, J.A. Brannaka, L. McElwee-White, O. Ingólfsson (in preparation)
15. A.D. Becke, Phys. Rev. A **38**, 3098 (1988)
16. J.P. Perdew, Phys. Rev. B **33**, 8822 (1986)
17. J.P. Perdew, K. Burke, M. Ernzerhof, Phys. Rev. Lett. **77**, 3865 (1996)
18. C. Adamo, V. Barone, J. Chem. Phys. **110**, 6158 (1999)
19. L.M.J. Huntington, M. Nooijen, J. Chem. Phys. **133**, 184109 (2010)
20. L.M.J. Huntington, A. Hansen, F. Neese, M. Nooijen, J. Chem. Phys. **136**, 064101 (2012)
21. F. Neese, A. Hansen, D.G. Liakos, J. Chem. Phys. **131**, 064103 (2009)
22. F. Neese, WIREs Comput. Mol. Sci. **2**, 73 (2012)
23. F. Weigend, R. Ahlrichs, Phys. Chem. Chem. Phys. **7**, 3297 (2005)
24. S. Grimme, J. Antony, S. Ehrlich, H. Krieg, J. Chem. Phys. **132**, 154104 (2010)
25. S. Grimme, S. Ehrlich, L. Goerigk, J. Comput. Chem. **32**, 1456 (2011)
26. E. van Lenthe, E.J. Baerends, J.G. Snijders, J. Chem. Phys. **99**, 4597 (1993)
27. C. van Wüllen, J. Chem. Phys. **109**, 392 (1998)

28. D.A. Pantazis, X.-Y. Chen, C.R. Landis, F. Neese, J. Chem. Theory Comput. **4**, 908 (2008)
29. T.H. Dunning, J. Chem. Phys. **90**, 1007 (1989)
30. R.A. Kendall, T.H. Dunning, R.J. Harrison, J. Chem. Phys. **96**, 6796 (1992)
31. K.A. Peterson, D. Figgen, M. Dolg, H. Stoll, J. Chem. Phys. **126**, 124101 (2007)
32. K.A. Peterson, D. Figgen, E. Goll, H. Stoll, M. Dolg, J. Chem. Phys. **119**, 11113 (2003)
33. F. Neese, J. Am. Chem. Soc. **128**, 10213 (2006)
34. E.H. Bjarnason, B. Ómarsson, S. Engmann, F.H. Ómarsson, O. Ingólfsson, Eur. Phys. J. D **68**, 121 (2014)
35. J.A. Spencer, J.A. Brannaka, M. Barclay, L. McElwee-White, D.H. Fairbrother, J. Phys. Chem. C **119**, 15349 (2015)
36. M. Bühl, H. Kabrede, J. Chem. Theory Comput. **2**, 1282 (2006)
37. M.P. Waller, H. Braun, N. Hojdis, M. Bühl, J. Chem. Theory Comput. **3**, 2234 (2007)
38. M. Bühl, C. Reimann, D.A. Pantazis, T. Bredow, F. Neese, J. Chem. Theory Comput. **4**, 1449 (2008)
39. M.M. Quintal, A. Karton, M.A. Iron, A.D. Boese, J.M. Martin, J. Phys. Chem. A **110**, 709 (2006)
40. C.A. Jiménez-Hoyos, B.G. Janesko, G.E. Scuseria, J. Phys. Chem. A **113**, 11742 (2009)
41. T. Weymuth, E.P.A. Couzijn, P. Chen, M. Reiher, J. Chem. Theory Comput. **10**, 3092 (2014)
42. C. Blondel, P. Cacciani, C. Delsart, R. Trainham, Phys. Rev. A **40**, 3698 (1989)
43. C. Riplinger, P. Pinski, U. Becker, E.F. Valeev, F. Neese, J. Chem. Phys. **144**, 024109 (2016)

Article III

Low energy electron-induced decomposition of (η^3-C_3H_5)$Ru(CO)_3Br$, a potential focused electron beam induced deposition precursor with a heteroleptic ligand set

Rachel M. Thorman, Joseph A. Brannaka, Lisa McElwee-White and Oddur Ingólfsson

Phys.Chem.Chem.Phys., 2017, 19, 13264

Rachel Thorman performed all experimental work and analysis presented in this manuscript, under the expertise of Prof. Oddur Ingólfsson. She also write the first draft of the manuscript and contributed to editing. The studied molecule was synthesized by Joseph A. Brannaka under the expertise of Prof. Lisa McElwee-White.

PCCP

PAPER

View Article Online
View Journal | View Issue

Cite this: *Phys. Chem. Chem. Phys.*, 2017, **19**, 13264

Low energy electron-induced decomposition of $(\eta^3\text{-}C_3H_5)Ru(CO)_3Br$, a potential focused electron beam induced deposition precursor with a heteroleptic ligand set

Rachel M. Thorman,[a] Joseph A. Brannaka,[b] Lisa McElwee-White[b] and Oddur Ingólfsson*[a]

Received 16th March 2017,
Accepted 2nd May 2017

DOI: 10.1039/c7cp01696d

rsc.li/pccp

Here we describe in detail low energy electron induced fragmentation of a potential focused electron beam induced deposition (FEBID) precursor, π-allyl ruthenium tricarbonyl bromide, *i.e.* $(\eta^3\text{-}C_3H_5)Ru(CO)_3Br$, specially designed to allow comparison of the effect of different ligands on the efficiency of low energy electron induced fragmentation of FEBID precursors. Specifically, we discuss the efficiency of dissociative electron attachment (DEA) and dissociative ionization (DI) with respect to electron-induced removal of the allyl, bromide and carbonyl ligands. We place this in perspective with a previous surface study on the same precursor and we propose a design strategy for FEBID precursor molecules to increase their susceptibility towards DEA.

1 Introduction

Focused electron beam induced deposition (FEBID)[1–3] is a nanofabrication technique that utilizes electron-driven reactions and the narrow focus of modern electron beams to direct-write three-dimensional nanostructures with present lateral resolution achievements of up to 3 nm.[4] Gaseous precursor molecules, commonly organometallics for metal deposition, are introduced to a substrate in a high vacuum chamber equipped with an electron beam, typically a scanning electron microscope. The precursor molecules are physisorbed onto the substrate in quasi-equilibrium with the inlet gas stream and are irradiated with a 1–30 keV tightly-focused electron beam. Ideally, electron-initiated reactions will produce pure deposits of the desired composition under the area of the primary electron beam, directly writing nanostructures as the electron beam is rastered across the substrate.

An ideal FEBID precursor will thus dissociate fully and deposit the desired material under the area of the primary electron beam, with little contamination derived from the ligands and minimal deposit broadening. However, this is generally not the case with currently used FEBID precursors. On the contrary, presently used FEBID precursors commonly lead to low purity deposits and deposit broadening is often a multiple of the electron beam diameter.[1,2,5]

High-energy electron irradiation of a surface results in elastic and inelastic scattering of the primary electrons, blurring their spatial distribution and concurrently generating a high flux of low-energy secondary electrons (SEs), the spatial distribution of which reflects that of the scattered primary electrons. These SEs generally range in energy from close to 0 eV to about 100 eV with peak intensity well below 10 eV; for practical purposes, we will refer to electrons with energy between 0 and 100 eV as SEs.[1,6–9] In this energy range, low energy electrons induce fragmentation reactions with FEBID precursors,[10–14] and are in fact the primary driver of the deposit formation.[8,9,14] However, such reactions typically result in incomplete ligand dissociation and may have considerable cross sections.[10–13] They are thus not only the cause of deposit formation but also determine the degree of co-deposition (contamination) in the deposit and its aspect ratio (resolution).

It is therefore important to choose precursors with ligands that will readily detach upon electron bombardment and will remain volatile under deposition conditions. It is further desirable to tailor the precursors in order to better control their reactions with low energy secondary electrons outside the area of the primary electron beam. Ultimately, the study of low-energy electron (LEE) interactions with FEBID precursors is important to understanding the chemistry governing the deposition process in FEBID and, eventually, for the design of future generations of FEBID precursors suitable to achieve the full potential of this emerging nanofabrication technology.

At energies below 100 eV – the range of low-energy secondary electrons – fragmentation can be induced through four distinct

[a] *Science Institute and Department of Chemistry, University of Iceland, Reykjavik, Iceland. E-mail: oddduring@hi.is; Fax: +365 552-8911; Tel: +365 525-4313*
[b] *Department of Chemistry, University of Florida, Gainesville, Florida 32611-7200, USA*

View Article Online
Paper PCCP

processes: Dissociative Ionization (DI), Dissociative Electron Attachment (DEA), Neutral Dissociation (ND) or Dipolar Dissociation (DD), as shown in eqn (1)–(4). Here; (#) denotes that the intermediate and/or final fragment(s) may be in a vibrational and/or electronically excited state and * denotes electronic excitation:

$$AB + e^- \rightarrow AB^{(\#)+} + 2e^- \rightarrow A^{(\#)+} + B^{(\#)} + 2e^- \quad (1)$$

$$AB + e^- \rightarrow AB^{(\#)-} \rightarrow A^{(\#)-} + B^{(\#)} \quad (2)$$

$$AB + e^-(\varepsilon_1) \rightarrow [AB]^* + e^-(\varepsilon_2 < \varepsilon_1) \rightarrow A^{(\#)} + B^{(\#)} \quad (3)$$

$$AB + e^-(\varepsilon_1) \rightarrow [AB]^* + e^-(\varepsilon_2 < \varepsilon_1) \rightarrow A^{(\#)+} + B^{(\#)-} \quad (4)$$

Dissociative ionization (1) leads to a positively charged fragment and one or more radical, neutral fragments. It is a non-resonant process with an onset slightly above the ionization threshold, and the total cross section typically reaches a maximum at around 50–100 eV before gradually decreasing again as energy transfer becomes less efficient with further increase in electron energy. The branching ratio typically shifts to the favour of multiple bond ruptures as the incident electron energy increases. Neutral dissociation (3) through electronic excitation shows threshold behaviour similar to that of DI (1), however, the threshold for this process is defined by the lowest antibonding electron excitations (as long as these are above the dissociation limit of the respective bonds). This produces two or more neutral (generally radical) fragments. Dipolar dissociation (4) proceeds similarly to ND, but this process is generally found to be less efficient than DI and DEA, and also expected to be less efficient than ND. This is generally attributed to the Coulomb interaction between the departing negatively and positively charged fragments. In contrast, dissociative electron attachment (2) is a resonant process, which constitutes the formation of a transient negative ion through electron attachment and subsequent relaxation through dissociation. This process generally occurs over a narrow energy range (on the order of a few meV to a few eV, depending on the nature of the respective resonances) below about 10 eV and is most efficient close to 0 eV incident electron energy. Close to 0 eV, DEA predominantly leads to a specific, single bond rupture and the formation of a stable negative ion fragment and a neutral radical fragment. However, substantial rearrangement reactions with multiple bond ruptures and new bond formations are not uncommon (see, for example, Ómarsson *et al.*).[15,16]

Which of these channels is most efficient and what chemistry is thus initiated at the surface in FEBID will be determined by a convolution of the energy dependence of the cross sections for the individual processes and the energy distribution of the available low energy secondary electrons. It is thus important to understand the role of these processes in the decomposition of potential FEBID precursors to eventually establish design criteria to improve their performance.

Current surface studies on electron induced decomposition of precursor molecules are typically performed with primary electron energies of about 4–500 eV, and in actual FEBID experiments the primary electron energy is typically in the keV range. In these experiments the precursor molecules are thus exposed to a broad distribution of low energy secondary electrons and, through well-controlled surface experiments, have revealed significant information on deposit formation under electron exposure. However, they do not probe the efficiency of individual fragmentation mechanisms. In contrast, while well-controlled gas phase studies reveal the extent and energy dependence of individual processes such as DEA, DI and DD, they neither reflect the actual secondary electron distribution in the FEBID process nor do they reveal the influence of the surface on the decomposition of the respective precursor molecules.

A comparison of gas phase and surface experiments on selected FEBID precursors has partly addressed this.[14] Most noticeably, such comparison for $MeCpPtMe_3$ and $Pt(PF_3)_4$ gives insight into the decomposition of these precursors where DEA leading to a single ligand bond rupture (losing Me or PF_3, respectively) is anticipated to be the initial step. It should, however, be noted that these studies do not address the role of ND, which still remains an open question.

Ligand architecture plays an important role in determining the efficiency of electron-induced dissociation – multicoordinate polyhapto ligands like cyclopentadiene have been found to be persistent,[17,18] while carbonyl ligands are commonly quite labile.[18–22] The comparison of the efficiency of different ligands for electron-induced dissociation is thus valuable in informing the synthesis of new precursors for FEBID. For this purpose, the current study examines π-allyl ruthenium tricarbonyl bromide, a potential FEBID precursor purposely synthesized in order to compare three different ligands that are commonly found in FEBID precursors: a multicoordinate polyhapto π-facial ligand, carbonyls and a halide. By examining the relative cross sections for dissociation of this molecule by DEA and DI, it is possible to determine which ligands are most susceptible to dissociation *via* these channels and thus potentially suitable for FEBID applications. Furthermore, a recent surface science study on this compound offers association of the gas phase channels observed here with the deposit formation at the surface when this molecule is exposed to high-energy (500 eV) electrons.

2 Experimental

Relative cross-sections were measured using the previously-described crossed electron/molecular beam apparatus in Reykjavik.[23] In brief, an effusive molecular beam was generated by subliming π-allyl ruthenium tricarbonyl bromide at room temperature from a stainless steel gas inlet system attached directly to a high-vacuum collision chamber maintained at 120 °C with internal halogen lamps. The heating of the chamber served to prevent sample deposition on the ion extraction and electron monochromator electric lens components. The inlet system was constructed of a 9 mm, capped Swagelok T-fitting separated from the chamber by a quarter turn plug valve. After placing the sample in the bottom cap of the T fitting, and initial evacuation with a rough pump, the valve was carefully opened. This resulted in a sharp initial pressure rise in

the chamber, which dropped gradually to a stable pressure of 6–8 × 10^{-7} mbar. This pressure was stable throughout the measurements as long as a sample was present. The background pressure of the collision chamber was approximately 1 × 10^{-8} mbar when no sample was introduced.

Inside the chamber, the effusive sample beam enters the interaction zone through a stainless steel capillary, where it crosses a well-defined electron beam generated with a trochoidal electron monochromator (TEM).[24] The electron energy was calibrated to the SF_6^- formation from SF_6 at 0 eV and the energy resolution was estimated from the full width at half maximum (FWHM) of the SF_6^- ion yield through this resonance. For the clean instrument, prior to measurements of $(\eta^3\text{-}C_3H_5)Ru(CO)_3Br$, the electron energy resolution was 110–120 meV. However, despite heating, ruthenium deposition onto the TEM lenses resulted in degradation of the resolution to about 160–180 meV during the experiments. Fragment ions were measured with a Hiden EPIC1000 quadrupole mass spectrometer (Hiden Analytical, Warrington UK) equipped with an RF generator operating within a 2–1000 *m*/*z*-range. The π-allyl ruthenium tricarbonyl bromide was prepared as previously described[18] and identified by comparison to literature data.[25,26]

3 Results and discussion

Fig. 1 shows the normalized negative ion yields obtained from DEA to π-allyl ruthenium tricarbonyl bromide between 0 and 15 eV. The negative ion yields were normalized to the pressure of π-allyl ruthenium tricarbonyl bromide present during each measurement and are shown as counts per second at nominal target pressure of 5 × 10^{-7} (see Experimental section). Dissociative electron attachment to this molecule is characterized by two dominant channels: (a) sequential carbonyl loss (shown in Fig. 1(a)) and (b) allyl loss accompanied by sequential carbonyl loss (shown in Fig. 1b). Bromide loss is also observed through Br^- formation (bottom panel in Fig. 1a), though with very low intensity. Hence, the bromide-containing fragment always retains the negative charge.

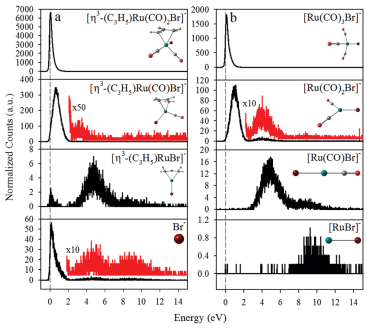

Fig. 1 Normalized negative ion yields for DEA to $(\eta^3\text{-}C_3H_5)Ru(CO)_3Br$ between 0 and 15 eV. Column (a) shows the sequential carbonyl loss channel (1–3 CO) and Br^- formation, while column (b) shows the allyl loss accompanied by sequential carbonyl loss channel (0–3 CO).

Fragments observed at the *m*/*z* ratios 278, 250 and 222 (Fig. 1a) are assigned to single $[M - 1CO]^-$, double $[M - 2CO]^-$ and triple $[M - 3CO]^-$ carbonyl loss, constituting the negative ion fragments $[(\eta^3\text{-}C_3H_5)Ru(CO)_2Br]^-$, $[(\eta^3\text{-}C_3H_5)Ru(CO)Br]^-$ and $[(\eta^3\text{-}C_3H_5)RuBr]^-$, respectively. Fragments observed at the *m*/*z* ratios 265, 237, 209 and 181 (Fig. 1b) are assigned to allyl loss $[M - allyl]^-$, allyl loss accompanied by single carbonyl loss $[M - 1CO - allyl]^-$, allyl and double carbonyl loss $[M - 2CO - allyl]^-$ and allyl and triple carbonyl loss $[M - 3CO - allyl]^-$, respectively. These constitute the fragments $[Ru(CO)_3Br]^-$, $[Ru(CO)_2Br]^-$, $[Ru(CO)Br]^-$ and $[RuBr]^-$, respectively. Finally the fragment observed at the *m*/*z* ratio 79, which is shown in the bottom panel of Fig. 1a, is assigned to the respective isotope of the bromide ion (Br^-). All fragments are clearly identifiable through the characteristic isotope distribution of ruthenium and bromine.

The most intense fragments observed upon DEA to π-allyl ruthenium tricarbonyl bromide are formed through a low energy resonance with a maximum probability for fragment formation at or close to 0 eV. This is as expected, as the electron attachment cross section close to threshold follows an $E^{-1/2}$ energy dependence (see *e.g.* Klar *et al.* and citations therein)[27] and the survival probability of the initially formed transient negative ion is highest close to the crossing point of the potential energy curve describing the initial neutral ground state of the molecule and the respective anionic curve describing the TNI formed.[28] The prerequisite here is that the respective dissociation channel must be thermochemically accessible at these low energies. All observed single ligand loss DEA channels, *i.e.* the formation of $[M - 1CO]^-$, $[M - allyl]^-$ and Br^-, appear with a maximum ion yield at 0 eV incident electron energy. This is in good agreement with a recent theoretical study, which placed the threshold for these single ligand loss channels at the LPNO-pCCSD/2a coupled cluster level of theory at −1.36, −0.91 and −0.76 eV respectively.[29] All single ligand loss reaction channels were thus found to be exothermic, with the most prominent channel observed experimentally, single carbonyl loss, as the most exothermic channel. While the bromide ion was *a priori* expected to be a very favourable leaving group due to the high electron affinity of bromine, it was found computationally to be the least exothermic single ligand loss channel.[29] In fact, it is by orders of magnitude the least effective single ligand loss channel at 0 eV incident electron energy. However, in the theoretical study,[29] bromine was found to retain a significant fraction of the electron spin density within the bromide-containing fragment anions, suggesting that it contributes to their stabilization through the increase of the respective electron affinities of the charge-retaining fragments. This then provides necessary energy for the respective channels to be thermochemically accessible.

In general, the threshold for a given DEA process is given by the sum of the bond dissociation energies (BDE) of the bonds

broken less the electron affinity (EA) of the charge-retaining fragment and the sum of the BDEs of the new bonds formed:

$$E_{\mathrm{th}}([\mathrm{P}-\mathrm{X}]^-) \approx \Delta H_{\mathrm{rxn}} = \sum_{i}^{N} \mathrm{BDE}(\mathrm{educt}) - \mathrm{EA}[\mathrm{P}-\mathrm{X}] - \sum_{j}^{M} \mathrm{BDE}(\mathrm{product}) \quad (5)$$

As DEA is by orders of magnitude most efficient at low incident electron energies, *i.e.* close to 0 eV, moving the threshold of the more extensive DEA channels below 0 eV is a viable approach to increase the extent of fragmentation through this channel.

This is apparent for the double ligand loss channels: double carbonyl loss and allyl loss accompanied by a single carbonyl loss were calculated to be endothermic by 0.07 and 0.16 eV, respectively.[29] In the current experiment, these are observed with a threshold close to 0 eV and a maximum intensity at 0.6 and 1.1 eV, respectively, indicating that these fragments are formed through the same low-lying resonance as the corresponding single ligand loss fragments. However, even at these energies the DEA cross section has dropped significantly. This is also reflected in the exponential decay of the single ligand loss ion yield slightly above 0 eV.

The low efficiency of the Br^- formation, despite its maximum being at 0 eV, does not fall within this picture. This is particularly true as the singly occupied molecular orbital (SOMO) of the TNI is found to have a significant Ru–Br antibonding character.[29] Hence, the comparatively low Br^- yield is likely rooted in the dynamics of this channel rather than the less favourable thermochemistry compared to the other single ligand loss channels.

Negative ion formation from π-allyl ruthenium tricarbonyl bromide is also observed through higher-lying resonances, though these channels are much less efficient and not likely to contribute significantly to ligand loss in FEBID. From these, a resonance through which the maximum ion yield is at around 4–5 eV also produces five fragments: $[M-2CO]^-$, $[M-1CO-allyl]^-$, Br^-, $[M-2CO-allyl]^-$ and $[M-3CO]^-$. This is the energy regime within which we expect the first transitions from the highest occupied molecular orbitals (HOMOs) to the lowest unoccupied molecular orbitals (LUMOs) to take place (around 4–5 eV). These contributions are thus likely to be through one or more core-excited resonances, but short-lived single-particle shape resonances are also commonly observed in DEA at these energies and cannot be excluded.

Aside from Br^- formation, all fragments observed at these energies are directly associated with multiple ligand loss. We attribute this to the excess energy within the produced single ligand loss fragment leading to further ligand loss within the detection timeframe of the current experiment. Multiple ligand loss is therefore more favourable than single ligand loss in this energy range. Correspondingly, we expect Br^- formation in this regime to be associated with further fragmentation of the neutral counterpart. The competition between these channels is also reflected in the shift in their ion yield curves to higher energies when proceeding from the double ligand loss channels $[M-2CO]^-$ and $[M-1CO-allyl]^-$, to the formation of Br^- and to the triple ligand loss channels leading to the fragments $[M-3CO]^-$ and $[M-2CO-allyl]^-$.

Another broad contribution is observed in the ion yields of Br^-, $[M-2CO-allyl]^-$, $[M-3CO]^-$, and $[M-3CO-allyl]^-$ around 9 eV. These are also weak contributions, due to the low survival probability of the TNI with regards to autodetachment at such high energies. No negative ion formation is observed above 12 eV, which suggests that dipolar dissociation does not play a significant role in electron-induced dissociation of this molecule.

Fig. 2 shows the dissociative ionization spectrum of π-allyl ruthenium tricarbonyl bromide at an electron impact energy of 75 eV. DI is a non-resonant process with an onset at or above the ionization energy of the parent molecule, wherein fragmentation channels will increase rapidly in intensity from their thresholds with increasing incident electron energy before levelling off. The energy used (75 eV) is past the point where

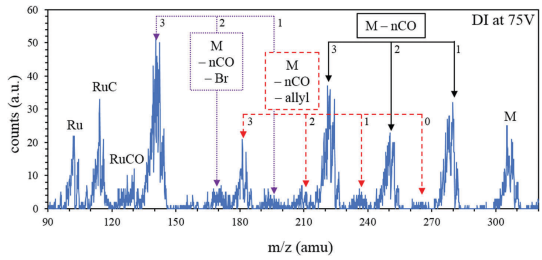

Fig. 2 Positive ion DI spectrum for $(\eta^3\text{-}C_3H_5)Ru(CO)_3Br$ at 75 eV. Three main channels are observed: sequential carbonyl loss (1–3 CO), allyl loss accompanied by sequential carbonyl loss (0–3 CO), and bromine loss accompanied by sequential carbonyl loss (1–3 CO).

all DI fragments have reached their maximum intensities and are therefore directly comparable. In the current experiment we cannot differentiate between isobaric ions; as ruthenium has multiple isotopes, ruthenium-centred fragments with varying amounts of hydrogen cannot be differentiated.

Fragmentation through DI is abundant at this energy and is characterized by three regressions. The first and dominant one is the loss of 1–3 CO ligands, reflecting that the carbonyl ligand is, as in DEA, significantly more susceptible to dissociation *via* DI than the allyl ligand. The second, much less prominent regression is that of allyl loss and allyl loss concurrent with loss of 1–3 CO. The third is that of the loss of bromine and bromine loss concurrent with 1–3 CO. The loss of the bromine alone overlaps with the isotope distribution for $[M - 3CO]^+$; however, comparison with calculated isotope distributions in this region suggests that bromine loss contributes minimally to this distribution. The signal intensity for both $[M - CO - Br]^+$ and $[M - 2CO - Br]^+$ are similarly very low. The most intense ruthenium-centred fragment, however, is $[(\eta^3\text{-}C_3H_5)Ru]^+$ (m/z = 143), which corresponds to the loss of bromine and three carbonyl ligands. This shows clearly that the bromine ligand is much more labile *via* DI than DEA. In addition to these fragments, both the parent cation and the bare ruthenium cation are detected with appreciable intensities as well as ruthenium carbide $[RuC]^+$ and the ligands/ligand fragments $[CO]^+$, $[C_3H_3]^+$ and $[C_3H_5]^+$.

Table 1 compares the relative intensity of the observed DEA and DI channels and the average carbonyl, allyl and bromide ligand loss per dissociation incident. For the DEA channels, the relative intensities were calculated by integrating the ion yield for each fragment (recorded at the principal m/z ratio) and normalizing it to the single carbonyl loss peak (m/z = 278, $[(\eta^3\text{-}C_3H_5)Ru(CO)_2Br]^-$). For the DI channels, the relative intensities were calculated by integrating the isotope distribution for each fragment and normalizing it to the single carbonyl loss distribution (m/z = 278, $[(\eta^3\text{-}C_3H_5)Ru(CO)_2Br]^+$). Care must be taken when comparing relative intensities of DEA channels to those of DI channels, though these may be compared internally. Average ligand loss (per incident) was calculated by adding up the relative intensities of each ruthenium-centred ligand loss fragment of each specific ligand weighted by the number of ligands lost and dividing these by the sum of the relative intensities of all ruthenium-centred fragments. Ultimately, π-allyl ruthenium tricarbonyl bromide molecules lose an average of about 0.9 carbonyl ligands, 0.2 allyl ligands, and close to 0 bromide ligands per molecule per incident *via* DEA. For DI these numbers are 2.1 CO, 0.3 allyl and 0.4 Br^-.

Table 1 Comparison between the relative cross-sections of the negative ion fragments observed in DEA and the positive ion fragments observed in DI. For each channel, the relative intensities were normalized to the relevant single carbonyl loss fragment (m/z = 278) (see text)

Fragments	m/z	DEA rel. intensity	DI rel. intensity
$[(\eta^3\text{-}C_3H_5)Ru(CO)_2Br]^{+/-}$	306	—	68.3
$[(\eta^3\text{-}C_3H_5)Ru(CO)_2Br]^{+/-}$	278	100.0	100.0
$[Ru(CO)_3Br]^{+/-}$	265	29.7	4.0
$[(\eta^3\text{-}C_3H_5)Ru(CO)Br]^{+/-}$	250	12.3	74.7
$[Ru(CO)_2Br]^{+/-}$	237	4.4	12.9
$[(\eta^3\text{-}C_3H_5)RuBr]^{+/-}$	222	0.4	119.7
$[Ru(CO)Br]^{+/-}$	209	1.2	14.2
$[(\eta^3\text{-}C_3H_5)Ru(CO)_2]^{+/-}$	199	—	12.5
$[RuBr]^{+/-}$	181	0.02	42.4
$[(\eta^3\text{-}C_3H_5)Ru(CO)]^{+/-}$	171	—	19.1
$[(\eta^3\text{-}C_3H_5)Ru]^{+/-}$	143	—	178.6
$[Ru(CO)]^{+/-}$	130	—	24.9
$[RuC]^{+/-}$	114	—	69.8
$Ru^{+/-}$	102	—	43.1
$Br^{+/-}$	79	1.6	—
$[RuC]^{2+/2-}$	57	—	6.2
$[C_3H_5]^{+/-}$	41	—	31.8
$[C_3H_3]^{+/-}$	39	—	30.9
$[CO]^{+/-}/N_2^{+/-}$	28	—	43.9
CO loss/molecule	—	0.9	2.1
Allyl loss/molecule	—	0.2	0.3
Br loss/molecule	—	0.0	0.4

As previously discussed, the desired outcome in FEBID is for precursors to completely dissociate all of their ligands under electron irradiation in order to produce pure deposits of the target metal. By studying this molecule, it is evident that the allyl ligand, which is an η^3 ligand, is not particularly labile *via* DEA. This is consistent with the behaviour of other π-bonded hydrocarbon ligands, *e.g.* the η^5 ligand cyclopentadienyl and its derivatives.[10,30] Bromide is also not particularly labile *via* DEA; however, the current study in conjunction with previously reported calculations suggest that bromide ligands provide stability to the ruthenium-centred negative fragments.[29] Hence, the halide may be used to increase the electron affinity of the charge retaining fragment, thus increasing the available excess energy and promoting more extensive fragmentation at low energies where the attachment cross section is highest. Finally, the carbonyl ligands are clearly quite labile *via* DEA, and single CO loss dominates the DEA ion yield at 0 eV. This is consistent with other metal carbonyl complexes.[11,13,31,32] Similarly to DEA, carbonyl loss dominates the DI spectra and the allyl group is a much less labile ligand. However, in contrast to DEA, DI leads to a fair amount of bromide loss, most evident in the formation of the fragment $[(\eta^3\text{-}C_3H_5)Ru]^+$ (m/z = 143). Comparison of the relative lability of each ligand *via* DEA *versus* DI, for this compound, can allow insight into the relative importance of carbonyl loss *versus* allyl loss *versus* bromide loss in each process.

In a recent study by Spencer *et al.*,[18] nanometre-thick layers of π-allyl ruthenium tricarbonyl bromide were deposited onto amorphous carbon and polycrystalline gold substrates under ultra-high vacuum (UHV) conditions. The films were irradiated with 500 eV electrons from a flood gun, and the change of the composition of the films during irradiation was observed through X-ray photoelectron spectroscopy (XPS). In addition, electron-induced desorption from the surface was observed by mass spectrometry (MS) during the initial electron irradiation. Both the MS and the XPS spectra reveal a rapid initial CO loss that levels off after about 20% remaining CO at an electron dose of about 10^{16} e^- cm^{-2}. Quantitative assessments of the CO loss from this compound *via* XPS is complicated by an overlap of the C(1s) signal and the Ru(3d) signal; thus, the O(1s) signal is used as a measure for the remaining CO on the surface. The CO reduction on the surface is also reflected in the mass spectra,

which show substantial CO desorption. The kinetics of CO desorption follow the reduction of the O(1s) signal in the XPS. Neither bromine nor allyl desorption is observed in these experiments, yet while the allylic carbon is found to stay at the surface even after prolonged irradiation, extended irradiation leads to bromine loss that levels off at about 20% of the initial value after an electron dose of about 5×10^{18} e^{-} cm^{-2}. In this context, the authors point out that a small number of carbonyl and halide ligands may be a viable molecular architecture to achieve high metal content FEBID deposits under precursor-limited conditions. This assertion was supported by the recent deposition by Spencer *et al.* of platinum from $Pt(CO)_2Cl_2$ under similar conditions.[22] The platinum-centred compound was again found to deposit under UHV conditions with low carbon and oxygen content, and chlorine content was found to reduce significantly under continued electron irradiation. Additionally, this compound was deposited under steady state conditions in an Auger spectrometer in order to more accurately mimic the conditions in a typical FEBID experiment. Deposits produced by this experiment did not contain carbon or oxygen. The authors suggest that this may provide a path to FEBID of pure platinum metal from $Pt(CO)_2Cl_2$ under precursor-limited conditions.

In the current gas phase experiment, average CO loss per incident is found to be considerably higher for DI than DEA, and allyl loss *via* DI is marginal compared to the CO loss while the allyl loss in DEA amounts to about 1/4 of the CO loss. Together with the lack of any allyl fragments in the MS recorded by Spencer *et al.* for the desorbing fragments,[18] this is consistent with DI, rather than DEA, dominating the initial decomposition step of this compound in the surface study. The lack of any bromine signal in the initial MS of desorbing species and the lack of any substantial reduction in the Br(3d) XPS signal, conversely, is in better agreement with the efficiency profile of the gas phase DEA process rather than the DI process.

The effective damage yield of precursor molecules in FEBID is, however, a convolution of the cross sections for the individual processes and the secondary electron energy distribution.[11,14] Furthermore, the potential contribution of neutral dissociation upon electronic excitation has not been considered in this study. Nonetheless, and despite the potential influence of surface interactions on the extent of these reactions, such gas phase studies give a good account of the lability of individual ligands and thus their suitability for the design of appropriate FEBID precursors.

From the current study it is evident that the carbonyl is a good leaving group both with regards to DEA and DI; this is also evident from earlier studies with carbonyl-containing compounds (*e.g.* $Co(CO)_3NO$, $Fe(CO)_5$, and $W(CO)_6$)[11,13,31,32] and most recently through the deposition of an 80% pure metal alloy in FEBID using the bimetallic precursor $HFeCo_3(CO)_{12}$, as well as a related gas phase study.[33,34] Further, it is clear that for π-allyl ruthenium tricarbonyl bromide the η^3-allyl ligand is not a good leaving group. This is similar to findings for trimethyl methylcyclopentadienyl platinum(IV) and is consistent with surface studies for both these molecules.[17,18] It is likely that these findings can be generalized, suggesting that such multicoordinate ligands should be avoided in the design of FEBID precursor molecules. To our knowledge, this study is the first gas phase study on low energy electron interaction with a potential FEBID precursor containing a halogen ligand. Halogens are generally good leaving groups in DEA: *i.e.* where the electron affinity of the halogen exceeds its binding energy in the parent molecule, DEA leading to the observation of the respective halide anion is commonly the dominating process observed close to 0 eV (see *e.g.* ref. 35 and 36 and references therein). In DEA to π-allyl ruthenium tricarbonyl bromide, conversely, the Ru–Br bond is generally not broken and the charge retention is almost exclusively on the RuBr-centred fragments. DI also does not lead to substantial bromine loss. Spencer *et al.* show, however, that prolonged irradiation may lead to removal of the halogen from the deposit formed in the initial decomposition process.[18,22] Hence, where DEA is the dominant initial step, it may be advantageous to include a halogen ligand despite its persistence. From the integrated intensities of $[M - 2CO]^-$ and $[M - 1CO - allyl]^-$ and their low appearance energies, we deduce that the presence of the bromide in these fragments contributes favourably to their electron affinities, which in turn enables the loss of two ligands even at these low energies. This is further supported by recent calculations, predicting the thresholds for these reactions to be very close to 0 eV and the bulk of the electron density to be on the bromide ligand.[29] Consequently, introducing a halide opens up a potential path to increase the electron affinity of the initial fragment. In combination with sufficiently labile ligands, the increase in available energy for the initial fragmentation process should ultimately favour more extensive fragmentation through DEA at low incident electron energies, where the attachment cross section is highest. However, due to the persistence of the bromide ligand, the prerequisite for this approach to be viable in FEBID is that the halide may be removed through extended electron exposure as indicated by the aforementioned surface studies by Spencer *et al.*[18,22]

Looking forward, this concept of designing energy sources into FEBID precursor architecture may be extended further. We use this opportunity to propose that exothermic intramolecular reaction pathways triggered by DEA may be designed into FEBID precursor molecules. Such reactions are known to enable extensive DEA fragmentation at 0 eV in organic molecules. One good example of this is the 0 eV decomposition of pentafluorophenol and -aniline, where extensive fragmentation is enabled through HF formation, providing the additional 6 eV HF BDE.[15] Another such example is difluoroformaldehyde production in DEA to tetrafluoro-*para*-quinone, leading to C_4^- formation at an incident electron energy of only 4 eV.[16] Such energy harvesting through predetermined rearrangement reactions may be a worthwhile path to explore toward the sensitization of FEBID precursor molecules to DEA.

4 Conclusions

We have presented DEA and DI ion yields and relative cross-sections for the potential FEBID precursor π-allyl ruthenium

tricarbonyl bromide, and compared these findings to surface studies performed on the same molecule. This specific molecule was used in these studies for its ligand architecture – as it contains a multicoordinate π-bonded ligand, three carbonyl ligands and a halide, it could therefore be used to directly compare the lability of these ligands *via* DEA and DI. We find that carbonyl ligands have high relative cross sections for dissociation both *via* DEA and *via* DI, while allyl and bromide ligands have significantly lower relative cross sections for dissociation *via* both reaction channels. As commonly observed, the extent of fragmentation is greater *via* DI than DEA. Furthermore, allyl and bromide ligands are more susceptible to dissociation *via* DI than *via* DEA. Ultimately, we find that π-bound ligands such as the allyl are unlikely to be desirable when designing molecules for use in FEBID due to their persistence both in the gas phase and in previously reported surface studies.[10,30] Halides are potentially more desirable, despite their persistence, in combination with more labile ligands like CO. They may lend stability to metal-centred anionic fragments, thus providing additional energy for further ligand loss. The prerequisite is that the halide can be eliminated through post-deposition processing, as has been found for some precursors.[18,22] This potential may be advantaged in order to sensitize FEBID precursors to electron-stimulated decomposition.

Acknowledgements

This research has been supported by the Icelandic Center of Research (RANNIS), Grant No. 13049305(1-3) and the University of Iceland Research Fund. It was conducted within the framework of the COST Action CM1301: Chemistry for ELectron-Induced Nanofabrication (CELINA). RMT acknowledges financial support from the COST Action CM1301: CELINA for a short term scientific mission (STSM). L. M.-W. and J. A. B. thank the donors of the American Chemical Society Petroleum Research Fund (Grant 54519-ND5) and the National Science Foundation (Grant CHE-1607547) for partial support of this work.

References

1 I. Utke, P. Hoffmann and J. Melngailis, *J. Vac. Sci. Technol., B: Microelectron. Nanometer Struct.–Process., Meas., Phenom.*, 2008, **26**, 1197.
2 W. F. van Dorp and C. W. Hagen, *J. Appl. Phys.*, 2008, **104**, 081301.
3 M. Huth, F. Porrati, C. Schwalb, M. Winhold, R. Sachser, M. Dukic, J. Adams and G. Fantner, *Beilstein J. Nanotechnol.*, 2012, **3**, 597–619.
4 W. F. van Dorp, B. van Someren, C. W. Hagen, P. Kruit and P. A. Crozier, *Nano Lett.*, 2005, **5**, 1303–1307.
5 R. Schmied, J. D. Fowlkes, R. Winkler, P. D. Rack and H. Plank, *Beilstein J. Nanotechnol.*, 2015, **6**, 462–471.
6 S. J. Randolph, J. D. Fowlkes and P. D. Rack, *Crit. Rev. Solid State Mater. Sci.*, 2006, **31**, 55–89.
7 J. Schaefer and J. Hoelzl, *Thin Solid Films*, 1972, **13**, 81–86.
8 A. Botman, D. A. M. de Winter and J. J. L. Mulders, *J. Vac. Sci. Technol., B: Microelectron. Nanometer Struct.–Process., Meas., Phenom.*, 2008, **26**, 2460–2463.
9 P. C. Hoyle, J. R. A. Cleaver and H. Ahmed, *Appl. Phys. Lett.*, 1994, **64**, 1448–1450.
10 S. Engmann, M. Stano, S. Matejčík and O. Ingólfsson, *Phys. Chem. Chem. Phys.*, 2012, **14**, 14611–14618.
11 S. Engmann, M. Stano, P. Papp, M. J. Brunger, S. Matejčík and O. Ingólfsson, *J. Chem. Phys.*, 2013, **138**, 044305.
12 O. May, D. Kubala and M. Allan, *Phys. Chem. Chem. Phys.*, 2012, **14**, 2979–2982.
13 K. Wnorowski, M. Stano, C. Matias, S. Denifl, W. Barszczewska and Å. Matejčík, *Rapid Commun. Mass Spectrom.*, 2012, **26**, 2093–2098.
14 R. M. Thorman, T. P. Ragesh Kumar, D. H. Fairbrother and O. Ingólfsson, *Beilstein J. Nanotechnol.*, 2015, **6**, 1904–1926.
15 B. Ómarsson, E. H. Bjarnason, S. A. Haughey, T. A. Field, A. Abramov, P. Klüpfel, H. Jónsson and O. Ingólfsson, *Phys. Chem. Chem. Phys.*, 2013, **15**, 4754.
16 B. Ómarsson, O. Ingólfsson, J. G. Carter, H. C. Schweinler, A. Abramov, P. Klüpfel, H. Jónsson, O. Ingólfsson, E. Apra, T. L. Windus and W. A. D. Jong, *Phys. Chem. Chem. Phys.*, 2013, **15**, 16758.
17 J. D. Wnuk, J. M. Gorham, S. G. Rosenberg, W. F. van Dorp, T. E. Madey, C. W. Hagen and D. H. Fairbrother, *J. Phys. Chem. C*, 2009, **113**, 2487–2496.
18 J. A. Spencer, J. A. Brannaka, M. Barclay, L. McElwee-White and D. H. Fairbrother, *J. Phys. Chem. C*, 2015, **119**, 15349–15359.
19 S. G. Rosenberg, M. Barclay and D. H. Fairbrother, *J. Phys. Chem. C*, 2013, **117**, 16053–16064.
20 S. G. Rosenberg, M. Barclay and D. H. Fairbrother, *Phys. Chem. Chem. Phys.*, 2013, **15**, 4002–4015.
21 J. Postler, M. Renzler, A. Kaiser, S. E. Huber, M. Probst, P. Scheier and A. M. Ellis, *J. Phys. Chem. C*, 2015, **119**, 20917–20922.
22 J. A. Spencer, Y.-C. Wu, L. McElwee-White and D. H. Fairbrother, *J. Am. Chem. Soc.*, 2016, **138**, 9172–9182.
23 E. H. Bjarnason, B. Ómarsson, S. Engmann, F. H. Ómarsson and O. Ingólfsson, *Eur. Phys. J. D*, 2014, **68**, 121.
24 A. Stamatovic and G. J. Schulz, *Rev. Sci. Instrum.*, 1970, **41**, 423–427.
25 G. Sbrana, G. Braca, F. Piacenti and P. Pino, *J. Organomet. Chem.*, 1968, **13**, 240–242.
26 K. R. Johnson, P. Arevalo Rodriguez, C. R. Brewer, J. A. Brannaka, Z. Shi, J. Yang, B. Salazar, L. McElwee-White and A. V. Walker, *J. Chem. Phys.*, 2017, **146**, 052816.
27 D. Klar, M.-W. Ruf and H. Hotop, *Int. J. Mass Spectrom.*, 2001, **205**, 93–110.
28 G. J. Schulz and R. K. Asundi, *Phys. Rev.*, 1967, **158**, 25–29.
29 R. M. Thorman, R. Bjornsson and O. Ingólfsson, *Eur. Phys. J. D*, 2016, **70**, 164.
30 G. M. Begun and R. N. Compton, *J. Chem. Phys.*, 1973, **58**, 2271–2280.

31 P. M. George and J. L. Beauchamp, *J. Chem. Phys.*, 1982, **76**, 2959–2964.
32 M. Lacko, P. Papp, K. Wnorowski and T. Matejčík, *Eur. Phys. J. D*, 2015, **69**, 84.
33 F. Porrati, M. Pohlit, J. Müller, S. Barth, F. Biegger, C. Gspan, H. Plank and M. Huth, *Nanotechnology*, 2015, **26**, 475701.
34 R. Kumar T. P., S. Barth, R. Bjornsson and O. Ingólfsson, *Eur. Phys. J. D*, 2016, **70**, 163.
35 I. Bald, J. Langer, P. Tegeder and O. Ingólfsson, *Int. J. Mass Spectrom.*, 2008, **277**, 4–25.
36 O. Ingólfsson, F. Weik and E. Illenberger, *Int. J. Mass Spectrom. Ion Processes*, 1996, **155**, 1–68.

Article IV

Low energy electron-induced decomposition of (η^5-Cp)Fe(CO)$_2$Mn(CO)$_5$, a potential bimetallic precursor for focused electron beam induced deposition of alloy structures

Rachel M. Thorman, Ilyas Unlu, Kelsea Johnson, Ragnar Bjornsson, Lisa McElwee-White, Howard Fairbrother and Oddur Ingólfsson

submitted

Rachel Thorman performed all gas phase experimental work and analysis presented in this manuscript, under the expertise of Prof. Oddur Ingólfsson. Surface studies were performed by Dr. Ilyas Unlu, under the expertise of Prof. Howard Fairbrother. Rachel also performed much of the computational work, with assistance from Dr. Ragnar Björnsson in performing the isosurface scans and under his expertise for analysis. She wrote the first draft of the manuscript and contributed to editing. The studied molecule was synthesized by Kelsea Johnson under the expertise of Prof. Lisa McElwee-White

Low energy electron-induced decomposition of (η^5-Cp)Fe(CO)$_2$Mn(CO)$_5$, a potential bimetallic precursor for focused electron beam induced deposition of alloy structures

Rachel M. Thorman,[a] Ilyas Unlu,[b] Kelsea Johnson,[c], Ragnar Bjornsson[a], Lisa McElwee-White[c], Howard Fairbrother[b] and Oddur Ingólfsson*[a]

The production of alloyed nanostructures presents a unique problem in focused electron beam induced deposition (FEBID). Deposition of such structures has historically involved the mixing of two or more precursor gases in situ or via multiple channel gas injection systems, thereby making the production of precise, reproducible alloy compositions difficult. Promising recent efforts to address this problem have involved the use of multi-centred, heterometallic FEBID precursor species. In this vein, we present here a study of low-energy electron interactions with cyclopentadienyl iron dicarbonyl manganese pentacarbonyl ((η^5-Cp)Fe(CO)$_2$Mn(CO)$_5$), a bimetallic species with a polyhapto ligand (Cp) and seven terminal carbonyl ligands. Gas phase studies and coupled cluster calculations of observed low-energy electron-induced reactions were conducted in order to predict the performance of this precursor in FEBID. In dissociative electron attachment, we find single CO loss and cleavage of the Fe−Mn bond, leading to the formation of $[Mn(CO)_5]^-$, to be the two dominant channels. Contributions through further CO loss from the intact core and the formation of $[Mn(CO)_4]^-$ are minor channels. In dissociative ionization (DI), the fragmentation is significantly more extensive and the DI spectra are dominated by fragments formed through the loss of 5 and 6 CO ligands, and fragments formed through cleavage of the Fe−Mn bond accompanied by substantial CO loss. The gas phase fragmentation channels observed are discussed in relation to the underlying processes and their energetics, and in context to related surface studies and the likely performance of this precursor in FEBID.

1 Introduction

The fabrication of magnetic nanostructures has become increasingly vital to many emergent fields both in academic research and industry, including information technology, nanoelectronics, and spintronics.[1,2] Currently, such nanostructures are commonly manufactured via the top-down approach ubiquitous in nanolithography – optical lithography has produced nanostructures as small as 22 nm, while ion milling has produced structures as small as 10 nm.[1] Despite these advances, there are clear drawbacks to these techniques. Optical lithography is a multistep process and each step has the potential to degrade the quality of the produced structure, which may affect device functionality; this is of particular concern at the nanoscale.[1,2] Additionally, expensive masks must be produced for use in photolithography, which are often themselves degraded by the lithography process. Ion milling, despite its improved lateral resolution, has the potential effect of ion implantation, which may affect the magnetic properties of the materials used.[1,3]

Focused electron beam induced deposition (FEBID),[4,5] conversely, is a single-step, bottom-up process wherein nanostructures can be directly written onto three-dimensional surfaces. In FEBID, electron-driven reactions are used to deposit pure metal nanostructures onto surfaces. In a high-vacuum instrument equipped with a tightly-focused electron beam (e.g. an SEM or TEM), a substrate is exposed to a constant flux of organometallic precursor. Ideally, electron-driven reactions will cause the metal centres of these precursors to deposit onto the substrate under the area of the primary electron beam, while the organic ligands fully dissociate and are pumped away. The electron beam can then be rastered around the surface, allowing it to deposit any lateral geometry, while the vertical dimension of the deposit may be controlled through variations in dwell time. FEBID has been used to deposit nanowires, nanosprings and nanodots, as well as many other structures.[1,4,5] High resolution capacity has been demonstrated through production of nanodots as small as 0.7 nm, as well as lines with a width of 1.9 nm and a spacing of 3.2 nm.[6] High purity nanostructures,[4,7] including magnetic nanostructures,[1,7–10] have also been produced with FEBID. Furthermore, though FEBID does currently not have the same capacity for high industrial throughput as do photolithographic techniques, it has been used successfully for research and prototyping.[4]

However, although FEBID has been used to deposit nanostructures with high lateral resolution and high purity, this is not routinely achieved. Presently, the two major challenges facing FEBID are (i) deposit contamination as a result of incomplete ligand dissociation and (ii) deposit broadening outside the area of the primary electron beam. This is in part due to suboptimal precursor chemistry and appropriate precursors must be designed in order to address these challenges. In order to design such optimal precursors, it is important to understand the electron-driven processes by which deposits are formed from precursors on surfaces. Low-energy electrons (commonly defined as electrons below 100 eV in energy) are abundant on surfaces during FEBID experiments. The energy distribution of secondary and backscattered electrons on surfaces irradiated with a high-energy primary electron beam generally reaches its peak well below 10 eV, and

[a] Science Institute and Department of Chemistry, University of Iceland, Reykjavik, Iceland. Fax: +365 552-8911; Tel: +365 525-4313; E-mail: oddur@hi.is
[b] Department of Chemistry, Johns Hopkins University, Baltimore, Maryland, USA.
[c] Department of Chemistry, University of Florida, Gainesville, Florida, USA.

such electrons are scattered within an area several times as large as the area of the primary electron beam.[4,5,11–15] Low-energy electrons are additionally known to react with FEBID precursors to produce incomplete ligand dissociation, and have previously been found to be important in the deposition of materials from various precursors.[11,16–23]

There are four major reaction pathways initiated by low-energy electrons: Dissociative Electron Attachment (DEA), Dissociative Ionization (DI), Neutral Dissociation (ND) and Dipolar Dissociation (DD).[11,24–30] These reactions are initiated by electrons from very different points along the secondary electron energy distribution and produce several different types of dissociation products. The respective reaction schemes for each of these pathways are shown here:

$$AB + e^- \rightarrow AB^{(\#)-} \rightarrow A^{(\#)-} + B^{(\#)} \quad (1)$$

$$AB + e^- \rightarrow AB^{(\#)+} + 2e^- \rightarrow A^{(\#)+} + B^{(\#)} + 2e^- \quad (2)$$

$$AB + e^-(\varepsilon_1) \rightarrow [AB]^* + e^-(\varepsilon_2 < \varepsilon_1) \rightarrow A^{(\#)} + B^{(\#)} \quad (3)$$

$$AB + e^-(\varepsilon_1) \rightarrow [AB]^* + e^-(\varepsilon_2 < \varepsilon_1) \rightarrow A^{(\#)+} + B^{(\#)-} \quad (4)$$

In the above reaction pathways, # denotes species that may be in vibrationally or electronically excited states, * identifies species that are in electronically excited states and ε_1 and ε_2 are the energy of the electron before and after the inelastic scattering event leading to ND or DD.

DEA (1) is a resonant process wherein a molecule captures a low energy electron, in essentially a vertical transition from the neutral molecule's ground state to the ground state or other accessible excited states of the anion (see e.g. refs. Bald *et al.*[25], Fabrikant *et al.*[30] and refs. therein). This forms a transient negative ion (TNI), which then relaxes, either by emitting the electron in a process called autodetachment or by dissociation, leading to the formation of a negative ion fragment and one or more neutral fragments. The DEA process is generally confined to a narrow energy range below the ionization threshold of the molecule, usually $0 - 10$ eV, and is most efficient at around 0 eV. The high efficiency close to 0 eV, is due to the cross section for electron attachment being proportional to $E^{-1/2}$,[31], allowing sufficient time for dissociation.[30] We note, however, that recent gas phase studies have been performed on an exceptional molecule, $HFeCo_3(CO)_{12}$, showing DEA more than 11 eV above the ionization threshold of the molecule (at above 20 eV!).[32,33]

Unlike DEA, DI, ND and DD are all non-resonant processes,[11,26,27,29] showing threshold behaviour rather than resonance behaviour. In DI (2), an electron positively ionizes a molecule via direct impact. DI thus has an onset at or above the ionization threshold of the parent molecule. The positive parent ion, which may also be electronically or vibrationally excited, may then dissociate in order to redistribute its excess internal energy, producing a positive ion and one or more neutral fragments, generally radicals. The total cross section for DI typically increases until reaching a maximum between 50 and 100 eV, with the branching ratio shifting toward multiple bond ruptures with increasing incident electron energy. After this maximum, the total cross section decreases as energy transfer becomes less efficient with increasing electron energy.

Neutral dissociation (3) proceeds through an electron-initiated transition of the parent molecule to electronically excited states higher in energy than the respective bond dissociation energies.[34] At threshold, these typically involve occupation of the lowest unoccupied antibonding orbitals; however, as the incident electron energy increases, the manifold of excited states that couple with dissociative channels also increases. In ND two or more neutral fragments are produced, most often radicals, and these fragments are commonly vibrationally or electronically excited. Dipolar dissociation (4) proceeds similarly to ND; however, it produces both an anionic fragment and a cationic fragment. It is less efficient than either DEA or DI and is likely also less efficient than ND, due to the Coulombic attraction between the product fragments. In organometallic compounds, where the first electronic excitations are at fairly low energies and the bond dissociation energy is generally low, the threshold for ND is expected to be close to 3-4 eV.

The products of each of these reaction pathways will differ significantly in their potential implications for FEBID – various positive and negative ions and radical neutrals, all of which may be in excited states, will have very different reaction profiles in FEBID and thus will initiate reactions leading to varying deposition dynamics. The secondary electron spectrum of the surface used in FEBID, in conjunction with the energy dependence and branching ratios of the individual reaction paths for the precursor molecule, will determine the importance of these channels and, ultimately, the composition of the FEBID deposits. It is thus important to understand the branching ratios of the electron-induced reactions of these precursor molecules in order to predict their viability for use in FEBID, as well as to optimize design of future FEBID precursors. Furthermore, a comparison of the observed extent and branching ratios of these different reaction channels in the gas phase, with the initial electron induced fragmentation observed when these molecules are adsorbed on surfaces, may provide additional information on the dominant reaction pathways to be expected under actual FEBID conditions.

Compared to the deposition of pure metals, production of alloyed deposits presents additional challenges in FEBID. Deposition of alloyed nanostructures via FEBID has previously been performed by mixing precursor gases in situ, using dual or multichannel gas injection systems.[1,4,35,36] However, production of precise, reproducible alloy compositions remains elusive, and use of multiple precursor gases increases the potential for deposit contamination via incomplete ligand dissociation.[37] Further, it can be difficult to predict how multiple precursor gases will interact in situ with both one another and with the surface. To combat these issues, the use of heterometallic organometallic species has been employed. In a 2015 FEBID study, Porrati et al. deposited CoFe alloy nanostructures from the heteronuclear precursor $HFeCo_3(CO)_{12}$, routinely achieving 80 at% pure metal deposits with the same stoichiometric Co:Fe ratio present in the precursor.[7] Gas phase studies have been performed by T P et al.[32,33]

on this same molecule in order to elucidate its electron-induced deposition mechanisms, and seek connections to the high performance of this precursor in FEBID. This molecule was found to be susceptible to DEA at up to 20 eV incident electron energy, which is about 11 eV above its ionization threshold. This unusual behaviour has been attributed to the high density of metal-based HOMOs coming from the four metal atoms and low-energy unoccupied CO π^* orbitals coming from the twelve carbonyl ligands, which include both bridging and terminal carbonyls. This combination allows long-lived multi-particle-multi-hole resonances at high energies, resulting in quasi-continuous electron attachment from about 1 eV up to 20 eV. This unusual behaviour has been discussed in context to the exceptional behaviour of $HFeCo_3(CO)_{12}$ in FEBID; however, a recently published UHV surface study by T P et al.[38] noted that the extent of the initial fragmentation of this precursor adsorbed on a gold surface is much closer to that observed through DI in the gas phase, suggesting that the behaviour of this molecule upon electron impact may be more relevant to its excellent FEBID performance than its unusual behaviour with respect to electron attachment. A recent combined gas phase, UHV surface and FEBID study on the similar bimetallic precursor $H_2FeRu_3(CO)_{13}$ demonstrated that, despite its apparent similarity to $HFeCo_3(CO)_{12}$, $H_2FeRu_3(CO)_{13}$ performs sub-optimally in FEBID.[39] It was found to have limited reproducibility and <26 at% metal content in the deposits. The authors attribute this to a higher thermal stability of the $H_2FeRu_3(CO)_{avg=4,5}$ intermediate observed in the initial deposition step in the UHV surface experiments, as compared to the thermally labile $HFeCo_3(CO)_{avg=3}$ intermediate formed in the initial electron-induced decomposition of adsorbed $HFeCo_3(CO)_{12}$. To our knowledge, these are the only two bimetallic precursors that have been studied to date, so there is obviously considerable work that needs to be done to further explore the potential of this strategy for the production of alloy nanostructures.

Here we present a gas phase study on dissociative electron attachment (DEA) and dissociative ionization (DI) of a similar, albeit smaller, binuclear heterometallic iron-manganese precursor: cyclopentadienyl iron dicarbonyl manganese pentacarbonyl ($(\eta^5$-Cp)$Fe(CO)_2Mn(CO)_5$).[40] Further, in order to elucidate its gas phase behaviour upon electron interaction we use quantum chemical calculations to aid the interpretation of the observed processes. We also compare experimental results from gas phase studies with the electron-induced decomposition of this bimetallic precursor adsorbed on a solid surface. Such a comparison can provide valuable insight into the behaviour of this precursor upon electron irradiation at surfaces, which in turn may provide insight into its behaviour under FEBID conditions.

2 Experimental

2.1 Synthesis of $(\eta^5$-$C_5H_5)Fe(CO)_2Mn(CO)_5$

All reactions were carried out under an inert atmosphere using Schlenk line and glovebox techniques, unless otherwise stated. $(\eta^5$-$C_5H_5)Fe(CO)_2I$ and $Mn_2(CO)_{10}$ were purchased from Sigma-Aldrich and used as received. Tetrahydrofuran (THF) was distilled from sodium benzophenone ketyl and was stored over 3 Å molecular sieves prior to use. IR spectroscopy was performed on a Bruker Alpha spectrometer using a sealed KBr liquid cell from Sigma-Aldrich.

Modified literature procedures were used to synthesize $(\eta^5$-$C_5H_5)Fe(CO)_2Mn(CO)_5$.40 A 1% Na/Hg amalgam was made by dissolving Na (0.1237 g, 5.381 mmol) in Hg (12.4140 g). $Mn_2(CO)_{12}$ (0.7690 g, 1.978 mmol) was dissolved in THF (15 mL) and added to the Na/Hg amalgam. The solution was allowed to stir for 1 hour. The organic layer was transferred to a Schlenk flask containing $(\eta^5$-$C_5H_5)Fe(CO)_2I$ (1.2056 g, 3.9767 mmol) and allowed to stir for 2 days, under the exclusion of light, during which time the product was formed via reaction (1)

Fig. 1 Synthesis of $(\eta^5$-$C_5H_5)Fe(CO)_2Mn(CO)_5$

MeOH (2.0 mL) was added to the deep red solution. The solvent was removed *in vacuo* and the solid was extracted with CH_2Cl_2. After filtration, the solvent was removed under reduced pressure and column chromatography was performed on a silica column with pentane as the eluent. Three bands were seen: yellow $Mn_2(CO)_{10}$, red product, and brown $(\eta^5$-$C_5H_5)Fe(CO)_2I$, which stays on the baseline. After chromatographic separation the product was obtained as a dark red solid after sublimation at 46 °C, 100 mTorr. Crude yield: 0.5418 g, 37%. Sublimed yield: 0.2840 g, 19%. The compound was characterized by comparison to literature data.[40] ^{1}H NMR (300 MHz, C_6D_6) δ 3.97 (s, 5H). IR (hexanes): 2082, 2014, 1991, 1976, 1945 cm^{-1}.

2.2 Crossed beam gas phase studies

The crossed electron/molecular beam instrument used to measure ion yields of fragments produced via DEA and DI to $(\eta^5$-Cp)$Fe(CO)_2Mn(CO)_5$ in the gas phase has been previously described;[41] a brief description of this apparatus is provided here. The bimetallic $(\eta^5$-Cp)$Fe(CO)_2Mn(CO)_5$ precursor was sublimed at a temperature of 40 °C in a stainless steel gas inlet system (GIS), which was attached to a high-vacuum collision chamber. The GIS consists of a 9 mm, capped Swagelok T-fitting separated from the chamber by a variable leak valve. The sample was placed in the bottom cap of the T-fitting and evacuated via a rough pump. The sample was then heated to 40 °C for sublimation, after which the variable leak valve was opened to produce a stable chamber pressure of approximately 1-2x10^{-7} mbar, although higher pressures (4 or 7x10^{-7} mbar) were used for particularly low-intensity fragments ($[CpFeMn(CO)]^-$ and $[Mn(CO)_4]^-$, respectively).

The effusive gaseous precursor beam produced by sublimation enters the interaction zone within the chamber via a stainless steel capillary. Within the interaction zone, it crosses an energetically well-defined electron beam generated by a trochoidal electron monochromator (TEM). This electron beam was energetically calibrated to the $[SF_6]^-/SF_6$ ion yield, which peaks in

intensity at 0 eV. The energy resolution of the electron beam was estimated from the full width at half maximum (FWHM) of the ion yield produced via this resonance and was found to be in the range from 120 to 130 meV during the current experiments. Ionic fragments produced in DEA and DI to (η^5-Cp)Fe(CO)$_2$Mn(CO)$_5$ were measured using a Hiden EPIC1000 quadrupole mass spectrometer (Hiden Analytical, Warrington UK) equipped with two separate RF generators, which operate within a high (2−1000) and low (0.4−50) m/z-range. Ion yields for fragments observed through DEA were recorded by setting the quadrupole mass filter to only allow transmission of the selected m/z ratio and scanning the electron energy. Positive ion mass spectra were recorded by scanning through the relevant mass range at fixed electron energy. The background pressure of the vacuum chamber was approximately 1x10^{-8} mbar and the TEM was maintained at a constant temperature of 120 °C using halogen lamps in order to prevent deposition of the gaseous precursor onto its lens components.

2.3 Quantum chemical calculations

All quantum chemical calculations were carried out using the ORCA program, version 4.0.[42] Geometries of the molecule and fragments were optimized using the density functional BP86[43,44] and the def2-TZVP basis set[45] including the D3BJ dispersion correction.[46,47] Harmonic vibrational frequencies at the same level of theory were used to derive zero-point energies and the thermal vibrational and rotational energy of the neutral molecule. Threshold energies were calculated by single-point coupled cluster calculations at the DLPNO-CCSD(T) level of theory[48–51] using basis sets aug-cc-pVTZ and aug-cc-pVQZ.[52,53] Quasi-restricted orbitals[54] (derived from the UHF orbitals) were used to define a reference determinant in the open-shell coupled cluster calculations that reduces spin contamination and were also used in the electronic structure analysis at the DFT level. Localized orbital analysis was performed using the IAO-IBO protocol by Knizia[55] and bond orders were calculated according to Mayer.[56–59]

Threshold calculations at the DLPNO-CCSD(T) level of theory were performed with both diffuse triple zeta and diffuse quadruple zeta basis sets in order to monitor basis set convergence and minimize basis set errors. It should be noted here that we previously found for the potential organometallic FEBID precursor (η^3-C$_3$H$_5$)Ru(CO)$_3$Br[60] that the use of coupled cluster calculations gave more accurate predictions of the threshold values than the GGA DFT BP86 functional. In that study, an approximate parameterized coupled cluster method, pCCSD/2a, was used in conjunction with the older local pair natural orbital (LPNO) methodology that reduces the dramatic scaling of coupled cluster methods. While the pCCSD/2a approximation is a decent approximation to CCSD(T), with the availability of the more favourable and more accurate domain local pair natural orbital (DLPNO) methodology for open-shell systems and the CCSD(T) method, it is now possible to perform even more accurate DLPNO-CCSD(T) calculations at similar computational cost. However, in the current case, the thresholds at the BP86 and DLPNO-CCSD(T) levels of theory are overall quite similar for this molecule, though they notably differ in one case by 1.1 eV (see table 1 in the results and discussion section).

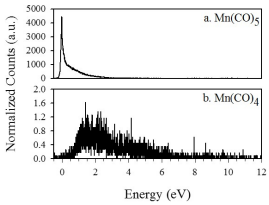

Fig. 2 Negative ion yield spectra of $[Mn(CO)_5]^-$ and $[Mn(CO)_4]^-$. $[Mn(CO)_5]^-$ is the dominant fragment observed in DEA to (η^5-Cp)Fe(CO)$_2$Mn(CO)$_5$, followed closely by $[CpFeMn(CO)_6]^-$ (see Fig. 3a). $[Mn(CO)_5]^-$ is most efficiently produced by direct Fe−Mn bond rupture, although it may be produced via a number of pathways (see Fig. 4 and Table 1), a combination of which likely contribute to the high energy tail of the ion yield.

3 Results and Discussion

3.1 Dissociative electron attachment to CpFe(CO)$_2$Mn(CO)$_5$ in the gas phase

Negative ion yields produced by DEA to CpFe(CO)$_2$Mn(CO)$_5$ are shown in Figures 2 and 3. The yields have been normalized to the pressure of CpFe(CO)$_2$Mn(CO)$_5$ present in each experiment and are expressed at a nominal target pressure of 1x10^{-7} mbar of the precursor. In order to aid the interpretation, we have calculated the thresholds for the most relevant DEA pathways using quantum chemistry at the BP86 and DLPNO-CCSD(T) levels of theory. These channels are the loss of one CO and the cleavage of the Fe−Mn bond leading to the formation of $[Mn(CO)_5]^-$. The threshold for the latter is calculated for cases where (i) the neutral CpFe(CO)$_2$ fragment stays intact, (ii) the neutral fragment loses one CO ligand or (iii) or the neutral fragment loses both CO ligands. The threshold values calculated at the DLPNO-CCSD(T)/aug-cc-pVQZ level of theory are shown in an energy diagram in Figure 4, along with the respective optimized molecular structures. The respective threshold values for all fragments calculated are also given in Table 1, along with their experimentally observed appearance energies. For comparison, we have also calculated the thermochemical threshold for the formation of $[CpFe(CO)_2]^-$, although this fragment is not observed.

The stoichiometries of the two most intense fragments produced are $[Mn(CO)_5]^-$ and $[CpFeMn(CO)_7]^-$, corresponding to the m/z ratios 195 and 344, respectively. Both fragments are produced with appreciable intensity via a low-lying resonance with maximum contribution to the ion yield near 0 eV. The thermochemical thresholds for these reactions calculated at the DLPNO-CCSD(T)/aug-cc-pVQZ level of theory are -1.8 and -1.5 eV respectively. Correspondingly, the significant contribution through these fragments is as expected, as electron attachment is most efficient close to 0 eV[31] and the survival probability of the TNI is highest

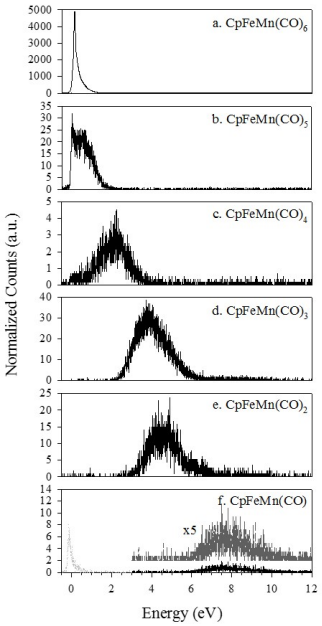

Fig. 3 Negative ion yield spectra of $[CpFeMn(CO)_{6-n}]^-$, where n = 0-5. Each molecular formula is written stoichiometrically; for example, it is likely that $[CpFe(CO)_2Mn(CO)_4]^-$ and $[CpFe(CO)Mn(CO)_5]^-$ both contribute to the ion yield of $[CpFeMn(CO)_6]^-$ (see table 1). $[Mn(CO)_5]^-$ (Fig. 2a) and $[CpFeMn(CO)_6]^-$ show signs of being competing pathways (see Fig. 4).

at low energies.[30] Further, such efficient low-energy dissociation channels must be exothermic, and this is clearly the case for both these channels as can be seen from Fig. 4 and Table 1.

From the fragments observed, the single carbonyl loss fragment $[CpFeMn(CO)_6]^-$ has the highest relative peak intensity, which reaches a maximum at 0.15 eV and then tapers off to the baseline at about 2 eV. However, the $[Mn(CO)_5]^-$ fragment produced by the rupture of the Fe−Mn bond has the highest integrated relative DEA cross-section. Notably, the $[Mn(CO)_5]^-$ intensity peaks at 0 eV – lower than $[CpFeMn(CO)_6]^-$ – and decreases as the single CO loss fragment intensity increases. At approximately 0.15 eV, where the single CO loss has peaked, the $[Mn(CO)_5]^-$ peak broadens, maintaining appreciable intensity until about 4 eV.

The energy dependencies of these two fragments thus bear signs of competing channels, which is typical for metastable decay processes. Although $[CpFeMn(CO)_6]^-$ can only be produced via single carbonyl loss, formation of $[Mn(CO)_5]^-$ may be produced directly (Eq. 5 and path c in Fig. 4), or it may be preceded by an initial CO ligand loss from the $CpFe(CO)_2$ moiety before the Fe−Mn bond rupture takes place (Eq. 6 and path a in Fig. 4):

$$[CpFe(CO)_2Mn(CO)_5]^- \rightarrow [CpFe(CO)_2] + [Mn(CO)_5]^- \quad (5)$$

$$\begin{aligned}[CpFe(CO)_2Mn(CO)_5]^- &\rightarrow [CpFe(CO)Mn(CO)_5]^- + CO \\ &\rightarrow [CpFe(CO)] + [Mn(CO)_5]^-\end{aligned} \quad (6)$$

The direct formation of $[Mn(CO)_5]^-$ and $[CpFe(CO)Mn(CO)_5]^-$, as stated above, was calculated to be exothermic by 1.8 eV and 1.5 eV, respectively. The threshold for Fe−Mn bond dissociation accompanied by a single CO loss from the Fe centre, conversely, was found to be endothermic by 0.5 eV (see Table 1 and path d in Fig. 4. Given the broadening of the ion yield of $[Mn(CO)_5]^-$ above approximately 0.2 eV, it is likely that both these reactions contribute to the negative ion yield spectrum. While the direct dissociation is predominant below 0.2 eV, the contribution through preceding CO loss from the iron moiety (Eq. 6 and path a in Fig. 4) is likely to be significant above that energy. The Fe−Mn bond dissociation accompanied by two CO ligands dissociating from the Fe centre was found to be endothermic by 2.5 eV and could thus in principle contribute to the $[Mn(CO)_5]^-$ ion yield above this energy, though this would clearly be a minor (if extant) contribution.

In this context, it should be noted that our observation window is the first 10 μs after electron attachment. This is the extraction time from the ionization region. Ions that fragment further during the flight through the quadrupole mass filter, which takes about 50 μs, do not maintain stable trajectories and are therefore not detected. Further, considering the energy resolution of the electron beam and the internal energy distribution of the parent molecule at the current experimental temperature (T = 40 °C), the appearance energy may be shifted below the actual thermochemical threshold.

Independent of the route of formation for $[Mn(CO)_5]^-$ at higher energies (above about 0.2 eV), the formation of $[CpFeMn(CO)_6]^-$ may in principle proceed through the loss of CO from the iron containing moiety, producing $[CpFe(CO)Mn(CO)_5]^-$, or from the manganese containing moiety, producing $[CpFe(CO)_2Mn(CO)_4]^-$ (routes a and b in Fig 4, respectively). These fragments are not distinguishable by means of mass spectrometry, so calculations were performed to deduce which isomer is more likely to dominate under the current experimental conditions. At the DLPNO-CCSD(T) level of theory using the aug-cc-pVQZ basis set, we find the threshold for the formation of $[CpFe(CO)Mn(CO)_5]^-$ to be -1.3 eV and that for $[CpFe(CO)2Mn(CO)_4]^-$ to be -1.5 eV. It is thus not obvious that the formation of one isomer rather than the other dominates at 0 eV. However, though with low intensity, we observe the forma-

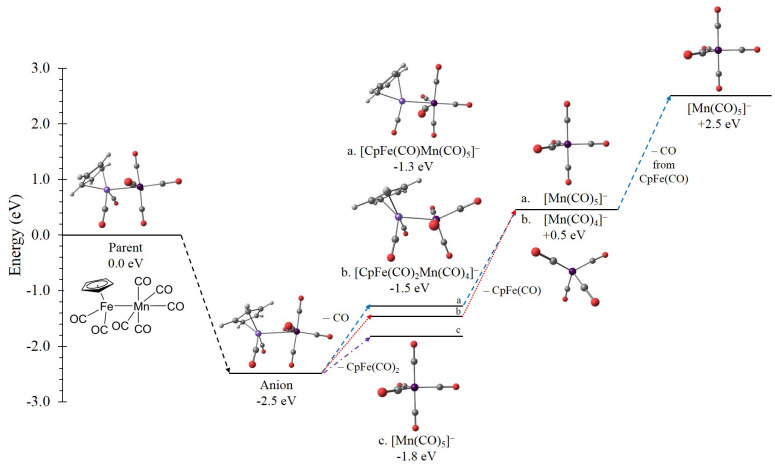

Fig. 4 A visualization of calculated thresholds of electron attachment and dissociation to produce $[Mn(CO)_5]^-$, $[CpFeMn(CO)_6]^-$ (as $[CpFe(CO)_2Mn(CO)_4]^-$ and $[CpFe(CO)Mn(CO)_5]^-$), and $[Mn(CO)_4]^-$. Electron attachment to the neutral parent molecule is exothermic by 2.5 eV and produces the parent anion. The Fe–Mn bond in the parent anion may then rupture (path c), producing $[Mn(CO)_5]^-$; this overall reaction is exothermic by 1.8 eV. Alternatively, the parent anion can lose a carbonyl ligand, either from the Fe-centred moiety (path a, producing $[CpFe(CO)Mn(CO)_5]^-$, exothermic by 1.3 eV) or from the Mn-centred moiety (path b, producing $[CpFe(CO)_2Mn(CO)_4]^-$, exothermic by 1.5 eV). Both paths are expected to contribute to the ion yield at the current experimental temperature. The Fe–Mn bond in either of these product anions may then rupture, producing $[Mn(CO)_5]^-$ (via path a, from $[CpFe(CO)Mn(CO)_5]^-$) or $[Mn(CO)_4]^-$ (via path b, from $[CpFe(CO)_2Mn(CO)_4]^-$). Both overall reactions are endothermic by 0.5 eV. Finally, a second CO can be lost from the neutral CpFe(CO) fragment produced by Fe–Mn bond rupture via path a, producing $[Mn(CO)_5]^-$. This reaction, however, is endothermic by 2.5 eV and is not expected to contribute significantly to the $[Mn(CO)_5]^-$ ion yield.

Table 1 Calculated thresholds (in eV) for electron attachment and dissociation to produce $[Mn(CO)_5]^-$, $[CpFeMn(CO)_6]^-$ (as $[CpFe(CO)_2Mn(CO)_4]^-$ and $[CpFe(CO)Mn(CO)_5]^-$), and $[Mn(CO)_4]^-$. Also shown are the calculated threshold values for the formation of $[CpFe(CO)_2]^-$, which is not observed experimentally. $[Mn(CO)_5]^-$ is produced by rupture of the Fe-Mn bond, and can be accompanied by the loss of one or two CO ligands from the Fe-centred moiety. Based on the calculated thresholds, it is likely that single CO loss from the Fe-centred fragment forms part of the higher-energy tail of the ion yield of $[Mn(CO)_5]^-$; it is unlikely that double CO loss forms any significant contribution. At energies above 0.5 eV, carbonyl loss from the $[Mn(CO)_5]^-$ fragment forms $[Mn(CO)_4]^-$.

Anionic fragment		Neutral fragment A	Neutral fragment B	Threshold (BP86, eV)	Threshold (CC, TZ, eV)	Threshold (CC, QZ, eV)	Threshold (exp, eV)
M^-		–	–	-2.4	-2.5	-2.5	–
$Mn(CO)_5$	(1)	$CpFe(CO)_2$	–	-1.6	-1.8	-1.8	0.0
$Mn(CO)_5$	(2)	CpFe(CO)	CO	1.0	0.5	0.5	–
$Mn(CO)_5$	(3)	CpFe	2CO	3.7	2.6	2.5	–
$CpFe(CO)_2Mn(CO)_4$	(a)	CO	–	-0.9	-1.2	-1.3	0.0
$CpFe(CO)Mn(CO)_5$	(b)	CO	–	-1.4	-1.4	-1.5	–
$Mn(CO)_4$		$CpFe(CO)_2$	CO	0.9	0.5	0.5	0.5

tion of $[Mn(CO)_4]^-$ with an appearance energy of about 0.5 eV, which is in good agreement with the calculated threshold of 0.5 eV (see Table 1). In principle, $[Mn(CO)_4]^-$ formation may proceed via CO loss from the $[Mn(CO)_5]^-$ fragment or via dissociation of the Fe−Mn bond in the $[CpFe(CO)_2Mn(CO)_4]^-$ fragment and the threshold is indifferent to which of these paths lead to the formation of this fragment. However, the very low intensity of $[Mn(CO)_4]^-$, <0.5% of that for the formation of $[Mn(CO)_5]^-$ at the same energy (around 1.5 eV), indicates insignificant CO loss from the Mn containing moiety of the initially formed TNI. We therefore expect the single CO loss from the iron moiety (path a in Fig. 4) to be the dominant initial CO loss channel rather than loss from the $Mn(CO)_5$ unit (path b in Fig. 4).

In addition to the major fragments and the formation of $[Mn(CO)_4]^-$ (Fig. 2b), we observe further CO loss from $[CpFeMn(CO)_6]^-$, leading to the fragments $[CpFeMn(CO)_{6-n}]^-$ with n = 1-5 (Figs. 3b-f). No cyclopentadienyl loss is observed, unlike in some similar organometallic species.[20,61] As mentioned above, the formation of $[Mn(CO)_4]^-$ is a minor channel and, at their respective maxima, its intensity is more than 3 orders of magnitude less than that of $[Mn(CO)_5]^-$.

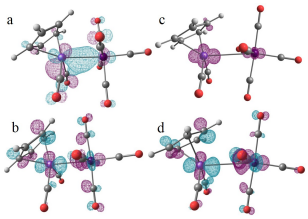

Fig. 5 Calculated orbital isosurfaces of: a) the Mn-Fe σ-bonding orbital (HOMO − 2) of the neutral (η^5-Cp)Fe(CO)$_2$Mn(CO)$_5$ molecule , b) the LUMO of the neutral (η^5-Cp)Fe(CO)$_2$Mn(CO)$_5$ molecule, c) the spin density map of the [(η^5-Cp)Fe(CO)$_2$Mn(CO)$_5$]$^-$ anion and d) the SOMO of the [(η^5-Cp)Fe(CO)$_2$Mn(CO)$_5$]$^-$ anion. Interestingly, the electron attaches into an orbital largely located on the Fe atom, while the charge upon separation of the two metal-centred moieties is retained by the Mn-centred fragment.

The formation of the fragments $[CpFeMn(CO)_{6-n}]^-$ with n = 1 and 2 is attributed to further CO loss from $[CpFeMn(CO)_6]^-$ through the same low energy resonance(s) that led to the formation of $[CpFeMn(CO)_6]^-$, $[Mn(CO)_5]^-$ and $[Mn(CO)_4]^-$. Here, hot band transitions from the high energy tail of the Maxwell-Boltzmann distribution of internal energies at the current experimental temperature are likely to constitute the main contribution to the sharp 0 eV feature in the $[CpFeMn(CO)_4]^-$ yield. The fragments $[CpFeMn(CO)_{6-n}]^-$ with n = 3 and 4, conversely, appear exclusively through fairly broad, but distinct contributions peaking close to 3.8 and 4.5 eV, respectively. We attribute these contributions to a distinct, higher-lying resonance associated with one of the first HOMO-LUMO transitions in this molecule, i.e. a core-excited resonance. The shift of the $[CpFeMn(CO)_2]^-$ ion yield towards higher energy with respect to that of $[CpFeMn(CO)_3]^-$ is accordingly attributed to the higher threshold for the formation of this fragment, making this channel more competitive through the higher energy side of the resonance. We note, however, that we cannot exclude contributions from higher-lying shape resonances at these energies. Finally, the loss of all but one CO, forming $[CpFeMn(CO)]^-$, proceeds explicitly through a yet higher-lying resonance, appearing through a contribution to the ion yield in the region from 6-10 eV with a maximum at about 8 eV.

As discussed above, metal-metal bond cleavage leading to the formation of $[Mn(CO)_5]^-$ is one of the two dominant channels observed in DEA to $[CpFe(CO)_2Mn(CO)_5]$; the counter fragment $[CpFe(CO)_2]^-$ with charge retention on the iron-centred moiety is not observed. The strongly electron-donating Cp anion ligand on the Fe centre, when compared to the 5 π-acid CO ligands on the Mn centre, produces an electron-rich iron centred moiety in the neutral parent molecule. The calculated electron affinity of $[CpFe(CO)_2]$ is positive (1.64 eV, although the electron affinity of $[Mn(CO)_5]$ is about 0.9 eV greater) and the formation of $[CpFe(CO)_2]^-$ from $[CpFe(CO)_2Mn(CO)_5]$ is exothermic by about 0.42 eV. It is therefore thermochemically possible for the charge to be retained by the iron-centred moiety after Fe-Mn bond cleavage; however, this is not observed. This observation is readily explained by the charge distribution within the initially formed TNI and its evolution during the separation of the metal-centred fragments: i.e. its dissociation dynamics.

To get a better understanding of the cleavage of the metal

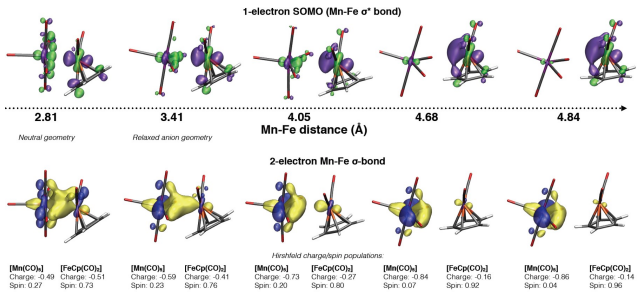

Fig. 6 Elongation of the Mn−Fe bond upon electron attachment. The top part of this figure shows the changing geometry of the singly occupied Mn−Fe σ^* antibonding orbital as the distance between the two metal centres increases, while the bottom part shows the changing geometry of the doubly occupied Mn−Fe σ-bonding orbital (IAO-IBO localized orbital), as well as the Hirshfeld charges and spin populations of the two metal-centred moieties. The electron of the singly occupied σ^* orbital remains primarily on the Fe-centred moiety, producing the spin density map seen in Fig. 5c. The electrons of the doubly occupied σ orbital, however, remain primarily on the Mn-centred moiety, resulting in the experimentally-observed negative charge on the Mn-centred fragments $[Mn(CO)_5]^-$ and $[Mn(CO)_4]^-$.

dimer in the attachment process and formation of $[Mn(CO)_5]^-$ it is useful to first consider the neutral molecule. For this purpose Fig. 5 shows several relevant molecular orbital isosurfaces of both the neutral precursor and the ground state anion. The metal-metal bonding orbital of the neutral precursor is shown in Fig. 5a (HOMO − 2), while the lowest unoccupied orbital of the neutral precursor (LUMO) is shown in Fig. 5b. The singly occupied HOMO of the relaxed molecular anion (SOMO) and the resulting spin density distribution within the ground state anion are shown in Fig. 5c and 5d, respectively. All isosurfaces shown are computed at the BP86 level of theory. Finally, Fig. 6 shows the results of an orbital analysis of the dissociating molecular anion, depicting a relaxed surface scan of the anion where the Mn-Fe distance was varied from 2.81 Å to 4.84 Å.

According to X-ray crystallography the Mn-Fe distance is 2.843 Å,[40] while our gas phase DFT calculations give a bond length of 2.81 Å, indicative of a single metal-metal bond similar to the 2.89 Å Mn−Mn bond length of $Mn_2(CO)_{10}$. Analysis of the occupied canonical molecular orbitals reveal that the HOMO − 2 (Fig. 5a) can be described as essentially a d-based σ-bonding orbital between Fe and Mn. A localized orbital analysis confirms that a stable 2-electron σ-bond exists, and a Mayer bond order of 0.4 between Mn and Fe is calculated (this can be compared to a Mayer bond order of 0.94-1.17 for the Mn−C bonds). The LUMO of the neutral parent molecule (Fig. 5b) is revealed to be the σ^* antibonding counterpart of the Mn-Fe bonding orbital.

Analysis of the SOMO of the parent anion (Fig. 5d), reveals that it is quite similar to the LUMO, suggesting that electron attachment can be envisioned as the attached electron occupying the LUMO of the neutral. As the LUMO is an antibonding Mn−Fe σ^* orbital, occupation of this orbital should lead to elongation of the Mn−Fe bond; in fact, the Mn−Fe bond elongates from 2.81 Å in the neutral to 3.41 Å in the relaxed geometry of the anion. While this analysis corresponds well with the major dissociation channel involving Fe−Mn bond rupture, the SOMO of the anion as well as the spin density (Fig. 5c) reveal that the attached electron is actually more on the Fe-based fragment than the Mn. The dynamics behind the charge retention in this dissociation process can be readily understood by analysis of a relaxed surface scan of the initially formed anion, as shown in Fig. 6. Here, the Fe−Mn bond length was systematically increased from the parent molecule bond length of 2.81 Å to 4.84 Å, producing the experimentally observed $FeCp(CO)_2$ and $[Mn(CO)_5]^-$ fragments. The 1-electron SOMO orbital gradually changes from a slightly Fe-centric Mn-Fe σ^* orbital in the 2.81 Å structure to a more localized Fe d-orbital in the 4.84 Å structure. This confirms that the attached electron is retained by the neutral $FeCp(CO)_2$ fragment. The 2-electron Mn−Fe σ-bonding orbital, however, gradually changes as well (here shown as a localized orbital from IAO-IBO analysis), and ultimately resides on the Mn-centred moiety. As the 2 electrons in the Mn−Fe bonding orbital are therefore retained by the Mn, this produces a $[Mn(CO)_5]^-$ anionic fragment. A Hirshfeld population analysis (also shown in Fig. 6) demonstrates this picture as well, with the anionic charge residing on the closed-shell $[Mn(CO)_5]^-$ fragment with a Mn(-1) oxidation state, d^8 (due to Mn retaining the 2 electrons of the Mn−Fe bond), and the spin residing on the open-shell Fe fragment with a Fe(+1) oxidation state. This reveals the final picture of the dissociation dynamics wherein the attached electron ends up on a different fragment (Fe) than the negative charge (Mn).

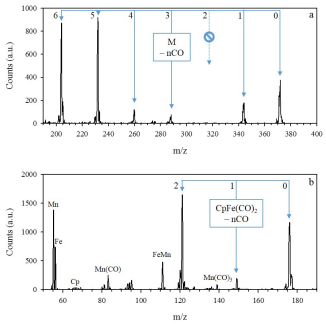

Fig. 7 DI spectra of (η^5-Cp)Fe(CO)$_2$Mn(CO)$_5$ with an incident electron energy of 70 eV. Fig. 7a shows the M-nCO (n = 0-6) progression, which interestingly excludes n = 2, likely due to fast decay processes. Fig. 7b shows the CpFe(CO)$_2$-nCO (n = 0-2) progression, which exhibits some similar behaviour as well as the naked metal fragments, Mn(CO) and the low intensity contribution from the cyclopentadienyl ring.

3.2 Dissociative ionization of CpFe(CO)$_2$Mn(CO)$_5$ in the gas phase

Dissociative ionization spectra of CpFe(CO)$_2$Mn(CO)$_5$ recorded at 70 eV impact energy are shown in Fig. 7. Dissociative ionization is a non-resonant process that sets in at or above the ionization threshold of the parent molecule and increases in efficiency with increasing incident electron energy before levelling off between 50 and 100 eV. Close to the ionization threshold, single bond ruptures commonly dominate the DI spectra; as the energy increases, contributions from more extensive fragmentation reactions increases. The spectra shown in Figure 7 are recorded at 70 eV, which is close to the maxima of all channels and thus gives a good picture of the relative integral cross sections for individual channels in the SE energy range relevant in FEBID. For completeness, Table S1 compares the relative intensities for the individual fragments recorded at 30, 40, 50 and 60 eV, showing that no significant changes are in this energy range.

The most intense fragment produced by dissociative ionization of CpFe(CO)$_2$Mn(CO)$_5$ at 70 eV is [CpFe]$^+$, followed by [CpFe(CO)$_2$]$^+$, [CpFeMn(CO)$_2$]$^+$ and [CpFeMn(CO)]$^+$. There is thus significantly more extensive fragmentation observed through DI of CpFe(CO)$_2$Mn(CO)$_5$ than through DEA. Similarly to DEA, however, the DI spectra is characterized through two principal processes: (a) progressive CO loss from the Fe-Mn moiety and (b) cleavage of the Fe−Mn bond to produce [CpFe(CO)$_2$]$^+$, followed by additional CO loss. Figure 7a shows a DI mass spectrum for CpFe(CO)$_2$Mn(CO)$_5$ in the m/z range from 190 to 400, which encompasses the CO ligand loss progression. As in DEA, 1-6 CO ligands are lost within this progression; however, DI favours much more complete fragmentation, with [M − 5CO]$^+$ and [M − 6CO]$^+$ ([CpFeMn(CO)$_2$]$^+$ and [CpFeMn(CO)]$^+$) being the most abundant fragments. Interestingly, [M − 2CO]$^+$ ([CpFeMn(CO)$_5$]$^+$) is simply missing from the spectra and [M − 3CO]$^+$ ([CpFeMn(CO)$_4$]$^+$) and [M − 4CO]$^+$ ([CpFeMn(CO)$_3$]$^+$) only appear with low intensity. We attribute this to the energetics of these processes in combination with their kinetics. The ionization energy of CpFeMn(CO)$_7$ was calculated at the DLPNO-CCSD(T) level of theory using the aug-cc-pVTZ basis set, and was found to be 6.4 eV. Thresholds for the formation of [CpFeMn(CO)6]$^+$ and [CpFeMn(CO)$_5$]$^+$ at the same level of theory were found to be 7.4 and 9.3 eV, respectively. However, the ground state of the [CpFeMn(CO)$_5$]$^+$ fragment was found to have three bridging CO, similar to the structure previously calculated for the ground state of the neutral CpFeMn(CO)$_5$.[62] The ground state of the [CpFeMn(CO)$_6$]$^+$ fragment, on the other hand, was found to have one bridging carbonyl. These structures are shown along with the respective threshold values in Figure S1 and Table S2 with the supporting information. We anticipate that the rearrangement and internal energy redistribution within [CpFeMn(CO)$_5$]$^+$ is slow compared to further CO loss: i.e. the subsequent CO loss producing [CpFeMn(CO)$_4$]$^+$, etc., takes place before rearrangement to the triply-bridged ground state and the consequent stabilization of the fragment with respect to further CO loss is complete. This in turn reduces its lifetime to such an extent that it is not detected within the current observation time window (see above). A similar situation must apply for [CpFeMn(CO)$_4$]$^+$ and [CpFeMn(CO)$_3$]$^+$; however, as these have dispersed energy by the dissociation of 2 and 3 CO units, respectively, a fraction of these ions still survives the approximately 50 μs flight through the quadrupole mass filter. Hence, while long-lived metastable intermediates may persist long enough to be detected by the mass spectrometer, short-lived intermediates will not. We thus conclude that [CpFeMn(CO)$_5$]$^+$ must quickly decay through further CO loss, while [CpFeMn(CO)$_7$]$^+$ and [CpFeMn(CO)$_6$]$^+$ are metastable products with longer decay times. Finally, the fragments [CpFeMn(CO)$_2$]$^+$ and [CpFeMn(CO)]$^+$ are expected to have discharged the bulk of the initial internal energy through the extensive CO loss leading to their formation and thus have comparably long lifetimes.

Fragment formation in the m/z range from 50 to 90 is shown in Figure 7b. The major contribution in this m/z range is through cleavage of the Fe−Mn bond to produce [CpFe(CO)$_2$]$^+$, accompanied by further CO loss. Here we see similar behaviour to that observed for sequential CO loss from the molecular cation: although [CpFe(CO)$_2$]$^+$ and [CpFe]$^+$ are abundant products, [CpFe(CO)]$^+$ is only observed with marginal intensity. We attribute this to [CpFe(CO)]$^+$ similarly being an unstable decay intermediate that generally fragments further, too quickly to be observed in the current experiment. The bare [FeMn]$^+$ cation, as well as both the bare Fe$^+$ and Mn$^+$ cations, are also observed with appreciable intensity via DI. The cyclopentadienyl ligand, on the other hand, is only observed with low intensity, and no significant fragmentation of the cyclopentadienyl is observed. This is unlike previous observations in DI of MeCpPtMe$_3$,[20] where hydrogen loss and fragmentation of the MeCp ligand dominates the DI spectra, an

effect that may be explained by the changed ion stabilities of H-loss products in the alkylated Cp derivative.

Table 2 Comparison of relative intensities of all DI fragments at 70 eV with those of all DEA fragments in the energy range from 0-12 eV. Relative DI intensities were calculated by integrating the isotope distribution for each fragment and normalizing to the single carbonyl loss fragment. For DEA these were calculated by integrating the intensity of the respective fragments over the energy range from 0-12 eV and normalizing again to the single carbonyl loss fragment. All relative intensities were pressure normalized. Average CO loss per incident was calculated by multiplying the relative intensity of each fragment by number of carbonyls lost and dividing by the total intensity of all fragments. The upper limit of CO loss was calculated by assuming total CO loss from any neutral counterparts, while the lower bound was calculated by assuming no neutral species fragmentation.

Mass	Fragment	DEA	DI
372	$CpFeMn(CO)_7$		190
344	$CpFeMn(CO)_6$	100	100
316	$CpFeMn(CO)_5$	2	
288	$CpFeMn(CO)_4$	0.4	31
260	$CpFeMn(CO)_3$	5	53
232	$CpFeMn(CO)_2$	2	387
204	CpFeMn(CO)	0.3	380
195	$Mn(CO)_5$	135	5
177	$CpFe(CO)_2$		458
167	$Mn(CO)_4$	0.2	7
149	CpFe(CO)		70
139	$Mn(CO)_3$		17
121	CpFe		491
111	$FeMn/Mn(CO)_2$		4118
83	Mn(CO)		45
66	Cp		15
56	Fe		114
55	Mn		196
44	CO_2		14
28	CO		185
16	O		6
Average CO loss	(lower bound)	0.6	3
Average CO loss	(upper bound)	2	6

3.3 Dissociative electron attachment vs. dissociative ionization and comparison of gas phase and surface experiments

Table 2 compares the relative intensities of all DI fragments at 70 eV with the relative intensities of all DEA fragments in the energy range from 0-12 eV. For DI, the relative intensities were calculated by integrating the isotope distribution for each fragment and normalizing it to the single carbonyl loss fragment. For DEA, these were calculated by integrating the intensity of the respective fragments over the energy range from 0-12 eV. In DEA, the two major fragments $[Mn(CO)_5]^-$ and $[CpFeMn(CO)_6]^-$ are fully dominant: they make up 96% of the total negative ion yield and the remaining fragments are insignificant in comparison. The fragmentation is much more extensive in DI, where about half of the total fragment intensity comes from CO loss from the molecular ion, with dominant contributions from the loss of 5 and 6 CO. The other half of the intensity is from fragments produced via rupture of the Fe−Mn bond, where the main fragments produced are $[CpFe(CO)_2]^+$ and $[CpFe]^+$, as well as the naked metal cations. For further comparison, we calculated the average CO loss per dissociation incident through DEA and DI by adding up the relative intensities of each fragment multiplied by the number of carbonyl ligands lost and dividing by the total intensity summed over all fragments formed. For fragments associated with Fe−Mn bond rupture, an upper limit of CO loss was calculated by assuming total CO loss from the neutral counterpart, and a lower bound was calculated by assuming no fragmentation of the neutral species. In this way we derive a lower bound of 3 CO ligands lost per DI incident while the upper bound is about 6 CO. The average CO loss per molecule in DEA, conversely, is about 0.6 ligands per molecule if no further CO loss from the neutral counterpart is assumed. The bulk of the negative ion intensity from DEA to $CpFe(CO)_2Mn(CO)_5$ is close to 0 eV, below the thermochemical threshold for further CO dissociation from the respective neutral counterparts. Considering the high energy tail of the 0 eV contributions and the fragments formed at higher energies, it is reasonable to bracket the average CO loss through DEA between 0.6 and 1.0 ligands per event. This demonstrates that significantly more fragmentation of the parent molecule is initiated by DI than by DEA, and deposition of $CpFe(CO)_2Mn(CO)_5$ via DI in FEBID experiments should produce less carbonaceous deposits than if deposition were to proceed via DEA.

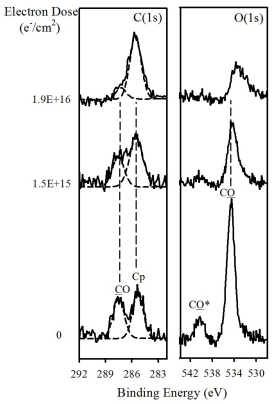

Fig. 8 XPS analysis of the C(1s) and O(1s) regions for ~0.5-3.0 nm thick films of $CpFe(CO)_2Mn(CO)_5$ molecules deposited onto a polycrystalline gold surface at 105K and exposed to 500eV electrons. The bottom spectra are recorded before electron irradiation (0 electron dose) while the upper traces are recorded after $CpFe(CO)_2Mn(CO)_5$ films were exposed to electron doses of $1.5x10^{15}$ and $1.9x10^{16}$ e^-/cm^2.

To provide a comparison with data from gas phase studies, electron-induced dissociation of $CpFe(CO)_2Mn(CO)_5$ molecules adsorbed onto a surface are also presented. Thus, Figure 8 shows X-ray photoelectron spectroscopy (XPS) data on the changes

in the C(1s) and O(2p) regions for 1-2 monolayer films of $CpFe(CO)_2Mn(CO)_5$, adsorbed on a gold surface at about 105 K, and exposed to incremental doses of 500 eV electrons generated from a flood gun source. The XPS data in Fig. 8 is part of a larger study conducted at the Johns Hopkins University, designed to provide a comprehensive assessment of various electron and thermal reactions relevant to FEBID. Full details of the experimental setup may be found in Spencer *et al.* [63].

Upon adsorption and prior to electron irradiation, Fig. 8 shows that the C 1s region contains two major peaks of roughly equal intensity: a lower energy peak at approximately 285.2 eV assigned to the cyclopentadienyl (Cp) carbon atoms, and a higher energy peak at approximately 287.6 eV assigned to the carbonyl carbon atoms.[64,65] There is an additional π to π^* shake-up peak (at higher binding energy) associated with the carbonyl (CO) peak; however, it is very weak in intensity and thus cannot be discerned from the background. As the film is exposed to increasing electron doses ($1.5x10^{15}$ e^-/cm^2 and $1.9x10^{16}$ e^-/cm^2) there is little or no change in the Cp peak, but the CO peak intensity decreases significantly in intensity, such that after an electron dose of $1.9x10^{16}$ e^-/cm^2 it is only observed as a small shoulder in the C(1s) spectral envelope. In the O (1s) region, two peaks are initially observed: a narrow peak at 534.5 eV comprising the carbonyl oxygen (CO) and a higher energy π to π^* shake-up peak (CO*) at 541.2 eV.[64,65] As the electron dose increases the intensity of the main O 1s peak decreases significantly in intensity, broadens and shifts to a slightly lower binding energy, while the shake-up peak disappears. Changes in both the C(1s) and O(1s) regions shown in Fig 8 are thus consistent with CO desorption from the film occurring as a result of electron irradiation, with no desorption of any carbon atoms from the Cp ring.

Quantitative analysis of the C(1s) and O(1s) areas measured as a function of electron dose, and conducted as part of the study at Johns Hopkins University, revealed that there was no further changes for electron doses in excess of $1.9x10^{16}$ e^-/cm^2. The oxygen-to-carbon ratio changed from being slightly above the stoichiometric 7:12 O:C ratio (about 0.6:1) prior to electron irradiation to an approximate ratio of 2:7 (about 0.3:1), while the O(1s) area decreases by approximately 70% of its initial value. Based on the stoichiometry of the $CpFe(CO)_2Mn(CO)_5$ molecule, these changes in the O:C ratio and O(1s) area indicate that ~5 CO molecules desorb from the surface as the molecularly adsorbed precursor undergoes electron stimulated decomposition. However, in contrast to gas phase experiments, adsorbed precursor molecules are simultaneously exposed to all of the secondary electrons generated by the interaction of the primary beam with the substrate. Consequently, the XPS data shown in Fig. 8 represents the ensemble averaged change in chemical composition in the $CpFe(CO)_2Mn(CO)_5$ film caused by the reactions of these secondary electrons with the adsorbed precursor molecules.

When compared with the gas phase data, however, surface data may allow us to elucidate the likely initial step in the decomposition/deposition of $CpFe(CO)_2Mn(CO)_5$ upon electron impact. In this respect the persistence of the cyclopentadienyl ligand and and the loss of CO ligands in the surface experiments is consistent with gas phase observations for both DEA and DI of $CpFe(CO)_2Mn(CO)_5$. The average number of CO groups lost from the surface in Fig. 8 (~5 CO), is much higher than observed in DEA (0.6-1 CO), but within range of our expectations from DI (3-6 CO). This analysis suggests that the initial step in the electron-induced decomposition of $CpFe(CO)_2Mn(CO)_5$ adsorbed on a surface is driven by DI rather than DEA. However, we stress that we cannot comment on the potential role played by ND or by surface-activation induced further dissociation of reactive intermediates in these experiments.

4 Conclusions

We have presented gas phase DEA and DI ion yields and relative cross-sections for the potential FEBID precursor $CpFe(CO)_2Mn(CO)_5$, and we have used high-level coupled cluster calculations to aid the interpretation of our gas phase observations and to better understand the nature of the underlying negative ion states in DEA. Additionally, we report on the electron-induced dissociation of adsorbed $CpFe(CO)_2Mn(CO)_5$ molecules and compare the nature of this process with the DEA and DI branching ratios observed in the gas phase. This specific molecule was studied for its bimetallic/heteronuclear architecture, as its FeMn metal core is considered to have potential for FEBID of functional alloy structures.

In summary, with regards to DEA to $CpFe(CO)_2Mn(CO)_5$, the dominant channels observed are single CO loss and cleavage of the Fe-Mn bond under $[Mn(CO)_5]^-$ formation, partly associated with a preceding single CO loss from the iron-containing moiety. Sequential CO loss from the molecular anion is also observed but to a much lesser extent than the two dominating channels. The average CO loss in these DEA processes is in the range from 0.6 to 1 CO unit per incident. For the metal-metal bond cleavage in DEA, charge retention is exclusively on the Mn-centred fragment; we rationalize that through quantum chemical calculations of the molecular orbital evolution during the dissociation process. The thermochemical thresholds, calculated at the DPLNO-CCSD(T) level of theory with aug-cc-pVTZ and aug-cc-pVQZ basis sets, agree well with our observations and allow a consistent interpretation of the experimental results. The persistence of the pi-bound cyclopentadienyl ligand is similar to that previously observed for other polyhapto ligands[19,63] and we do not observe the quasi-continuous attachment profile recently reported for the high-performance heteronuclear FEBID precursor $HFeCo_3(CO)_{12}$.[32,33] On the contrary, we consider the electron attachment profile of $CpFe(CO)_2Mn(CO)_5$ to be characterized by discrete resonances with insignificant overlap. With regards to DI, the predominant channels are the loss of 5 and 6 CO, the formation of $[CpFe(CO)_n]$ + with n = 0 and 2 and the formation of the bare metal cations Fe^+ and Mn^+. The fragmentation through DI is considerably more extensive than we observe through DEA, and we derive a lower limit of 3 and a higher limit of 6 for the average CO loss per incident through DI.

Electron-induced fragmentation of adsorbed $CpFe(CO)_2Mn(CO)_5$ molecules is qualitatively in good agreement with the gas phase data, showing evidence of CO desorption but no indication of cyclopentadienyl group desorption. In the initial electron induced fragmentation of adsorbed $CpFe(CO)_2Mn(CO)_5$

molecules an average of 5 CO molecules desorb. In direct comparison with the DI and DEA branching ratios observed in the gas phase, this suggests that DI-initiated deposition is dominant in the decomposition of $CpFe(CO)_2Mn(CO)_5$ on the surface, rather than DEA.

We do not expect $CpFe(CO)_2Mn(CO)_5$ to produce high metal content depositions in FEBID, largely due to the persistence of the cyclopentadienyl ligand both in the gas phase and on the surface. The likelihood of significant co-deposition of carbon from this ligand may require the use of post-deposition processing [4,5] in order to use this molecule as a precursor for the production of FeMn alloys via FEBID.

5 Acknowledgements

This work was conducted under the support of the Icelandic Center of Research (RANNIS; Grants No. 13049305 and 141218051), the University of Iceland Research Fund. The authors acknowledge the collaborative platform provided by the COST Action CM1301, CELINA and RMT acknowledges financial support for a STSM within CELINA. LM-W and DHF thank the US National Science Foundation for support through the linked collaborative grants CHE-1607547 and CHE-1607621.

References

1 J. M. De Teresa, A. Fernández-Pacheco, R. Córdoba, L. Serrano-Ramón, S. Sangiao and M. R. Ibarra, *Journal of Physics D: Applied Physics*, 2016, **49**, 243003.

2 J. MartÄŚÍĄn, J. Nogués, K. Liu, J. Vicent and I. K. Schuller, *Journal of Magnetism and Magnetic Materials*, 2003, **256**, 449–501.

3 W. M. Kaminsky, G. A. C. Jones, N. K. Patel, W. E. Booij, M. G. Blamire, S. M. Gardiner, Y. B. Xu and J. A. C. Bland, *Applied Physics Letters*, 2001, **78**, 1589–1591.

4 I. Utke, P. Hoffmann and J. Melngailis, *Journal of Vacuum Science & Technology B: Microelectronics and Nanometer Structures*, 2008, **26**, 1197.

5 W. F. van Dorp and C. W. Hagen, *Journal of Applied Physics*, 2008, **104**, 081301.

6 Willem F. van Dorp, Bob van Someren, , . Cornelis W. Hagen, P. Kruit and P. A. Crozier, 2005.

7 F. Porrati, M. Pohlit, J. Müller, S. Barth, F. Biegger, C. Gspan, H. Plank and M. Huth, *Nanotechnology*, 2015, **26**, 475701.

8 L. Serrano-Ramón, R. Córdoba, L. A. Rodríguez, C. Magén, E. Snoeck, C. Gatel, I. Serrano, M. R. Ibarra and J. M. De Teresa, *ACS Nano*, 2011, **5**, 7781–7787.

9 E. Begun, O. V. Dobrovolskiy, M. Kompaniiets, R. Sachser, C. Gspan, H. Plank and M. Huth, *Nanotechnology*, 2015, **26**, 075301.

10 R. Córdoba, D.-S. Han and B. Koopmans, *Microelectronic Engineering*, 2016, **153**, 60–65.

11 R. M. Thorman, R. Kumar T. P., D. H. Fairbrother and O. Ingólfsson, *Beilstein Journal of Nanotechnology*, 2015, **6**, 1904–1926.

12 J. Schaefer and J. Hoelzl, *Thin Solid Films*, 1972, **13**, 81–86.

13 R. Schmied, J. D. Fowlkes, R. Winkler, P. D. Rack and H. Plank, *Beilstein Journal of Nanotechnology*, 2015, **6**, 462–471.

14 T. Verduin, S. Lokhorst, C. Hagen and P. Kruit, *Microelectronic Engineering*, 2016, **155**, 114–117.

15 N. Silvis-Cividjian, C. Hagen, L. Leunissen and P. Kruit, *Microelectronic Engineering*, 2002, **61-62**, 693–699.

16 P. C. Hoyle, J. R. A. Cleaver and H. Ahmed, *Applied Physics Letters*, 1994, **64**, 1448–1450.

17 S. G. Rosenberg, M. Barclay and D. H. Fairbrother, *The Journal of Physical Chemistry C*, 2013, **117**, 16053–16064.

18 S. G. Rosenberg, M. Barclay, D. H. Fairbrother, D. H. Fairbrother, K. A. Dunn, J. J. L. Mulders, S. J. Randolph, M. Toth, K. Al-Shamery, T. Kluner and M. Baumer, *Physical Chemistry Chemical Physics*, 2013, **15**, 4002.

19 J. D. Wnuk, J. M. Gorham, S. G. Rosenberg, W. F. van Dorp, T. E. Madey, C. W. Hagen and D. H. Fairbrother, *The Journal of Physical Chemistry C*, 2009, **113**, 2487–2496.

20 S. Engmann, M. Stano, Š. Matejčík and O. Ingólfsson, *Physical Chemistry Chemical Physics*, 2012, **14**, 14611.

21 S. Engmann, M. Stano, P. Papp, M. J. Brunger, Š. Matejčík and O. Ingólfsson, *The Journal of Chemical Physics*, 2013, **138**, 044305.

22 O. May, D. Kubala, M. Allan, A. A. Viggiano, G. K. Rekha, A. E. Stevens and G. A. Tolstikov, *Phys. Chem. Chem. Phys.*, 2012, **14**, 2979–2982.

23 K. Wnorowski, M. Stano, C. Matias, S. Denifl, W. Barszczewska and Š. Matejčík, *Rapid Communications in Mass Spectrometry*, 2012, **26**, 2093–2098.

24 O. Ingólfsson, F. Weik and E. Illenberger, *International Journal of Mass Spectrometry and Ion Processes*, 1996, **155**, 1–68.

25 I. Bald, J. Langer, P. Tegeder and O. Ingólfsson, *International Journal of Mass Spectrometry*, 2008, **277**, 4–25.

26 E. Böhler, J. Warneke, P. Swiderek, H. D. Fairbrother, S. Matejcik, P. Swiderek and P. Swiderek, *Chemical Society Reviews*, 2013, **42**, 9219.

27 L. G. Christophorou, *Electron-molecule interactions and their applications*, Academic Press, 1984.

28 H. Hotop, M.-W. Ruf, M. Allan and I. Fabrikant, *Physica Scripta*, 2004, **2004**, 85–216.

29 C. R. Arumainayagam, H.-L. Lee, R. B. Nelson, D. R. Haines and R. P. Gunawardane, *Surface Science Reports*, 2010, **65**, 1–44.

30 I. I. Fabrikant, S. Eden, N. J. Mason and J. Fedor, *Advances In Atomic, Molecular, and Optical Physics*, 2017, **66**, 545–657.

31 D. Klar, M.-W. Ruf and H. Hotop, *International Journal of Mass Spectrometry*, 2001, **205**, 93–110.

32 R. K. T P, S. Barth, R. Bjornsson and O. Ingólfsson, *The European Physical Journal D*, 2016, **70**, 163.

33 R. K. T P, R. Bjornsson, S. Barth, O. Ingólfsson, C. Gspan, H. Plank, M. Huth, M. R. Ibarra and J. M. D. Teresa, *Chem. Sci.*, 2017, **8**, 5949–5952.

34 M. Zlatar, M. Allan and J. Fedor.

35 R. C. Che, M. Takeguchi, M. Shimojo, W. Zhang and K. Furuya, *Applied Physics Letters*, 2005, **87**, 223109.

36 L. Bernau, M. Gabureac, R. Erni and I. Utke, *Angewandte Chemie International Edition*, 2010, **49**, 8880–8884.

37 F. Porrati, B. Kämpken, A. Terfort and M. Huth, *Journal of Applied Physics*, 2013, **113**, 053707.

38 R. K. T P, I. Unlu, S. Barth, O. Ingólfsson and D. H. Fairbrother, *submitted*, 2017.

39 R. K. T P, P. Weirich, L. Hrachowina, M. Hanefeld, R. Bjornsson, H. R. Hrodmarsson, S. Barth, D. H. Fairbrother, M. Huth and O. Ingólfsson, *submitted*, 2017.

40 P. J. Hansen and R. A. Jacobson, *Journal of Organometallic Chemistry*, 1966, **6**, 389–398.

41 E. H. Bjarnason, B. Ómarsson, S. Engmann, F. H. Ómarsson and O. Ingólfsson, *The European Physical Journal D*, 2014, **68**, 121.

42 F. Neese, *Wiley Interdisciplinary Reviews: Computational Molecular Science*, 2017, e1327.

43 A. D. Becke, *Physical Review A*, 1988, **38**, 3098–3100.

44 J. P. Perdew, *Physical Review B*, 1986, **33**, 8822–8824.

45 F. Weigend, R. Ahlrichs, K. A. Peterson, T. H. Dunning, R. M. Pitzer and A. Bergner, *Physical Chemistry Chemical Physics*, 2005, **7**, 3297.

46 S. Grimme, J. Antony, S. Ehrlich and H. Krieg, *The Journal of Chemical Physics*, 2010, **132**, 154104.

47 S. Grimme, S. Ehrlich and L. Goerigk, *Journal of Computational Chemistry*, 2011, **32**, 1456–1465.

48 C. Riplinger and F. Neese, *The Journal of Chemical Physics*, 2013, **138**, 034106.

49 C. Riplinger, B. Sandhoefer, A. Hansen and F. Neese, *The Journal of Chemical Physics*, 2013, **139**, 134101.

50 C. Riplinger, P. Pinski, U. Becker, E. F. Valeev and F. Neese, *The Journal of Chemical Physics*, 2016, **144**, 024109.

51 M. Saitow, U. Becker, C. Riplinger, E. F. Valeev and F. Neese, *The Journal of Chemical Physics*, 2017, **146**, 164105.

52 T. H. Dunning, *The Journal of Chemical Physics*, 1989, **90**, 1007–1023.

53 N. B. Balabanov and K. A. Peterson, *The Journal of Chemical Physics*, 2005, **123**, 064107.

54 F. Neese, 2006.

55 G. Knizia, *Journal of Chemical Theory and Computation*, 2013, **9**, 4834–4843.

56 I. Mayer, *Chemical Physics Letters*, 1983, **97**, 270–274.

57 I. Mayer, *International Journal of Quantum Chemistry*, 1984, **26**, 151–154.

58 I. Mayer, *Theoretica Chimica Acta*, 1985, **67**, 315–322.

59 I. Mayer, *Modelling of Structure and Properties of Molecules*, Ellis Horwood: Chicester, 1987, ch. On the che.

60 R. M. Thorman, R. Bjornsson and O. Ingólfsson, *The European Physical Journal D*, 2016, **70**, 164.

61 R. M. Thorman, J. A. Brannaka, L. McElwee-White, O. Ingólfsson, F. Biegger, C. Gspan, H. Plank, M. Huth, A. V. Walker, T. L. Windus and W. A. D. Jong, *Phys. Chem. Chem. Phys.*, 2017, **19**, 13264–13271.

62 X. Feng, N. Li, L. Lv, R. B. King, J. P. Piquemal, D. N. Beratan, W. Yang, N. S. Dalal, N. Kaur and D. Zipse, *New J. Chem.*, 2016, **40**, 7482–7492.

63 J. A. Spencer, J. A. Brannaka, M. Barclay, L. McElwee-White and D. H. Fairbrother, *The Journal of Physical Chemistry C*, 2015, **119**, 15349–15359.

64 M. Barber, J. A. Connor, M. F. Guest, M. B. Hall, I. H. Hillier and W. N. E. Meredith, *Faraday Discuss. Chem. Soc.*, 1972, **54**, 219–226.

65 E. W. Plummer, W. R. Salaneck and J. S. Miller, *Physical Review B*, 1978, **18**, 1673–1701.